



# THIN FILM OPAL PHOTONIC CRYSTALS

(PHOTONISCHE KRISTALLE AUS DÜNNEN OPAL-FILMEN)

DISSERTATION

zur Erlangung des akademischen Grades eines Doktors der  
Ingenieurwissenschaften (Dr.-Ing.)

vorgelegt im

Fachbereich Elektrotechnik, Informationstechnik und  
Medientechnik der Bergischen Universität Wuppertal

von

**Dipl.-Phys. Torsten Maka**

aus Wuppertal

*“If only it were possible to make dielectric materials  
in which electromagnetic waves cannot propagate at  
certain frequencies, all kinds of almost-magical things  
would be possible.”*

John Maddox, *Nature* **348**, 481 (1990)

Erstgutachter: Prof. Dr. rer. nat. Clivia M. Sotomayor Torres

Zweitgutachter: Prof. Dr. rer. nat. Ludwig Josef Balk

Drittgutachter: Prof. Dr. rer. nat. Rudolf Zentel

Tag der mündlichen Prüfung: 14.07.2004

## German Abstract Zusammenfassung

Die heute in allen Gebieten der Technik gegenwärtige moderne Elektronik wurde im Prinzip durch das Verständnis der elektronischen Struktur diverser Halbleitermaterialien und insbesondere durch die Möglichkeit, die elektronischen Eigenschaften dieser Materialien gezielt zu beeinflussen, ermöglicht. Das Ziel auf dem Weg zu optischen Schaltkreisen ist eine ähnlich umfassende Kontrolle der Eigenschaften von Licht in Materie. Der Schlüssel zum Erreichen dieses Ziels könnte eine neue Materialklasse, sogenannte *Photonische Kristalle* sein.

Photonische Kristalle können in mehrfacher Hinsicht als ein optisches Analogon zu klassischen elektronischen Halbleitern angesehen werden; so bilden sie z.B. eine photonische Bandstruktur. Sie bieten daher ein großes Potential zur Realisierung neuartiger optischer Schaltkreiskonzepte mit dem Ziel integrierte optische Schaltungen zu entwickeln, die ohne elektronische Komponenten auskommen.

Ein Beispiel für einen dreidimensionalen Photonischen Kristall ist der Edelstein Opal. Opale bestehen aus Kugeln mit Durchmessern im sub- $\mu\text{m}$  Bereich, die in einer kubisch-flächenzentrierten Kristallstruktur angeordnet sind. Sie können künstlich durch einen Selbstorganisationsprozeß hergestellt werden und sind daher seit einigen Jahren ein Modellsystem zur Untersuchung von Photonischen Kristallen.

Im Rahmen dieser Arbeit wurden dünne Kristallfilme aus künstlichem Opal und deren invertierte Repliken aus hochbrechenden Halbleitermaterialien mittels Rasterelektronenmikroskopie und spektroskopischer Verfahren untersucht. Insbesondere wurde die kristalline Qualität von großflächigen Photonischen Kristallen, die aus einer Suspension von Polymerkugeln auf hydrophilisierten Substraten hergestellt wurden, betrachtet und im Hinblick auf deren Tauglichkeit als Photonische Kristalle bewertet. Die Eignung dieses Herstellungsverfahrens konnte gezeigt werden.

Optische Phänomene in Photonischen Kristallen, die auf deren Brechungseigenschaften beruhen, wurden ebenso untersucht, wie der Einfluß auf die Emissionseigenschaften von eingebetteten Laserfarbstoffen. Die gefundenen Effekte, wie die Modifikation der Spontanen Emission, konnten als Konsequenz der photonischen Bandstruktur erklärt und mit theoretischen Modellen verglichen werden. Eine Methode zur zerstörungsfreien Messung der Schichtdicke von dünnen Photonischen Kristallfilmen, basierend auf der Analyse von Fabry-Pérot Interferenzen, wurde entwickelt und mit direkten und invertierten Opalfilmen getestet.

Zusätzlich wurde eine Reihe von Machbarkeitsstudien durchgeführt, um den Einsatz von opalbasierten Photonischen Kristallfilmen in möglichen Anwendungen zu testen. Hier sind insbesondere das Wachstum von Photonischen Kristallen auf strukturierten Substraten, und die Möglichkeit polymerbasierte Photonische Kristallfilme durch Elektronenstrahlithographie zu strukturieren, zu nennen.

**Abstract**

Modern electronics plays a vital role in almost all aspects of modern technology and was made possible by understanding and controlling the electronic properties of certain materials. As an increasingly achievable and desirable goal is to tailor the properties of light, the key might be a new class of materials called "*Photonic Crystals*".

Photonic crystals are regarded in many ways as the optical analogue to semiconductor crystals. They offer the potential for major breakthroughs in optoelectronics, leading to novel device concepts for integrated optical circuits.

One example of a three-dimensional photonic crystal is an artificial opal that grows in a self-assembly process as a face centred cubic crystal; it has been used as a model system for photonic crystals for several years.

Thin films of artificial opals and their high-index semiconductor replicas have been studied by scanning electron microscopy and optical spectroscopy. In particular the crystal quality of large area thin film photonic crystals, grown by casting a suspension of polymer beads on hydrophilised substrates, was evaluated regarding the suitability to grow photonic crystals. The feasibility of this growth-concept was proven by optical and SEM inspections.

Optical diffraction phenomena in opals such as the stop band dispersion and band branching have been investigated and compared to theoretical calculations. A novel, destruction free method based on the analysis of Fabry-Pérot oscillations was revealed to measure the thickness of thin photonic crystal films and judge their crystalline quality. It was tested with direct and inverse opals.

The modification of the emission properties of laser-dye impregnated opals, such as emission suppression / enhancement and changes in the directionality of emission, have been interpreted as the consequence of the photonic band gap.

## Table of Contents

<b>THIN FILM OPAL PHOTONIC CRYSTALS .....</b>	<b>I</b>
<b>1. INTRODUCTION .....</b>	<b>1</b>
<b>2. PHOTONIC CRYSTALS .....</b>	<b>4</b>
2.1. CONCEPT OF PHOTONIC CRYSTALS .....	4
2.2. ELECTROMAGNETIC WAVES IN PERIODIC MEDIA.....	7
2.2.1. <i>The macroscopic Maxwell equations</i> .....	7
2.2.2. <i>The reciprocal lattice</i> .....	10
2.2.3. <i>Influence of the lattice type on the existence of omnidirectional photonic band gaps</i> .....	11
2.2.4. <i>The Plane Wave Expansion method</i> .....	13
2.2.5. <i>The filling factor</i> .....	18
2.3. BASIC DIFFRACTION PROPERTIES IN OPALS .....	18
2.3.1. <i>Diffraction resonances and Bragg's law</i> .....	18
2.3.2. <i>The refractive index</i> .....	21
2.3.3. <i>Dispersion surfaces and photon focussing</i> .....	24
2.4. DIMENSIONAL ASPECTS OF PHOTONIC CRYSTALS .....	25
2.4.1. <i>One-dimensional Photonic Crystals</i> .....	25
2.4.2. <i>Two-dimensional Photonic Crystals</i> .....	27
2.4.3. <i>Three-dimensional Photonic Crystals</i> .....	28
2.4.4. <i>Thin film Photonic Crystals</i> .....	28
2.5. APPLICATIONS OF PHOTONIC CRYSTALS .....	30
<b>3. ANALYTICAL TECHNIQUES .....</b>	<b>31</b>
3.1. SPECTROSCOPY .....	31
3.1.1. <i>The spectrometer</i> .....	31
3.1.2. <i>Reflection and transmission spectroscopy</i> .....	36
3.1.3. <i>Photoluminescence spectroscopy</i> .....	36
3.1.4. <i>Raman spectroscopy</i> .....	36
3.2. SCANNING ELECTRON MICROSCOPY .....	39
<b>4. EXPERIMENTAL SET UP .....</b>	<b>44</b>
4.1. REFLECTION AND TRANSMISSION MEASUREMENTS .....	44
4.1.1. <i>Reflection / transmission set up</i> .....	44
4.2. PHOTOLUMINESCENCE MEASUREMENTS.....	47
4.2.1. <i>Ar<sup>+</sup> ion laser</i> .....	48
4.2.2. <i>Photoluminescence set up</i> .....	48
4.3. RAMAN SPECTROMETER .....	51
<b>5. OPAL BASED PHOTONIC CRYSTALS .....</b>	<b>55</b>
5.1. SILICA OPALS .....	55
5.2. OPAL POLYMER COMPOSITES.....	57
5.3. POLYMERIC THIN FILM OPALS.....	58
5.3.1. <i>Synthesis of polymer spheres</i> .....	59
5.3.2. <i>Preparation of thin film crystals</i> .....	61
5.4. INVERTED STRUCTURES.....	75
5.4.1. <i>Semiconductor-infilled opals and semiconductor replicas</i> .....	75
5.4.2. <i>Preparation of TiO<sub>2</sub> and SnS<sub>2</sub> thin film opal replicas</i> .....	77

<b>6. OPTICAL DIFFRACTION IN OPALS .....</b>	<b>84</b>
6.1. REFLECTANCE OF DIRECT OPALS .....	84
6.2. FABRY-PÉROT OSCILLATIONS.....	89
6.3. REFLECTANCE OF INVERTED OPALS.....	97
6.4. BAND BRANCHING IN THIN FILM OPALS .....	101
6.5. BAND BRANCHING IN INVERTED OPALS .....	107
6.6. POLARISATION DEPENDENCE OF BRAGG REFLECTION .....	108
6.7. CONCLUSIONS .....	116
<b>7. EMISSION FROM OPAL PHOTONIC CRYSTAL STRUCTURES .....</b>	<b>118</b>
7.1. SPECTRAL REDISTRIBUTION OF THE EMISSION INTENSITY.....	121
7.2. CHANGES OF THE EMISSION RATE.....	128
7.3. DIRECTIONALITY OF EMISSION IN SNS <sub>2</sub> REPLICAS .....	130
7.4. EMISSION FROM CdTe LOADED OPAL FILMS .....	137
<b>8. FEASIBILITY STUDIES.....</b>	<b>145</b>
8.1. METALLO-DIELECTRIC OPALS. ....	145
8.2. PHOTONIC CRYSTAL PRESSURE SENSOR.....	147
8.3. STRUCTURING OF OPAL BASED THIN FILM PHOTONIC CRYSTALS.....	151
8.3.1. <i>Sedimentation on patterned substrates</i> .....	151
8.3.2. <i>Multi-layer opals</i> .....	153
8.3.3. <i>Electron-beam structuring of PMMA opals</i> .....	155
<b>9. CONCLUSIONS.....</b>	<b>158</b>
<b>BIBLIOGRAPHY .....</b>	<b>162</b>
<b>LIST OF PUBLICATIONS AND PRESENTATIONS ARISEN FROM THIS WORK .....</b>	<b>170</b>
<b>ACKNOWLEDGEMENTS.....</b>	<b>172</b>
<b>CURRICULUM VITAE .....</b>	<b>173</b>
<b>EIDESSTATTLICHE ERKLÄRUNG .....</b>	<b>174</b>

## Notation and Symbols

### I. Abbreviations

a.u.	arbitrary units
fcc	face centred cubic
hcp	hexagonal close packed
pDOS	photonic density of states
APCVD	atmospheric pressure chemical vapour deposition
BZ	Brillouin zone
EM	electromagnetic
FP	Fabry-Pérot
FT	Fourier transformation
FWHM	full width at half-maximum
IES	iso-energy surface
LDOS	local density of photonic states
MFP	mean free path
NIR	near infrared
PBG	photonic band gap
PhC	Photonic Crystal
PL	photoluminescence
PMMA	poly(methylmethacrylate)
PMT	photomultiplier tube
PWM	plane wave expansion method
RI	refractive index
RIC	refractive index contrast
SE	spontaneous emission
SEM	scanning electron microscope
SFEP	surfactant free emulsion polymerisation
THF	tetrahydrofuran
TMM	transfer matrix method
UV	ultraviolet
VIS	visible

## II. Symbols

$\vec{k}$	wave vector
$\vec{r}$	arbitrary position vector
$\vec{E}$	electric field
$\vec{H}$	magnetic field
$a$	lattice constant in <i>fcc</i> lattices
$c$	velocity of light
$d$	film thickness
$\hbar$	Planck's constant
$f$	filling factor = volume fraction of high- $\epsilon$ material in composites
$l^*$	mean free path
$m$	diffraction order
$n$	refractive index ( $= \sqrt{\epsilon}$ )
$n_{eff}$	effective refractive index
$t$	time
$D$	sphere diameter
$E$	energy (in eV)
$I$	intensity
$L_B$	Bragg attenuation length
$P$	power
$\epsilon$	dielectric constant
$\lambda$	wavelength (in nm)
$\omega$	angular frequency
$\varphi$	azimuthal angle
$\theta$	angle of incidence (with respect to the surface normal)
$\Omega$	solid angle

## 1. Introduction

The movement of electrons in semiconductors is well understood and can be controlled and harnessed in electronic devices; this is the basis of modern electronics. The next goal is the replacement of microelectronic components by optical micro-devices. The flow of light is much harder to control and manipulate. However, for all-optical components it would be necessary to control the propagation of photons, similar to the electric current flow in conventional electronics. In certain dielectric nanostructures, a so-called “*Photonic Crystal*” (PhC), a fundamentally new electromagnetic effect can be realised: the localization of light. This might be the key to the utilisation of light-waves in micro-photonic circuits, which use novel device concepts.

PhCs are of great interest for both fundamental and applied research. Since they were first proposed in 1972 by V. P. Bykov [1] and then further in the late 1980s by E. Yablonovitch and S. John [2, 3] PhCs have gained increasing interest.

PhCs are periodic dielectric structures that are designed to affect the propagation of electromagnetic (EM) waves in the same way as the periodic potential in a conventional crystal affects the electron motion. In the latter case, “allowed” and “forbidden” electronic energy bands build up, whereas for PhCs “allowed” and “forbidden” energy bands for the propagation of photons are created, known as “*photonic band gaps*” (PBG). The cause for the existence of a PBG is resonant scattering of light from a periodic modulation of the refractive index in one, two, or three dimensions. The length scale of the modulation is of the same order of magnitude as the wavelength of the EM waves of interest – i.e.  $\approx 250$  nm for a PBG in the visible region of the EM spectrum. This implies a range of technological challenges put on the fabrication of PhCs, especially in three dimensions.

The absence of permitted propagating EM modes of certain energies inside PhC structures gives rise to distinct optical phenomena, such as the inhibition of spontaneous emission or directional and spectral re-distribution of light emission. These effects can be used for building high-reflecting omnidirectional mirrors, low-loss-waveguides, on-chip optical interconnects, or low-threshold lasers, among others. Thus PhCs or, more generally, photonic band-gap structures, are particularly attractive optical materials for controlling and manipulating the flow of light.

PhCs are expected to enter commercial devices soon [4]. Two dimensional PhCs can be produced by using a range of established nanotechnological approaches, such as lithography and etching. They have already reached a level, where applications are within sight. Their three-dimensional counterparts are still far from commercialization. Nevertheless, they will offer additional advantages that will become important, when some technological challenges,

such as manufactureability, are under control, as well as when some principal difficulties, such as disorder in self-assembled systems, are solved. Active research on three-dimensional PhCs is currently in progress to understand the underlying light matter interactions and to synthesise high quality three-dimensional PhCs by self-assembly or nanotechnological approaches.

On the other hand, nature has produced certain living organisms with photonic band gap structures working in the visible. One prominent example is found in the colours of butterfly wings, which are textured with periodic features in the micron and submicron scale leading e.g. to the iridescent blue colour of the Morpho rhetenor butterfly [5]. A less well known example is the sea mouse, a marine worm that is partly covered with long, feltlike threads that produce a brilliant iridescence [6].

Possibly the most widely known PhC is the precious gem stone opal, that disperses visible light since it consists in fact of a 3-D grating with periodicities in the sub- $\mu\text{m}$  range. Its well known opalescent play of colour, depicted in figure 1.1, is the result of a PBG effect. Synthetic opals are therefore seen as promising PBG material for optoelectronics applications.

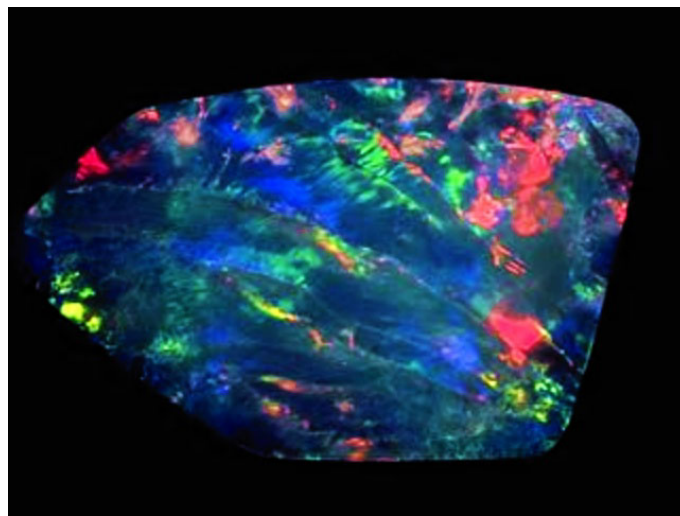


**Figure 1.1:** Natural opal found in Andamooka, South Australia. The gem stone opal is in fact a three-dimensional PhC. Its opalescence is the result of a PBG effect (image from <http://www.gem.org.au>).

Artificial opals are, for example, produced by sedimentation of monodisperse amorphous silica spheres [7]. The spheres self-assemble into closely packed face centred cubic (*fcc*) crystals. Opals made from spheres with diameters in the 200 nm range show photonic band gaps in the visible region of the spectrum (2 - 3 eV, 500 - 650 nm). Thus the whole visible and near infrared (NIR) spectrum is accessible. It is possible to obtain very homogenous *fcc*

lattices that can be used as matrix material for different PBG materials [8]. Intense work to use the optical properties of opal as PBG material are in progress [9, 10]. One key advantage of opaline structures in contrast to PhCs produced by means of nanotechnology is the self-assembling nature of opal which allows it to avoid many constraints still connected to the artificial production of nanostructures. Despite big technological improvements achieved during the last years, man-made three-dimensional structures still suffer from the lack of periods in the third dimension, from alignment problems etc.

Opal structures can also be build also from monodisperse polymer beads that similarly self-assemble in *fcc* structure. From these polymer beads thin film opal crystals can be grown on Si or glass substrates and offer a number of advantages over their silica-based bulk counterparts. They, for example, can be impregnated with organic laser-dyes, offer an improved structural quality and they can easily be inverted by filling the voids with high-refractive-index-material and subsequent removal of the polymer beads.

The *fcc* structure of opal with its close-to-spherical Brillouin zone is an attractive configuration for the development of PBGs. Therefore opals have been used as a model system for PhCs since 1995.

In this work opal based PhCs and their inverted replicas have been investigated and their optical properties have been studied as a function of different parameters, such as refractive index contrast and filling factor.

In chapter 2 the basic concepts and physics of PhCs are recapitulated, including some considerations on calculation methods and applications of PhCs. The experimental methods based on optical spectroscopy and electron microscopy as well as the used experimental set-ups are described in chapter 3 and 4.

Chapter 5 outlines the preparation of direct silica and polymer thin film opals and their high-refractive-index replicas and describes some details of the synthesis routes and obtained sample quality..

The main result of the thesis are presented in chapter 6 (diffraction) and 7 (emission). They include the analysis of stop band dispersion, band branching and Fabry-Pérot oscillations in angle resolved reflectance / transmission measurements as well as investigations of modifications in the emission properties of laser-dyes embedded in PhCs.

The results of some small feasibility studies are shown in chapter 8 where also some suggestions for further work are made. In chapter 9 a summary of the obtained results is given.

## 2. Photonic Crystals

### 2.1. Concept of Photonic Crystals

A “*Photonic Crystal*” (PhC) represents a novel class of dielectric materials that exhibit a periodically varying dielectric constant. This leads to a band of forbidden frequencies where propagation of electromagnetic (EM) waves is inhibited. This behaviour is well known from the electronic band structure in conventional semiconductor crystals and has led to the term “optical semiconductor” for photonic crystals.

A widely used example of a one-dimensional (1D) PhC is the well known dielectric mirror, or “quarter wave stack” of alternating layers of different dielectric materials. Light of a matched wavelength incident on this mirror is completely reflected. The physical reason is, that the incident wave is scattered at the layer interfaces and the multiple scattered waves interfere destructively for certain frequencies. This effect is used in many devices such as Fabry-Pérot filters, coated lenses and many more.

To build two- or three-dimensional PhCs the object has to show periodic variations in the dielectric constant in two or three dimensions, respectively, as sketched in figure 2.1.

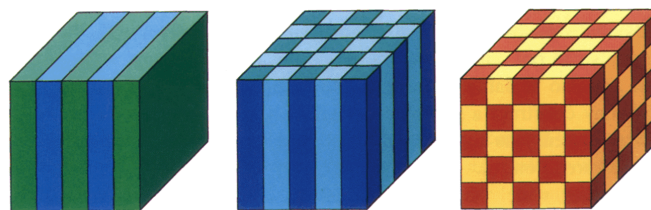


**Figure 2.1:** Sketch of a 1D, 2D and 3D PhC. The different colours represent materials with different dielectric constants. The important characteristic of a PhC is its periodicity in one or more directions (reproduced from [11]).

The band structure for photons is called a “photonic band structure” and the ranges of forbidden frequencies are therefore named “*photonic band gaps*” (PBG). “If, for some frequency range, a PhC reflects light of any polarisation incident at any angle, we say that the crystal has a complete photonic band gap” [11]. In other words, for any polarisation both, the electric and magnetic fields, have to experience a band gap. This is a very strong condition which has not been achieved for visible light to date.

In figure 2.2 the band structure diagram of a 1D PhC is shown. The PBGs are shaded. Regardless of the wave vector  $\vec{k}$ , no EM modes can exist within the crystal in this frequency range, building up an omnidirectional PBG. Since the main power of the  $E$ -field of electromagnetic modes *below* the gap is concentrated in *high- $\epsilon$*  regions and vice versa, the band directly below a gap is referred to as the *dielectric band* and the band above the gap is the *air band*. This is pretty much the same situation as the electronic band structure in semiconductor physics where the fundamental gap has the *valence band* below and the *conduction band* above.

The depth of the modulation of the periodically varying dielectric constant, in other words the refractive index contrast (RIC), determines the width of the PBGs. Theoretical calculations show that for the *fcc* symmetry – which is the preferred symmetry to obtain an omnidirectional PBG in 3D since the Brillouin-zone is close to a spherical shape, as described in chapter 2.2.3 – the RIC should be larger than 2.8 for the existence of a omnidirectional PBG [12, 13]. A “*directional PBG*” or “*pseudo-gap*”, that only exists in certain directions can be realised for much lower RIC.

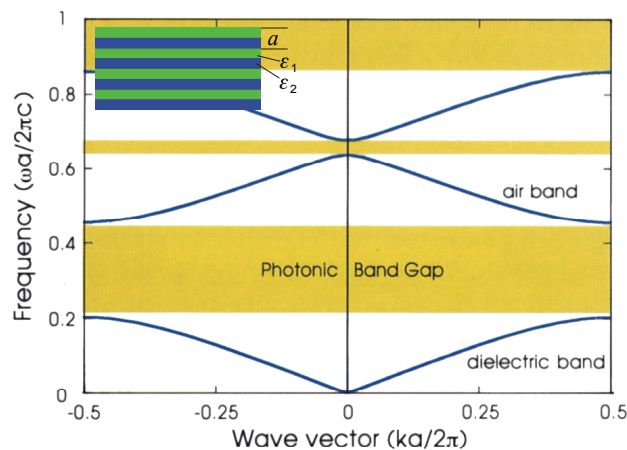


**Figure 2.2:** Sample photonic band structure of a 1D multilayer film with lattice constant  $a$  and alternating dielectric constants  $\epsilon_1$  and  $\epsilon_2$ . Within the shaded regions no allowed mode can exist, regardless of  $k$ , thus a full PBG builds up (adopted from [11]).

PBG structures can be used to increase the efficiency of active and passive optical devices due to the suppressed spontaneous emission within the PBG leading to lower losses through unwanted spontaneous emission [2] or lower scattering losses in waveguides. This has been clearly demonstrated for microwaves and in the visible regime by various groups [14].

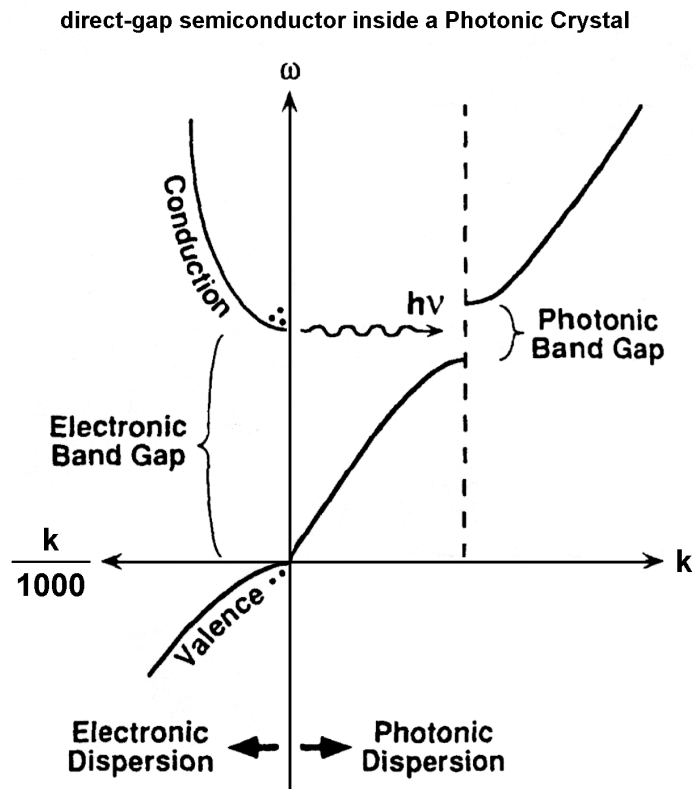


**Figure 2.3:** Principle mechanism of inhibiting spontaneous emission inside of a perfect photonic crystal. On the right hand side the photonic dispersion relation is depicted. It shows a PBG covering the band edge of the conduction band. It shares the same frequency axis with the electronic dispersion relation of a typical direct-gap semiconductor on the left hand side. The dots above the conduction band and below the valence band represent electrons and holes, respectively. A radiative electron-hole recombination under emission of a photon is forbidden since the frequency of the photon lies inside of the PBG (adopted from [15]).

The principle mechanism of inhibition of spontaneous emission is depicted in figure 2.3 for a direct-gap semiconductor embedded in a PhC. The plot shows on the left hand side electronic dispersion of the semiconductor. The black points in the conduction and valence bands represent electrons and holes, respectively. The right side shows the photonic dispersion, sharing the same frequency axis. If an electron and a hole would recombine radiatively, a photon with a frequency of the band-to band transition would be produced. Since the PBG covers the electronic band edge, the radiated photon would have a frequency falling into the PBG range. It would not be allowed to propagate within the PhC thus the spontaneous radiative recombination of electrons and holes is inhibited.

The underlying physical concepts to describe the building up of PBGs will be explained in more detail in the following sections.

## 2.2. Electromagnetic waves in periodic media

The underlying physical effect is the interference between incident and scattered EM waves inside a periodic dielectric lattice. For a 3D lattice the effect is comparable to Bragg scattering of x-rays in a atomic lattice, therefore many of the well known concepts of crystallography are applicable to these materials.

### 2.2.1. The macroscopic Maxwell equations

Electromagnetic phenomena in dielectric materials are described in their general form, including wave propagation inside of photonic crystals, by the macroscopic Maxwell-equations [16]. In their differential form they are in cgs units:

$$\nabla \cdot \vec{B} = 0 \qquad \nabla \times \vec{E} = -\frac{1}{c} \frac{\partial \vec{B}}{\partial t} \qquad (2.1)$$

$$\nabla \cdot \vec{D} = 4\pi\rho \qquad \nabla \times \vec{H} = \frac{1}{c} \frac{\partial \vec{D}}{\partial t} + \frac{4\pi}{c} \vec{J} \qquad (2.2)$$

where  $\rho$  and  $\vec{J}$  describe the free charges and current density, respectively;  $c$  is the velocity of light in vacuum and  $t$  the time.  $\vec{E}$  and  $\vec{B}$  are the macroscopic electric field and the strength of the magnetic field induction, that can be obtained by averaging the  $\vec{E}$  and  $\vec{B}$  fields derived from the microscopic Maxwell equations. The macroscopic values  $\vec{D}$  and  $\vec{H}$ , described as dielectric displacement and magnetic field strength, respectively, are being introduced to account for the electric and magnetic polarisability of media.

These equations are difficult to solve even numerically in their general form. Therefore certain assumptions on the material properties have to be made to simplify the calculations. Restricting the calculations to macroscopic, homogeneous, linear, optically isotropic media, we find a simple proportional relationship between  $\vec{D}$  to  $\vec{E}$  and  $\vec{B}$  to  $\vec{H}$ :

$$\vec{D} = \varepsilon(\vec{r}, \omega) \cdot \vec{E} \qquad \text{and} \qquad \vec{H} = \frac{\vec{B}}{\mu} \qquad (2.3)$$

Here  $\varepsilon$  and  $\mu$  are the dielectric function and magnetic permeability, respectively (i.e. in general a tensor 2. order). The explicit frequency dependence of  $\varepsilon(\vec{r}, \omega)$  can be omitted since the dielectric function is almost constant in the visible wavelength region. It should be mentioned that the refractive index (RI) is connected to  $\varepsilon$  via  $n = \sqrt{\varepsilon}$ . Since the dielectric function is obviously not spatially constant in photonic crystals, this dependence has to be taken into account by using  $\varepsilon(\vec{r})$  as the general form. For most common dielectric materials  $\mu$  is very close to unity and can be neglected. This approximation is of course not valid for ferromagnetic materials but for dielectric materials the restriction to  $\mu = 1$  is a very good

approximation. The further assumption of no free charges and currents and a real dielectric constant (i.e. no absorption losses) leads to the following set of simplified Maxwell equations by setting  $\rho = \vec{J} = 0$ :

$$\nabla \cdot \vec{H} = 0 \qquad \nabla \times \vec{E} = -\frac{1}{c} \frac{\partial \vec{H}}{\partial t} \qquad (2.4)$$

$$\nabla \cdot \varepsilon(\vec{r}) \vec{E} = 0 \qquad \nabla \times \vec{H} = \frac{\varepsilon(\vec{r})}{c} \frac{\partial \vec{E}}{\partial t} \qquad (2.5)$$

For all PhCs investigated in this thesis, the given approximations and simplifications are fully justified, thus the equations (2.4) and (2.5) will deliver reliable results.

In general the spatial and temporal behaviour of the electric and magnetic fields can be separated (because of the linearity of the Maxwell equations) using an harmonic waves-approach:

$$\vec{H}(\vec{r}, t) = \vec{H}(\vec{r}) \cdot e^{i\omega t} \qquad \text{and} \qquad \vec{E}(\vec{r}, t) = \vec{E}(\vec{r}) \cdot e^{i\omega t} \qquad (2.6)$$

Combining with the simplified Maxwell equations (2.4) and (2.5) leads to

$$\nabla \times \vec{E} = -\frac{i\omega}{c} \vec{H}(\vec{r}) \qquad (2.7)$$

$$\nabla \times \vec{H} = \frac{i\omega}{c} \varepsilon(\vec{r}) \vec{E}(\vec{r}) \qquad (2.8)$$

The combination of both equations results in the wave equations for the magnetic and electric eigenmodes of the system:

$$\nabla \times \frac{1}{\varepsilon(\vec{r})} \nabla \times \vec{H}(\vec{r}) = \left(\frac{\omega}{c}\right)^2 \vec{H}(\vec{r}) \qquad (2.9)$$

$$\nabla \times \nabla \times \vec{E}(\vec{r}) = \varepsilon(\vec{r}) \left(\frac{\omega}{c}\right)^2 \vec{E}(\vec{r}) \qquad (2.10)$$

These equations represent a linear eigenvalue problem on  $\vec{H}$  or  $\vec{E}$  that can be solved using standard numerical techniques. The information about the PhC is fully given by the dielectric function  $\varepsilon(\vec{r})$ , which periodic in space.

It should be noted that for a spatially constant dielectric function  $\varepsilon$  the dispersion relation of plane waves in a homogenous medium is obtained from the master equations (2.9) or (2.10) if the electric or magnetic fields are expanded into plane waves of the form  $e^{i\vec{k} \cdot \vec{r}}$ :

$$\frac{\vec{k}^2}{\varepsilon} = \left(\frac{\omega}{c}\right)^2 \quad \text{or} \quad \omega(\vec{k}) = \frac{c}{\sqrt{\varepsilon}} |\vec{k}| \quad (2.11)$$

The term  $\omega(\vec{k})$  – representing the dispersion relation of light in a homogenous medium – is known as the “light line”. The wave vector  $\vec{k}$  of a plane wave propagating within a dielectric medium with frequency  $\omega$  will be enlarged by a factor of  $n = \sqrt{\varepsilon}$  and therefore the wavelength  $\lambda = 2\pi/|\vec{k}|$  will be reduced by a factor of  $1/\sqrt{\varepsilon}$ . This has to be taken into account for all calculations.

Because of the periodic modulation of  $\varepsilon$ , the equations (2.9) or (2.10) have to be solved explicitly for a periodically modulated dielectric constant. In section 2.2.2 the basic concepts to handle phenomena in periodic media are briefly illustrated.

### 2.2.1.1. Comparison between electronic and photonic band structure problem

A comparison with the electronic band structure problem, described by the (time independent) Schrödinger equation:

$$\left[-\frac{\hbar}{2m}\nabla^2 + V(\vec{r})\right]\Psi(\vec{r}) = E\Psi(\vec{r}) \quad (2.12)$$

with a periodic Potential  $V(\vec{r})$  shows a very strong analogy between the description of electron movement in a periodic potential and photon movement in a periodic dielectric structure.

In conventional crystals the periodic potential is created by atom cores (black dots in figure 2.4 right), whereas in a photonic crystal the periodically modulated dielectric constant plays a similar role.

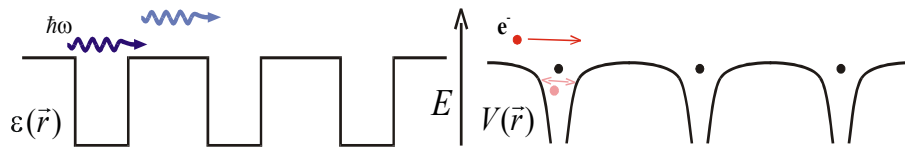


**Figure 2.4:** The propagation of Photons (left) and electrons (right) through a periodic medium can be described by a similar formalism. In contrast to electrons no localised photons are possible.

Despite the similarity of both equations of motion there are important differences:

- Electrons have – in contrast to photons – a rest mass, therefore their dispersion relation is parabolic in the vicinity of the origin, whereas the photon dispersion relation is linear (cf. equation (2.11)).
- Photons are bosons, but electrons are fermions and therefore only one electron can occupy one quantum mechanical state, whereas an unlimited number of photons can exist in the same state. This implies that the solution of the Maxwell equations is exact, whereas the solutions of the Schrödinger equation is only an approximation for multi-electron systems that has to be corrected to account for electron-electron interaction.
- In contrast to the scalar wave function of electrons the electromagnetic field has a vector character. It has been proven that this fact has substantial influence on the existence and position of the PBGs. It is responsible for the polarisation dependence of PBG features and leads to much more restrictive conditions for band gap opening.
- The Schrödinger equation has also negative eigenvalues and thus allows the existence of localised electrons. In the Maxwell equation only the square of the eigenfrequencies are present and thus negative solutions are forbidden. This indicates that localised photons are much more difficult to realise. Thus for a thorough simulation of the PBG properties a full vector calculation of Maxwell's equations has to be performed.
- Electrons carry a charge, photons do not. Thus electrons interact via Coulomb forces with the lattice potential leading to the existence of quasi-particles such as excitons, polaritons or plasmons. They do not exist in the photonic case.

Nevertheless, many well established concepts of solid state physics to solve problems of wave propagation in periodic potentials can be applied to the case of PhCs without major changes. Here the concepts of the reciprocal space, Brillouin zones, Bloch functions etc. are extremely useful and will be explained in brief in the next sections.

### 2.2.2. The reciprocal lattice

A crystal in general and the PhC in particular is characterised by a periodic arrangement of its “atoms” in space. The crystal structure can be described by a translation operator. This lattice is produced by three vectors  $\vec{a}, \vec{b}, \vec{c}$ , the primitive translation vectors. They are defined such that every lattice point can be reached from any other lattice point by a simple translation  $\vec{R} = u_1\vec{a}_1 + u_2\vec{a}_2 + u_3\vec{a}_3$  with integers  $u_1, u_2, u_3$ . This also means that each local property of the crystal is invariant under translations  $\vec{R}$ .

It is often more feasible to use the respective *reciprocal* lattice. This is defined analogous by three primitive vectors  $\vec{b}_1, \vec{b}_2, \vec{b}_3$ , which are connected to the primitive vectors of the direct lattice by the following relations:

$$\vec{b}_1 = 2\pi \frac{\vec{a}_2 \times \vec{a}_3}{\vec{a}_1 \cdot (\vec{a}_2 \times \vec{a}_3)}, \quad \vec{b}_2 = 2\pi \frac{\vec{a}_3 \times \vec{a}_1}{\vec{a}_1 \cdot (\vec{a}_2 \times \vec{a}_3)}, \quad \vec{b}_3 = 2\pi \frac{\vec{a}_1 \times \vec{a}_2}{\vec{a}_1 \cdot (\vec{a}_2 \times \vec{a}_3)} \quad (2.13)$$

The transformation from the real to the reciprocal lattice is equivalent with a transition to the Fourier space, which is a natural step in analysing periodical features.

The Wigner-Seitz Cell is defined as the primitive cell of a crystal in real space – which is formed as the set of points that are closer to a given lattice point than to any other lattice point. Its analogy in reciprocal space is called the first *Brillouin zone* (BZ). It plays a crucial role in the description in the analysis of the energy band structure in electronic and photonic crystals and also offers a vivid picture of diffraction within the crystal. Details can be found in every solid state physics textbook (see for example Refs. [17, 18]).

### 2.2.3. Influence of the lattice type on the existence of omnidirectional photonic band gaps

The centre-frequency of the PBG is determined by the Bragg-condition, that is fulfilled by wavevectors ending on the surface of the first BZ. Depending on the lattice the Bragg condition is satisfied for different frequencies in different directions. The gaps in generally do not overlap unless they are very wide. A directional PBG is the result.

A two dimensional example for a square lattice is shown in figure 2.5. Due to the square shape of the Brillouin zone the wavevectors  $\vec{k}_1$  and  $\vec{k}_2$  have different magnitudes at the different positions on the surface of the first BZ. Thus the gaps in  $\Gamma$ - $X$  and  $\Gamma$ - $W$  direction open up at different frequencies and do not overlap (unless they are very wide).

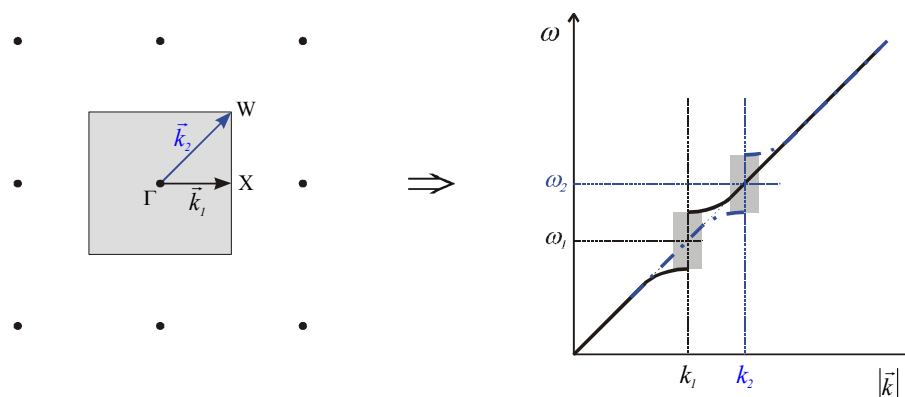


**Figure 2.5:** First BZ of the square lattice (left, shaded). The Bragg condition is satisfied for different magnitudes of  $k$  along different propagation directions. Thus the gap opens at different frequencies for different propagation directions that do not generally overlap – resulting in a directional PBG.

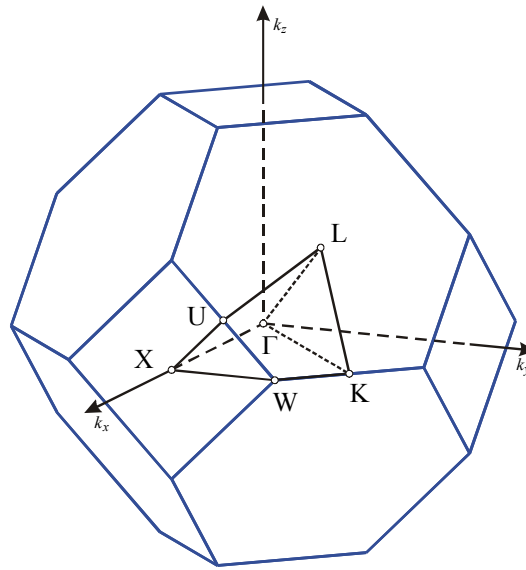


**Figure 2.6:** First Brillouin zone of the *fcc* lattice with standard naming of high-symmetry points. The lines connecting the circles define the boundaries of the irreducible part of the Brillouin zone.

To improve the chances to build up an omnidirectional or full PBG the shape of the Brillouin zone has to be as close to spherical as possible [19].

In three dimensions the *fcc* lattice is favourable since its Brillouin zone is a truncated octahedron and therefore close to spherical (compared to the other Bravais lattices). An omnidirectional PBG can be expected to open up between the 8th and 9th bands (cf. figure 2.7). Since the band is located between high-frequency bands it is unfortunately very sensitive to disorder within the crystal structure [20]. In figure 2.6 the first BZ for a *fcc* crystal is shown, together with the common naming of high symmetry points.

It should be mentioned that the diamond structure is even more favourable to show an omnidirectional PBG. The Bravais lattice of the diamond structure is *fcc* as well, but with a two-atom basis, thus with a different structure factor that supports the opening of an omnidirectional PBG. The gap opens between the 2<sup>nd</sup> and 3<sup>rd</sup> band and is approximately three times wider than the gap in a simple *fcc* structure [21] and more robust against disorder and structural defects [22]. Unfortunately the diamond structure is difficult to produce artificially and can not be created by a self-assembly process of spheres. Therefore the considerations are restricted to the simple *fcc* structure in the following.

The above mentioned considerations illustrate once more that it is difficult to obtain an omnidirectional PBG because of the requirements to the crystal structure and that opal is – from the structural point of view – a promising material to show an omnidirectional PBG.

#### 2.2.4. The Plane Wave Expansion method

To analyse wave propagation in periodic systems and to compute the photonic band structure the plane wave expansion method (PWM) is a widely used technique. It is based on the Bloch-Floquet theorem, which allows to expand the eigenfunctions  $\Psi$  of a wave equation in a periodic environment in the form of plane waves, which are modulated by a lattice-periodic function:

$$\Psi_{\vec{k}}(\vec{r}) = u_{\vec{k}}(\vec{r}) \cdot e^{i\vec{k} \cdot \vec{r}} \quad (2.14)$$

with a periodic function  $u_{\vec{k}}(\vec{r})$ , which has the same periodicity as the lattice, i.e.

$$u_{\vec{k}}(\vec{r}) = u_{\vec{k}}(\vec{R} + \vec{r}) \quad \forall \vec{R} \quad (2.15)$$

with any allowed translation vector  $\vec{R}$  as defined in chapter 2.2.2. Thus the eigenfunction of a wave equation on a periodic lattice is the product of a plane wave  $e^{i\vec{k} \cdot \vec{r}}$  and the lattice periodic function  $u_{\vec{k}}(\vec{r})$ , where the wave vector  $\vec{k}$  can be restricted to the first BZ.

Because of its periodicity, the expansion into plane waves of  $u_{\vec{k}}(\vec{r})$  can only contain lattice-periodic wave vectors. A set of these vectors is represented by the reciprocal lattice vectors. Thus, in general, we can expand  $u_{\vec{k}}(\vec{r})$  into a Fourier series over all allowed reciprocal lattice vectors  $\vec{G}$ :

$$u_{\vec{k}}(\vec{r}) = \sum_{\vec{G}} \tilde{u}_{\vec{G}} \cdot e^{i\vec{G} \cdot \vec{r}} \quad (2.16)$$

Different approaches has been introduced to construct a suitable master equation from Maxwell's equations to present a fast-converging and robust algorithm to compute the photonic band structure [21, 23, 24]. The solution proposed by Ho, Chan and Soukoulis [21] using (2.9) as master equation is most commonly used at the moment.

Applying the plane wave expansion concept to the photonic band structure problem, the (lattice periodic) dielectric tensor  $\varepsilon(\vec{r})$  or, more precise, its reciprocal value is expanded into a Fourier series:

$$\varepsilon^{-1}(\vec{r}) = \sum_{\vec{G}} \tilde{\varepsilon}_{\vec{G}}^{-1} \cdot e^{i\vec{G} \cdot \vec{r}} \quad (2.17)$$

with Fourier coefficients  $\tilde{\epsilon}$ . In addition, the Bloch theorem is applied to the electromagnetic fields propagating within the periodic medium.  $H(\vec{r})$  can be written as a Bloch function, which is expanded into plane waves. In three dimensions the vector-nature of  $H$  has to be taken into account (since there is no decoupling of the two transverse polarisations). As a consequence the full vector problem has to be solved

The expansion of the magnetic field results in :

$$H(\vec{r}) \equiv H_{\vec{k}}(\vec{r}) \stackrel{Bloch}{=} u(\vec{r}) \cdot e^{i\vec{k} \cdot \vec{r}} = e^{i\vec{k} \cdot \vec{r}} \cdot \sum_{\vec{G}} \sum_{\lambda=1}^2 \tilde{h}_{\vec{G}}^{\lambda} \hat{e}_{\vec{G}}^{\lambda} \cdot e^{i\vec{G} \cdot \vec{r}} = \sum_{\vec{G}} \sum_{\lambda=1}^2 \tilde{h}_{\vec{G}}^{\lambda} \hat{e}_{\vec{G}}^{\lambda} \cdot e^{i(\vec{k} + \vec{G}) \cdot \vec{r}} \quad (2.18)$$

Here the fact  $\nabla \cdot H(\vec{r}) = 0$  allows to restrict the expansion of (2.18) to two orthogonal polarisation unit-vectors  $\hat{e}_{\vec{G}}^{\lambda=1,2}$  that label the two transverse polarisations for any plane wave  $\vec{G}$  and have to be calculated for every  $\vec{G}$  [21].

Insertion of the two equations (2.17) and (2.18) into master equation (2.9) leads to an infinite, hermitic matrix eigenvalue problem for the eigenfrequencies  $\omega(\vec{k})$  of the crystal for given wave vector  $\vec{k}$  of the form:

$$\sum_{\vec{G}} \sum_{\lambda'=1}^2 M_{\vec{G}\vec{G}'}^{\lambda\lambda'} h_{\vec{G}}^{\lambda} = \left( \frac{\omega}{c} \right)^2 \tilde{h}_{\vec{G}}^{\lambda} \quad (2.19)$$

with matrix elements given by:

$$M_{\vec{G}\vec{G}'}^{\lambda\lambda'} = \left| \vec{k} + \vec{G} \right| \left( \hat{e}_{\vec{G}}^{\lambda} \cdot \epsilon_{\vec{G}-\vec{G}'}^{-1} \cdot \hat{e}_{\vec{G}'}^{\lambda'} \right) \left| \vec{k} + \vec{G}' \right| \quad (2.20)$$

To get the photonic band structure (2.19) has to be solved for both, eigenvalues and eigenvectors. This can be done using standard numerical methods by truncating the infinite matrix by retaining only a finite number of reciprocal lattice vectors. The main numerical difficulty is to compute the Fourier coefficients of  $\epsilon^{-1}(\vec{r})$ . There are basically (for isotropic dielectric tensors as in cubic systems) two way this can be done. The first (direct) method relies on calculating the dielectric tensor in real space, inverts it and calculates the Fourier coefficients. The second method, suggested by Ho, Chan and Soukoulis, requires evaluation of the real-space dielectric tensor in the primitive unit cell, Fourier-transforming it into reciprocal space and then inverting it [21]. The latter method has been proven to converge substantially faster than the direct method [25]. To calculate the lowest bands with an accuracy better than 1% approx. 750 plane waves are sufficient in most cases.

Since the Fourier coefficients  $\tilde{\kappa}$  carry all information on the crystal they play a central role to determine the photonic band structure. They are determined by the known structure of  $\varepsilon(\vec{r})$  in real space by integrating over the volume  $V$  of the lattice's primitive unit cell (Wigner-Seitz cell):

$$\tilde{\varepsilon}_{\vec{G}}^{-1} = \frac{1}{V} \int_{\text{cell}} d^3r \varepsilon^{-1}(\vec{r}) \cdot e^{-i\vec{G}\cdot\vec{r}} \quad (2.21)$$

The Fourier coefficients can be calculated for a given geometry and any set of reciprocal lattice vectors. For any given wavevector  $\vec{k}$  a set of allowed eigenfrequencies  $\omega_n(\vec{k})$  is obtained, sorted by frequency and numbered with the band-index  $n$ . Thus the dispersion relation of PhCs can be calculated and plotted as the photonic band-diagram as it is shown in figure 2.7 for a face centred cubic lattice of silica balls in air and inverted opal, where an omnidirectional PBG emerges between the 8<sup>th</sup> and 9<sup>th</sup> band. The band structures shown here were computed<sup>†</sup>, using a freely available software package based on the PWM [26]. More

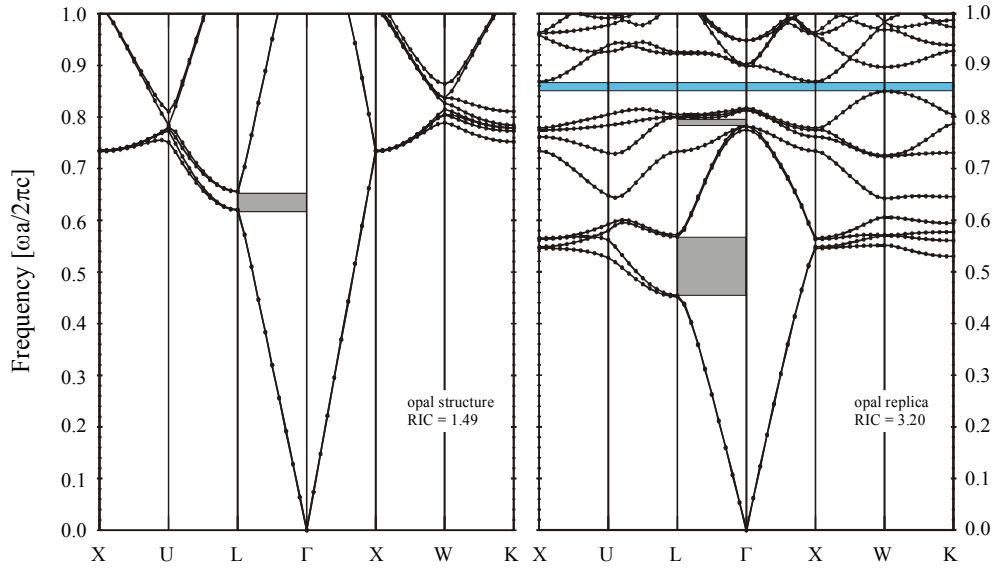


**Figure 2.7:** Photonic band structure for direct and inverted opal of different RIC. A full PBG can not build up in direct opal due to insufficient RIC (left). For inverted opal with a high refractive index an omnidirectional PBG emerges between the 8<sup>th</sup> and 9<sup>th</sup> band (right, blue shaded). A directional gap in  $\Gamma$ -L direction is always present between the 2<sup>nd</sup> and 3<sup>rd</sup> band (grey shaded).

<sup>†</sup> band structure calculations were done by Dr. D.N. Chigrin, Institute of Materials Science, University of Wuppertal, Germany.

details on the calculation of PBG structures can be found in numerous publications [for an overview see 27, 28].

A second important source of information on the optical properties of PhCs is the photonic density of states (pDOS)  $N(\omega)$ . The pDOS represents the allowed number of photonic states at a given frequency. The basic idea is the “enumeration” of all allowed states in all photonic bands for a given frequency  $\omega$ .

This can be done by calculating the sum over all bands of the integral over the first BZ of a Dirac- $\delta$ -function:

$$N(\omega) = \sum_n \int_{BZ} d^3k \delta(\omega - \omega_n) \quad (2.22)$$

The result is the overall pDOS or availability of modes of a given frequency.

For a detailed analysis however it is necessary to know the local coupling strength between, for example, dye molecules sitting at specific positions within the unit cell and the electromagnetic field inside a photonic crystal. If this dye molecule wants to emit a photon with frequency  $\omega$ , the overlap matrix element of the atomic dipole moment and the photons existing in this mode at the dye-molecule’s location determines the emission rate. This can be taken into account by looking at the local density of states (LDOS), defined as:

$$N(\vec{r}, \omega) = \sum_n \int_{BZ} d^3k \left| \vec{E}_{n,\vec{k}}(\vec{r}) \right|^2 \delta(\omega - \omega_n) \quad (2.23)$$

The LDOS differs usually considerably from location to location in the unit cell and also from the pDOS. This indicates that the location of the active species within the unit cell strongly influences its emission properties. It therefore makes a difference to have emitters uniformly distributed all over the unit cell or only at well defined locations [29].

The calculation of pDOS and LDOS requires suitable discretisation of the integrals in (2.22) or (2.23) and is very similar to electronic band structure calculations [26, 30]. As for the electronic band structure, flat bands lead to high pDOS and vice versa. Inside of a complete PBG the pDOS/LDOS vanishes per definition. In figure 2.8, the pDOS of a PhC with an incomplete PBG (direct opal) and a PhC with an omnidirectional PBG (inverted silicon opal) are compared. In the latter case the pDOS is strongly altered compared to the free space case. It is significantly reduced in the vicinity of pseudo-gaps and it vanishes completely in the omnidirectional PBG.

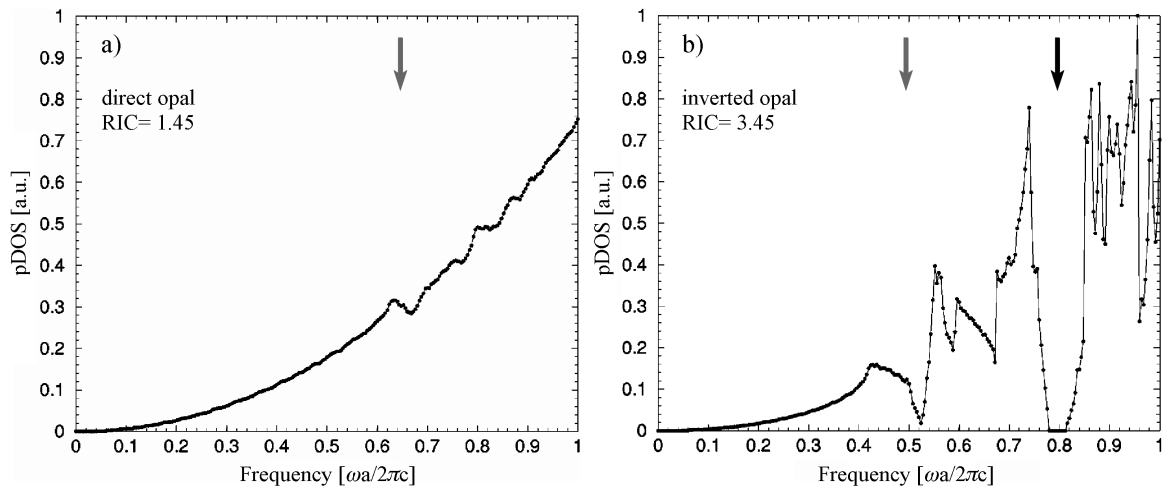


**Figure 2.8:** pDOS of a fcc lattice of silica spheres in air (opal),  $n_{Sph} = 1.45$ . The total pDOS (integrated over all directions) is only perturbed slightly by the presence of photonic pseudo-gaps (indicated by the grey arrow) (a). pDOS of air spheres in a silicon matrix (inverted opal),  $n_{Si} = 3.45$ . The increased RIC leads to a stronger alteration of the pDOS in the vicinity of pseudo-gaps (grey arrow) and a vanishing pDOS in the omnidirectional PBG (black arrow) (b) (adopted from Ref. [29]).

If a full gap can not be obtained as for the example in figure 2.8a, the pDOS is only changed marginally – this illustrates the difficulty to analyse the influence of the photonic structure on the spontaneous emission etc. in PhCs with directional PBGs. Although the emission properties are influenced strongly in certain directions, the averaged effect can be very small.

### 2.2.5. The filling factor

Apart from the refractive index contrast the volume fraction that is filled with high refracting material is a variable that can be used to optimise the width of a photonic band gap. The so called “*filling factor*”,  $f$ , is defined as the part of the total volume of a PhC that is actually filled with high- $\epsilon$  material. Calculations show that the width of a PBG in a PhC changes, depending on the filling factor, as shown qualitatively in figure 2.9 for a given RIC of 3.4. The grey bars indicate the filling factors that are expected in opals (74%) and their inverted replicas (26%), respectively. It is clearly visible, that a filling factor of  $\approx 30\%$  favours the opening of the PBG. Therefore inverted opals are more suitable to show a wide PBG than their non-inverted matrices.

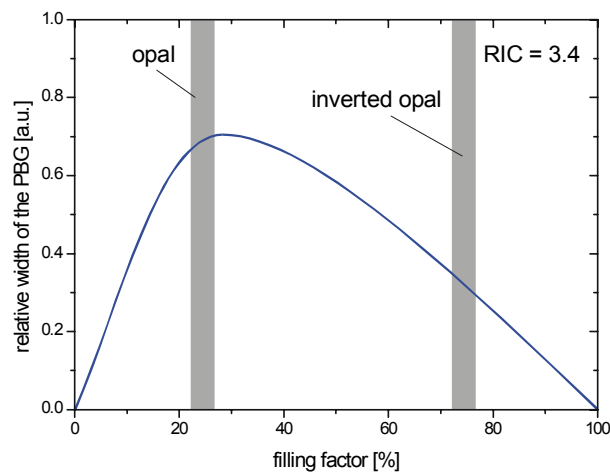


**Figure 2.9:** Sketch of the relative width of the PBG as function of the volume fraction of high-refractive material present in the structure.

## 2.3. Basic diffraction properties in opals

### 2.3.1. Diffraction resonances and Bragg's law

As there are no PBGs available for opal based PhCs with low refractive index contrasts ( $\text{RIC} < 2.8$ ), the experiments were undertaken by investigation of directional PBG or pseudo-gaps, where light propagation in certain directions is prohibited. They can be experimentally detected by peaks in reflectance spectra or dips in transmission spectra in certain directions. The RIC is defined to be  $n_{Hi} : n_{Lo}$  in this work, where the subscript *Hi* (*Lo*) refers to the

material with the higher (lower) refractive index, independent if the spheres or the filled voids have the higher refractive index.

Self-assembled opals usually grow with their (111) planes parallel to the substrate, thus the optic properties along the  $\Gamma$ -L direction are experimentally accessible. The first pseudo-gap band in this direction, centred at  $a/\lambda \approx 0.67$ , was used to perform all experiments presented in this thesis (cf. figure 2.7).

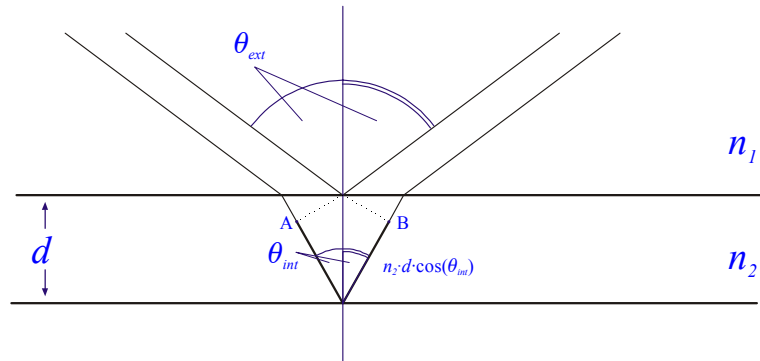


**Figure 2.10:** Bragg's law: Reflection of light from crystal planes leads to constructive interference if the path difference ( $\overline{AB}$ ) of two reflected beams is an integer multiple of the wavelength – in analogy to x-ray diffraction. The refractive index inside the PhC ( $n_2$ ) is substantially different from unity. This has to be taken into account.

To compare experimental data to theoretical predictions it is most accurate to use band structure calculations as described in the previous chapter. Nevertheless, a simple analytical expression based on the well known Bragg equation is quite accurate for the lowest energy bands. By regarding the spheres as point scatterers forming crystallographic planes, interferences of light scattered from different planes can arise, in analogy to the well known Bragg-peaks in x-ray diffraction. In contrast to x-rays – where the refractive index is always very close to unity – for PhCs the refractive index has to be taken into account by merging Snell's law with the Bragg equation (see figure 2.10.):

Starting from the Bragg equation [31]

$$2n_2d_{hkl} \cos\theta_{int} = m \cdot \lambda \quad (2.24)$$

with an inter-plane distance  $d_{hkl}$ , diffraction order  $m$  and refractive indices  $n_1$  and  $n_2$  the substitution of the internal incident angle  $\theta_{int}$  with the external incident angle derived from Snell's law

$$n_1 \sin \theta_{ext} = n_2 \sin \theta_{int} \quad (2.25)$$

leads to the ‘‘Bragg law of photonic crystals’’:

$$m\lambda = 2d_{hkl} \sqrt{n_2^2 - n_1^2 \sin^2 \theta_{ext}} \quad (2.26)$$

For observations along the  $\Gamma$ -L direction in opal (111) planes of an *fcc* lattice have to be considered:

$$d_{111} = \frac{a}{\sqrt{3}} = \frac{\sqrt{2}}{\sqrt{3}} D \approx 0.816D \quad (2.27)$$

with  $a$  being the lattice parameter and  $D$  the sphere diameter, assuming touching spheres.

Restricting the case to opals in air ( $n_1 = 1$ ), observations of the first diffraction order ( $m = 1$ ) and touching spheres leads to the following simplified equation:

$$\lambda_{Bragg} = 1.63D \sqrt{n_{eff}^2 - \sin^2 \theta_{ext}} \quad (2.28)$$

This simple analytical approach allows the principal explanation of different optical features found in photonic crystals, such as the shift of the first stop band position with changing angle of observation. Whereas the behaviour of the lowest bands close to the  $\Gamma$ -L can be modelled quite accurately, at higher energies and other directions the differences to the Bragg predictions become large and can only be explained by more sophisticated approaches. For example there is no pseudo-gap in  $\Gamma$ -X direction – a fact connected with the symmetry of the BZ – that can not be explained by the Bragg approach.

In figure 2.11 a comparison of the position of the first pseudo-gap in  $\Gamma$ -L,  $\Gamma$ -U and  $\Gamma$ -K direction is presented for a  $\text{SiO}_2$  direct opal with a filling factor of 74%. At low angles the agreement with the Bragg law is reasonable but deteriorates towards the BZ edges. It should be mentioned that the band positions at low angles are almost identical for the different directions of observation along the BZ surface (i.e. the azimuthal orientation of the sample). Since for the experiment it is difficult to adjust the sample in a specific direction this is a big advantage for the experimentalist, as the influence on the result is hardly noticeable in the vicinity of the L-point.

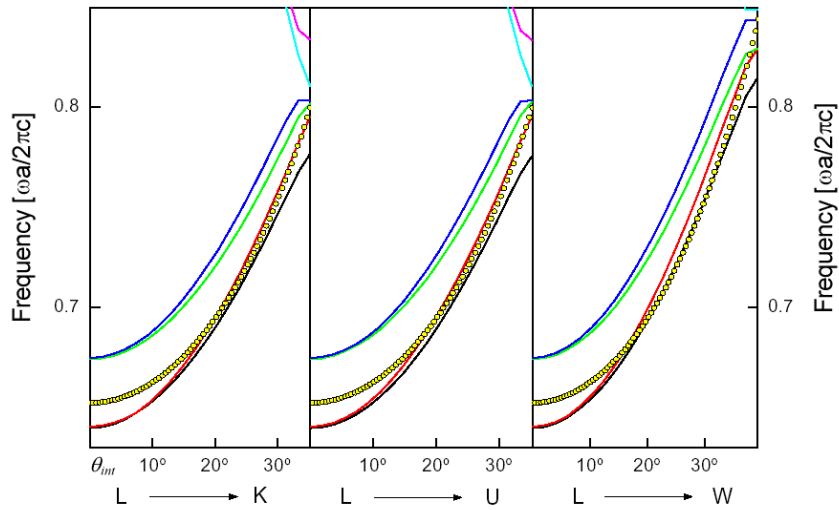


**Figure 2.11:** Position of the four lowest bands calculated by PWM (lines) and Bragg's law (circles) for different directions around the L-point (adopted from [32]).

One of the most prominent shortcomings of the analytical Bragg approach is the use of a constant refractive index  $n_{eff}$ . This approximation is not always valid and there are several different approaches to determine the effective RI of a composite.

It is noteworthy that the RI of a PhC is not easy to determine nor constant or well defined, as discussed in the next chapter.

### 2.3.2. The refractive index

The refractive index (RI)  $n$ , or more precisely the dielectric constant  $\epsilon$  is one of the key parameters in photonic crystals. It is not a well defined parameter as in many solids but a complex function of energy and wave vector i.e. its value changes with propagation direction of light inside the PhC [33]. Thus for a realistic simulation of the dielectric properties, band structure calculations are inevitable.

At the long wavelength limit it can be obtained from the slope of the lowest energy bands for  $\vec{k} \rightarrow 0$  [34]. This value is, strictly speaking, only valid below the first pseudo-gap because near the Brillouin zone boundaries the bands begin to deform already.

Nevertheless, the RI can be defined relatively well for low energies and approximated with a constant value ( $n_{eff}$  in the previous chapter). The question is, how this “effective refractive index” can be calculated and how good is the approximation – a nice summary can be found in Ref. [32].

There have been numerous approaches to determine the effective dielectric constant of a composite material known as *Effective Medium Approximations* [35].

The simplest approach – ignoring the vector nature of light – is the use of the average dielectric constant:

$$\varepsilon_{avg} = f \cdot \varepsilon_i + (1 - f) \cdot \varepsilon_h \Rightarrow n_{avg} = \sqrt{f \cdot n_i^2 + (1 - f) \cdot n_h^2} \quad (2.29)$$

with dielectric constants of infilled ( $\varepsilon_i$ ) and host ( $\varepsilon_h$ ) material and the volume filling fraction  $f$  of the infilled material.

Another, more sophisticated, approach widely used is the Maxwell-Garnett (MG) model [36]. Within the framework of this theory the local field within the composite is taken into consideration. The Maxwell-Garnett relation demonstrates that a medium of small, isolated spherical inclusions in a continuous host material is optically equivalent to a medium with a dielectric constant  $\varepsilon_{MG}$  given by:

$$\varepsilon_{MG} = \varepsilon_h \frac{1 + 2\eta f}{1 - \eta f}, \quad \eta \equiv \frac{\varepsilon_i - \varepsilon_h}{\varepsilon_i + 2\varepsilon_h} \quad (2.30)$$

The subscripts  $i$  and  $h$  denote infilled material and host values, respectively, and  $f$  represents the filling fraction. Note that as  $f$  approaches zero  $\varepsilon_{MG}$  approaches  $\varepsilon_h$ , as expected. Moreover,  $\varepsilon_{MG}$  depends only on  $f$  and the dielectric constants of the constituents and not on the size or separation of the individual spheres.

The results for  $\varepsilon_{eff}$ , obtained for the three different approaches (average, Maxwell-Garnett and band-structure-calculations) are depicted in figure 2.12 (reproduced from Ref. [32]). Three different scenarios are shown: A direct opal of dielectric spheres in air (left), an opal of silica spheres infilled with a dielectric (centre) and an inverted opal structure of air spheres in a dielectric matrix.

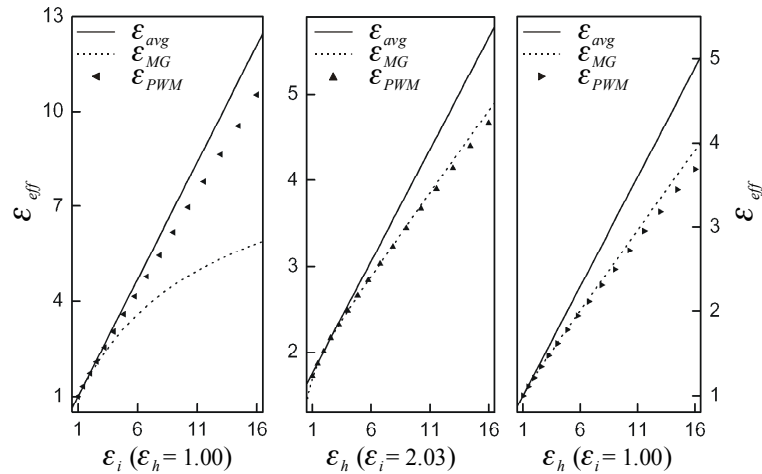


**Figure 2.12:** Comparison of effective dielectric constants obtained by the three different approaches described: averaging (solid line), Maxwell-Garnett model (dashed line) and from band-structure-calculations by the plane-wave-expansion-method (triangles). The calculation was done for an fcc structure of dielectric spheres in air (bare opal, left), silica spheres in a dielectric host material (infilled opal, centre) and air spheres in a dielectric matrix (inverted opal, right). The filling factor has been set to 0.74 (image adopted from [32]).

For low dielectric constants all three approaches result in very similar values but when the dielectric contrast increases the analytical values start to differ considerably from the plane-wave-expansion results.

In general the averaging method tends to overestimate  $n_{eff}$ , whereas the MG approach underestimates it slightly. Whereas for direct opal it seem to be favourable to use the average dielectric constant, for inverted opals the Maxwell Garnett approach yields better results. Nevertheless, at very high dielectric constants the values have to be obtained from band structure calculations.

Since the dielectric constants of the materials investigated in this work are relatively low, the difference of results obtained with either method is small – especially for inverted opals. Thus the choice of the calculation method of the effective RI is of smaller importance for the investigated opal based PhCs. For a detailed theoretical analysis of small effects band structure calculations are the reference anyway and the Bragg approach (and the value of  $n_{eff}$ ) can be used as a first (qualitative) explanation only.

In this thesis the average dielectric contrast was used to calculate the effective RI for direct opals and the Maxwell-Garnett approach for inverted structures of high dielectric infills ( $\text{SnS}_2$ ,  $\text{TiO}_2$ ). For a more detailed analysis band structure calculations (PWM) were used.

### 2.3.3. Dispersion surfaces and photon focussing

It is well known that in a isotropic medium the propagation direction of light can be derived from the gradient of the group velocity in reciprocal space  $v_g = \nabla_k \omega$  [37]. It can be shown that in a periodic media the energy flow transported by EM wave is governed by the topology of the dispersion surfaces, the iso-energy surfaces in reciprocal space. In fact, the average Pointing vector is parallel to the group velocity vector and so it is always perpendicular to dispersion surfaces [38].

Since the dispersion relation of light has the form  $\omega = ck/n$  the surfaces of constant energy (Iso-energy surface (IES)) have circular shape in  $k$ -space. In isotropic media the propagation direction is always parallel to the group velocity. But this does not hold any longer in strongly anisotropic media as a PhC. The IES then show a more complicated geometry as shown in figure 2.13. Since the group velocity is always perpendicular to the IES, a number of interesting effects are present in PhCs, such as strong wavelength dependent refraction, known as super-prism phenomena [38] and photon focusing [39]. The latter effect plays a role especially when photons are emitted within a PhC. It can be explained in principle as a spatial redistribution of emission energy due to the curvature of the IES.

The shaded regions of figure 2.13 show how solid angles (into which photons are emitted)  $k$ -space are transformed into solid angles in real space. The large blue region in reciprocal space is converted in to a small solid angle in  $k$ -space, whereas for a different direction a small

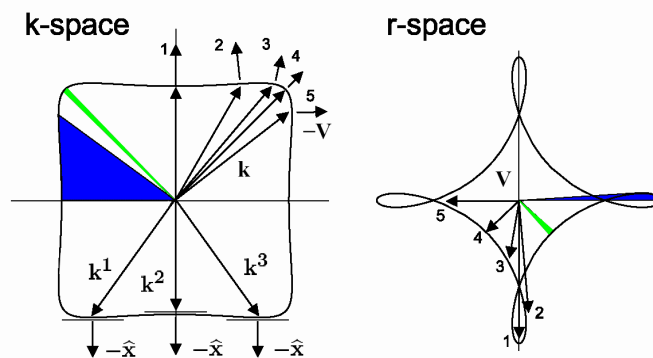


**Figure 2.13:** Iso energy surfaces in reciprocal space (left) and corresponding wave contours in real space (right) of a PhC. The wavevectors  $k_1 - k_3$  correspond to emission directions that are observed in the same direction  $\hat{x}_1$  in real space. The blue and green region illustrate how two equal solid angles in real space convert into different solid angle sections in reciprocal space. This leads to a different photon flux in different directions (image from [39]).

region of the  $k$ -space is transformed into a similar cone in real space (green). The photon flux into the solid angle corresponding to the “blue” region in real space is therefore higher than in the “green” direction. A detailed theoretical derivation of this effect can be found in [39].

## 2.4. Dimensional aspects of Photonic Crystals

PhCs can be built in one, two or three dimensions. Whereas 1D PhCs offer an intuitive way into the underlying concept, 2D and 3D PhCs both offer certain advantages / disadvantages in manufactureability and photonic properties that have to be considered when heading towards specific applications harnessing the unique optical properties of PhCs.

### 2.4.1. One-dimensional Photonic Crystals

To illustrate the underlying physics that lead to the emergence of a photonic band structure it is illustrative to look at the simple case of an one-dimensional periodic multilayer film or “quarter-wave-stack”: Alternating layers of two dielectric materials with (slightly) different dielectric constants are stacked infinitely.

For a small variation of  $\varepsilon$  the periodicity can be regarded as a small perturbation of the homogeneous case. Thus the expected dispersion relation for a uniform material – the light line, cf. equation (2.11) – will only be altered in a small region near the edge of the first BZ, where, as mentioned above, the Bragg condition is fulfilled.

The Bragg reflection leads to the development of a standing wave with wavelength  $2a$ . Two different orthogonal eigenmodes are allowed to exist in that point: The electrical field can be concentrated in regions of high or low dielectric constant – any other configuration would violate the symmetry of the system. Since the electric field is concentrated in different materials for both above mentioned cases, the waves experience a different  $\varepsilon_{eff}$ . This is sketched in figure 2.14. The electric field of the two allowed eigenmodes are depicted as well as the corresponding energy densities. One wave (bottom) has its maximum energy concentrated within the region of high  $\varepsilon$ , whereas the field crosses zero in the low  $\varepsilon$  region and vice versa. Since, according to equation (2.11), the wave vector in regions of high  $\varepsilon$  is enlarged corresponding to the vacuum case the frequency is lowered. On the other hand the frequency for the other mode (top) is increased. In between the two energy levels a frequency gap – the PBG – develops, where no extended modes can exist inside of the material.

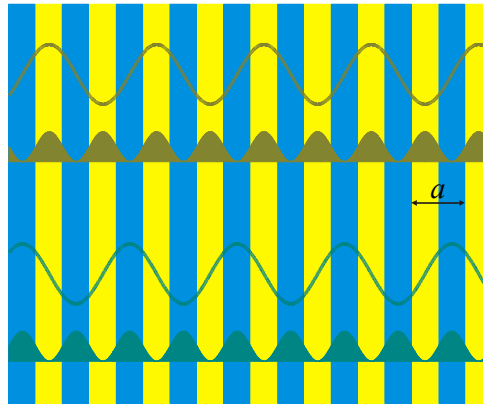


**Figure 2.14:** Sketch of the electromagnetic eigenmodes satisfying the first Bragg condition ( $k = \pi/a$ ) in a periodic layer system with lattice constant  $a$ . The yellow areas correspond to material with lower refractive index than the cyan area. The intensity of the field is depicted as lines, as well as the local power density of the fields (shaded graphs). The upper wave's energy is concentrated in regions with low refractive index, thus its frequency is increased compared to the lower wave with its energy concentrated in the high-refractive-index regions. Consequently a frequency gap exists in between the two modes.

An EM wave with a wavevector inside of the PBG can only have a complex wavevector, which means that only evanescent (i. e. exponentially decaying) waves of that frequency can exist within the crystal. These modes are allowed solutions of the eigenvalue problem, nevertheless they do not satisfy the symmetry conditions within the crystal. It is thus not possible to couple light of a frequency within the PBG into an infinite, perfect PhC. Nevertheless, defects open under certain conditions a way to couple light into these modes. This effect can be harnessed in applications to define waveguides within PhCs.

It is understandable that the width of the band increases with increasing difference in  $\epsilon$ . For drastically different dielectric functions, both modes will be concentrated in the area of high dielectric material, but in different ways, to minimise their frequency. Since the perturbation calculation breaks down for big differences in  $\epsilon$ , the Maxwell equations have to be solved exactly for a periodically varying dielectric function  $\epsilon(\vec{r})$  to allow quantitative predictions, as sketched in section 2.2.

1D PhCs offer useful applications in a couple of applications, ranging from high reflecting mirrors to miniature antennas with improved radiation-characteristics.

### 2.4.2. Two-dimensional Photonic Crystals

The extension of the periodic modulation of the RI to two directions leads to a 2D photonic crystal. The PBG is naturally restricted to a plane, whereas in the third dimension EM waves can propagate freely. An example of a 2D PhC are lattices of dielectric rods in air or pores etched in to Si. The only problem is how to confine the light into a planar region. Therefore most 2D PhCs are made by defining a 2D structure on a material that is layered in the third

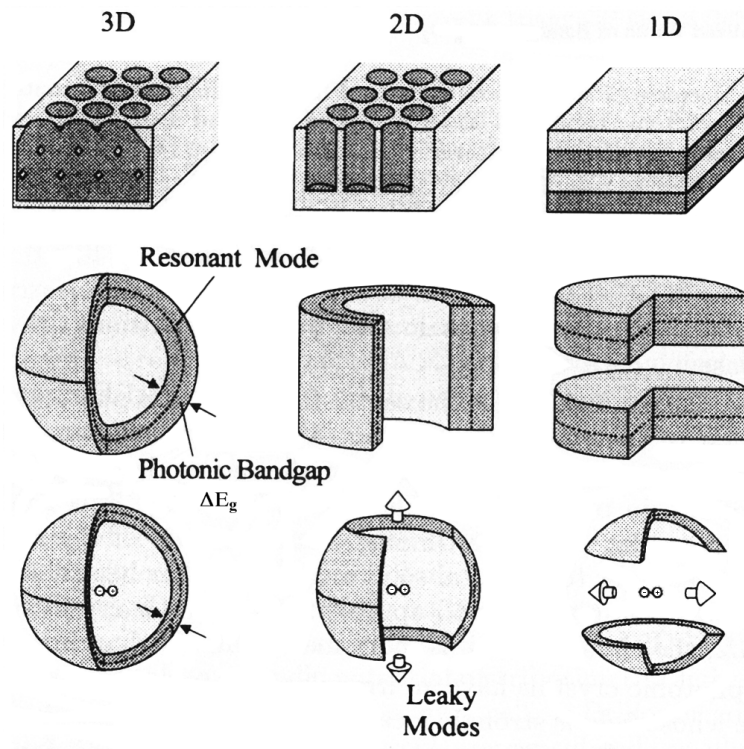


**Figure 2.15:** Sketch of the basic differences in 1D, 2D, 3D PhCs regarding emission properties for frequencies within a PBG. The PBG covers an increasing volume so basically the available space for energy dissipation through leaky modes reduces from 1D to 3D PhCs.

dimension. The 2D structure can e.g. be embedded between two layers with a RI lower than the effective RI of the 2D PhC – so light is confined in the third dimension by conventional total reflection. 2D PhCs show a strong polarisation dependence of the PBG as explained in detail in Ref. [11] and what can be harnessed in device applications.

In practice 2D PhCs are sufficient for many applications, although they that can not provide a full gap in all directions for both polarisations, thus leaving channels for energy dissipation via spontaneous emission and leaky modes (cf. figure 2.15).

Nevertheless for certain applications, including many opto-electronics device concepts, 2D structures are the material of choice, mainly due to their – compared to 3D structures – relatively cheap and easy synthesis with high precision and low defect densities.

2D PhCs are normally produced by lithography and etching processes. They have the great advantage that many established nanotechnological approaches can be used [9, 40, 41].

#### 2.4.3. *Three-dimensional Photonic Crystals*

As 3D PhCs are periodic in all three dimensions they offer in theory the chance to build a full, omnidirectional PBG. This means that EM waves of frequencies inside a PBG cannot propagate in any direction. Therefore there are no unwanted dissipation channels available, such as leaky modes etc.

As in the 2D case defects offer the possibility to alter the pDOS within the band gap locally. A point defect for example leads to a localised state within the PBG: A wave that is resonant to the eigenfrequency of this point-defect cannot leave the location of the defect i.e. it is backscattered and thus can be regarded as localised at the point defect. In analogy, line defects can be used define propagation channels within the PBG that can be used as lossless waveguides with sharp bends.

An infinite number of geometries can be chosen to define a 3D PhC but only very few are favourable to the existence of a full PBG, as mentioned above. Unfortunately 3D PhCs are much more complex to produce artificially than their 2D counterparts. Different approaches have been followed in the past to produce three-dimensional PhCs ranging from putting together spheres “by hand” by nano-manipulators [42] over different lithographic approaches [43], combined with layer-by layer growth methods [38, 44, 45]. They all are very complex and too expensive to produce large 3D PhCs. An alternative is therefore the self-assembled growth of PhCs from dielectric spheres [46-48] that has been used for the PhCs under study in this work.

#### 2.4.4. *Thin film Photonic Crystals*

The above mentioned calculations hold, strictly speaking, only for infinite, perfect crystals. Since the samples under study in this thesis are thin film PhCs i.e. their thickness is in the  $\mu\text{m}$  range they can not be regarded to be infinite. The question arising is the applicability of the theoretical predictions to thin films consisting of 30–500 monolayers.

Bertone et al. [49] tried to answer this question with some theoretical considerations and experimental results extracted from optical density spectra of thin film silica opals. Their results showed that a low number of layers (about 13 for silica spheres in air) should be enough to have a constant Bragg peak width and intensity.

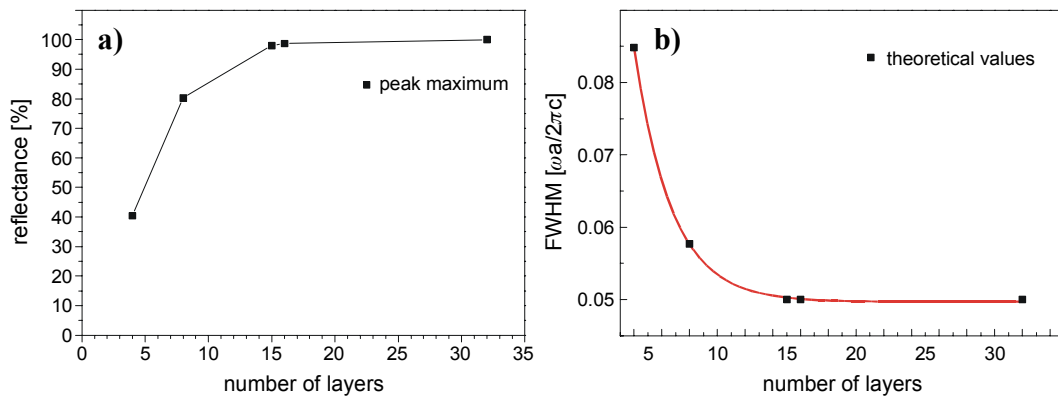


**Figure 2.16:** Peak position (a) and FWHM variation (b) vs. the number of layers in a thin film PhC. A stabilisation of the obtained values above  $\approx 15$  layers is evident (adopted from [50])

This result was confirmed by transfer matrix method (TMM) calculations for PMMA spheres in air. For the calculation a perfect, defect free crystal was assumed. The results are shown in figure 2.16, that addresses important parameters to characterise a PhC, i.e. relative width of the Bragg resonance and reflectivity. It is evident that the calculated reflectivity of a thin film PhC for frequencies in the PBG increases quickly for small number of layers and approaches the theoretically expected value of 100% for  $\approx 15$  layers. Above this thickness, perfect thin film PhCs return more than 99% of the light in the stop band frequency range (figure 2.16a).

The width of the stop band is characterised by the full width at half-maximum (FWHM) of the reflectance peaks. With increasing film thickness a narrowing of the peak can be observed. For film thicknesses above  $\approx 15$  monolayers the difference to an infinity crystal is negligible [50] (figure 2.16b). The width of the stop band is then determined by the PBG width [51]. Thus calculations done for infinite PhCs are also valid for thin film PhCs.

In figure 2.17 a comparison of the calculated reflection in [111] direction of a thin film PMMA opal with different thickness is sketched. The maximum reflectance for propagation along the [111] direction is directly related to the photonic band gap in the  $\Gamma$ -L direction. It is evident that the Bragg peak quickly increases in intensity and its FWHM decreases as mentioned in figure 2.16. The period of Fabry-Pérot oscillations, which exist on each side of the reflectance maximum, decreases if the film thickness increases.

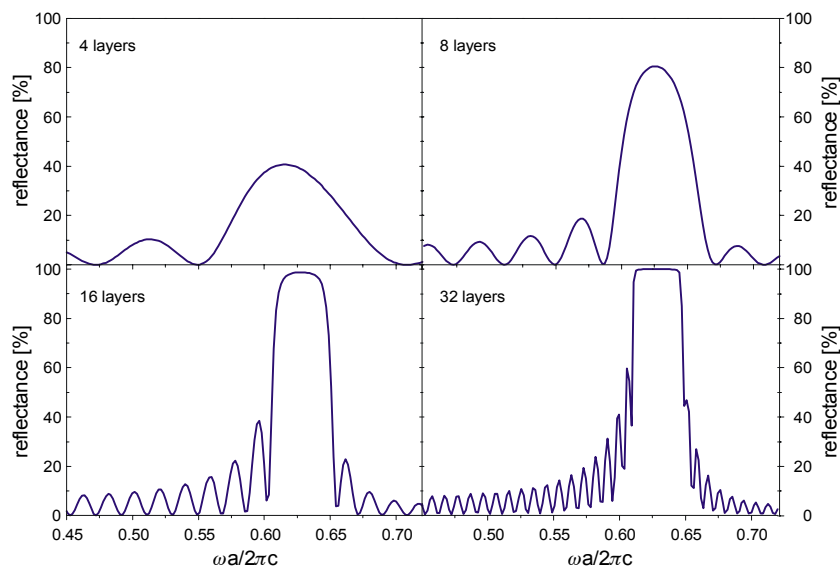


**Figure 2.17:** Evolution of the reflectance spectrum in  $[111]$  direction with increasing number of monolayers for a PMMA opal (from [50]).

In summary it may be said that the optical properties of thin film PhCs quickly sew to the bulk-crystal values. This allows to treat thin film PhCs in very good approximation as infinite crystals, when comparing the experimental results to theoretical values.

## 2.5. Applications of Photonic Crystals

As mentioned, PhCs are expected to have a number of applications in optoelectronics and photonics [52]. They are mainly based on the modification (suppression) of spontaneous emission and localization of light. Nevertheless, also applications

A promising application that seems to be on the way to commercial application soon are photonic crystal fibers (PCF) that have made great progress in the last years. The losses of hollow core PCFs are falling dramatically. Researchers from Corning reported 13 dB/km at 1.55  $\mu\text{m}$  wavelength – which is an improvement of almost two orders of magnitude within one year. Taking into consideration greatly reduced signal degradation, 100 times lower nonlinearities than current fibers and almost perfect control of chromatic dispersion PCFs are supposed to become an interesting alternative to standard optical fibers in the future [53]

True PBG behaviour at visible wavelengths also promises real advantages for light emitting devices. Applications include ultra-compact, low threshold lasers [54, 55], low loss waveguides, wavelength-dependent highly refractive beam-splitters [38], smart lenses [56], optical switches, single mode LEDs [19], add/drop multiplexers and many more. For a recent overview see Ref. [9].

### 3. Analytical techniques

In this chapter the underlying principles of the various analytical techniques and instruments used will be introduced.

#### 3.1. Spectroscopy

##### 3.1.1. The spectrometer

The reflection/transmission experiments and the photoluminescence measurements were performed using grating spectrometers. The reflection/transmission experiments were done with a SPEX 270M spectrometer, whereas for the photoluminescence experiments a SPEX 1680B spectrometer was used.

Both spectrometers are those of a Czerny-Turner design. The Czerny-Turner configuration is sketched in figure 3.2. It offers good resolution for short dispersion distances because the slit image is relatively free of aberrations of mirror distortions. Stray light is minimised by using multiple mirrors. The ISA 270M Rapid Scanning Imaging Spectrograph/Monochromator is a medium resolution single grating type, whereas the SPEX 1680B spectrometer is a high resolution double grating type with additive dispersion coupling.

The optical specification described here can be applied for the double grating spectrometer by simply applying the dispersion formulae twice.

Spectrometers are characterised in principle – independent of their type – by resolution ( $R$ ), luminosity, and optical light rejection. As usual, a compromise based on the experimental requirements has to be found.

##### *Grating equation and free spectral range*

The grating is without doubt the key optical element for uncountable applications in spectroscopy. The dispersion of a plane grating is caused by interference of light diffracted by the grating's grooves. Constructive interference of diffracted wavefronts occurs when the path difference of beams from adjacent grooves is an integral multiple of  $\pi$ . leading to the well known grating equation [37, 57]:

$$m \cdot \lambda = \frac{1}{G} (\sin(\alpha) + \sin(\beta)) \quad (3.1)$$

Here  $\lambda$  is the wavelength,  $m$  the diffraction order,  $\alpha$  and  $\beta$  the angles of incidence and diffraction, respectively and  $G$  the groove density of the grating (see. figure 3.2).

From this equation it is evident that spectral orders of the diffracted light overlap. I.e. light of one wavelength in the first order is diffracted into the same direction as light of half the wavelength in second order and so on.

The range of wavelengths in a given spectral order for which superposition of light from adjacent orders does not occur is called the *free spectral range*,  $F$ . The wavelength of light  $\lambda_2$  that diffracts along one and the same direction in order  $m+1$  is  $\lambda_1 = \lambda_2 + \Delta\lambda$  in order  $m$ :

$$\lambda_2 + \Delta\lambda = \frac{m+1}{m} \lambda_2 \quad (3.2)$$

$$\Rightarrow F = \Delta\lambda = \frac{\lambda_2}{m}$$

The concept of free spectral range applies to all gratings capable of operation in more than one diffraction order.

Free spectral range and order sorting are intimately related, since grating systems with greater free spectral ranges may have less need for filters (or cross-dispersers) that absorb or diffract light from overlapping spectral orders. This is one reason why first-order applications, as used here, are very popular. Apart from the decrease in free spectral range the grating efficiency – especially for blazed gratings – decreases and stray light increases as the square of the order.

### *Angular dispersion*

The angular spread  $d\beta$  of a spectrum of order  $m$  between wavelength  $\lambda$  and  $\lambda+d\lambda$  is called the *angular dispersion* ( $D$ ), which can be obtained by differentiating the grating equation (assuming  $\alpha$  to be constant):

$$D = \frac{d\beta}{d\lambda} = \frac{G \cdot m}{\cos \beta} \quad (3.3)$$

### *Linear Dispersion*

Combining the angular dispersion with the focal length of the spectrometer leads to the linear dispersion.

For practical applications its reciprocal value, also called plate factor ( $P$ ) is a well comparable figure of merit. It is usually measured in nm/mm:

$$P = \frac{d\lambda}{dx} = \frac{1}{f} \frac{d\lambda}{d\beta} = \frac{\cos(\beta)}{f \cdot G \cdot m} \quad (3.4)$$

with the effective focal length of the spectrometer  $f$ .

It should be noted that at small angles of diffraction  $\cos(\beta) \rightarrow 1$  and thus the plate factor is basically constant.

### *Spectral band-pass*

From equation (3.4) the spectral band-pass  $B$  of the instrument depending on the exit slitwidth is easily calculated with the slitwidth  $s$  by:

$$B = s \cdot P \quad (3.5)$$

As usual for grating spectrometers: a doubling of the slit width leads to halving of the (spectral) resolution.

### *Resolving Power*

The numerical resolving power of a plane grating is given by :

$$R = \frac{\lambda}{\Delta\lambda} = \frac{W(\sin(\alpha) + \sin(\beta))}{\lambda} \quad (3.6)$$

with the ruled width of the grating  $W$ . For a square plane 600g/mm grating of 50mm length this leads to a theoretical resolving power 100,000 ( $5 \cdot 10^{-3}$  nm at 500 nm). Of course the degree to which this theoretical value can be attained depends not only on the angles  $\alpha$  and  $\beta$  available but also on the optical quality of the grating and optics used. Any departure from the optimal values leads to significant loss in resolving power due to aberrations at the image plane etc. In practice the resolving power is limited by mechanical and optical imperfections of the spectrometer and set up used.

Since the spectrometers were not operated near their theoretical resolution limits (eq. (3.6)), the slit widths play a dominant role in determining the resolution of the spectrometer-system.

### *Slit functions*

For an optimal performance of the spectrometer the influence of the slits has to be considered as well. Since the exit slit can be thought of as a band-pass filter to determine the spectral resolution, as shown in equation (3.5), the slit width of entrance and exit slit have to be matched to find the optimal compromise between throughput, resolution and signal-to-noise ratio. The slit function is the convolution of the entrance- with the exit-slitfunction. It has generally a trapezoidal shape as depicted in figure 3.1. As a measure for the imaging quality the full width at half-maximum (FWHM), the *effective spectral bandwidth* and the full width at zero height (FWZH), the *full spectral bandwidth* are indicated in the graphs.

Assuming a fixed entrance slitwidth, reducing the exit slitwidth in general leads to a reduction of the effective bandwidth. If the image of the entrance slit on the exit slit plane is equal to the exit slitwidth, a further reduction of the slitwidth does not lead to a reduction of the effective

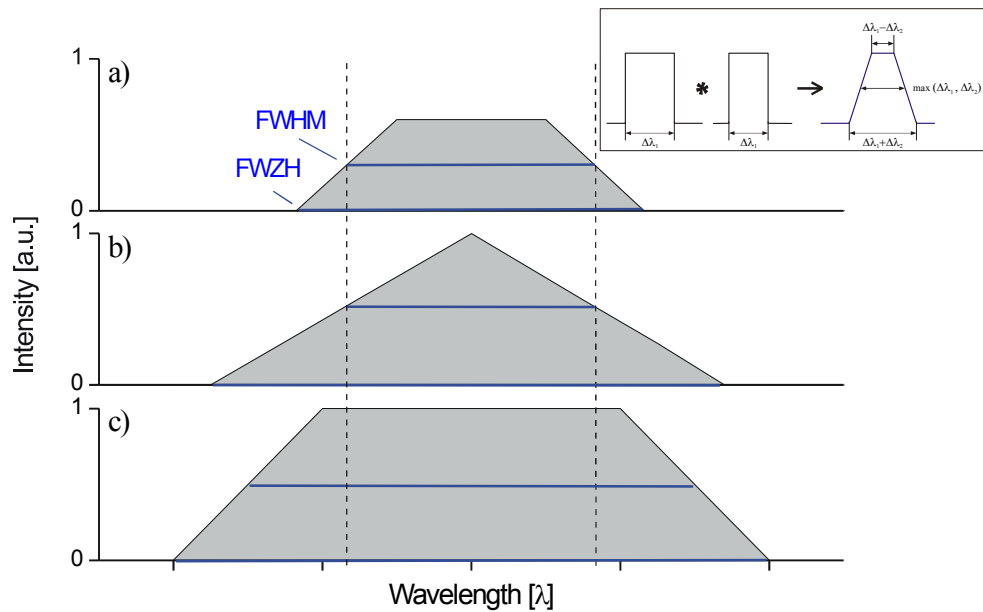


**Figure 3.1:** The slit function of the spectrometer system is the convolution of the entrance- with the exit slit function (see inset). For optimal performance the exit slitwidth should match the input slitwidth. If the exit slit is too small the throughput is reduced (a). Optimal settings lead to small values of FWHM/FWZH (b). A too wide exit slit causes unnecessary reduction of spectral resolution (c).

bandwidth any more. This can be seen in figure 3.1, where reducing the exit slitwidth from case (c) to (b) leads to a smaller FWHM, whereas further reduction beyond the entrance slitwidth does not reduce the FWHM any more (a).

If the image of the entrance slit width is smaller than the exit slit width, the throughput is low without benefit in narrowing the effective bandwidth, since the exit slit is too small to collect all of the diffracted light at once. The opposite situation is undesirable, too since the band-pass becomes large (without gain in throughput due to the small entrance slit). Thus for optimal performance the exit slitwidth should match the image of the entrance slit: the relative intensity is maximised, while the FWHM is minimised.

#### *The Czerny Turner Configuration*

A Czerny Turner spectrometer consists of two concave mirrors and a plane diffraction grating illuminated by collimated light (cf. figure 3.2). The first concave mirror (collimating mirror) collimates the incident light that is usually diverging from a slit upon a plane grating. The diffracted light is focussed by the second concave mirror (focussing mirror) on the exit slit [57].

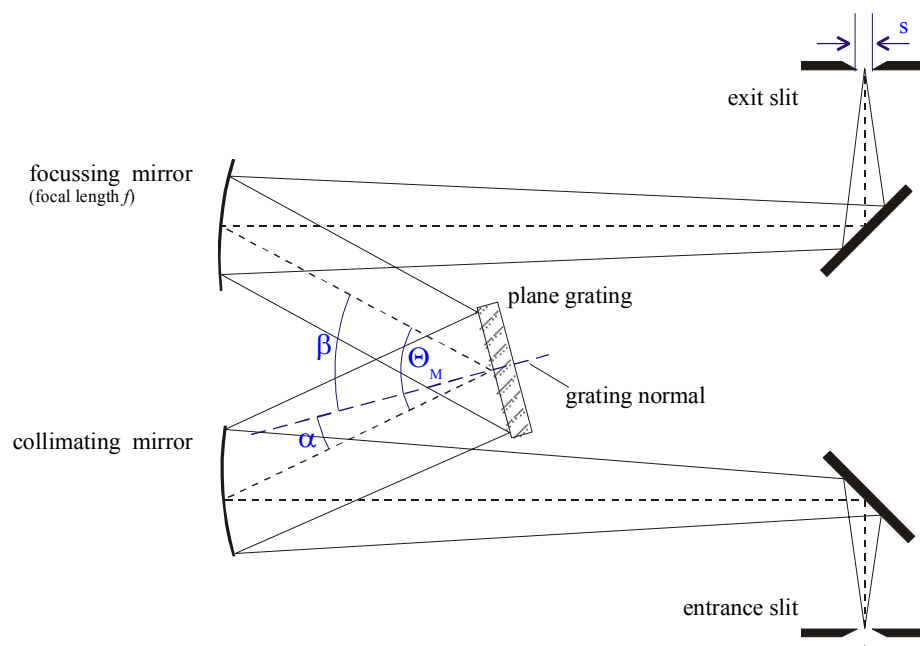


**Figure 3.2:** Sketch of a Czerny Turner spectrometer. Collimated light is dispersed by a plane grating and focussed on the exit slit. The deviation angle of the spectrometer ( $\Theta_M$ ) is fixed. The wavelengths are scanned by rotating the grating. Additional plane mirrors and apertures can be used to reduce stray light. This mount offers good resolution and small aberrations for small focal lengths.

Since the grating is planar and used with collimated incident light, ideally no aberrations should be introduced into the diffracted wavefronts. In practice, aberrations are contributed by the off-axis use of the concave spherical mirrors.

The spectrum is scanned by rotating the grating. According to equation (3.1) this changes the wavelength diffracted toward the exit slit by moving the grating normal relative to the incident and diffracted beams. For the Czerny Turner configuration the spectrum remains at focus at the exit slit for each wavelength, since only the grating can introduce wavelength-dependent focusing properties. Aberrations caused by the auxiliary mirrors include astigmatism and spherical aberration but are usually negligible.

Since the Czerny Turner mount is usually used at small diffraction angles, the plate factor is in first approximation constant – especially independent of  $\lambda$  (cf. equation (3.4)). This makes the usage a lot simpler.

### 3.1.2. Reflection and transmission spectroscopy

The photonic properties along certain directions can be probed easily by measuring the transmission and reflectance of PhC samples at certain directions. Since self-assembled thin film photonic crystals usually grow in [111] direction, directions around the L-point are accessible experimentally. Since light propagation within the photonic (pseudo) gap is inhibited a peak in reflectance or a dip in transmission is expected. To probe the photonic band structure experimentally angle resolved reflectance / transmission spectroscopy was done using the set up described in more detail in section 4.1. The samples under investigation were illuminated by with light from a tungsten lamp and the reflectance / transmission was recorded. To analyse the resulting spectra they were corrected by the emission spectrum of the tungsten lamp and the efficiency of the spectrometer/detector system by dividing on reference spectra.

### 3.1.3. Photoluminescence spectroscopy

To probe the emission properties of the investigated thin film photonic crystals laser-dyes were infiltrated into the crystals and their luminescence properties were measured using photoluminescence (PL) spectroscopy.

In general many different ways can be followed to induce the luminescence of organic dyes. In this work the photoluminescence under laser excitation was used. PL spectroscopy is a very simple and powerful technique. Carriers are excited by a pump beam with a photon energy higher than the electronic band gap of the dyes. They relax by non radiative channels to the band edge, where they eventually recombine under the emission of a photon. To obtain information, on the influence of the PBG on the emission properties of the laser-dyes the PL emission is measured angular and spectrally resolved.

As the signal can be relatively weak, a laser is used as the excitation source together with a high sensitivity detector, such as a photomultiplier tube. The possibility to use the as grown samples without any further treatment is a big advantage of this technique.

The experimental set up is described in more detail in section 4.2.

### 3.1.4. Raman spectroscopy

The usefulness of this technique to characterise semiconductor structures and all kinds of molecules is well known. With only minimal sample preparation, Raman spectroscopy is used to study specimen with a lateral spatial resolution of  $\approx 1 \mu\text{m}$  if using micro Raman systems [58].

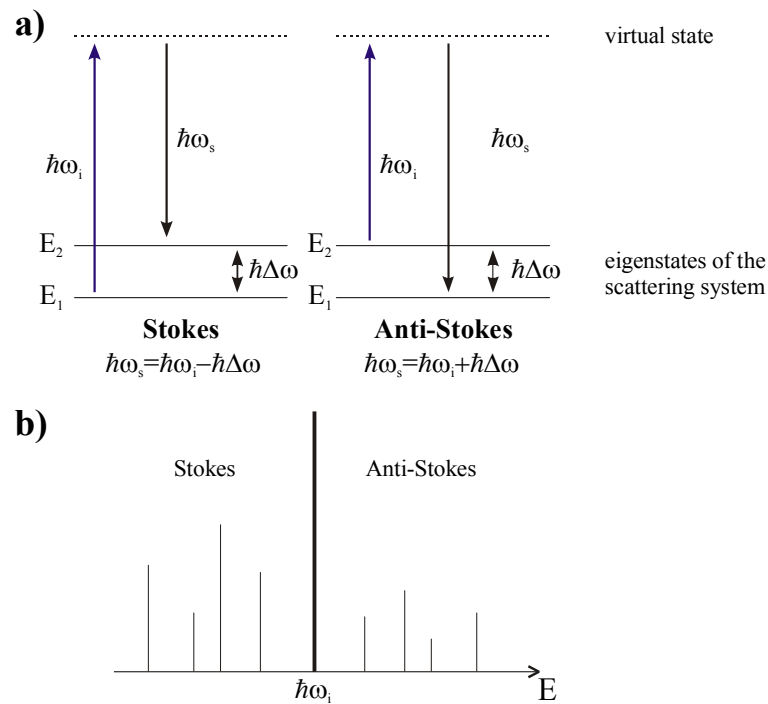


**Figure 3.3:** Sketch of the processes in Raman scattering. A photon is scattered inelastically and lifts the system into a higher (virtual) state. From this state the system returns into a real state. It can return to the start state (Rayleigh scattering) or to another allowed state, emitting a photon. If the final state is higher, the energy of the emitted photon is lower than the incident photon's energy (Stokes case). If the final state is higher, the emitted photon energy is higher (Anti-Stokes) (a). Sample Raman spectrum. The Stokes lines usually have higher energies since they belong to transitions from the higher populated ground state (b).

In Raman spectroscopy the symmetry and energy of vibrational (phonons), electronic (plasmons) and magnetic (magnons) states of solids as well as molecular vibrational levels are monitored by inelastic light scattering. The Raman scattering has become a standard method in chemistry and physics since powerful lasers and efficient detectors are readily available. Since the Raman effect is weak – only  $10^{-6}\%$  of the incident photons are scattered inelastically the recording of Raman spectra was time consuming and difficult before and therefore not routinely used.

The Raman effect describes the inelastic scattering of a photon in a crystal or by a molecule. Incident (scattered) photons are characterised by energy  $\hbar\omega_i$  ( $\hbar\omega_s$ ), polarisation  $\hat{e}_i$  ( $\hat{e}_s$ ) and wavevector  $\vec{k}_i$  ( $\vec{k}_s$ ). In first order process one or several elementary excitations are created (Stokes-process) or annihilated (Anti-Stokes-process).

The energy difference remains in the molecule or crystal. The energy conversion of the spontaneous Raman scattering can be written as:

$$\hbar\omega_i = \hbar\omega_s + \hbar\Delta\omega \quad \text{Stokes} \quad (3.7)$$

$$\hbar\omega_i + \hbar\Delta\omega = \hbar\omega_s \quad \text{Anti-Stokes}$$

with  $\hbar\Delta\omega$  being the energy of the excitations. The scattered photons are thus shifted by  $\hbar\Delta\omega$  from their start energy (Raman shift), consequently the shifts are usually given in wavenumbers ( $\text{cm}^{-1}$ ) or nm rather than in eV. Typical energies for the excitation probed by Raman spectroscopy are in the range of 0.01 – 0.1 eV which corresponds to a frequency shift of about 100 – 1000  $\text{cm}^{-1}$  for typical experiments. A sketch of the Stokes and Anti-Stokes process is given in figure 3.3. Stokes Lines usually have higher intensity since the transition takes place from the higher populated ground state.

Apart from energy conversion the (quasi) impulse conversion has to be obeyed as well. This can be described for phonons in solids as:

$$\vec{p}_s = \vec{p}_i \pm \Delta\vec{p} + n\hbar\vec{G} \quad (3.8)$$

$$\vec{k}_s = \vec{k}_i \pm \Delta\vec{k} + n\vec{G}$$

with  $\vec{p}$  being the impulses and  $\vec{k}$  the wavevectors of these elementary excitations.  $\vec{G}$  represents a reciprocal lattice vector. The + (–) signs refer to the Stokes- (Anti-Stokes-) process. The absolute value of a phonon wavevector is given by

$$\Delta k = \sqrt{\vec{k}_i^2 + \vec{k}_s^2 - 2\vec{k}_i\vec{k}_s \cos\theta} \quad (3.9)$$

with  $\theta$  being the angle between  $\vec{k}_i$  and  $\vec{k}_s$ .

This leads for inelastic photon scattering with the energy-impulse-relation  $\omega = c \cdot k$  to :

$$\pm \Delta\omega = c \left[ \vec{k}_i^2 (\cos(\theta) - 1) \pm \sqrt{\vec{k}_i^2 (\cos^2(\theta) - 1) + \Delta k^2} \right] \quad (3.10)$$

The smallest (largest) angle of  $\Delta\vec{k}$  is experimentally realised by  $\theta \approx 0^\circ$  ( $180^\circ$ ) in forward (backscattering) direction. For experimental reasons micro Raman scattering experiments were undertaken using the backscattering geometry as shown in figure 3.4.

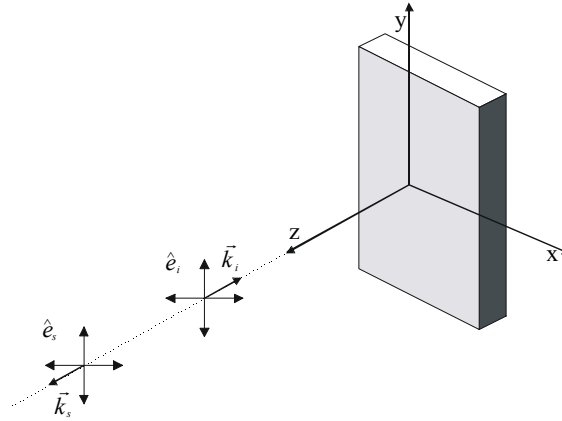


*Figure 3.4: Sketch of the Raman backscattering geometry*

### 3.2. Scanning electron microscopy

Scanning Electron Microscopy was used as a quick and destruction-free technique to investigate the topology of opaline samples.

The Scanning Electron Microscope (SEM) has become a standard method to gather morphological, and, to a smaller extent, also chemical and electrical information with a nanometer scale lateral resolution [59].

The wavelength of electrons accelerated by a voltage  $U$  is given by the well known de Broglie wavelength:

$$\lambda = h / \sqrt{2m_0eU} \quad (3.11)$$

in the non-relativistic case, which is a good approximation for voltages below ca. 100kV. Here  $h$  is Plank's constant,  $m_0$  the rest-mass of electrons and  $e$  the elementary charge The corresponding wavelength ranges from 38 pm for 1 keV electrons to 7 pm for 30 keV electrons.

Due to the short de Broglie wavelength of electrons in comparison to visible light, the SEM offers a much better resolution which, is not diffraction limited, in comparison to optical microscopes. Whereas the resolution of optical microscopes is limited by the wavelength of

the used light ( $\approx 500$  nm) to circa 200 nm, the resolution in modern SEMs is limited by lens aberrations. Recent efforts to compensate these errors using magnetic correction lenses resulted in resolutions better than 0.1 nm [60, 61]. With the used standard SEMs spatial resolutions down to several nm can be expected routinely.

There are many additional advantages in using SEM rather than light microscopy. The most obvious probably being a large depth of focus that allows non planar samples (such as artificial opals) to be in focus almost completely at the same time, thus simplifying the investigation greatly.

A main disadvantage of SEM investigation of non-conducting samples is the need to metal-coat the specimen to build a conductive surface. Although the process of sputter coating the samples with a gold (or platinum) film is easy and uncritical, the metal layer obstructs fine structures of the morphology and hinders a subsequent optical investigation of the samples. Thus it is desirable to avoid a metal coating prior to SEM investigations. Dielectric samples can be looked at without metal coating using very small accelerating voltages and low beam currents to avoid charging. Most SEM micrographs presented here, unless stated otherwise, were taken from uncoated structures.

All SEM micrographs presented were obtained using a Philips XL 30 TMP or XL 30 SFEG microscope. The main difference between both machines is the electron source. Whereas the XL 30 TMP is equipped with a tungsten cathode, the XL 30 SFEG contains a Schottky field emitter cathode, which allows a better spatial resolution and lower excitation voltages and thus makes the investigation of non metal-coated opal structures possible.

More details on the work principle of electron microscopes will be given in the subsequent paragraphs.

#### *The electron source*

The spatial resolution that can be expected is highly influenced by quality of the electron beam, meaning its coherence, extraction area, energy distribution among others.

Basically there are two different emitter types used in SEM electron guns. The first “conventional” method is the extraction of thermoelectrons from filaments. These are normally made from metal (W) or metal borides with low work functions such as LaB<sub>6</sub>.

In one of the machines used, a Philips XL 30 TMP microscope, a sharp tungsten filament is used that is heated by an external current to high temperatures. Electrons are extracted from a relatively large area and show a rather broad energy spectrum, what is a disadvantage to form a well collimated coherent beam. In contrast the second machine available in Wuppertal, a Philips XL 30 SFEG microscope, is equipped with a field emitter gun. This has certain advantages over thermal emitters. The field emitter gun (FEG) is based on a sharp metal tip with a curvature radius of  $\approx 100$  nm. The resulting high fields of  $\approx 10^7$  V/cm extract electrons

by the tunnel effect. Field emitters offer an increased brightness – the current emitted per area and solid angle ( $A/cm^2sr$ ) – of about three orders of magnitude. This is due to the small area of emission ( $\approx nm^2$ ) and also leads to a strongly increased coherence of the resulting beam [62].

The electrons are excited by a high voltage (1–30 kV) and directed through an optical column, consisting of a set of magnetic lenses (condenser, stigmator, objective lenses) and scanning coils to allow the beam to be rastered across the specimen surface. Imperfections of the lenses, the energy distribution of the electrons forming the beam etc. lead to distortions and a widening of the resulting electron beam that eventually limit the resolution of the system. They are especially critical at low acceleration voltages. The resolution of the Philips XL30 SFEG is about 5 nm compared to  $\approx 20$  nm for the XL 30 TMP.

After passing the column, the electrons hit (of course) the sample surface and interact in different ways by elastic and inelastic scattering processes there.

#### *Electron beam - specimen interaction*

The penetration of the primary electrons into the sample provokes a widening of the spot and a progressive loss of energy in deeper zones of the specimen. This defines a volume range of interaction between electrons and matter. The depth of the volume strongly depends on the type of substrate and on the beam energy. Typical values are penetration depth of  $\approx 1 \mu m$  for a 20 keV beam and a specimen with a density of about  $5 g \cdot cm^{-3}$ .

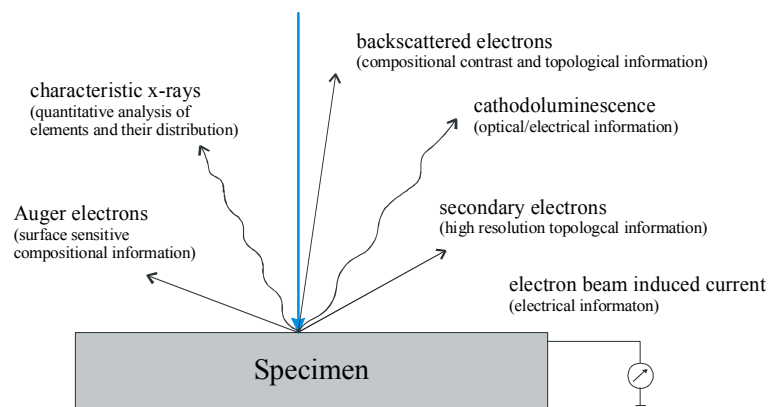


**Figure 3.5:** Different types of interaction of electrons and specimen. When the electron beam strikes the sample, both, electrons and photons, are emitted

Depending on the beam energy and type of the sample the different emitted electrons and photons carry complementary information on the sample [63].

The most important processes involved are, as sketched in figure 3.5:

- Elastic backscattering
- Inelastic backscattering
- Characteristic x-rays
- Auger electrons
- Secondary electrons

While all these signals are present, not all of them are detected and used for information. The signals most commonly used are the secondary electrons, the backscattered electrons and x-rays.

#### *Elastically scattered primary electrons*

As the name implies, elastic scattering results in basically no energy transfer of scattered beam electrons, although there is a change in momentum. Since momentum,  $p = mv$ , and mass  $m$  do not change, the direction of the velocity vector must change. The angle of scattering can range from 0–180°, with a typical value being about 5°.

Elastic scattering occurs mainly between the negative electron and the positive nuclei. This is essentially Rutherford scattering. Some electrons are scattered back in the direction of the incident beam either by multiple scattering events or by experiencing scattering angles near 180°. These are backscattered electrons. They are detected by a semiconductor detector mounted in pairs below the pole piece of the objective lens. Signal addition and subtraction allow separate generation of topological and compositional contrast.

The function of the semiconductor detector is based on the generation of electron-hole pairs induced by the electron beam and their subsequent separation by diffusion processes in the space-charge region of the semiconductor structures.

#### *Inelastically backscattered primary electrons*

During inelastic scattering, energy is transferred to the electrons surrounding the atoms and the kinetic energy of the energetic electron involved decreases. A single inelastic event can transfer a various amount of energy from beam electrons ranging from a fraction to many eV. This energy transfer causes a number of different processes within the specimen, which can partly be used to gain information from the sample.

The main processes include phonon excitation, plasmon excitation, secondary electron excitation, x-ray generation, and ionisation of inner shells.

X-rays emitted by electrons that fall back to the ground state can be detected and analysed by their characteristic energy. Since every element emits characteristic x-ray radiation, this gives the possibility to characterise the chemical composition of the sample with a resolution better

than 1  $\mu\text{m}$  (EDX analysis). Photons of lower energy can be used in cathodoluminescence experiments.

Instead of emitting a photon, the excess energy can be transferred to another shell electron, which leaves the atom. These *Auger electrons* are highly element-specific and provide surface sensitive compositional information. Their energies range from 100 eV to 1 keV.

The most widely used source of topological information are secondary electrons, though.

### *Secondary electrons*

Secondary electrons are electrons that undergo multiple scattering events on their way to the sample surface. They are defined as electrons emitted from the specimen showing a broad energy distribution with a maximum below ca. 50 eV. Secondary electrons are predominantly produced by interactions between beam electrons and weakly bonded conduction-band electrons in metals or the valence electrons of insulators and semiconductors. Because of the big energy difference between the accelerated beam electrons and the bound specimen electrons only a small fraction of their kinetic energy can be transferred to the secondary electrons.

Depending on the acceleration voltage the primary electrons penetrate up to several micrometers into the sample. If a high material contrast is desired, high electron energies are chosen. In this case beside secondary electrons also elastically backscattered primary electrons can be detected. As the latter ones primarily originate from a high depth, the resolution is rather low, thus for topography imaging secondary electrons are used. These have low energies and can therefore leave the sample only from a near surface area of some nm in depth. With this method the highest spatial resolution is achieved.

The secondary electrons emitted from the specimen are collected over a large solid angle by a positively biased mesh collector-electrode which is in front of a scintillator crystal. The electrons penetrate the scintillation layer and generate photons which are detected by a photomultiplier tube (PMT). The amplified electrical signal can be processed electronically and eventually forms the topological image.

Using a secondary electron detector produces a clear and focused topographical image of the sample thus this detector is used normally to gather morphological information. The backscattered electron detector produces an image that is useful when determining the composition of the specimen since it allows to distinguish between different elements.

## 4. Experimental set up

### 4.1. Reflection and transmission measurements

To investigate the optical properties of the described PhCs basically two different types of measurements were undertaken:

To determine the position of the photonic stop-band and the “passive” optical properties transmission / reflectance measurements using a white light source were undertaken. To probe the “active” properties measurements of the photoluminescence of embedded laser-dyes in opal matrices and their inverted replicas were performed.

Both types of measurements were taken angle resolved in a basically very similar set up. In what follows a brief description of these set ups is given.

#### 4.1.1. Reflection / transmission set up

Transmission / reflection measurements were undertaken with a modified spectroradiometer set up consisting of an ISA SPEX 270 single grating spectrograph of the Czerny-Turner type with attached Si-diode detector. A lock-in amplifier was used to enhance the signal to noise ratio where appropriate. To avoid the overlay of first and 2<sup>nd</sup> order diffraction of the spectrum a motorised filter wheel is attached to the front entrance of the spectrometer allowing several colour filters to be inserted into the light path which suppress unwanted parts of the spectrum. The equipment allows in principle to measure in a spectral range between 300 and 1600 nm using an auxiliary liquid nitrogen cooled InGaAs-detector and a second grating (600 g/mm). For the measurements presented here only the Si-detector and the first grating (1200 g/mm) was used. This configuration allows continuous measurements in a spectral range from ca. 350 – 1100 nm. The limiting factors are the emission spectrum of the tungsten lamp on the high energy side and the sensitivity the Si-Diode on the low energy side. The spectral resolution using fixed entrance and exit slits of 1.5 mm is 5 nm.

The data were collected either using lock-in techniques or by direct measurement of the diode current using an internal A/D converter supplied by the controller (ISA DataScan2). A principal sketch of the angle resolved transmission / reflectance set up is depicted in figure 4.1. The basic idea is to measure the Transmission and Reflectance under white-light illumination. This is done using a Köhler Illuminator containing a tungsten halogen lamp (Glenn spectra model KI 125, 125W lamp) in a lamp housing combined with a focusing optics assembly. It is powered by a regulated power supply. The power supply is specially

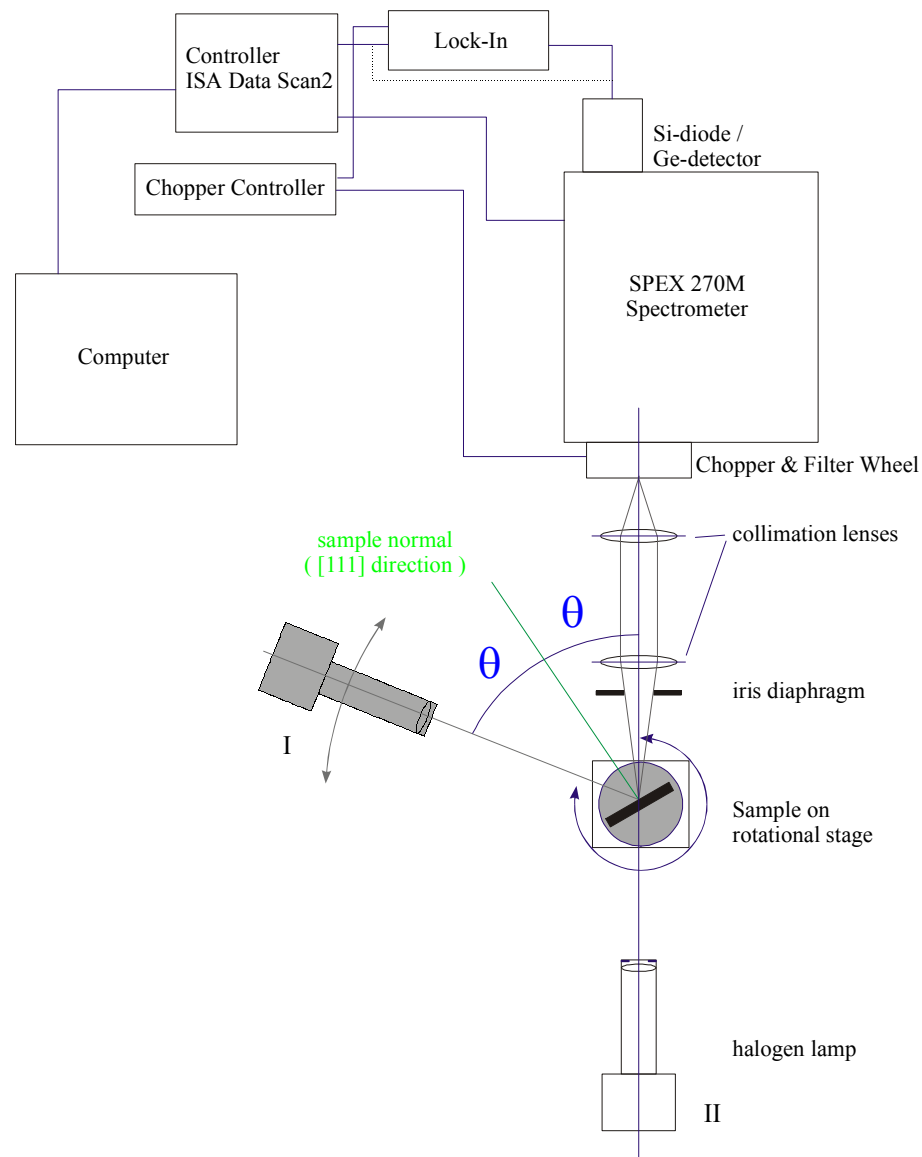


**Figure 4.1:** Set up used for transmission/reflectance measurements. A calibrated tungsten lamp was used as source. On the detector side a single grating spectrograph with a silicon or germanium detector (with lock-in technique for small signals) was used. Reflectance measurements were usually taken in  $\theta$ - $2\theta$ -configuration, where the incident angle equals the observation angle.

designed to operate the bulb at a precisely determined current ( $\Delta I < 1$  mA, Labsphere LPS-200H) to produce a reproducible spectrum as well as determined absolute intensity.

The Köhler Illuminator is designed for applications requiring uniform illuminance in the UV-VIS-NIR region of the spectrum. The image of the halogen lamp filament is focused on a glass rod that evenly mixes the light distribution and directs the radiance through a fixed aperture before it passes through a baffled lens assembly and an adjustable iris diaphragm.

The iris diaphragm controls the amount of illumination at the working plane without altering the spectral characteristics of the beam. The KI-125 Köhler illuminator provides a maximum illuminance output of 20,000 lux at a normal working distance of about 50 cm. A filter holder allows the placement colour balancing filters, narrow band filters or neutral density filters between the lamp and the glass rod (cf. figure 4.2)

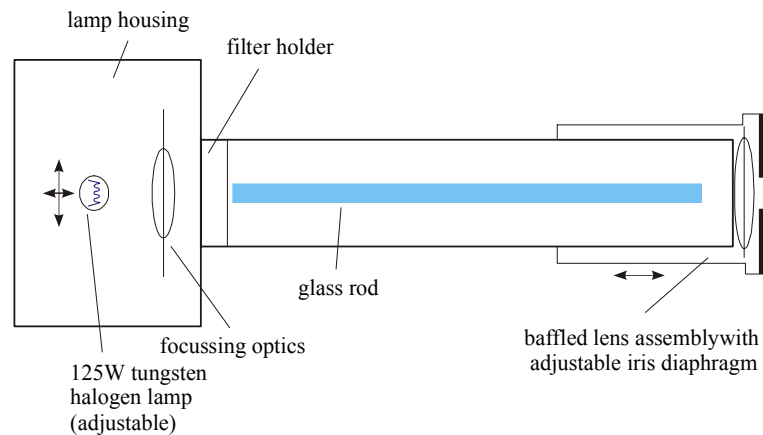


**Figure 4.2:** Assembly of the KI-125 Köhler Illuminator that was used in the transmission/reflectance measurements. A glass rod is used to evenly mix the light distribution leading to a uniformly illuminated spot of variable size on the sample.

The experiments usually were undertaken by imaging the illuminated face of the glass rod onto the sample, what ensures a uniformly irradiated spot on the sample of controllable size. For specific measurements a second collimating lens was placed between lamp and sample to reduce the size of the illuminated spot on the sample. For certain measurements pinholes with different diameters ( 1 – 5 mm) were placed directly in front of the sample to control area and location of the investigated spot on the sample more precisely.

For a precise control of the illumination angle the sample is mounted on a rotational stage that allows to adjust the angle with a precision better than  $0.5^\circ$

The sample is illuminated either from the backside for transmission measurements or from the front side for reflectance measurements (turning the lamp and sample holder in  $\theta/2\theta$  configuration, cf. figure 4.1).

An aperture in front of the collimating lenses restricts the solid angle of observation.

The actual solid angle of observation is determined by the distance between sample and aperture, aperture diameter and beam diameter. It can be determined to be (assuming that aperture and incident light beam are perfectly centred):

$$\Omega = 2\pi\left(1 - \cos\frac{\beta}{2}\right)$$

$$\beta = 2 \arctan \frac{r + R}{l}$$
(4.1)

with the solid angle  $\Omega$ , the opening angle of the light cone  $\beta$ ,  $2r$  being the beam diameter on the sample,  $2R$  the iris aperture's diameter and  $L$  the distance from sample to aperture (cf. figure 4.3).

Typical values for the parameters ( $2r = 5$  mm,  $2R = 20$  mm,  $L = 150$  mm) result in an opening angle of the observable cone of  $\beta \approx 9.5^\circ$ . This converts into a solid angle of observation of  $\Omega \approx 0.02$  sr.

This set up offers certain advantages over other possibilities, for example, illuminating the sample with monochromatic light. Since in this set up the full reflex can be easily seen by eye the adjustment is far easier.

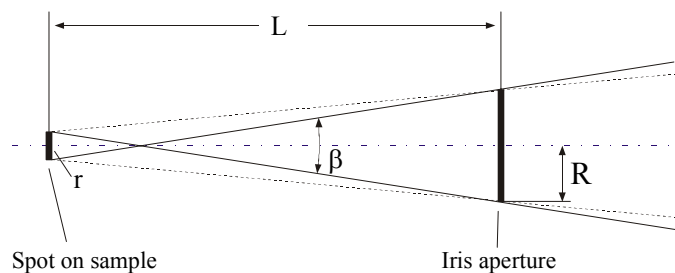


**Figure 4.3:** Solid angle of observation. The opening angle of the light cone  $\beta$  is about  $10^\circ$  for standard transmission/reflectance measurements.

## 4.2. Photoluminescence measurements

Setting up a PL system in Wuppertal was part of this work, it shall be described in more detail in the following chapter. As a light source a  $\text{Ar}^+$  ion laser was used, providing access to several excitation energies in the visible and UV range. As analyser a double grating spectrometer with a focal length of 0.22 m was used (SPEX 1680B as described in section 3.1.1) in combination with a photo multiplier tube (PMT) using a lock-in technique to improve the signal-to-noise ratio.

#### 4.2.1. $Ar^+$ ion laser

To excite the photoluminescence from dye loaded samples, a 20W Argon ( $Ar^+$ ) ion-laser was used (Spectra Physics, model Beam Lok 2080 ). This model was operated in constant power mode, where the output power is monitored and stabilised to a drift smaller than  $\pm 0.3\%$  in two hours.

Several lines are accessible in the UV and visible (351.1 nm – 528.7 nm) and the optical power density can be precisely controlled. In contrast to the visible, where a prism-coupler was used to select the appropriate laser line in the UV broadband emission using a mirror was used. The excitation line (351.1 nm) was selected by using a band-pass interference filter (Melles Griot, FWHM = 10 nm). A principal sketch of the whole PL set up is shown in figure 4.4.

To enable a fine tuning of the excitation power also in the low power regime ( $\mu W$ -mW optical output power) a set of neutral density filters (ND filter) can be inserted into the light path. The attenuation provided by these filters can be chosen in fine steps. The beam is focussed onto the sample by an adjustable lens for most measurements.

$\lambda$ [nm]	relative intensity
<b>351.1+351.4</b>	<b>0.19</b>
454.5	0.06
<b>457.9</b>	<b>0.16</b>
465.8	0.07
472.7	0.11
476.5	0.26
<b>488.8</b>	<b>0.78</b>
496.5	0.27
501.7	0.16
<b>514.5</b>	<b>1.00</b>
528.7	0.16

**Table 4.1:** Available  $Ar^+$  laser lines and their relative intensities. The most used lines are indicated in bold.

#### 4.2.2. Photoluminescence set up

The sample itself is mounted on a rotational stage to enable angle dependent PL measurements. The iris aperture in front of lens allows to select a small solid angle from which the photoluminescence is detected.

The light emitted by the sample is focussed into the entrance slit of a SPEX 1680B double monochromator. To avoid distortions from 2<sup>nd</sup> order reflexes – especially from the laser

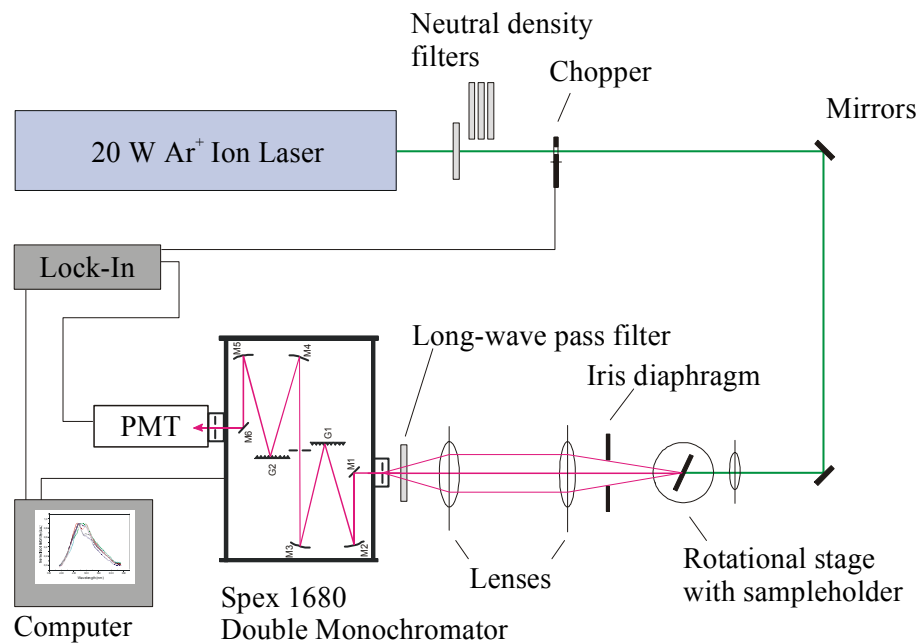


**Figure 4.4:** Set up used for photoluminescence measurements. The luminescence signal has been recorded using a lock-in amplifier with a mechanical chopper and a PMT. The laser was attenuated via variable neutral density filters, when necessary. The sample was mounted on a rotational stage. The Iris diaphragm allows to define a small solid angle from which the luminescence is collected. Different configurations have been used based on this layout as shown in figure 4.5.

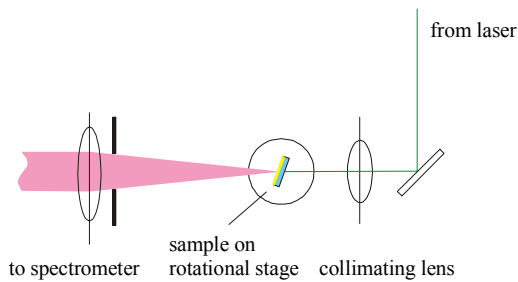
beam – a long-wave pass (LWP) filter, which cuts off all wavelengths below 350 nm, is placed in front of the spectrometer.

The signal is detected using a PMT (Hamamatsu R1387, multi-alkali cathode,  $\lambda$ : 300–800 nm) at room temperature, operated at -1000V and standard lock-in technique. The whole set-up is controlled by a personal computer using a modular TestPoint Program which has been written as part of the set up.

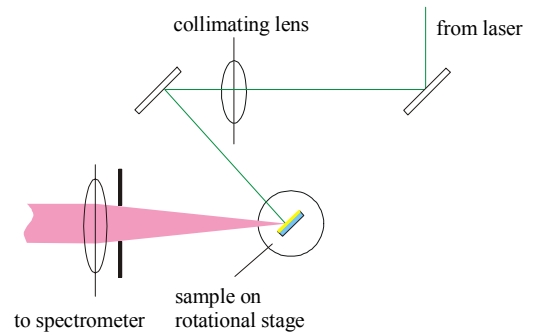
The spectrometer used is a SPEX 1680B double grating monochromator. The principle advantage of a double grating monochromator compared to its single-grating counterpart is (although not essential for the described measurements) a drastically reduced stray light outside the pass-band of the monochromator and significantly enhanced spectral resolution.

The incoming light is directed by a 45° mirror to the first grating stage (focusing mirror, grating, focussing mirror) a small fraction of the spectrum passes an aperture and is directed to the similar second stage where the light is dispersed again. Thus the spectrometer is working in additive-dispersion mode, being responsible for the high spectral resolution that can be expected from the system. To scan the wavelengths, both gratings are rotated simultaneously by a stepper motor.

a) Back-Window Configuration



b) Front-Window Configuration



c) Top-Window Configuration

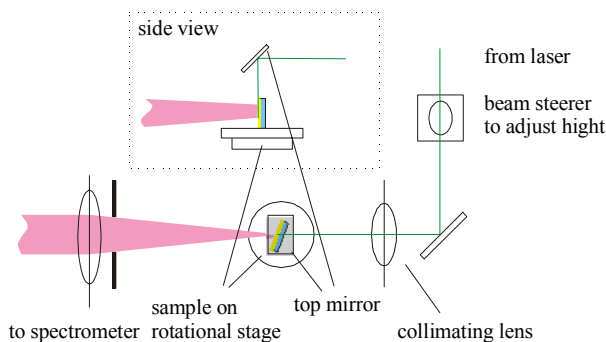


**Figure 4.5:** Sketch of different configurations used in the photoluminescence set ups. In Back Window configuration the sample is illuminated from the back side through the (transparent) substrate (a). In Front Window configuration the sample is illuminated from the front (film) side (b). In Top Window configuration the sample is illuminated from the top at grazing incidence resulting in a stripe-shaped illuminated area (c).

The spectral dispersion can be calculated to be  $3.4 \text{ nm/mm}_{\text{slit width}}$ . Since the measured photoluminescence usually is a spectrally broad feature the slits were opened to 0.5-2 mm with entrance and exit slit having the same width for optimum performance.

Depending on the type of measurement, the set up was slightly modified to allow front-window, side-window or top-window excitation configurations as sketched in figure 4.5.

Most measurements were taken in Back-Window configuration. This means that the luminescence was excited by illuminating the sample with a (collimated) beam from the backside. This ensures that the larger part of the excited PL travels through the crystal before it reaches the detector.

	Photoluminescence	Transmission / Reflectance
<i>Spectrometer</i>	SPEX 1680B	SPEX 270M
<i>Type</i>	Double Grating, Additive dispersion coupling	Single grating, Scanning imaging spectrograph
<i>Focal length</i>	220 mm	270 mm
<i>Dispersion</i>	3.4 nm/mm	3.1 nm/mm
<i>max. spectr. resol.</i>	0.2 nm @ $\lambda=500\text{nm}$	0.1 nm @ $\lambda=546\text{ nm}$
<i>Aperture</i>	f/4	f/4
<i>Grating</i>	600 g/mm	1200 g/mm
<i>Spectral range</i>	185-900 nm	0-1100 nm
<i>Detector</i>	PMT (multi-alkali)	Si Diode
<i>used spectr. band-pass</i>	1.5–6.8 nm (slits 0.5–2 mm)	4.6 nm (slits fixed 1.5 mm)
<i>used angular resol.</i>	2-14°	5-20°

**Table 4.2:** Comparison of key parameters of the set-ups used for photoluminescence and transmission/reflectance measurements. For both configurations a lock-in technique has been used to improve the signal-to-noise ratio.

For Front-Window-excitation the sample is irradiated on the front surface and detected in reflectance configuration. This bears usually the risk of the photonic crystal effects being shaded by a large contribution of light that is emitted from the surface and which does not interact with the photonic crystal structure. For strongly absorbing samples this configuration was used, though.

In Top-Window configuration the beam was steered to reach the sample from the top and focussed using a lens with long focal length to illuminate a stripe of the whole width of the sample, located in the rotation axis. This set up avoids changes of the illuminated area of the sample while rotating and offers a large illuminated area at the same time. A drawback is the high sensitivity to misalignment.

A comparison of the key optical parameters of the used set ups for PL and transmission / reflectance spectroscopy is given in table 4.2. The indicated parameter “angular resolution” should be understood as the opening angle of the light cone emitted by the sample, passing the iris aperture and thus probed by the set-up.

### 4.3. Raman spectrometer

Figure 4.6 shows the schematic of the set up used for the Micro-Raman experiments. The entrance optics of a modular Dilor XY800 spectrometer focuses the laser beam on the sample, reduces stray light and collects the scattered light. With the set up it is possible to choose

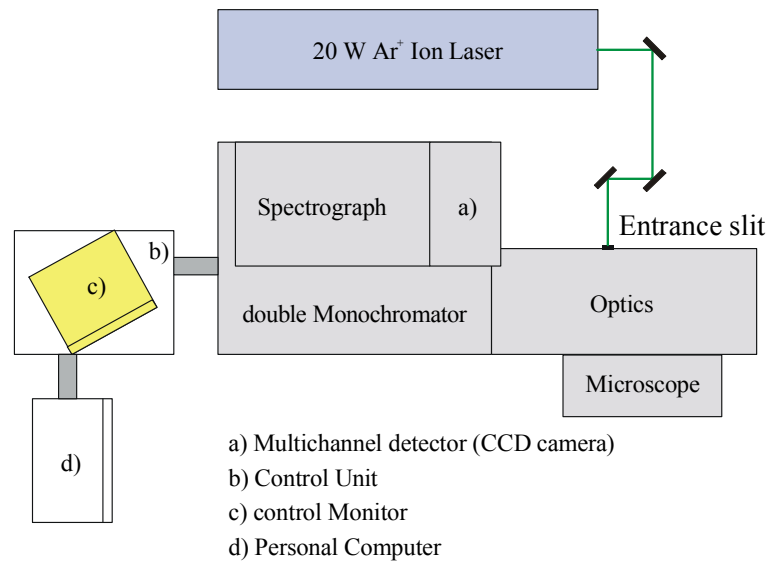


**Figure 4.6:** Sketch of the Micro-Raman set up using a Dilor XY-800 triple spectrometer.

between a Macro- and Micro-Raman mode. However, in this work all experiments were performed in the micro-Raman mode using an Olympus BX40 microscope to focus the laser beam to a spot diameter of about  $3\ \mu\text{m}$  (with the  $\times 100$  objective). For the 25 mW power level used in the Raman experiments this produced a power density on the sample in the  $2\ \text{kWcm}^{-2}$  range. The power was measured after the microscope objective at a distance of about 20 mm from the sample surface. The samples were measured at room temperature in air environment.

The Dilor XY800 Raman spectrometer system is essentially composed of a double monochromator and a spectrograph. In this experiment the double monochromator was used in the subtractive mode to provide a wide detection range to the spectrograph and to increase the signal. The path of the beam through the double monochromator is shown in figure 4.7.

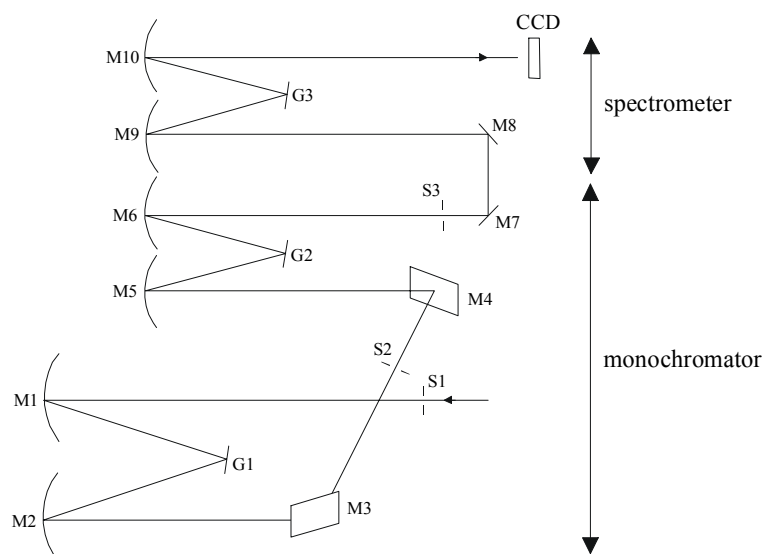


**Figure 4.7:** Optical path inside the double monochromator for the subtractive mode (as used for all experiments).

Two plane holographic gratings with 1200 groves/mm are used as a pre-filter for the monochromator. The spectrograph contains a 1200 groves/mm grating allowing a spectral coverage of  $31000\text{--}11000\text{ cm}^{-1}$  ( $322.5\text{--}909.0\text{ nm}$ ). In the subtractive mode slits S1 and S3 are determining the resolution and have to be set to the same value. S2 reduces the stray light. The resolution was determined experimentally by measuring the laser line at different slit widths. As the laser line width is much smaller than the expected resolution of the system, this technique is valid to approximately determine the upper limit of the resolution.

All Raman experiments were performed in the subtractive mode with a slit width of  $100\text{ }\mu\text{m}$  resulting in a resolution  $\leq 1.6\text{ cm}^{-1}$ . In additive mode the resolution would be  $\leq 0.6\text{ cm}^{-1}$  using a slit width of  $100\text{ }\mu\text{m}$ , with a much reduced signal intensity, however. Since ultra-high resolution was not needed for the experiments, subtractive mode was used to benefit from improved signal intensity.

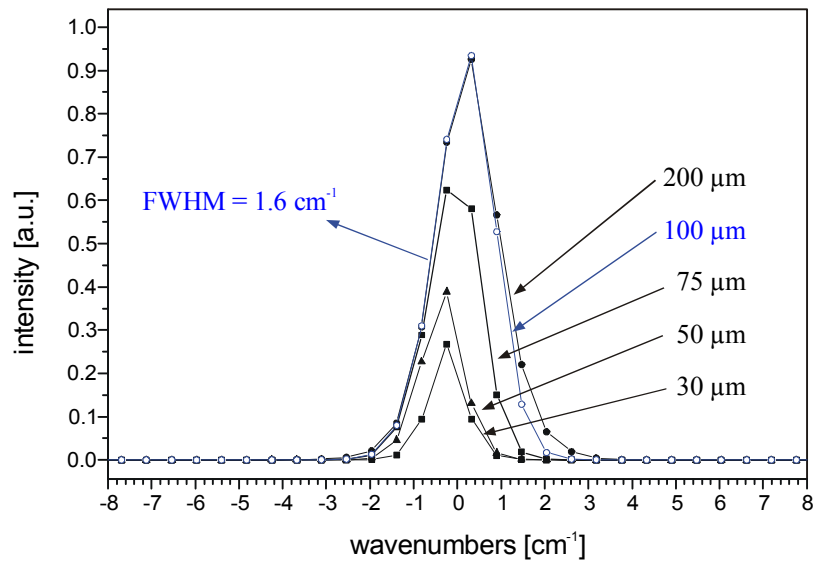


**Figure 4.8:** Resolution of the Dilor XY-800 Raman spectrometer. Measured linewidths (FWHM) of the 514.5 nm laser line recorded at different slit sizes in subtractive mode. All Raman spectra were recorded at a slit width of 100  $\mu\text{m}$ , resulting in a resolution better than 1.6  $\text{cm}^{-1}$ .

A liquid-nitrogen cooled SpectrumONE CCD camera was used as detector. The chip offers a resolution of 2000 $\times$ 800 pixels. The vertical extent of the detector (800 pixels) was integrated over to obtain a decent signal level. The horizontal extent of the detector of 2000 pixels was used to read out a spectral region of ca. 30 nm ( $\approx 1000 \text{ cm}^{-1}$ ) at once without moving the spectrometer.

## 5. Opal based Photonic Crystals

The investigations presented in this work are focussed on a special class of PhCs, that are manufactured by a self-assembly approach. In the following chapter a more detailed description of the structural properties and fabrication methods of opal based PhCs is given, starting with a brief overview of the state of the art in this research topic.

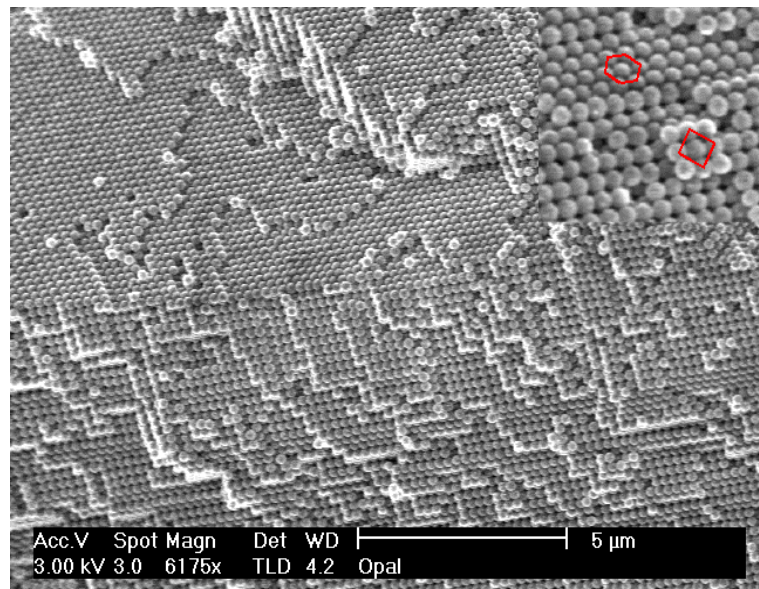


**Figure 5.1:** SEM micrograph of an artificial opal crystal made by sedimentation from monodisperse SiO<sub>2</sub> spheres into a *fcc* structure. Two sets of crystallographic planes are visible (*111*) planes (upper half) with hexagonal symmetry and (*100*) planes (lower half) with square symmetry, as indicated in the inset.

### 5.1. Silica opals

Opal is, as mentioned, a naturally occurring 3D periodical package of monodisperse silica (SiO<sub>2</sub>) spheres arranged in a *fcc* lattice. The diameter of the spheres in opal can be varied from 150 nm to 1 μm, thus the Bragg resonance can cover the range of optical frequencies from near infrared (NIR) to the ultraviolet (UV). Opals with periods of 200-350 nm show PBGs in the visible region of the spectrum. Since natural gem stones are expensive and their voids are filled with amorphous material in most cases they are difficult to study – apart from the fact

that good control of the sphere diameter is necessary to obtain reliable experimental results. Attempts to mimic the opal structure artificially by sedimentation of monodisperse silica spheres have been made starting in the 1970s:

Silica spheres can be synthesised in different diameters using the Stöber process [64]. After purification, centrifugation and separation an aqueous solution of monodisperse silica spheres is obtained (the standard deviation of the sphere diameter should be less than 5%, better less than 1%). These spheres are the basic compound of artificially grown opals.

To fabricate silica opals, the SiO<sub>2</sub> spheres are sedimented [7, 46] to form ordered packages which are sintered afterwards [65] to improve their mechanical stability.

The arrangement of spheres in the form of colloidal *fcc* lattices has been observed for different materials such as silica spheres [7], and different polymers [48, 66, 67].

Sedimentation under gravitational force only works for a limited range of sphere diameters from ca. 200 to 550 nm. The sedimentation of small spheres on the one hand (diameter < 200 nm) can lead to settling times of several month, whereas sedimentation of big spheres (diameter > 550 nm) on the other hand leads to high sedimentation rates which prevent a good long range *fcc* ordering. The average sedimentation process takes a few hours to a few weeks, depending on the sphere diameter and sedimentation conditions.

To produce high-quality crystals it is crucial to control the sedimentation rate very precisely. To achieve this, an electrophoretic approach has been introduced [68]. By applying an electric field the sedimentation velocities can be changed by will, allowing the synthesis of opal crystals with a wider range of sphere diameters. With this method it is possible to synthesise opals with diameters up to 1000 nm thus realising PBG structures working beyond the visible and NIR range.

The result are opal PhCs of lateral sizes up to several mm and thicknesses of a few mm. They are not single crystalline but consist of smaller crystalline domains with sizes up to 500 μm<sup>2</sup> which are all oriented.

Since the spheres are arranged in a *fcc* structure, empty voids occur between touching balls and these, in turn, form their own regular lattice. There are two types of interpenetrating voids in the opal lattice: large 8-fold coordinated voids each of which is connected with four small 4-fold coordinated voids. Thus, large and small voids follow each other in an alternating manner. The size of the voids ( $d_1 - d_3$ ) in between the spheres for an ideal *fcc* package relates to the sphere diameter ( $D$ ) as  $d_1 = 0.41D$  for the large voids and  $d_2 = 0.23D$  for the smaller ones. The minimum diameter of a connecting window is  $d_3 = 0.15D$  [69-73]. This minimum diameter is altered slightly if the sintering process is taken into account and has to be beard in mind if opals are infilled with high RI materials. Low viscosity or gaseous materials should be used to infill the voids to prevent blocking of the interconnecting windows which could prevent a complete infill. The density of voids in the opal depends on the sphere diameter and

is typically around  $10^{13} \text{ cm}^{-3}$ . The *fcc* packing provides a close approximation to a spherically shaped Brillouin zone that is ideal for the existence of omnidirectional PBGs [19] (cf. chapter 2.2.3).

As the RI of silica is about 1.26-1.45 [74] for the visible and IR region, the RIC is too low to build a omnidirectional PBG thus only a *pseudo-gap* or *directional gap* can be expected in bare opals. Consequently light propagation is suppressed significantly only in certain crystallographic directions. This has been demonstrated as a stop band in transmission in opals immersed in solvents [75]. In fact the *relative band gap width* ( $\Delta E/E$ ) for bare silica opal does not exceed 5–6% which is far below the theoretical necessary value of 17-19% [76, 77].

The infilling of opal with high-RI materials such as  $\text{SnS}_2$ ,  $\text{TiO}_2$  is a possible approach to improve the PBG width. The use of coated spheres or the inverted structure can increase the depth of a pseudo gap [78]. This makes dye-polymer-opal composites and especially their inverted replicas an interesting material system.

The crystallinity of bulk opals is intrinsically limited by the self-organising nature of the sedimentation process. Usually there is about 1 defect per 100 unit cells. Moreover, stacking faults disturb the ABCABC... sequence of layers that is found for perfect *fcc* crystals in [111] direction (cf. figure 5.11). They give rise to less pronounced PBG properties [79]. To improve the optical data, single domain spectroscopy of a polycrystalline opal was suggested. In particular, the micro-reflectance spectroscopy – projecting the microscope image of the sample into a spectrometer – has been employed by Vlasov et. al [80]. Obviously, the drawback of microdiffraction measurements is the dependence of results upon the choice of a particular domain. In following sections we will show how to tackle with ordering of opals and how to overcome the problem of the refractive index contrast. Disorder is certainly one of the key problems in self-assembled systems.

## 5.2. Opal polymer composites

The relatively low viscosity of dye-loaded oligomers makes the task of impregnating it into the opal matrix uncomplicated. The polymerisation is then carried out inside the matrix via either thermally or photochemically activated initiators:

To begin with, the bare opal samples are flushed with dry nitrogen and then immersed, in a  $\text{N}_2$ -atmosphere, into a solution of monomers and dyes which also contains the selected initiator. After the solution has penetrated the complete opal crystal, polymerisation is started either by irradiation of the impregnated opal with UV-light or by heating it slightly (figure 5.2a). After the polymerisation step is completed, the sample is a rigid dye/polymer-opal composite [81]. The sample is cut out of the polymer block (figure 5.2b).

The well known initiators benzoyl-peroxide (thermal polymerisation of styrene) and diphenyl(2,4,6-trimethylbenzoyl)phosphine (photochemical polymerisation of acrylates) have been used. The photochemical reaction has slight advantages as no gases are produced resulting in more homogeneous samples. If the reaction temperature for thermally polymerised samples is too high, the risk of uncontrolled acceleration of the reaction

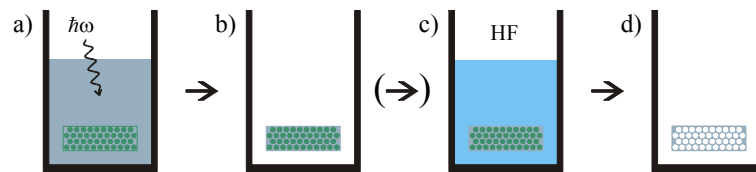


**Figure 5.2:** Infill process for opal with a dye loaded polymer: Dry opal is immersed in a dye/oligomer solution, which subsequently is polymerised photochemically (a). The polymer/opal block is cut out of the polymer (b). To produce an inverted structure the  $\text{SiO}_2$ -spheres can be etched in HF solution (c). The result is an inverted polymeric opal-replica (d).

(Thombsdorff-effect) combined with production of gases increases dramatically.

Although the refractive index contrast (RIC) cannot be pushed high enough to expect a full gap, as depicted in section 2.2, the structure can be inverted by removing the silica balls with diluted hydrofluoric acid solution (figure 5.2c). These inverted replicas offer improved photonic properties.

### 5.3. Polymeric thin film opals

Polymer spheres, e.g. poly(methylmethacrylate) (PMMA) or polystyrene, are an alternative to silica spheres and allow the extension of the self-assembly to a variety of tailored materials [10]. The polymers can be easily doped with light emitting species prior to the sedimentation, modified by deposition of functional groups or made into nanostructured media themselves by deposition of inorganic shells [82].

The basis of polymer based crystals are monodisperse polymer spheres. The growth process of a PhC from polymer spheres is comparable to the fabrication of silica based crystals. The polymer PhC samples can cover areas up to several  $\text{cm}^2$ .

In what follows the synthesis of monodisperse polymer spheres is briefly explained as well as the growth of PhCs from the spheres.

### 5.3.1. Synthesis of polymer spheres

The organic chemistry offers several ways to synthesise spherical shaped polymers [10]. The main prerequisite is a two phase-system of solvent and monomer- or polymer-phase. Since PhCs demand high monodispersity and good size control the number of synthesis routes is reduced significantly. Basically two widely used ways to produce polymeric spheres – Suspension- or Emulsion-Polymerisation – seem to be promising. Both routes are intrinsically different:

*Suspension polymerisation* can be used if solvent and monomer are non-miscible. In that case the monomer-phase can be dispersed into small droplets by heavy stirring of the suspension. These droplets are polymerised by an initiator which is soluble in the monomer, thus the polymerisation takes part in within the monomer phase. The diameter of the resulting spheres is dependent on the reaction parameters as stirring technique, viscosity of the monomer, temperature etc. The resulting sphere diameters can be controlled to be between 10  $\mu\text{m}$  and 5 mm [83] – Thus the diameters are too big to be used in PhCs for the visible regime (apart from the fact that the particle size distribution is not small enough).

The other, more suitable, reaction is the *Emulsion polymerisation* [84]. The main difference in the reaction kinetics is, that the polymerisation does not take place within the monomer droplets – they simply act as reservoir – but in the solvent. Standard Emulsion Polymerisation bears some disadvantages regarding monodispersity of the spheres and aggregation of spheres, though. Thus a surfactant free emulsion polymerisation (SFEP) approach has been followed. One key advantage using the SFEP is the absence of emulsifiers which would tend to glue the spheres together so the sedimentation into a photonic structure would be impossible. The polymer spheres grown by this method show surface charges which give rise to electrostatic repulsion that prevent aggregation. It is also possible to modify the surface of the spheres to implement a variety of other effects.

In principle the SFEP mechanism works as shown in figure 5.3:

The reaction takes part in aqueous solution. A non water-soluble monomer and a water soluble initiator are mixed under heavy stirring to produce an emulsion of monomer droplets in aqueous initiator solution. containing a small concentration of monomers.

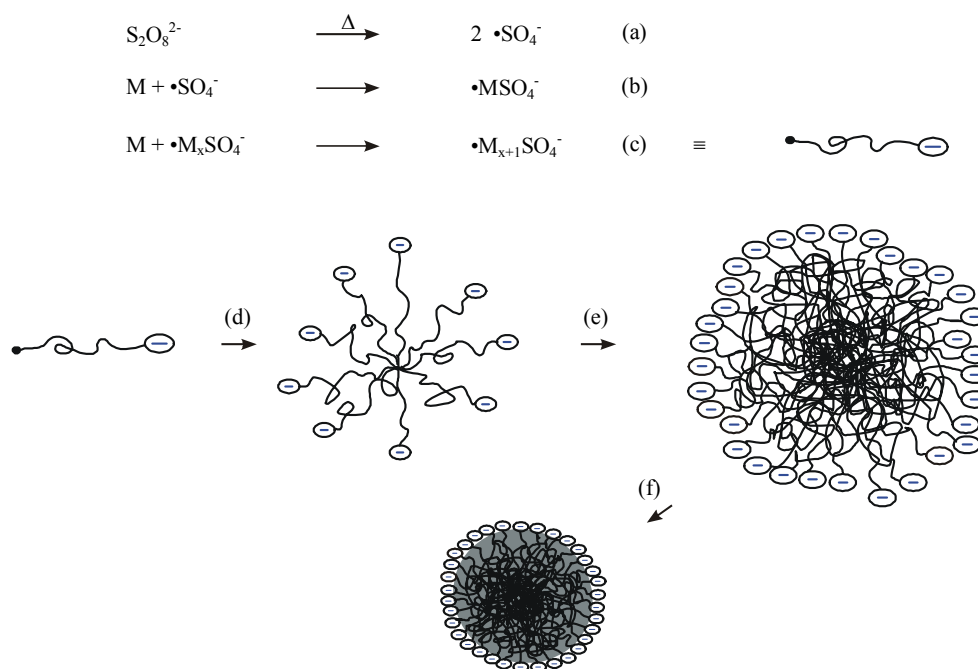


**Figure 5.3:** Principle mechanism of a surfactant free emulsion polymerisation. A water soluble initiator (a) starts a radical polymerisation (b). Monomers in the water phase are added, resulting in oligomers(c). Oligomers that reach a certain length aggregate to spherical micellae (d). They grow by aggregation of oligomers and Monomers (e) until a certain size is reached beyond which no aggregation occurs and growth takes place by the dissolved Monomers only (f) until the initiator is inhibited or no free monomers are available. Adopted from [85].

Thermal decomposition of this initiator (a) starts a radical polymerisation of the monomers that are dissolved in water (b). Oligomers are formed (c). They can be regarded as interface-active anionic emulsifiers. The oligomers start to aggregate in micellae in the aqueous phase after they reach a certain length (d). Their growth is now supported by dissolved monomers and oligomers (e). At a certain point an oligomer concentration is reached where no more aggregation of oligomers occurs. The growth of the micellae, now called spheres, from this point onwards is only supported by dissolved monomer – the concentration of which remains constant since reacted monomer is replaced by monomer diffusion from monomer droplets in the solution.

The polymerisation speed is determined by the decomposition rate of the initiator (which is constant). By stopping the reaction at a certain time, the size of the spheres can be controlled. By this method monodisperse (< 10% deviation in diameter) spheres can be obtained with diameters ranging from 10 to 1000 nm [85].

After the reaction is stopped the Product is purified in a multi-step process by filtration centrifugation and washing. The different centrifugation steps also induce a separation of spheres of different diameters, a careful separation of different parts of the product allows to improve the monodispersity of the resulting spheres considerably. The result is a suspension of quasi-monodisperse polymer spheres (standard deviation of diameters <1% ) in water. Details can be found in Refs. [86] and [87].

### 5.3.2. Preparation of thin film crystals

Once monodisperse spheres are obtained they have to self-assemble into *fcc* crystals. A number of different approaches have been followed to synthesise PhCs from polymer spheres have been suggested.

The straight forward method is to sediment the spheres under gravitational force in analogy to silica opals. The lower relative density of polymers makes this approach very slow. An alternative is the casting of polymer suspensions on suitable substrates [48]. A disadvantage of both methods is a lack of control on the film's thickness. Thin film PhCs, the thickness of which is controlled by growing them in physically confined cells under sonic agitation, were prepared successfully by Xia et. al. [88]. A different method was suggested by Veleev, who used the capillary forces to grow opal films on vertical substrates [47, 89]. Apart from better crystallinity, this method allows to change the film thickness more precisely.

The most successful growth methods will be presented in the following chapters.

#### 5.3.2.1. Sedimentation

Monodisperse spheres can be easily sedimented on hydrophilised glass or other suitable substrates. They sediment under gravitational force and form *fcc* ordered films (with the (111) plane parallel substrate) at the bottom of the sedimentation cylinder (figure 5.4). This process is similar to the growth of silica opals.

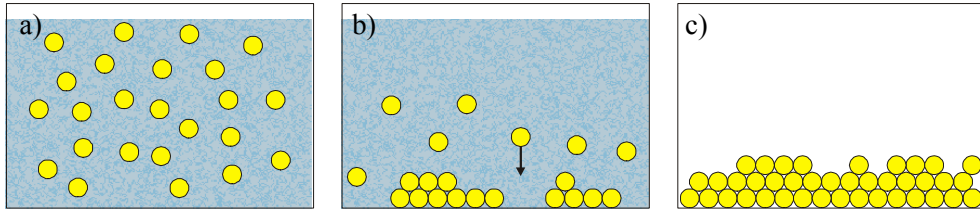


**Figure 5.4:** Sedimentation process of colloidal spheres into fcc crystals. Spheres in aqueous solution (a) slowly sediment under gravitational force (b) into solid crystals that remain stable after the solvent is removed (c).

The sedimentation process essentially can be described by Stokes-law [90]. The sedimentation speed is a crucial parameter here . It is given by:

$$v_{sed} = \frac{(\rho_{sphere} - \rho_{solvent}) g D_{sphere}^2}{18\eta_{solvent}} \quad (5.1)$$

With sphere diameter  $D_{sphere}$ , gravitational constant  $g = 9.81 m/s^2$ , densities of spheres and solvent  $\rho_{sphere}$  and  $\rho_{solvent}$  and viscosity of the solvent  $\eta_{solvent}$  .

For high volume densities of spheres in the initial suspension the sedimentation speed  $v_{sed}$  is reduced due to sphere-to-sphere interaction [91], which should be taken into account in a more detailed quantitative analysis. For the qualitative view presented here, this dependency can be neglected.

	PMMA	SiO <sub>2</sub>
$\rho_{sphere}$ [g/cm <sup>3</sup> ]	1.18	2.10
$D_{sphere}$ [nm]	280	280
$v_{sed}$ [nm/s] ([ $\mu$ m/day])	7.5 ( 648 )	46.6 ( 4026 )
$t_{sed}$ [h] ([weeks])	1851 ( 11 )	298 ( 1.7 )

**Table 5.1:** Estimated sedimentation times for PMMA and SiO<sub>2</sub> based opaline PhCs. For the estimated sedimentation time  $t_{sed}$  a suspension height of 5 cm is assumed.

Calculating the sedimentation speeds for an average sphere of 280nm diameter leads to the sedimentation times given in table 5.1 for both materials, PMMA and SiO<sub>2</sub>. For both cases an aqueous solution with  $\rho_{solvent} = 1.003 g/cm$  and  $\eta_{solvent} = 1006 \mu Pa \cdot s$  at room temperature was assumed [90]. It was further assumed that the suspension height is about 5cm. It is

evident, that the resulting long sedimentation times of several weeks (vs. several days for SiO<sub>2</sub>-spheres) makes synthesis of crystals by sedimentation under gravity unattractive for PMMA spheres. Therefore a different approach has been followed to produce thin film PMMA based PhCs.

### 5.3.2.2. Casting of PMMA spheres on hydrophilised substrates

To circumvent the long sedimentation times, a suspension of PMMA spheres was simply cast on hydrophilised glass slides or other suitable substrates and dried in an atmosphere of controlled humidity. The solvent evaporates slowly, forcing the spheres eventually to self-assemble in *fcc* structure because of the shrinking available space.

A key difference to the sedimentation method is the strong influence of capillary forces and sphere-to-sphere interactions (caused by surface charges, sticking etc.) in contrast to the quasi sphere-to-sphere interaction free (Edwards-Wilkinson) behaviour of the sedimentation process.

For identical spheres two non-equivalent ways exist to build a closely packed structure: The *fcc* and the hexagonal close packed (*hcp*) structure. Both structures offer a solidity of 74% and differ essentially only in their stacking sequence, as sketched in figure 5.5. In [111] direction – the growth direction of the PhCs – the *hcp* structure consists of a bilayer stacking sequence (ABABAB...), whereas the *fcc* structure shows a tri-layer sequence (ABCABCABC...). The *fcc* arrangement is energetically slightly favoured compared to the *hcp* configuration, so the crystallisation takes place predominantly as *fcc* crystals if close to equilibrium state.

If the sedimentation takes place slow enough close-to-equilibrium-conditions can be assumed. In this case the sedimentation follows an Edwards-Wilkinson growth law – which assumes the independent minimisation of the total energy for every sedimented sphere [92]. Then the slight energetic advantage of the *fcc* structure over the *hcp* structure can be understood qualitatively by a simple consideration of the fact that in the *fcc* lattice the third monolayer (C) is placed above the voids of layer (A), whereas in the *hcp* lattice the third layer is placed directly on top of the first layer (figure 5.5). Assuming a weak repulsive force between the spheres (due to surface charges) growing in *fcc* arrangement is energetically slightly favoured. Since the energy difference is relatively weak, numerous stacking faults can be expected.

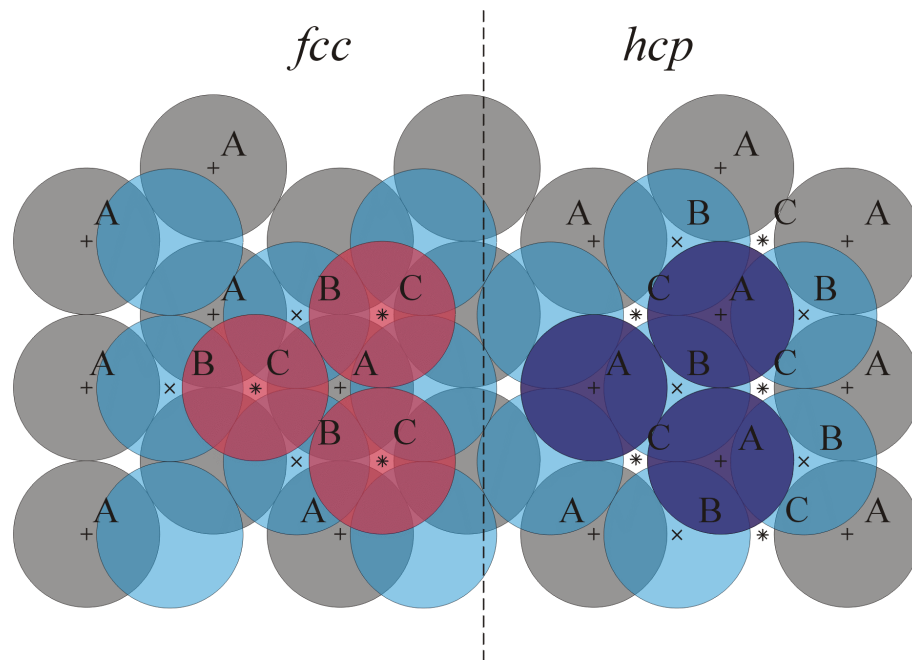


**Figure 5.5:** Top view of a closely packed structure of spheres. The spheres can be arranged in two configurations. One is the fcc structure (left), the other the hcp structure (right). For both configurations the filling fraction is 74%. Both structures differ in their stacking sequence: A closely packed layer of identical spheres with their midpoints in A (grey) can be covered with a second layer of spheres with midpoints in B (light blue). For the third layer two non-equivalent possibilities exist to obtain a closely packed structure: On top of C (fcc structure - red) or on top of A (hcp structure - dark blue). This lead to a stacking sequence of ABCABCABC... or ABABABAB..., respectively.

Of course many other effects and parameters influence the degree of order in colloidal PhCs, such as capillary forces, concentration of the suspension, ball diameter, surface charges, speed of drying etc.

In principle the growth mechanism of cast thin film PCs is understood to work as follows [87]:

A few droplets of dispersed PMMA balls in aqueous solution (5-10 wt-%) are cast on hydrophilised substrates and dried in an atmosphere of controlled humidity (98%) to slow down the drying speed. The suspension starts to evaporate until the water film reaches the thickness of the spheres diameter. Now capillary forces start to transport water from the centre of the cast area to the borders to replace the evaporated water. Spheres are transported with the water to the borders where they aggregate with other spheres that have already crystallised there. Due to surface charges that have been formed in the polymerisation process by the initiator, a weak repulsive force between the spheres exist which suppresses early aggregation

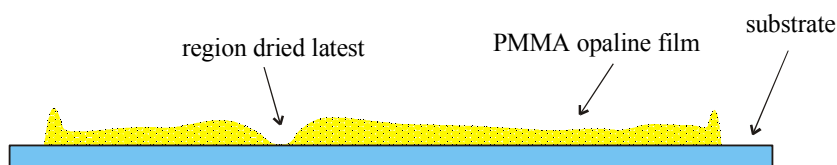


**Figure 5.6:** Sketch of a typical height profile of a cast PMMA opaline film. It is worth to mention that the film's height is usually big at the borders, small in the regions dried latest and relatively constant in-between. Adopted from [87]

of spheres in solution and supports the crystallisation process into the *fcc* lattice. The material transport from the centre to “drying zones” at the border of the film causes a concentration gradient that has strong influence on the film thickness. Therefore the thickness of the obtained PMMA opaline films is not precisely (on the monolayer level) controllable nor homogeneous.

In general the borders are relatively thick (up to several 100 monolayers) whereas the parts dried latest are usually thin (a few monolayers) or do not contain any spheres. A typical height profile is sketched in figure 5.6. Some films show strong fluctuations in their height profile or areas of poor crystallinity as it can be seen from the measured height profile in figure 5.7. The “middle” parts of the films have relatively constant thickness, though.

The height profile of the film depicted in figure 5.7a, was measured using a profilometer (Dektak) with a tip force of 5 mg (to avoid the destruction of the brittle opal film). The whole scan was done along the red line marked on the photograph by stitching several individual scans covering ca. 5mm each (figure 5.7b). The film was chosen because it shows all features that were observed in different films. The height profile shows the typical high borders (I), followed by a plateau of constant thickness (II). A region of weaker crystalline quality appears white in the photograph. It coincides with a strong fluctuation in the height profile (III). This feature is not present in all films and seems to be strongly dependent on the drying conditions and local morphological abnormalities such as dust particles on the substrate etc. In contrast, the decay of the film's height in the region dried latest (IV) is typical for cast films. More details on the synthesis process of thin film polymeric PhCs can be found in [67, 86, 87].

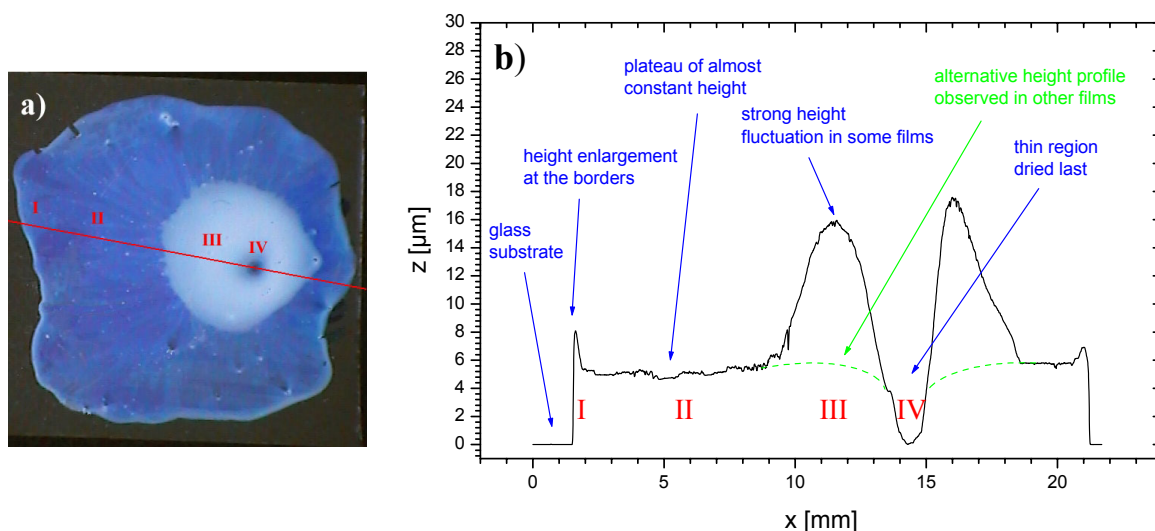


**Figure 5.7:** Photograph of a cast film (a) and its corresponding height profile measured along the red line (b). The film shows typical features of cast films: Height enlargement at the borders (I), a plateau of almost constant height (II), strong height fluctuation in an area of weaker crystalline quality (III) – this feature appears in some films only, others have the height profile sketched with dashed lines in (b); and a decrease of the height to a few monolayers or no spheres in the region dried last (IV).

Another big problem in the preparation of these films is the formation of macroscopic cracks during the drying process, which has not been properly explained yet (figure 5.8). The films' morphologies resemble dried mud or cracks in drying starch-water suspensions and the form of basalt-pillars. The same physical principle can be made responsible for all three phenomena [93].

The main reason in case of PMMA opaline films is probably dwelling of the spheres in solvent and shrinking during the drying process. This leads to strain within the film that results in the formation of macroscopic cracks. Another possible explanation, which induces essentially the same mechanism, is the existence of a thin solvent film around the spheres which eases the movement of the spheres during the sedimentation process but also leads to a reduction of the distance between neighbouring spheres after drying.

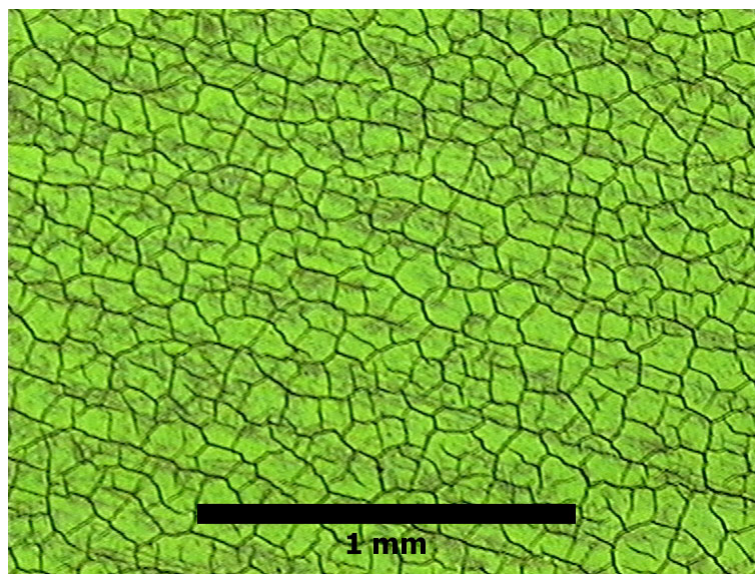


**Figure 5.8:** Formation of macroscopic cracks in polymeric thin film crystals during the drying process, possibly due to dwelling of the spheres by the solvent. The single crystal domains are up to 100  $\mu\text{m}$  in length in this sample.

In both variants the cracks are induced at the surface by the strain accompanied with the drying process. They grow vertically into the depth of the film as the water inside of the film diffuses to the surface. As the spheres shrink the strain becomes too strong so the film breaks up into the typical pattern that can be seen in figure 5.8. The strain field at the surface is dominated by numerous local inhomogeneities that lead to irregularly shaped crystallites. In contrast, dried starch suspensions show irregular crack patterns at the surface which develop – driven by minimalisation of crack energy – into a polygonal pattern (dominated by hexagons and pentagons) in the depth of the film. The irregular pattern in PMMA films is an indication that the cracks have been formed under strong nonequilibrium conditions without the possibility to minimise the crack energy due to the small film thickness.

Fortunately the crystallites are relatively flat and the crystallographic orientation is preserved over the cracks (cf. figure 5.9). This is indicated by the blue lines in the figure that connect the high symmetry directions of the crystallites. The Fourier Transform (FT) of the image shown in the inset allows to visualise the crystallographic orientation and structural quality of the crystal qualitatively by transforming the SEM image into reciprocal space. The hexagonal order is well established, without pronounced signs of mosaic spread of the different crystallites (that would manifest in the existence of double-spots or elongated spots). The white cross near the origin of the FT image is the manifestation of the big cracks. The angle of the two cross bars of  $60^\circ$  indicates that the cracks form predominantly along the high

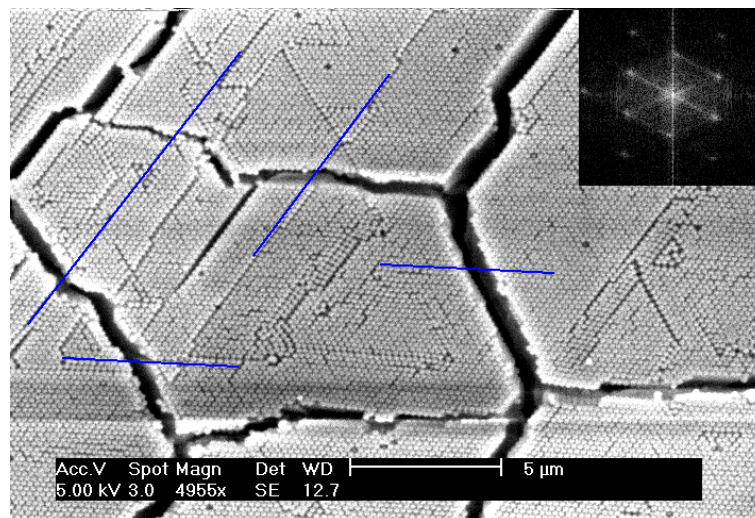


**Figure 5.9:** The crystallographic orientation is preserved over the different crystallites as indicated by the blue lines. The crystal has a relatively flat top surface and grows in fcc structure with the  $[111]$ -direction perpendicular to the surface. The hexagonal structure of the sample with homogeneous orientation over the whole sample is confirmed by the FT of the image shown in the inset.

symmetry directions of the crystal lattice. These results reads to the conclusion that the long range ordering is not lowered substantially by the cracks, thus the films can be treated as single crystals in first approximation.

In Summary, the film quality is mainly dependent on the speed of the evaporation of the solvent (in general slower drying leads to better films) but other factors such as concentration of the suspension, ball size, monodispersity etc. have to be matched and precisely controlled also to obtain decent results, making it a difficult task to grow high-quality films<sup>‡</sup>.

---

<sup>‡</sup> the samples under study were prepared by Dr. Manfred Müller, B. Griesebock and Dr. M. Egen, Institute for Organic Chemistry, Dept. of Chemistry and Pharmacy, Johannes Gutenberg University Mainz, Germany

### SEM studies of PMMA thin film opals

In the following section more detailed SEM studies on the morphology of different films are shown.

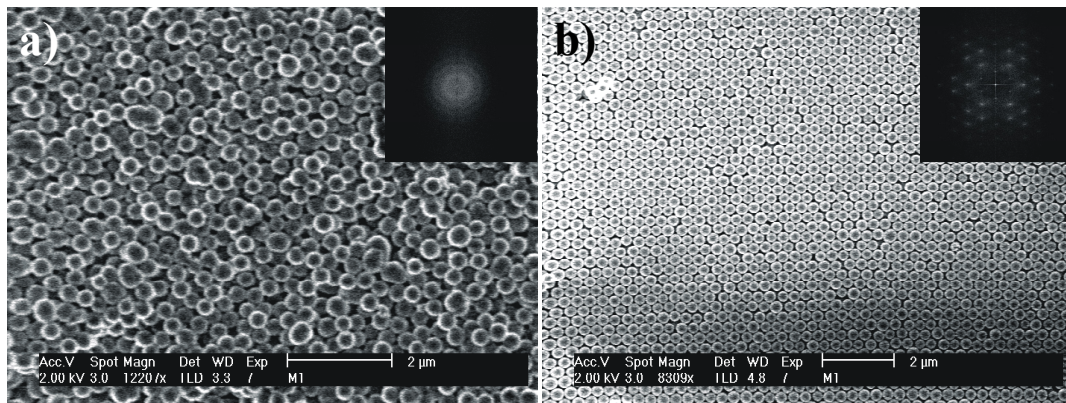


**Figure 5.10:** SEM micrographs of cast PMMA opals grown from the same spheres under different growth conditions.

- (a) The film shows a complete lack of crystalline order as visible from the FT (inset). The spheres are randomly distributed without any sign of long-range ordering.
- (b) The film grown under slightly modified conditions is well ordered in *fcc* structure. The FT image shows a pronounced hexagonal pattern indicating the presence of a high degree of order in the film.

In figure 5.10a comparison of the morphology of two film grown from the same sphere-suspension is given. Both films were cast from the same suspension on hydrophilised glass substrates. The growth conditions were slightly different. Whereas film (a) was left for drying in the laboratory film (b) was kept under an atmosphere of elevated humidity and thus dried more slowly. The fast evaporation of the solvent obviously prevented an ordered growth in the film. The spheres are randomly distributed, without any pronounced ordering. This is obvious from the FT shown in the inset. The blurred circular pattern without clearly visible spots is the sign for the absence of order. However, the situation is completely different in film (b). The slow evaporation of the solvent in humid atmosphere is favourable to the development of order. Presumably the individual spheres have more time to minimise their total energy before they stick together, which leads to the building of a *fcc* crystal. The FT of this film shows a hexagonal “diffraction” pattern that can be expected from (111) planes of a *fcc* crystal.

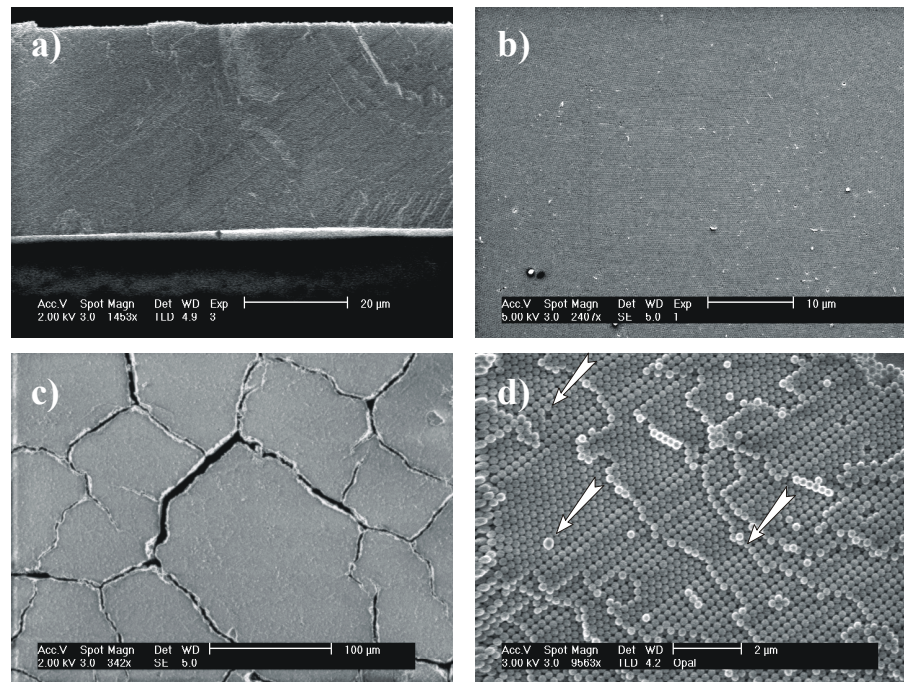


**Figure 5.11:** SEM images of PMMA thin film crystals highlighting different aspects of their morphology.

- (a): cleavage edge showing the homogeneity of the film over its full height  
 (b): low magnification image underlining the flatness of the film over large areas  
 (c): cracks are formed during the drying process. The remaining domain sizes are in the 100 μm range  
 (d): the films suffer from different imperfections as indicated by the arrows: Dislocations, spheres of wrong diameter, stacking faults

To give an impression of the morphological properties of an average PMMA thin film PhC a series of SEM images, that illuminate different aspects are given in figure 5.11. The thickness of the crystals can be steered coarsely by varying the suspension concentration and the drying speed. Film with thicknesses ranging from  $\approx 5\text{-}50\ \mu\text{m}$  can be grown by this method. The structure is very homogeneous over the whole height of the films, as well as the thickness is constant on small ( $\mu\text{m}$ ) length scales (figure 5.11a). The films are well ordered within one domain and do not show strong height fluctuations (figure 5.11b). During the drying process cracks form. The resulting domains range from a few  $\mu\text{m}^2$  up to some  $\text{mm}^2$  under optimised growth conditions [94]. The average film shows domain sizes of  $\approx 10,000\ \mu\text{m}^2$ , as shown in figure 5.11c. Caused by the self-assembly nature of the growth process the films are not defect-free. They suffer from various imperfections such as dislocations, stacking faults, spheres of wrong diameter, badly ordered areas etc. that are shown in figure 5.11d.

In general, thin film PMMA-based opals combine the advantage of a cheap and quick synthesis with easy machinability and post-deposition processing and are thus an interesting material system for the investigation of PhCs.

### 5.3.2.3. Vertical Growth Method

The crystallisation by vertical growth in the meniscus of the liquid phase is an alternative that has been proven to result in more homogenous films with improved crystallinity [87]. The

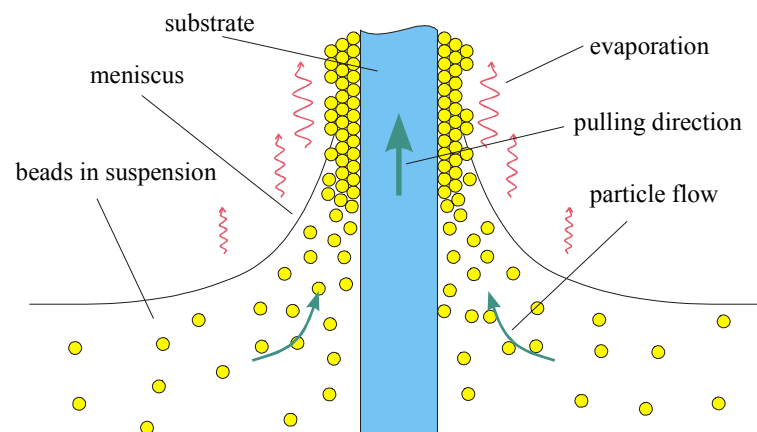


**Figure 5.12:** The vertical growth method can be used to grow homogenous films of large areas. A glass substrate is slowly pulled out of a suspension of monodisperse spheres. Due to enhanced evaporation of solvent at the meniscus spheres are transported to the substrate and crystallise there. A balance between drawing speed and crystallisation rate establishes under certain conditions that leads to a constant film thickness. Adopted from [87].

basic principle is a slow drawing of a substrate out of a suspension of monodisperse spheres that is depicted in figure 5.12. A meniscus is formed by surface tension and wetting forces when the hydrophilic substrate is immersed upright into a suspension of PMMA spheres in water. The evaporation of solvent is enhanced at the upper thin part of the meniscus. This results in an upward flow of solvent to replace the evaporated water. PMMA spheres are carried with the solvent to the upper part of the meniscus where they start to assemble. Since the substrate is pulled slowly ( $\approx 100$  nm/s) out of the suspension an equilibrium of crystallisation rate and drawing speed leads to the formation of a film with constant thickness. This thickness is mainly controlled by the drawing speed and the evaporation rate. The crystallised film eventually leaves the meniscus and the last drying step sets in. Similar to cast films macroscopic cracks form at this stage.

Key parameters to control the film quality and thickness are evaporation rate of the solvent, i.e. humidity, sphere diameter, temperature and drawings speed. With an optimised parameter set it is possible to draw films of several  $\text{cm}^2$  area in two to three days. More details on advantages and drawbacks of this method can be found in Ref. [87].

As it is clearly visible in figure 5.13 the comparison of a drawn film and a (low quality) cast film shows an improved homogeneity of the latter film.

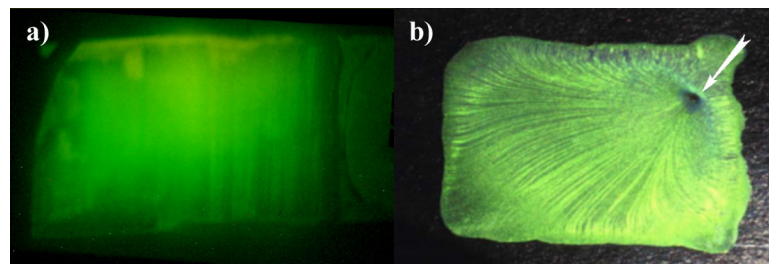


**Figure 5.13:** Comparison of the film quality of a drawn (a) and a cast film (b). (a) Film grown by the vertical deposition method, area ca.  $2.5 \times 4 \text{ cm}^2$  [87] (b) Film grown by casting [86], area ca.  $1.5 \times 2.5 \text{ cm}^2$ . The region dried latest is marked by the arrow and clearly visible. To clarify the difference, a cast film of low quality has been chosen. It is evident that the homogeneity films grown by the vertical growth method is superior.

#### 5.3.2.4. Liquid Substrates

Another method was tested to avoid shrinkage-induced cracks: Deposition on liquid substrates. The method is basically equivalent to the casting method but in contrast to hydrophilised solid substrates liquid metals are used as basis to deposit onto. Experiments with Mercury and slightly supercooled Gallium were undertaken as sketched briefly in figure 5.14. Due to the liquid substrate the formation of cracks during the drying process is expected to be suppressed since the shrinkage-induced strain can be relaxed by moving a large number of spheres that are floating in first approximation frictionless on the substrate. Thus the strain is carried off to the borders of the film.

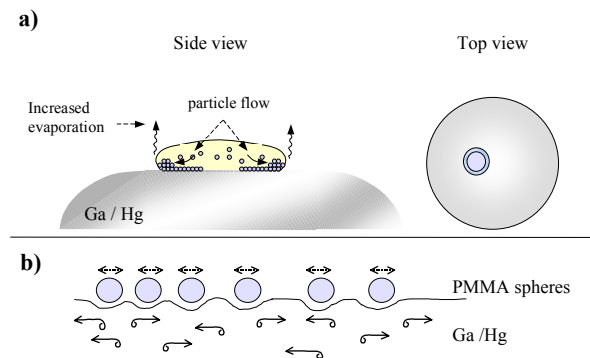


**Figure 5.14:** Crystallisation on liquid substrates – basic idea. A suspension of PMMA spheres is placed on a liquid Gallium or Mercury substrate. Evaporation of the solvent leads to the formation of a PhC film (a). The spheres can move on the liquid substrate during crystallisation thus strain is driven out of the film leading to the formation of large crack-free films (b) (adopted from [50]).

The SEM micrograph in figure 5.15 shows an example of a PMMA based opal film grown by B. Griesebock on liquid Gallium [50]. The large degree of order and its domain size of about  $2.8 \text{ cm}^2$  are remarkable. Unfortunately the film has to be removed from the substrate for practical applications. During this process it very often breaks up into smaller domains since it is – due to its small thickness and lack of sintering – very fragile. Closer investigations on this method have to address these issues.

However, since PMMA spheres are subject to shrinking during the evaporation of the solvent as described above, these films break up into smaller domains during the drying process. This makes their handling and post-processing cumbersome and limits the possible applications.

There are several other synthesis routes under investigation to enhance the crystalline quality of opaline films at the moment. In what follows a brief list of recent approaches is given:

A prominent example is the application of alternate external forces during the crystallisation of the colloid. Particularly shear alignment has been suggested to enhance the crystallinity of opals and to produce large-area ( $\approx \text{cm}^2$ ) defect-free opaline crystals [95]. Illuminated with monochromatic light, these crystals show a prominent Laue diffraction pattern in transmission. Their long-range order in the form of predominantly twinned *fcc* lattice was confirmed by observation of this pattern from the whole area of the crystal.

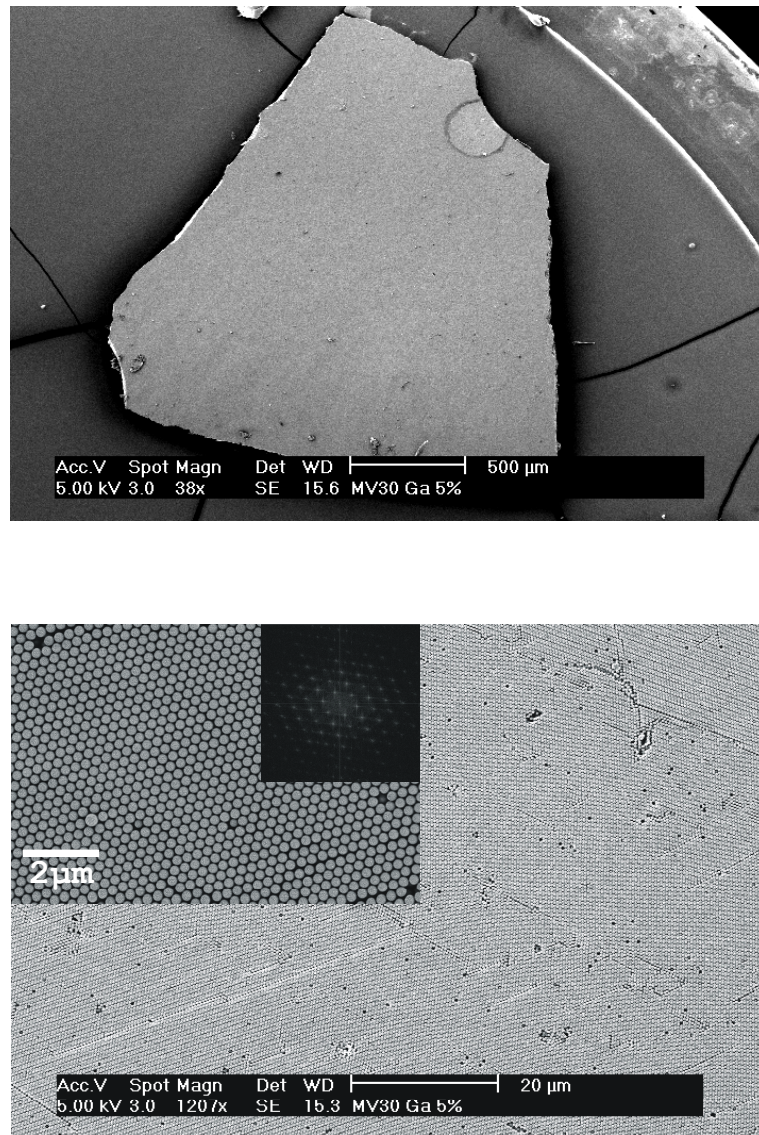


**Figure 5.15:** SEM micrographs of a film grown on liquid Ga at room temperature. The domain size of the crystallite is  $\approx 2.8 \text{ mm}^2$ . No macroscopic cracks are visible over the whole area (top) (details see [87]). The fcc order of the single spheres is preserved over large areas, suffering from only very few dislocations, missing spheres and badly ordered areas (bottom). The inset shows an enlargement underlining the high degree of order. This is confirmed by the FT of the inset that shows well defined spots of several orders.

Another suggestion is the growth in confined areas such as trenches or hexagon shaped patterned substrates. This would pave the way for photonic crystal based integrated circuits. First results of PMMA photonic crystal films grown on structured silicon wafers look promising [96] but more detailed investigations on structural aspects and detailed analysis of optical data are still necessary to evaluate the full potential of this method.

It is widely acknowledged that the homogeneity of opals is critical for optical measurements, especially when taking into account that the PBG is very susceptible to disorder since the gap opens up at high frequency bands [20]. Crystallite sizes up to  $0.5 \text{ mm}^2$  in bulk opals [97] and several square millimetres in films [49, 87, 94] have been reported. The improvement of the crystalline quality both in polymer- and silica-based samples is crucial to obtain distinct PBGs.

#### 5.4. Inverted structures

Achieving the RIC in a PhC is a serious problem for the development of an omnidirectional PBG structure. The increase of the RIC leads to a broadening of all stop-bands and to the development of an omnidirectional band gap between the 8<sup>th</sup> and 9<sup>th</sup> band in an *fcc* lattice of dielectric scatterers occupying about 30% of the PhC volume [13], as shown in figure 2.7. To enhance the RIC of opaline PhCs the filling of the matrix with semiconductors has been suggested. The subsequent removal of the matrix produces a so-called inverted opal structure (“*opal replicas*”). For SiO<sub>2</sub> based opals the matrix can be removed by a diluted HF solution (cf. figure 5.2) if the infill material permits it. In case of a PMMA matrix the spheres are simply dissolved by an organic solvent making this process compatible to virtually any semiconductor or metal infill material. As mentioned, to achieve an omnidirectional PBG, a RIC > 2.8 is necessary for defect-free crystals [29]. This PBG is believed to be very susceptible to disorder, therefore a good margin by RIC contrast has to be kept. Practically, this assumes the application of semiconductors with the RI larger than three.

The first example of inverted opaline structures was presented by W. Vos et. al in inverted TiO<sub>2</sub> opal [98], whereas the first evidence for a full PBG in the IR has been reported in inverted Si-opal for the 1.5  $\mu\text{m}$  wavelength range [99]. To reach the visible part of the spectrum semiconductors, whose RI is high enough and whose electronic band gap is above  $\approx 2 \text{ eV}$  in the visible have to be chosen, what is not easy.

##### 5.4.1. Semiconductor-infilled opals and semiconductor replicas

Opal matrices infilled with InP, CdS, CdSe, TiO<sub>2</sub>, SnS<sub>2</sub>, InSb and more recently GaP, Si and Ge have been investigated regarding their feasibility as PhCs by several research groups.

Different approaches to infill a guest semiconductor material into the opal matrices have been investigated. For example, InP and GaP have been introduced by metal-organic chemical vapour deposition (CVD) but have not yet led to sufficiently high filling factors to produce inverted structures [100]. Using a similar CVD process Si and Ge can be infilled into opal matrices with a high filling factor [99]. InSb has been introduced in its molten state in a high-pressure high-temperature process and CdSe as well as CdS have been introduced using a sol-gel process as well as TiO<sub>2</sub> which can also be infilled by CVD, as well as SnS<sub>2</sub>.

The next step has been to demonstrate that the material introduced retains to some degree its crystalline properties. This has been done by several techniques and among those phonon Raman scattering has been successful in showing that the guest semiconductor exhibits bulk-like phonon modes.

Other techniques confirmed that the material goes into the opal voids in a non-uniform manner and this is the first disadvantage of opal-semiconductor nanocomposites. The volume-fraction of guest material going into the void is usually a few percent of the void volume. Moreover, it is not a foregone conclusion that the semiconductor goes in uniformly as in some cases it forms nanocrystals (CdSe) and in other cases a thin film (TiO<sub>2</sub>). Moreover, the small feature size of the semiconductor going into the voids permits regions where size quantisation occurs, as it has been seen in blue shifts of the absorption edge of CdSe in SiO<sub>2</sub>-opal, which partly confuse the interpretation of the data. These aspects partly limit the use of opal-semiconductors. On the other hand, it was in CdSe-opal, that the first evidence for cooperative emission was observed in the form of a super-linear dependence of the luminescence intensity upon laser power, hinting clearly at photonic crystal behaviour [8]. Moreover, the first demonstration of a rich range of transport phenomena was demonstrated in InSb-opal, which combined tunnelling, percolation and Coulomb blockade, depending on the temperature regime [101].

In any case, semiconductor-opal structures have shown the presence of a pseudo-gap and their versatility to be used directly as templates for PhCs or as templates to make another template [98] and therefore increase the RIC.

Recently, opal loaded with CdSe semiconductor nanocrystals (quantum dots) have been processed to remove the opal matrix and leave behind a 3D photonic crystal of air and quantum dots of CdSe [102].

Concluding it can be said that semiconductor infilled opals show a rich variety of PBG related optical phenomena and are a promising route to synthesise inverted opals with high RIC.

#### 5.4.2. Preparation of $\text{TiO}_2$ and $\text{SnS}_2$ thin film opal replicas

Since the achieving a high RI contrast makes infilling with inorganic materials necessary, attempts have been made to invert PMMA based PhCs with high-RI semiconductors

The choice of materials, which do not absorb the visible light and posses a high RI, is very limited.  $\text{TiO}_2$  in its rutile form is one of the rare materials with a RI of about 2.8 in the visible range. Therefore it was material of choice to prepare inverted opaline structures as done by different other groups [66, 98].

$\text{SnS}_2$  is another semiconductor that offers a high RI of about 3.2–3.4 [103] while being transparent in the visible. Thus the compound was chosen as a second infill material to be tested. Advantages of these thin film inverted structures include:

- i. the glass or other substrate support to overcome the inherent fragility of the structure
- ii. the ease of the preparation routine as compared to bulk inverted opals and
- iii. the crystallinity of the lattice structure is high compared to the density of defects in bulk opals.

Investigations to infill PMMA thin film PhCs with both materials have been undertaken<sup>§</sup>. To judge their structural quality the samples were investigated by SEM and optical methods.

##### 5.4.2.1. $\text{TiO}_2$ replicas

A synthesis of  $\text{TiO}_2$  opaline replicas and infilling them with dyes was performed in order to obtain chemically stable high RIC structures capable of light emission.

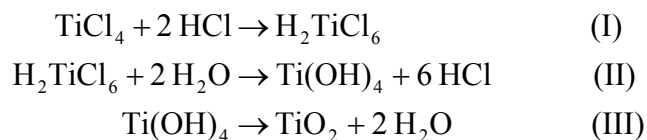


**Figure 5.16:** Reactions to synthesise  $\text{TiO}_2$  in a sol-gel process.

---

<sup>§</sup> most samples under investigation in this thesis were prepared by Dr. Manfred Müller, Institute for Organic Chemistry, Dept. of Chemistry and Pharmacy, Johannes Gutenberg University Mainz, Germany

The following synthesis route was followed as summarised in the reactions in figure 5.16:

- A thin crystalline film of monodisperse PMMA spheres was prepared on a microscope slide as described in detail in the previous chapter. The film shows a Bragg peak with maximum at 708 nm (see figure 5.18).
- By dipping the slide into a solution of  $\text{TiCl}_4$  in hydrochloric acid (I), hydrolysis (by the moisture of the air was initiated) (II). During heating for 1h at  $160^\circ\text{C}$  (III), the solution is converted into solid  $\text{TiO}_2$ .
- By stirring in tetrahydrofuran (THF) the polymer spheres were dissolved and the replica obtained (figure 5.17).

The result is a fragile network of 26vol% filled with the semiconductor. The starting *fcc* structure is preserved as visible in figure 5.17. The SEM micrograph illustrates the quality of the sample, that can also be seen by the pronounced hexagonal pattern of the FT (figure 5.17a,

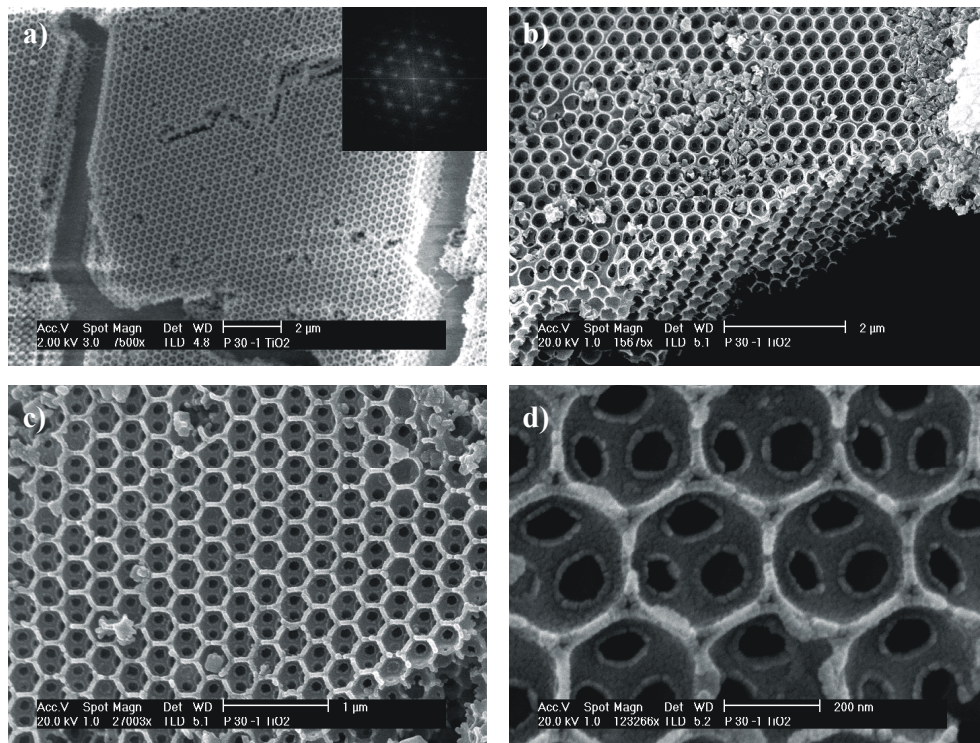


**Figure 5.17:** SEM micrograph of the  $\text{TiO}_2$  inverted opaline film at different magnifications. The *fcc* structure is preserved after removal of the PMMA spheres and inverted over the whole depth of the film (a,b). The result is a very fragile structure that is . The connections of the first layer to the underlying spheres are visible as dark circles (c,d).

inset). The interconnecting voids to the next layer (small dark circles) are well visible (figure 5.17b,c). In figure 5.17b fragments of the structure are visible on the top surface that broke off during the preparation for SEM observations. The fragility of the structure of is evident.

The  $\text{TiO}_2$  replica shows a Bragg peak with maximum at 518 nm (figure 5.18). Due to the decrease of the effective refractive index of the complete composite a strong blue-shift of the Bragg peak compared to the PMMA template is caused as explained in more detail in chapter 6.3.

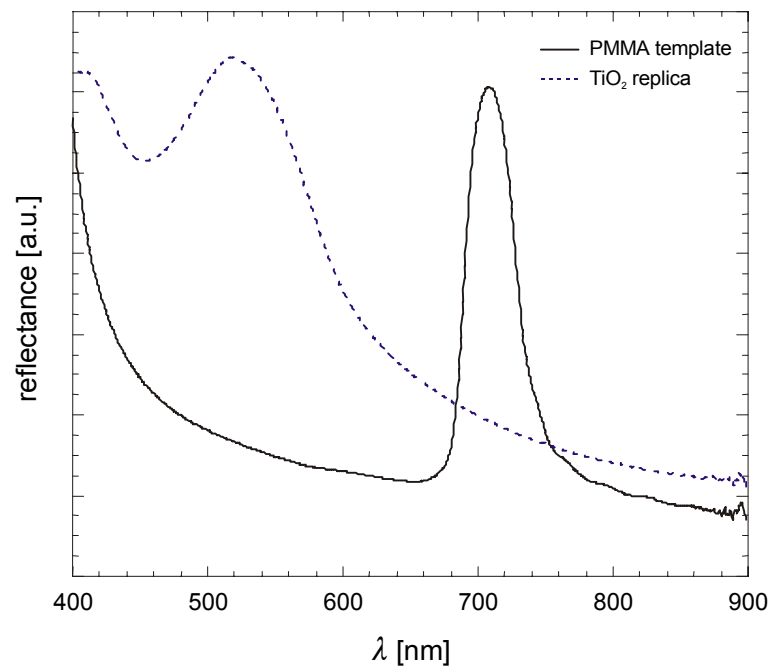


**Figure 5.18:** Reflectance spectra of the bare film of PMMA spheres and of the resulting  $\text{TiO}_2$  replica ([50]).

To emit light from the replica it was doped with a solution of Coumarin 6 (a fluorescence dye; the mass was too small to weigh) and PMMA (10 mg/ml) in THF. The PMMA was necessary to avoid quenching of the fluorescence by diluting the dye.

While an ordered replica could be obtained, a full photonic band gap has not yet been achieved from  $\text{TiO}_2$  replicas for two main reasons. First, the  $\text{TiO}_2$  replicas are always microporous, because the solvent necessary for the sol-gel process or the infilling with nanoparticles occupies some space too. So the samples suffer from a low volume fraction of  $\text{TiO}_2$  in the replica. Second, the  $\text{TiO}_2$  replicas investigated so far were composed of the anatase form of titania with a RI of at most 2.2–2.5. Thus the RIC achieved was therefore fundamentally limited to about 2.0.

#### 5.4.2.2. $\text{SnS}_2$ replicas

Tin disulphide ( $\text{SnS}_2$ ) is a wide band gap n-type semiconductor. Due to its refractive index of 3.4 at 600 nm (3.2 at 700 nm) and its wide electronic gap  $\approx 2.1$  eV for the indirect transition and  $\approx 2.5$  eV for the direct transition [104], inverted  $\text{SnS}_2$  opals are potentially attractive as PBG structures operating up to the green part of the spectrum. Direct opaline films infilled with  $\text{SnS}_2$  can be converted subsequently into opaline replicas by dissolving the spheres from the nano-composite using an organic solvent (THF).

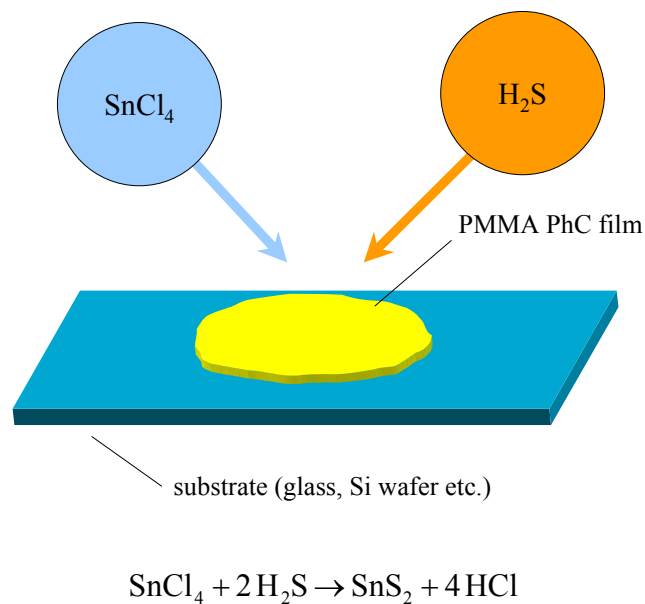


**Figure 5.19:** Sketch of the infilling process of a PMMA opal template with  $\text{SnS}_2$  by APCVD. The reaction takes place at ambient temperature for about 24 hours.

PMMA opaline films were infilled with  $\text{SnS}_2$  at ambient temperature using an Atmospheric Pressure Chemical Vapour Deposition Process (APCVD). This approach allows to grow chlorine-free crystalline  $\text{SnS}_2$  film of good quality at high growth rates [105, 106]. Additionally it does not destroy the PMMA spheres due to the low temperatures used and the synthesis from the gaseous phase allows, in contrast to a sol-gel process, higher filling fractions and the formation of almost solid infills.

PMMA opaline films with spheres with diameters of  $\approx 250$  or  $\approx 290$  nm were simultaneously incubated with  $\text{SnCl}_4$  vapour and with  $\text{H}_2\text{S}$  gas at ambient pressure and room temperature (cf. figure 5.19) using the following process:

- After placing the slides with the films inside a desiccator, about 0.5 ml of  $\text{SnCl}_4$  was dripped onto the bottom.

- The desiccator was stored 3 hours in an icebox, evacuated and then filled with H<sub>2</sub>S from a balloon. The hydrogen sulphide was prepared before from Na<sub>2</sub>S and hydrochloric acid and dried over a short column filled with CaCl<sub>2</sub>.
- After about 24 hours the filled films were washed with water and dried. By varying the incubation time or the thickness of the film, different filling factors can be achieved.
- To remove the PMMA spheres the films were stored for 30 minutes in tetrahydrofuran (THF), under careful stirring, leaving the semiconductor replica film on the glass substrate, analogous to TiO<sub>2</sub> replicas.

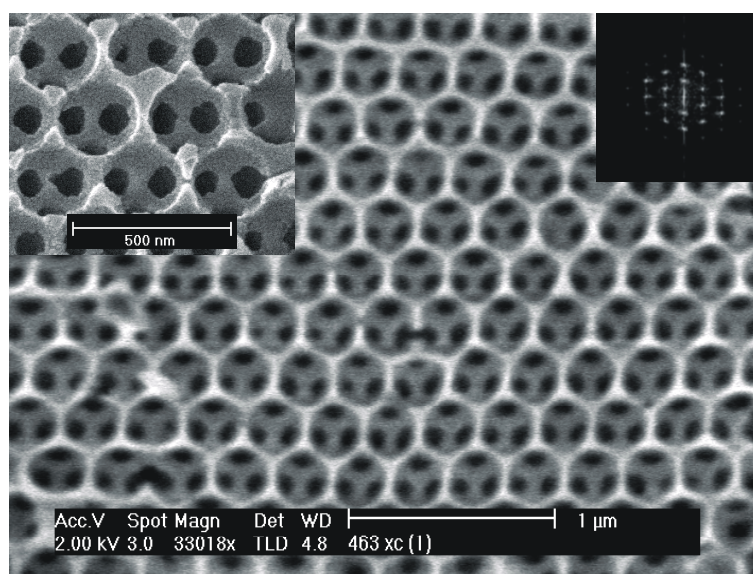


**Figure 5.20:** SEM micrograph of an inverted SnS<sub>2</sub> sample at two different magnifications. Note the connecting holes to the underlying layers. The crystalline order is persevered during the inversion process as evident from the FT shown in the right inset.

Figure 5.20 shows a SEM image of the PhC film replica after infilling with SnS<sub>2</sub> and extraction of the PMMA spheres ( $D = 289$  nm). The resulting structure has a filling factor of  $\approx 26\%$  and is thus very hollow and fragile. Nevertheless, the structure was not damaged dramatically during the inversion process as it can be seen from the FT image shown in the right inset. The interconnections of the top layer to the next neighbouring spheres in the underlying layer are visible as black holes from the SEM image.

The replica is uniform on a centimetre length scale as is can be judged by the naked eye by noting the uniform colour of the sample depicted in figure 5.21. The photos show thin film PhCs made from similar spheres: the PMMA template as grown (left) and after infilling with

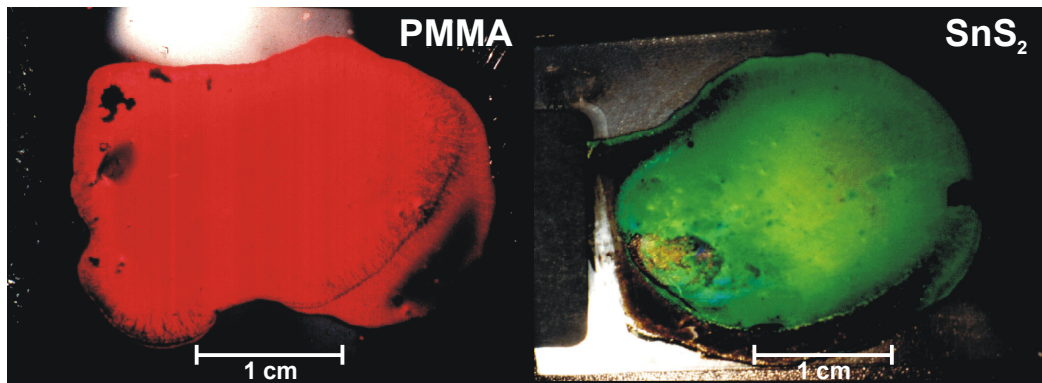


**Figure 5.21:** Optical impression of PhC films grown from PMMA spheres dried slowly at high humidity (diameter of the spheres: 289 nm), left panel, and its SnS<sub>2</sub> replica, right panel (courtesy of Dr. Manfred Müller, University of Mainz).

SnS<sub>2</sub> and removal of the PMMA spheres (right). It is visible that the inversion process took place homogeneously over the whole area of the sample.

Raman scattering measurements show a well-formed peak at 311.7 cm<sup>-1</sup> for the replica that coincides with the bulk LO phonon of crystalline SnS<sub>2</sub> (figure 5.22). This proves that the SnS<sub>2</sub> has the same structure of the crystalline bulk material. The relatively broad appearance of this peak suggests that the semiconductor body of the opaline replica consist of small crystallites.

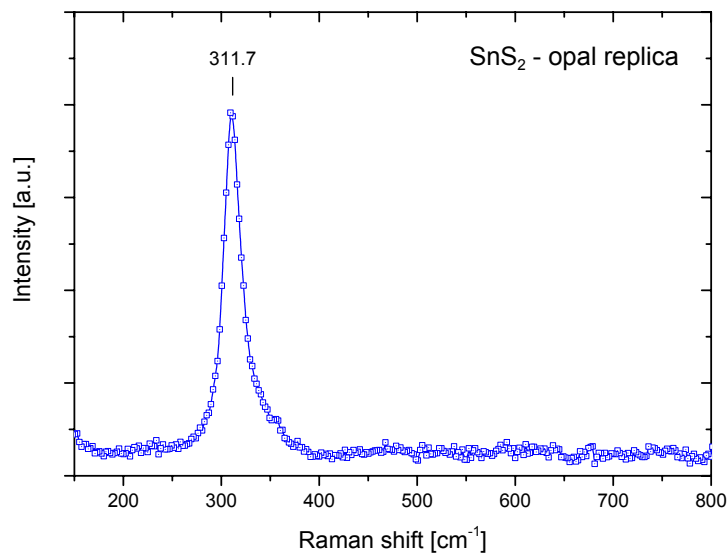


**Figure 5.22:** Raman spectrum of a SnS<sub>2</sub> inverted replica (sample 463/xc1). The data are baseline-corrected. The peak position is consistent with lattice vibrations in crystalline SnS<sub>2</sub>.

Potentially, the refractive index of SnS<sub>2</sub> is high enough to open a full photonic band gap for the higher order than Bragg stop-band gaps. For the system under investigation (spheres of  $\approx 250$  or  $\approx 290$  nm) the higher order bands are expected at wavelengths shorter than 550 nm, overlapping with the absorption band of SnS<sub>2</sub>. To shift the higher order bands into the range of optical transparency, larger spheres have to be prepared. In our experiment we dealt with the zero order photonic stop-band (Bragg diffraction resonance) and therefore cannot document to what degree the full PBG is approached. A crucial point in the assessment of inverted opals is the density of the dielectric constituting the structure or the effective filling factor, which limits the effective refractive index contrast. Although SEM pictures of the inverted structure look as a solid wire frame, tiny voids may be present in the body of semiconductor framework, which reduce its density compared to solid crystalline SnS<sub>2</sub>. Therefore optical constants were estimated from reflectance measurements as shown in chapter 6.3. These measurements suggest the presence of a porous semiconductor structure with a reduced density (and RI) compared to bulk SnS<sub>2</sub>.

## 6. Optical diffraction in opals

### 6.1. Reflectance of direct opals

Since the first fabrication of opals for PBG applications, they have been studied by angle resolved reflection experiments to characterise the Bragg resonance of the (111) crystalline planes and to probe the crystalline structure of PhCs [8, 76]. The experiments are performed by illuminating a specific area of the surface ( $\approx \text{mm}^2$ ) of the specimen with white light and collect the reflected light within a small ( $\approx 2^\circ$ - $10^\circ$ ) cone, using the experimental set-up, described in chapter 4.1.1.

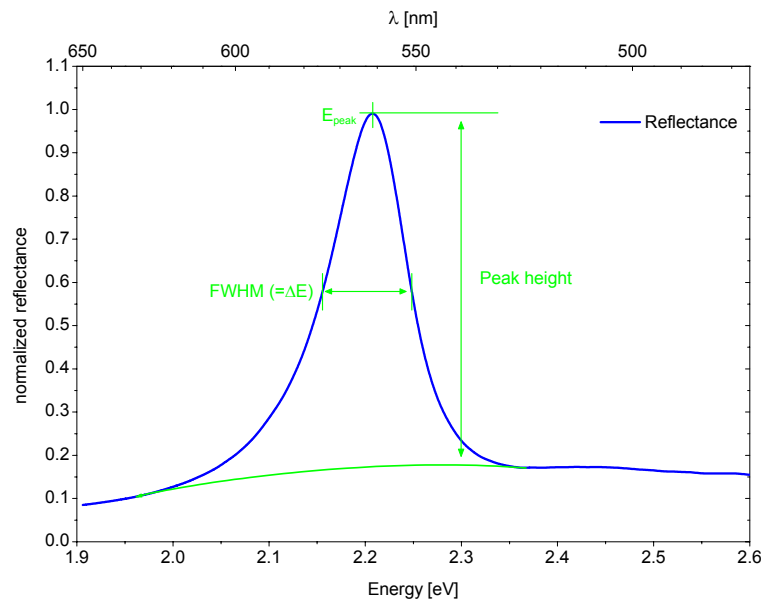


**Figure 6.1:** Typical reflectance curves from thin film opal PhCs at the first pseudo-gap in [111] direction. Some important parameters to characterise the diffraction resonance – peak height,  $E_{peak}$  and  $\Delta E$  – are indicated on the plot.

As shown in figure 6.1 the optical reflectance spectra of opal contains a diffraction resonance, which can be characterised by the following parameters: the resonance frequency ( $E_{Peak} = \hbar\omega_{Peak}$ ), the full width at the half-maximum of (FWHM) of the peak, the resolution of the reflectance maximum. From these values the relative bandwidth of the peak, defined as  $\Delta E/E_{Peak}$ , can be defined as a measure to compare different samples. Another important

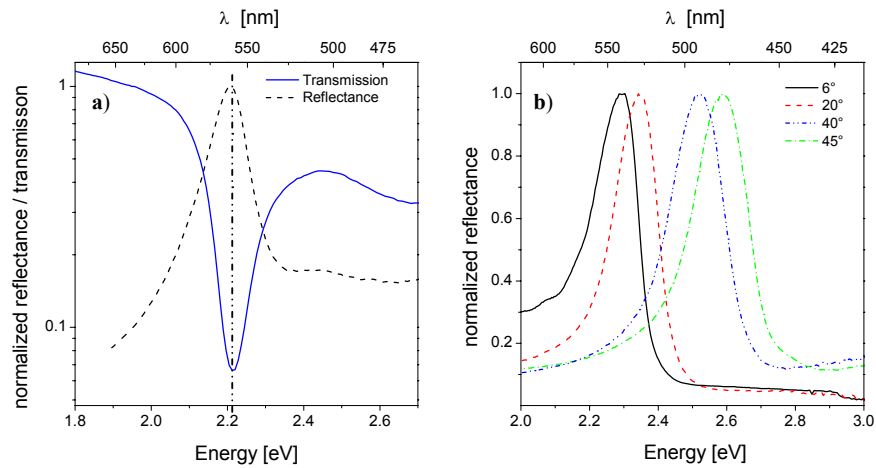


**Figure 6.2:** Typical reflectance and transmission spectra of opal-based PhCs: Transmission and Reflectance spectra at normal incidence. The Bragg resonance appears as a dip in the transmission at the same energy as the Peak in the reflectance spectrum (a). Angle resolved Reflectance measurements: The shift of the Resonance follows the Bragg law. The overlap of two spectra recorded at different angles and the FWHM of the peaks are important characteristics (b).

parameter is the overlap of these diffraction resonances recorded at different angles of observation (cf. figure 6.2), which feature can be used to characterise the dispersion of the PBG.

As shown in figure 6.2, optical transmission and reflectance spectra of opal contain diffraction resonances, which appear at one and the same frequency either as dip or peak (cf. figure 6.2a).

The spectral position of the resonance is trivially defined by the Bragg condition  $\lambda_B = 1.63D\sqrt{n_{eff}^2 - \sin^2\theta}$  (cf. chapter 2.3.1). Its position can be varied by changing the sphere diameter  $D$  (figure 6.4), the external angle of incidence  $\theta_{ext}$  (figure 6.2b) and the effective RI  $n_{eff}$  (figure 6.3).

In contrast to the spectral position of the Bragg peak, the width of the resonance – which relates to the dielectric contrast and the filling factor – and its resolution – which is connected to the crystallinity of the opal – are subjects of material design.

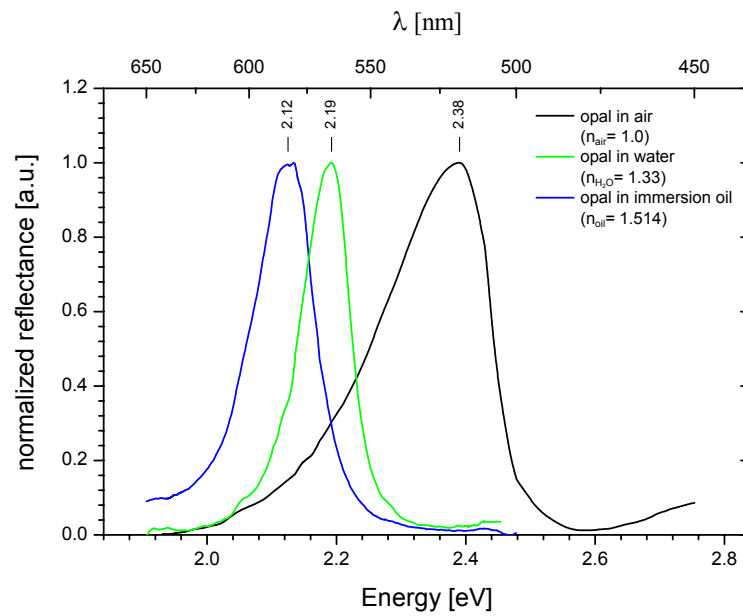


**Figure 6.3:** Reflectance curves of a  $\text{SiO}_2$  PhC, bare and infilled with different liquid materials. The spectra were corrected by division by the lamp reference spectrum and normalised.

As seen in figure 6.3, the position of the reflectance maxima changes depending on the RIC as expected from the Bragg equation. The figure shows a comparison of reflection measurements made from the same sample with different dielectric infills. The expected shifts from the Bragg law coincide to the measured results. Note that the relative stop bandwidth also changes with filling factor and RIC [107]. Alternatively the shift of the resonance can be achieved by changing the angle of the incident light.

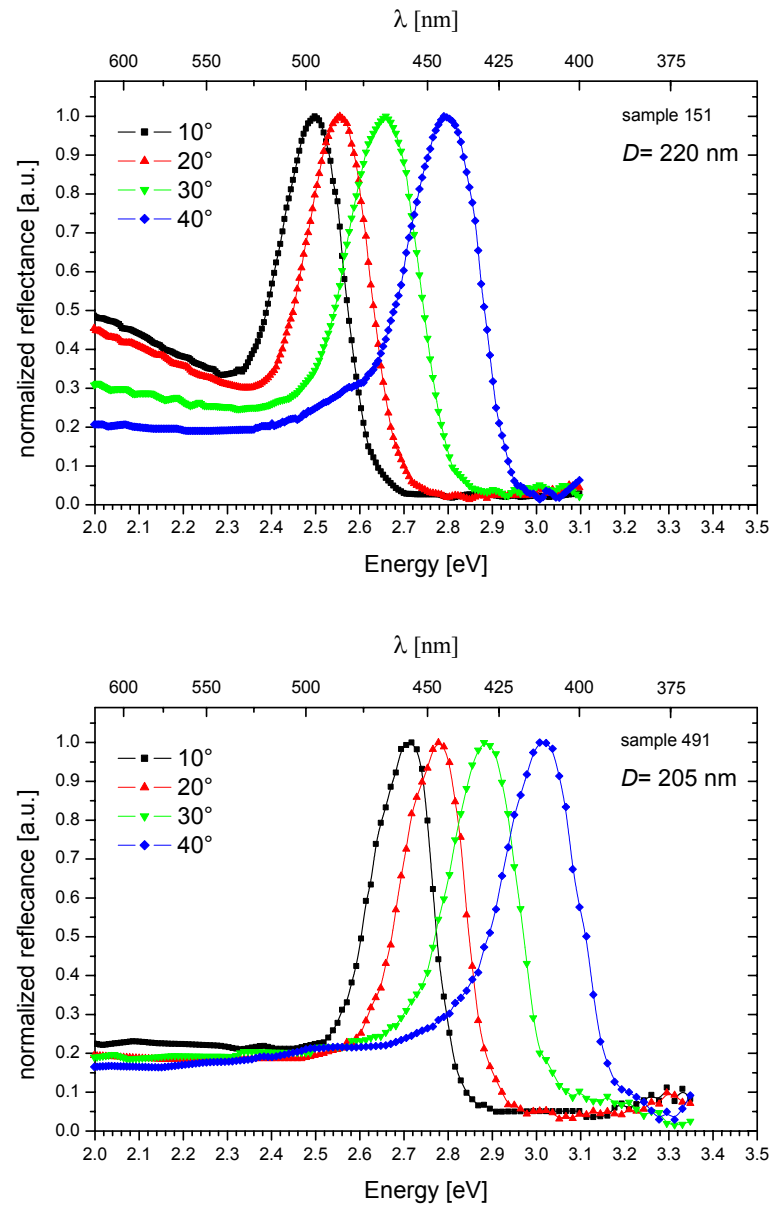


**Figure 6.4:** Angle resolved reflectance spectra of two different PMMA opal PhCs. The spectra were taken for incident angles between  $10^\circ$  and  $40^\circ$ . A blue shift of the Bragg resonance is found with increasing angle of incidence. Due to different sphere diameters the whole spectrum of sample 151 (top) is shifted compared to that of sample 432 (bottom).

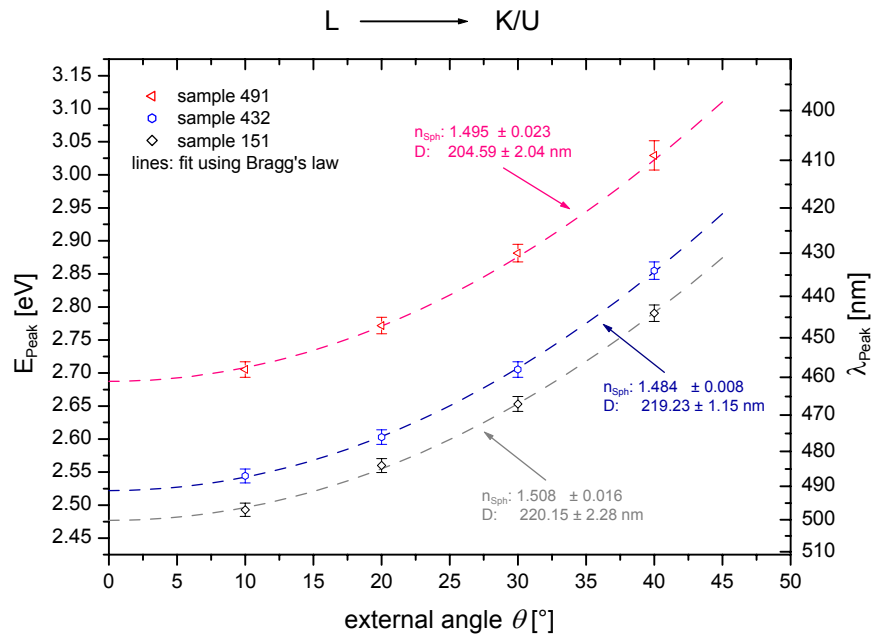


**Figure 6.5:** Experimentally observed Bragg-peak positions for a variety of incident angles  $\theta$  of different samples. The dashed lines show least square fits of the Bragg law with sphere diameter  $D$  and their RI  $n_{Sph}$  as fit parameters. The experimental values agree well to the theoretical prediction.

The angle resolved reflectance and transmission of different samples is shown in figure 6.4 and figure 6.7. As expected, the reflectance peaks shift to higher energies with increasing incident angle as depicted in figure 6.5.

The positions of the Bragg peaks from reflectance measurements of the samples shown in figure 6.4 and figure 6.7 are plotted vs. the incident angle  $\theta$ . A value of  $0^\circ$  corresponds to the surface normal, thus the experiment probes the path from L to K/U points in the Brillouin zone (cf. fig figure 2.6). As shown in figure 2.11 the evolution of the first stop band is very similar in L-U and L-K direction. For L-W direction the phase volume is lower than for the

sample	$D_{Bragg}$ [nm]	$D_{SEM}$ [nm]
151	$220.2 \pm 2.3$	$229 \pm 5$
432	$219.2 \pm 1.2$	$225 \pm 5$
491	$204.6 \pm 2.0$	$208 \pm 5$

**Table 6.1:** Sphere diameters determined by SEM observations ( $D_{SEM}$ ) and reflectance measurements ( $D_{Bragg}$ ) for different samples under study. The results are in good agreement.

other directions, but for  $\theta < 40^\circ$  the difference can be neglected. Therefore it is not necessary to orient the sample in azimuthal direction, facilitating the experiment substantially. The Bragg law is well reproduced experimentally as it can be seen from the fits (dashed lines). The data were fitted by a least square fit using Bragg's law with the sphere diameter  $D$  and the sphere's RI  $n_{Sph}$  as the only free parameters. Here a filling fraction of 74% (corresponding to touching spheres) was assumed. The obtained values are in good agreement with the expected value of  $n_{PMMA}$  taken from Ref. [108] and sphere diameters measured by SEM observations as summarised in table 6.1.

## 6.2. Fabry-Pérot oscillations

An indicator for the quality of thin film PhCs is the occurrence of interference fringes in the reflectance spectrum (figure 6.7). These oscillations can be understood as Fabry-Pérot (FP) oscillations occurring due to the interference of the light reflected by opposite surfaces of the opal films. FP oscillations are a good indicator of the homogeneity of thickness and average RI of PhCs since in inhomogeneous samples they vanish rapidly. In the case of opal thin films FP oscillations have been routinely observed from a spot up to  $1 \text{ cm}^2$ , indicating the high crystalline quality of these films compared to bulk opals [109], where single domain spectroscopy is necessary. Quantitatively, with increasing the spot area from  $1 \text{ mm}^2$  to  $1 \text{ cm}^2$ , the magnitude of Fabry-Pérot oscillations reduces approximately by factor of three. Additionally, FP oscillations can be used as an independent destruction-free optical method to measure the film thickness as explained in the following chapter.

To explain the occurrence of FP oscillations in PhC thin films their internal substructure is neglected and the film is treated as a homogeneous film with a constant RI.

The condition for constructive interference of reflected beams from the top and bottom sides of a homogeneous planar film can be calculated, in analogy to a Fabry-Pérot interferometer, to be [31]:

$$\lambda = \frac{2d \cdot \sqrt{n_{eff}^2 - \sin^2 \theta}}{m} \quad (6.1)$$

with wavelength  $\lambda$ , sample thickness  $d$ , external angle of incidence  $\theta$  and peak order  $m$ .

The effective RI  $n_{eff}$  was calculated from the known refractive indices  $n_{PMMA}$  and  $n_{air}$  of PMMA and air, respectively by simply determining the average RI:  $n_{eff} = n_{avg} = \sqrt{f \cdot n_{PMMA}^2 + (1-f) \cdot n_{air}^2}$  with  $f$  being the filling fraction of PMMA in the PhC.

Conversion of  $\lambda$  into energy units and solving equation (6.1) for  $m$  leads to

$$m = \frac{2E \cdot \sqrt{n_{eff}^2 - \sin^2 \theta}}{h \cdot c} \cdot d \quad (6.2)$$

with Planck's constant  $h$ , velocity of light in vacuum  $c$  and photon energy  $E$ .

From this it is obvious, that by plotting the peak order  $m$  vs.  $2E \sqrt{n_{eff}^2 - \sin^2 \theta} / hc$  the film thickness can be obtained from a linear regression as the slope of the regression line.

It is worth mentioning that the energy difference of two consecutive FP maxima

$$\Delta E_{m,m+1} = \frac{hc}{2\sqrt{n_{eff}^2 - \sin^2 \theta} \cdot d} \cdot (m - m + 1) = const \quad (6.3)$$

is constant in the simple Fabry-Pérot model. As shown in figure 6.9, this does not fit exactly the experiment but is a very good approximation to determine the film's thickness by optical methods. To explain the small deviations in the maxima positions and the amplitudes seen in the experiment a full 3D model has to be implemented. Nevertheless, they can qualitatively be understood by assuming an increase of  $n_{eff}$  in the vicinity of a band edge.

To demonstrate that the assumptions on the underlying physical mechanism leading to the appearance of these oscillations are true, it is instructive to look on a PhC film grown on a multi-layered substrate. The result of reflectance measurements done on a PhC grown on a SiO<sub>2</sub>//Si substrate (oxidised wafer) is shown in figure 6.6.

The superposition of two oscillations with different period is clearly visible on both sides of the Bragg resonance. They occur due to reflection on the thick PMMA opal (short period) and on the thin SiO<sub>2</sub> sublayer (low frequency). The analysis of the oscillation periods results in a film thicknesses of  $d_{PhC} = 5.90 \pm 0.15 \mu\text{m}$  for the PMMA film ( $\approx 15$  monolayers) and for the SiO<sub>2</sub> layer  $d_{SiO_2} = 1.03 \pm 0.13 \mu\text{m}$ .

To investigate the behaviour of FP oscillations in greater detail, a series of reflectivity measurement were done at different angles in standard  $\theta$ - $2\theta$ -configuration as described in chapter 3.1.2. Figure 6.7 shows the reflectance of a thin PMMA PhC film with well visible Fabry-Pérot oscillations at different angles as indicated in the figure. The measurements were taken observing a light cone of  $5^\circ$  from a spot of ca.  $1\text{mm}^2$  on the sample. As expected the oscillation period changes with the observation angle in accordance with the 1D Fabry-Pérot model (as well as the Bragg peaks shifts towards higher energies in accordance to the Bragg law).

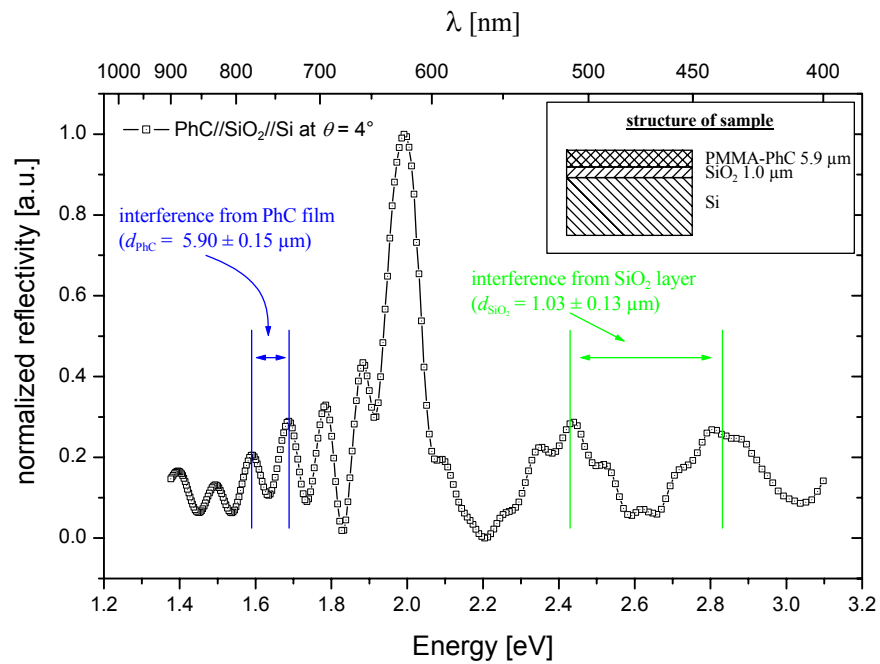


**Figure 6.6:** Interference of FP oscillations in a two-layer system. Reflectivity measurements show two superimposed oscillations. The layer thickness revealed from the oscillation periods are indicated in the plot. The sample structure is sketched in the inset.

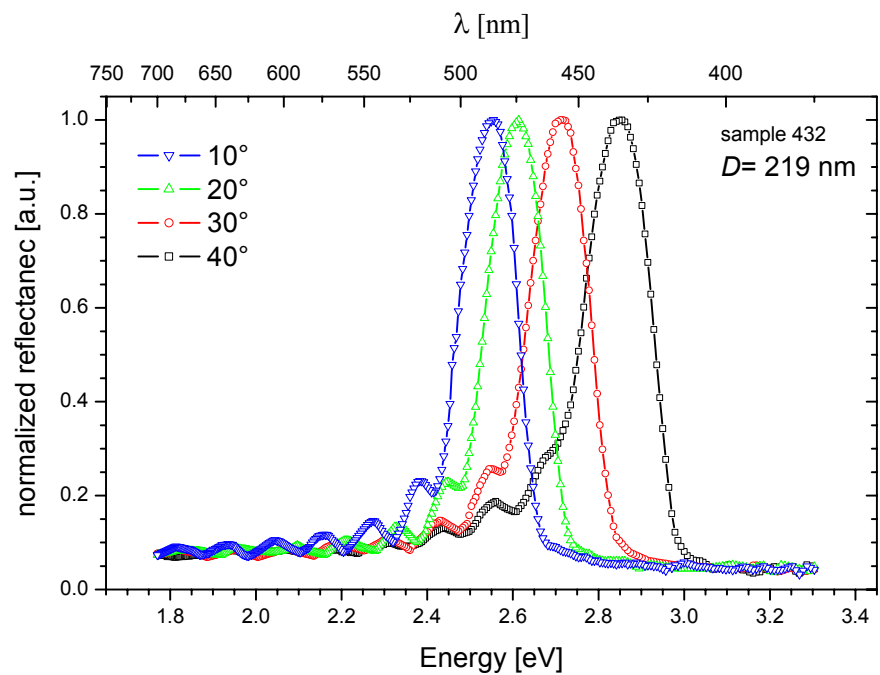


**Figure 6.7:** Normalized reflectance of a PMMA thin film PhC (sample 432) showing Fabry-Pérot oscillations. Measurements were taken at different angles between  $10^\circ$  and  $40^\circ$  as indicated. The oscillation period changes with observation angle.

By determining the positions of the Fabry-Pérot maxima and performing a linear regression on equation (6.2) the film thickness can be calculated: The FP oscillation order  $m$  is plotted vs.  $2E\sqrt{n_{\text{eff}}^2 - \sin^2 \theta}/hc$ . This leads to a linear relationship between film thickness  $d$  and oscillation order  $m$ . Thus by determining the gradient of the data by a linear regression  $d$  can be obtained. This is shown in figure 6.8.

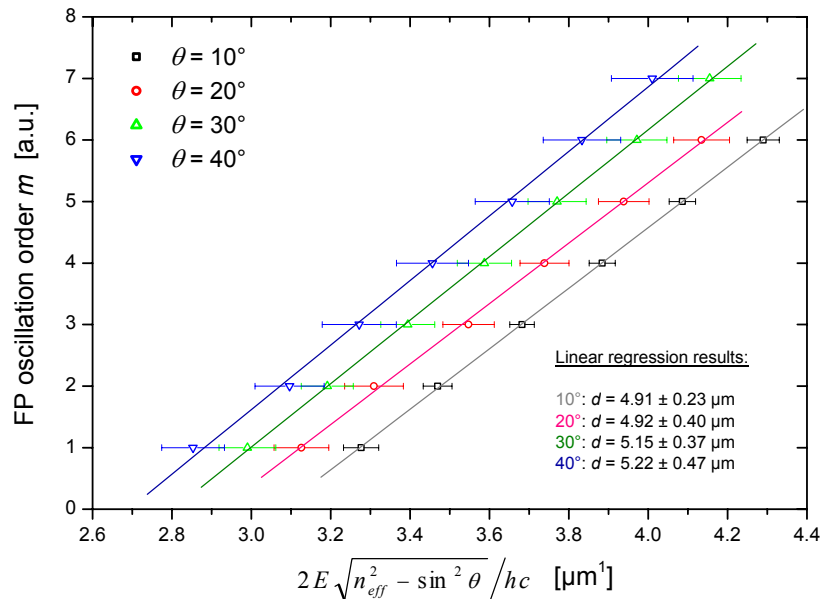


**Figure 6.8:** Peak positions of the Fabry-Pérot oscillation of sample 432 for different observation angles. The slope of linear regressions (lines) on the experimental data (symbols) gives the film thickness  $d$ . The calculated values coincide with SEM observations.

The maxima position of the FP interferences were determined by Gauß fits to the individual oscillations from figure 6.7. The error in x-direction, indicated on the plot, was calculated using error propagation of equation (6.2). The uncertainty of the peak maxima positions was determined by using the error resulting from the Gauß fits. For the uncertainty of observation angle  $\theta$  a value of  $\pm 5^\circ$  was assumed, which matches the experimental conditions. Comparing the error bars in figure 6.8 it is evident, that the main contribution results from uncertainties in  $\theta$ . The straight lines are least square fits to the data. From these regression lines, taking the errors as weights, the film thickness can be determined as indicated in the plot. The measurements taken at different angles show good agreement and are compatible to SEM observations of the film thickness. Although only a very limited number of oscillations could be observed from this sample, the thickness can be determined easily by this method. With an

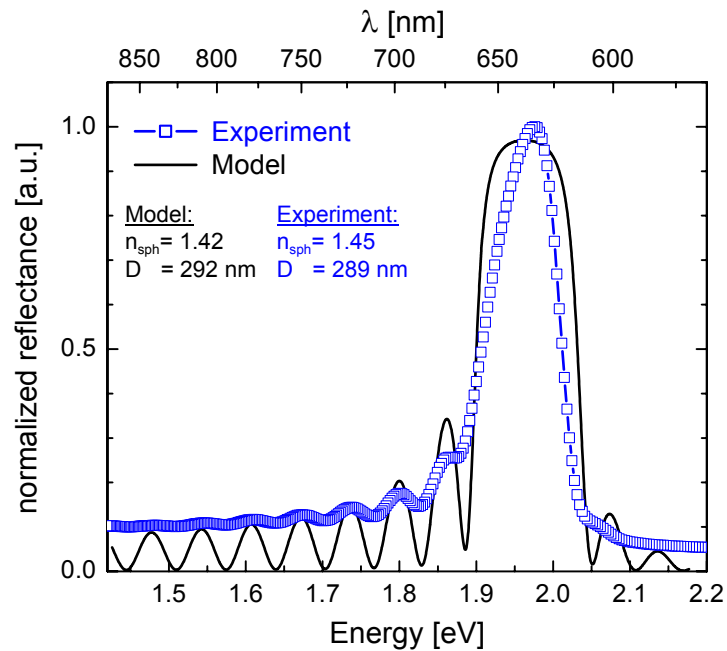


**Figure 6.9:** Bragg resonance of a PMMA thin film PhC (sample 463/3a). The reflectance measurements show Fabry-Pérot oscillations. In the model 45 layers of beads with a diameter of 292 nm were considered in good agreement with SEM data ( $D = 289$  nm). The experimental data (squares) and simulated results (line) show excellent agreement

improved optical set up, especially by reducing the error in  $\theta$  it is easy to improve the accuracy of the measurement by orders of magnitude.

For a more detailed analysis the reflectance spectra of PMMA thin film PhCs were modelled\*\* using a 3-dimensional transfer matrix method [110, 111]. The calculated period of the Fabry-Pérot oscillations was found to coincide with experimental values for a film thickness of 45 bead layers as depicted in figure 6.9, which compares the experimental and theoretical reflectance curves. The diameter of the spheres as determined by SEM inspection to be  $D = 289$  nm also compares well to the modelled value of  $D = 292$  nm. The RI of the PMMA spheres obtained from the Bragg peak position differs slightly from its theoretical value of  $n_{PMMA} = 1.4893$  [108] but is close to the value obtained from the 3D model.

The film thickness obtained from the linear fit to the FP peak positions (figure 6.10a) results in a film thickness of  $8.68 \pm 0.33$   $\mu\text{m}$  what is slightly below the value of  $10.2$   $\mu\text{m}$  used in the theoretical calculations.

\*\* TMM calculations were done by Dr. D. Cassagne, Groupe d'Étude des Semiconducteurs, Université de Montpellier II, France

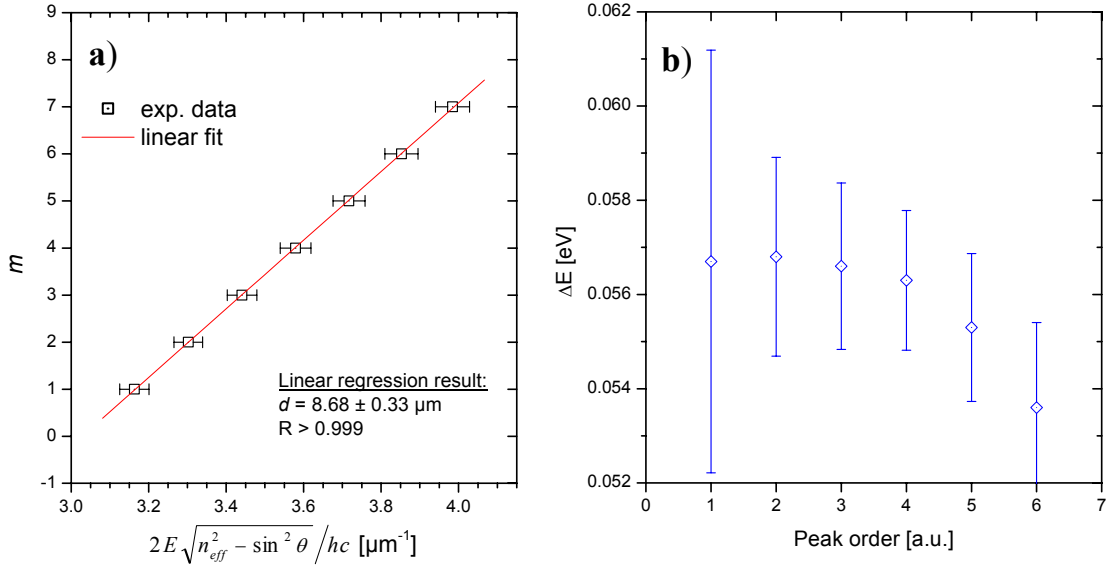


**Figure 6.10:** A linear regression of reflectance data from figure 6.9 gives a film thickness of  $d = 8.68 \pm 0.33 \mu\text{m}$  (a). The distance of two consecutive Fabry-Pérot oscillation maxima decreases close to the Bragg peak (b). This can be explained by an increase of the effective RI close to the band gap.

For energies below the gap, the amplitude of the calculated oscillations increases towards the Bragg resonance and rapidly decreases above it, which is in a good qualitative agreement for the observed evolution.

Remarkably, the Fabry-Pérot oscillations appear differently from both sides of the Bragg resonance. Their oscillation period changes close to the Bragg peak as shown in figure 6.10b and they show a rapid decrease of the oscillation magnitude on the high-energy side. The errors indicated in the plot have been calculated by error propagation from the experimental errors and can be mainly attributed to the uncertainty in determining the exact maxima positions of the FP oscillations and the error of the incident angle  $\theta$ .

These second order effects can be modelled by a full 3D approach. The evolution of the amplitude of Fabry-Pérot oscillations can be explained by a rapid variation of the dielectric properties (i.e.  $n_{eff}$ ) of the material in the vicinity of the photonic band gap [112].

From equation (6.3) it is evident that the effective RI  $n_{eff}$  can be expressed as:

$$n_{eff} = \sqrt{\frac{h^2 c^2}{\Delta E^2 4d^2} + \sin^2 \theta} \quad (6.4)$$

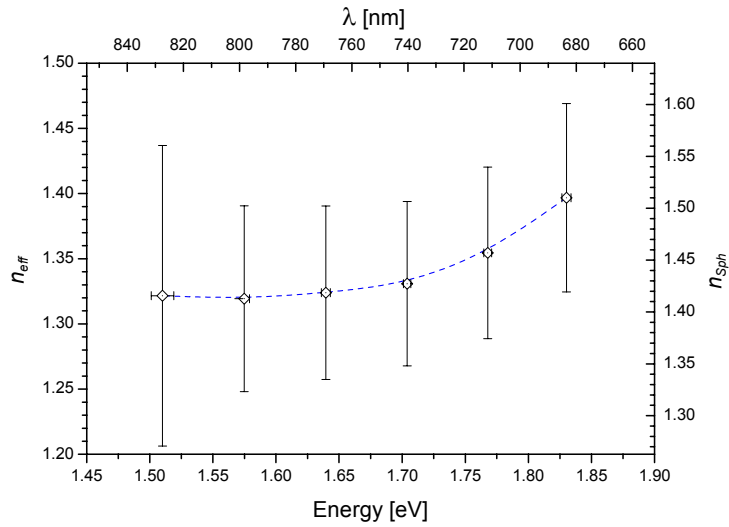


**Figure 6.11:** Changes of the effective RI of the PMMA PhC structure in the vicinity of the first pseudo-gap as estimated from the FP oscillation periods. The dashes line serves as a guide for the eye only. Assuming a filling factor of 74% this value is transformed into a virtual RI of the PMMA spheres as indicated on the right y-axis.

$\Delta E$  is the energy difference of two consecutive oscillation maxima. By using the measured film thickness this equation can be used to estimate the energy-dependence of  $n_{eff}$  in the vicinity of the band gap.

This is plotted in figure 6.11. For every pair of FP maxima  $n_{eff}$  was calculated and associated with  $|E_m - E_{m+1}|/2$ . A clear increase of  $n_{eff}$  is evident from the curve which qualitatively can be understood from the flattening of band close to the first pseudo gap:

The effective RI can be estimated from the dispersion relation of the photonic bands [112] to be  $n_{eff} = c/(\delta\omega/\delta k)$ , thus as the photonic band becomes flatter in the vicinity of the first L-pseudo-gap  $n_{eff}$  increases (cf. figure 2.7).

A comparison of the obtained  $n_{eff}$  with the expected value from the Bragg peak position reveals that RI of the PMMA beads seems to be underestimated slightly. Nevertheless, taking the errors into account a fairly good agreement with the TMM calculations is given. – Again the main contribution are from the uncertainty of the FP oscillation maxima positions and of the film's thickness  $d$ . Since only a few FP oscillations could be observed, the error of the calculated  $n_{eff}$  is rather big and quantitative statements are difficult. Thus a detailed comparison with theoretical calculations was not performed. A set of measurements on high quality films showing more FP oscillations would be necessary to perform a meaningful cross-check with band-structure calculations.

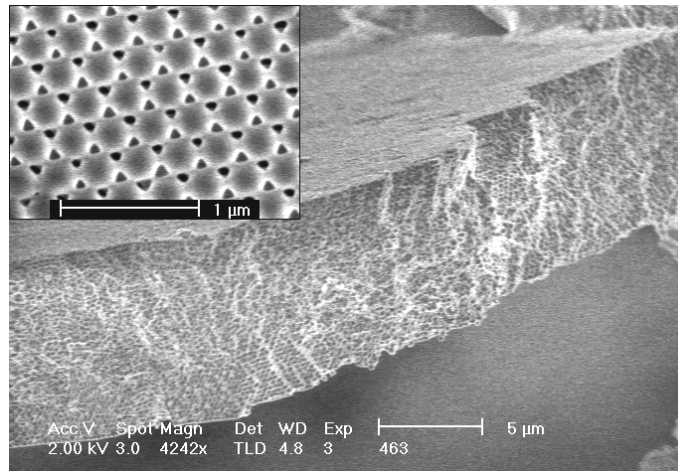


**Figure 6.12:** SEM micrograph of sample 463/3a. The film thickness was determined by measuring a cut-off piece of the sample as depicted here. The inset shows a close up of the surface of the same sample. It was used to measure the bead diameter.

A SEM micrograph of sample 463/3a, that shows the Fabry-Pérot oscillations, is shown exemplary in figure 6.12. The inset shows a top view at higher magnification, illustrating the good crystalline quality. To determine the film's thickness, the sample was cut and the resulting edge measured from the SEM picture as well as the bead diameter.

To determine the bead diameters experimentally at different spot on the sample SEM pictures were taken and the bead diameter was measured by averaging over 8-10 beads. The individual results were averaged to compute the resulting bead diameter.

The film thickness was determined in the same way by averaging over several measurements. The result here is less precise because the angle under which the sample edge is observed is not well determined.

A comparison of the film parameters obtained by the three independent methods is given in table 6.1. A good agreement of the obtained values is given. The underestimation of the film thickness in the 1D FP model can be attributed to the increasing RI close to the band gap (cp. figure 6.11) that is not taken into account in the model: An increasing  $n_{eff}$  leads to a decreased slope of the data in figure 6.10a and thus to a reduced resulting film thickness. This plays a role here since only a few FP oscillations in the vicinity of the band gap were experimentally accessible.

	<i>SEM observation</i>	<i>1D model</i>	<i>full 3D approach</i>
film thickness $d$	$8.9 \pm 0.5 \mu\text{m}$	$8.68 \pm 0.3 \mu\text{m}$	$10.2 \mu\text{m}$
bead diameter $D$	$289 \pm 5 \text{ nm}$	-	$292 \text{ nm}$
refractive index $n_{sph}$	$1.45^*$	$1.45^*$	1.42

**Table 6.2:** Comparison of film thickness and bead diameters obtained by different methods for sample 463/3a. \*:  $n_{sph}$  calculated from the Bragg peak position assuming a filling fraction of 74%.

More detailed studies on improved samples (i.e. more Fabry-Pérot oscillations visible) would be helpful here in the future, especially to verify the 3D model and to verify the increase of  $n_{eff}$  close to the band gap quantitatively.

The good agreement of experimental data with theory, which assumes perfect arrangement of spheres, underlines the high order quality of the thin film sample [109].

### 6.3. Reflectance of inverted opals

In comparison with the PMMA templates, in  $\text{SnS}_2$  inverted PhC films the Bragg resonance shifts to the blue with the change of the effective RI of the structure as a whole.

An obvious increase of the FWHM is achieved with the inversion of the PMMA opal as apparent from figure 6.13, where the evolution of the Bragg peak during the inversion process is represented. Starting from a PMMA opal template the infilling of  $\text{SnS}_2$  (as described in detail in chapter 5.4.2) leads to a shift of the reflection peak and a modification of the width of the pseudo band gap, represented by the relative bandwidth  $\Delta E/E_B$  (calculated from the FWHM of the Bragg peaks) for better comparability of different samples.

The PMMA template shown in figure 6.13, consists of spheres of diameter  $D \approx 244 \text{ nm}$ . The stop-bandwidth is about 5% in good agreement with theoretical calculations.

When a PMMA template is infilled with  $\text{SnS}_2$  the effective RI of the whole sample increases, leading – again in accordance with the Bragg law – to a red shift of the diffraction peak. At the same time the RIC decreases from 1.49 : 1 in PMMA templates to  $\approx 1.75 : 1.49$  in the PMMA /  $\text{SnS}_2$  composite. Thus the relative bandwidth decreases slightly to 3.5%. As the PMMA spheres are removed in the subsequent step, the effective RI decreases – leading to a blue-shift of the Bragg peak. The RIC increases to  $\approx 1.75 : 1$  and the filling factor of the inverted structure favours the broadening of a gap so the relative bandwidth increases to 11% in the inverted  $\text{SnS}_2$  sample.

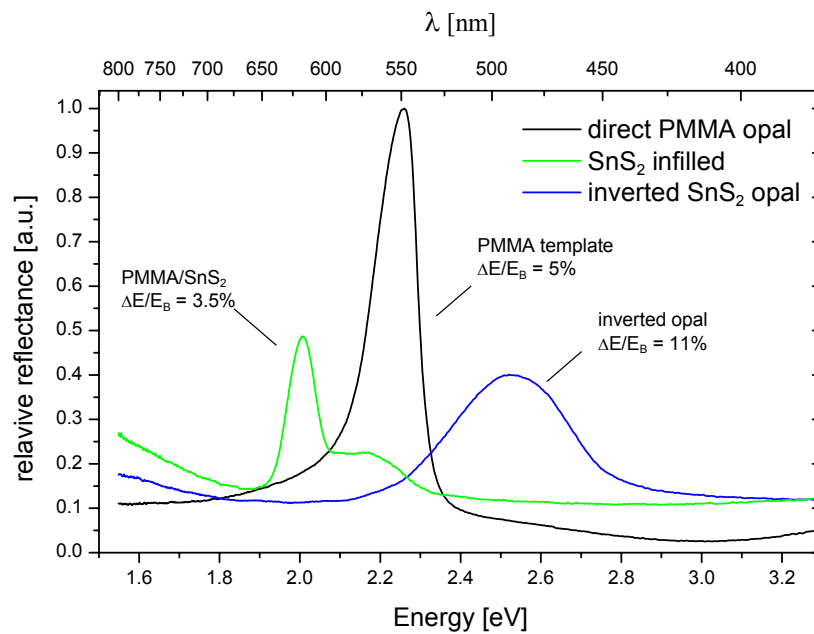


**Figure 6.13:** Evolution of the Bragg peak during the inversion process. The reflectance is plotted as relative value with respect to the direct PMMA opal used as template for the inversion (black line). After infilling with SnS<sub>2</sub> the peak is red shifted do to the increase of the effective RI. At the same time the relative stop-bandwidth increases slightly due to the changed RIC (green). After removing the PMMA the increased RIC of the inverted SnS<sub>2</sub> structure causes an increase of the FWHM and the reduced RI gives rise to a blue-shift of the Bragg peak (blue). The peak height decreases because of structural damages during the inversion process.

Comparing the peak amplitude of the template and the infilled and inverted samples it is apparent that the sample quality has suffered during the inversion process. The amplitude decreased by 50% and the diffuse background increased considerable. Additionally a shoulder on the high energy side of the infilled sample's reflection peak developed. This indicates that the infill process is likely to induce cracks and disorder on the sample as depicted on SEM micrographs in chapter 5.4. A careful choice of preparation parameters is essential to avoid degradation.

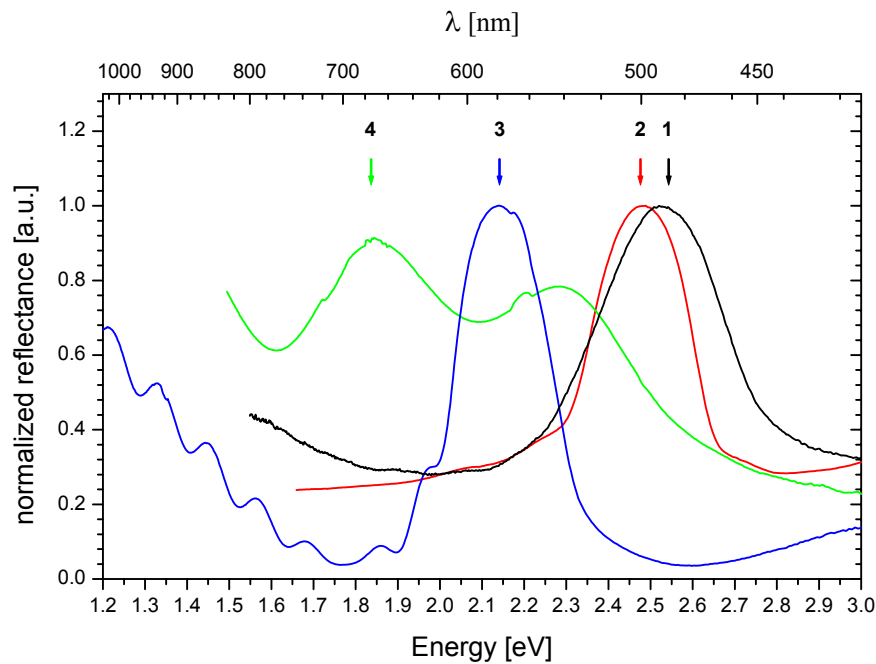


**Figure 6.14:** Reflectance spectra of different inverted  $\text{SnS}_2$  samples. Samples 2-4 were prepared from PMMA opal templates with sphere diameters  $D = 289$  nm. The different peak positions reflect the different amount of  $\text{SnS}_2$  infilled into the samples. Sample 1 was prepared from a template with  $D = 244$  nm. The amplitude and shape of the peaks reflect the structural quality of the samples ranging from poor (sample 4, green) to good (sample 3, blue).

The reflectance spectra of four different inverted  $\text{SnS}_2$  samples are shown in figure 6.14. The samples were prepared from PMMA opals with sphere diameters of 244 nm (sample 1) and 289 nm (sample 2-4). The diameter obtained from the Bragg peak shift during the infill and deviates from SEM measurements on the template by ca. 3.9%. This is attributed to a shrinkage of the lattice after the removal of the PMMA beads. It is evident from the peak position and their form that these samples contain different amounts of  $\text{SnS}_2$  and thus have different RICs and possess different structural quality. Sample 4, containing the highest semiconductor volume, was prepared from a very thin template (fewer than 10 layers). The deposition proceeds therefore more efficiently in this sample.

Since the templates were all of comparable crystalline quality, the structural damages induced during the inversion process are directly reflected by the reflection peak amplitude and shape. Whereas from sample 3, still FP oscillations are visible (cf. figure 6.15) – a sign of high structural quality and thus little damage induced by the inversion process – samples 1, 2, and 4 suffered from bigger structural changes, such as cracks, during the process. Especially

samples with high filling factors of SnS<sub>2</sub> suffer most from damages, restricting their use in further optical experiments. There is definitely room to optimise the process parameters.

By using the known sphere diameter and the shift of the Bragg peak in inverted opals compared to their templates the RI of the infilled material was calculated for different samples as summarised in table 6.3.

<i>sample</i>	<i>n<sub>SnS<sub>2</sub>-replica</sub></i>	<i>SnS<sub>2</sub> porosity</i>	<i>RIC</i>	<i>sample quality</i>
1	1.23	54 %	1.75 : 1	average
2	1.10	34 %	1.35 : 1	average
3	1.28	58 %	1.86 : 1	good
4	1.50	76 %	2.42 : 1	poor

**Table 6.3:** Summary of the key parameters of different SnS<sub>2</sub> replicas.

The value  $n_{\text{SnS}_2\text{-replica}}$  replica refers to the effective RI of the whole sample, whereas the RIC indicates the RI of the infilled semiconductor. The porosity specifies the fraction of the opal voids that is actually infilled with material. The corresponding reflectivity curves are shown in figure 6.14.

It is evident, that the theoretical value [103] of  $n_{\text{SnS}_2} = 3.2$  could not be reached so far. It is reasonable to ascribe the difference between the effective RI and its nominal value to a porous structure of semiconductor particles in the template voids (with the bulk RI of 3.2). This assumption is in agreement with Raman peaks obtained from these samples that show a peak centred at  $311 \text{ cm}^{-1}$  that is in accord with the lattice vibrations from crystalline SnS<sub>2</sub>. The relatively broad appearance of the peak (cf. figure 5.22) suggests that the semiconductor consists of small crystallites. Thus, although the voids of the template are completely filled with the semiconductor the resulting effective RI is lower than the theoretical values for bulk material.

Assuming the same lattice parameter for the semiconductor replica as for the PMMA template, the effective RI of the semiconductor is below 2.42 in the best case, which needs an adjustment to the effective filling factor of the composite with the Bragg estimate of the effective RI ( $n_{\text{eff}}$ , as defined by the effective medium approach in ch. 2.3.2). Assuming that the effective index of refraction of the infill (n.b.  $n_{\text{eff}}$ , not  $\epsilon_{\text{eff}}$ ) depends linearly upon the density of the semiconductor, the filling factor of SnS<sub>2</sub> in the voids of PMMA template is about 76 volume percents (vol-%) in the best case (table 6.3, ‘SnS<sub>2</sub> porosity’), which is about 20 vol-% of the whole composite. The effective medium expression using  $n_{\text{SnS}_2} = 3.2$  a porosity of 76% and  $f_{\text{SnS}_2} = 0.26$  results in  $n_{\text{eff}} \approx 1.5$ , which correlates well with the Bragg estimate.

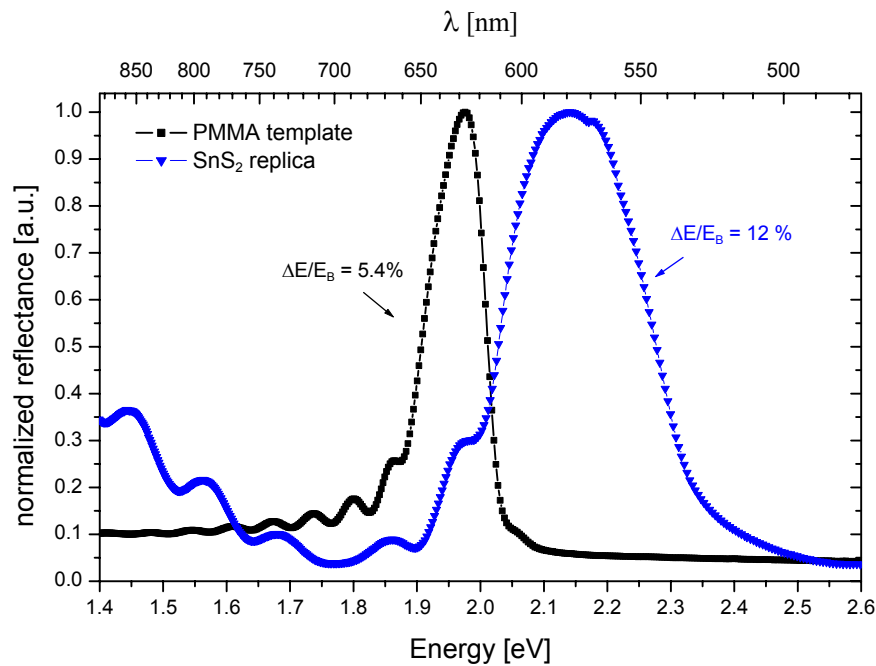


**Figure 6.15:** Reflectance spectra of a PMMA opaline film made from spheres with diameter  $D=289$  nm, and its  $\text{SnS}_2$  replica. The  $\text{SnS}_2$  spectrum is shifted to the blue due to the decreased effective RI and broadened because of the improved RIC and filling factor. Note that the Fabry-Pérot oscillations on the low-energy side of the spectra are preserved, indicating the good crystalline quality of both films.

Figure 6.15 depicts the Bragg resonances from a PMMA template and its  $\text{SnS}_2$  replica of high quality in comparison. The FWHM of the Bragg peak increases from 5% to 12% in the replica, mainly due to the enhanced RIC and a filling factor closer to the theoretical optimum, thus favouring the broadening of the PBG.

Apart from these effects  $\text{SnS}_2$  replicas demonstrate an optical behaviour similar to their PMMA templates, namely Fabry-Pérot oscillations (figure 6.15) and multiple diffraction (figure 6.21). In particular, this indicates the preserving a high level of ordering, characteristic for a template, during the inversion process if it is chosen carefully.

#### 6.4. Band branching in thin film opals

The improvements of experimental techniques have given the possibility to have opal samples that testify diffraction from planes other than the (111) plane. Recently the presence of multiple resonances has been reported in high quality  $\text{TiO}_2$  inverse opals [113]. The physical considerations of the presence of multiple Bragg resonances peaks can play an important role

in practical devices. In reference [114] a strong modification has been shown over the emission spectra due to the simultaneous diffraction from the (111) and (200) planes.

Reflectance spectra of a representative PMMA opaline film collected at a wider range of different angles  $\theta$  are shown in figure 6.16. They were performed for an angular range from  $\theta = 5^\circ$  to  $70^\circ$  in the  $\theta$ - $2\theta$  configuration, where the angle of incidence is equal to the angle of collection of the reflected light. The measurements shown were performed using unpolarised light. A sphere diameter of 283 nm was measured from SEM observations and the dielectric constant of PMMA is set to its theoretical value of 1.4893 [108]. Some 50 layers of spheres have been determined to exist in this sample. Assuming touching spheres this results in a effective RI of the sample of  $n_{eff} = 1.379$ .

A relative stop-bandwidth of  $\Delta E/E_0 \approx 5\%$  can be determined as the FWHM from the Bragg resonance at near normal incidence ( $\theta \approx 5^\circ$ ). This value matches the [111] relative gap width calculated by the plane wave method [51].

The most remarkable feature of the reflectance spectra shown is the occurrence of double peaks for external angles  $\theta_{ext} \approx 45^\circ$ - $55^\circ$ . The splitting of the Bragg resonances into two peaks can be attributed to Bragg reflections from (200) crystalline planes. Assuming a simultaneous

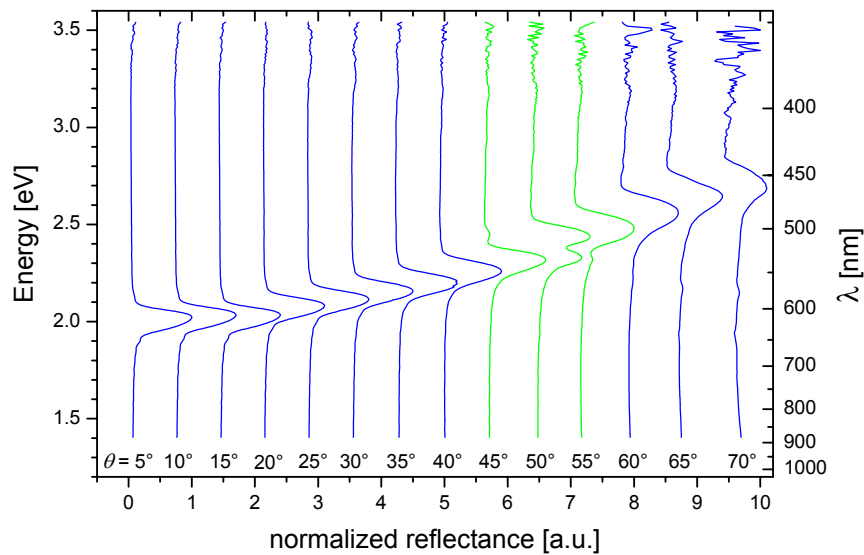


**Figure 6.16:** Bragg reflectance peaks from a PMMA thin film PhCs. For angles between  $45^\circ$  and  $55^\circ$  (green curves) a splitting of the reflectance peak into 2 branches is observed. For better comparability to theoretical calculations the energy was plotted on the y-axis. The curves are normalised and shifted horizontally for clarity.

diffraction from two sets of planes – (111) and (200) – the existence of double peaks can be explained by means of the Bragg law. Nevertheless, the shape of the curves can not be explained by the Bragg law alone. Here the analysis of exact band structure calculations [109] is necessary.

The evolution of the Bragg resonances from (111) and (200) planes – calculated for a PMMA opal film – with external angle  $\theta_{ext}$  is shown in figure 6.17.

Since for *fcc* crystals the angle between [111] and [200] directions is  $54.74^\circ$  the effective angle of incidence for diffractions from (200) planes is  $\theta_{int}^{(200)} = 54.74^\circ - \theta_{int}^{(111)}$ . The external angle  $\theta_{ext}$  has to be obtained by Snell's law (cf. sect. 2.3.1) to be  $\sin \theta_{ext} = n_{eff} \sin \theta_{int}$ . Thus the Bragg resonances from (200) planes decrease in energy with increasing incident angle, whereas the (111) resonances increase as seen in figure 6.17.

According to whether a reflection peak is closer to the (111) or (200) Bragg curves, it can be associated with one of two families of lattice planes. Thus, double peaks appear in the vicinity of the crossing between the two Bragg curves obtained at  $\theta_{ext} = 51.48^\circ$ .

The dots represent data that can be linked with reflections from (111) planes, whereas triangles can be associated with reflections from (200). For incident angles  $\theta_{ext}$  between  $45^\circ$  and  $55^\circ$  the Bragg condition is nearly satisfied for both plane sets, consequently both

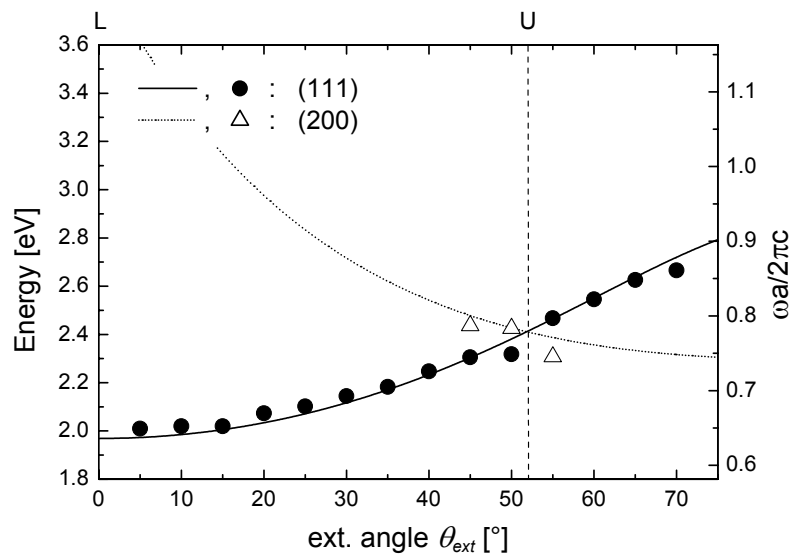


**Figure 6.17:** Bragg law predictions for the diffraction from (111) and (200) planes. Experimental data (• and Δ indicate peaks associated to (111) and (200) reflections, respectively) and theoretical calculations (solid and dashed line). The crystallographic directions corresponding to the external angles are indicated on the top axis, the reduced frequency units used for band structure calculations with  $a$  being the lattice parameter ( $a = \sqrt{2} \cdot D$ ) are shown on the right axis.

reflections can be observed. Having a closer look on the correlation between experimental data and Bragg predictions reveals that near the crossing of the curves for the (111) and (200) planes the position of the peak maxima does not follow exactly the Bragg law. It is also evident, that peaks associated to the (111) diffraction can be observed in a wide angular range, whereas peaks associated to the (200) diffraction can only be observed in a narrow angular interval. This reveals that the explanation solely based on the Bragg law is not sufficient to interpret the phenomenon fully.

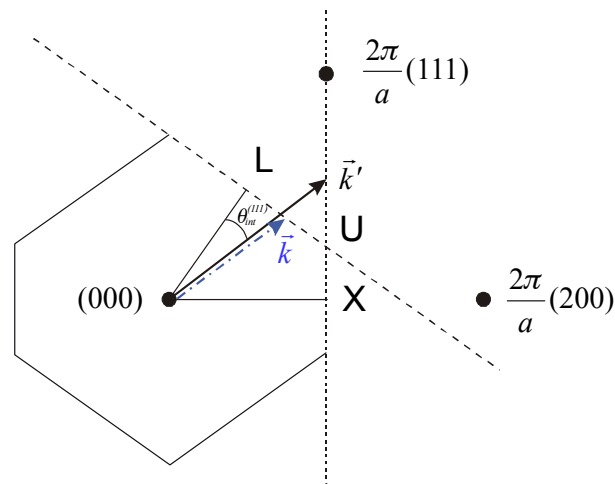


**Figure 6.18:** Cross-section of  $(IXL)$  plane of the fcc Brillouin zone in reciprocal space. The dotted and dashed bisecting lines indicate the positions where the tips of wavevectors have to point to satisfy the Laue condition for diffraction at (111) and (200) planes, respectively. For a given internal incident angle  $\theta_{in}$  this is the case for both vectors  $\vec{k}$  and  $\vec{k}'$ , thus two reflection peaks can be found near the U-point. It is noteworthy that  $\vec{k}'$  is outside the first Brillouin zone.

To obtain a better understanding it is instructive to view the problem in reciprocal space. This is depicted in figure 6.18. As it can be obtained from every textbook on solid state physics [17] the diffraction condition is satisfied if (and only if) the scattering vector is a reciprocal lattice vector. Using a graphic description: The tip of a scattering wavevector must lie on a plane that is the perpendicular bisector of a line joining the  $\Gamma$  point and a reciprocal lattice point. These planes are indicated in figure 6.18 as dotted and dashes lines for (111) and (200) reflections, respectively. They also build the border of the first Brillouin zone (BZ). Several wavevectors satisfy this condition simultaneously for a given reciprocal lattice direction. Two wavevectors satisfying the stated condition are indicated in figure 6.18. Wavevector  $\vec{k}$  corresponds to diffraction at (111) planes, whereas wavevector  $\vec{k}'$  corresponds to scattering of (200) planes.

The latter wavevector is outside the first Brillouin zone. It can be translated into a wavevector within the first BZ of course, but for clarity the continuous evolution along the X-U and L-U lines inside and outside the first BZ space is considered.

Detailed band structure calculations were carried out using the plane wave method to model the experimental data<sup>††</sup>. 1067 plane waves of the reciprocal lattice were used to obtain good convergence. Using Snell's law to define the internal angle, the position of the experimental peaks we associate with (111) diffraction are plotted in figure 6.19, together with the band structure calculations. The plot shows the data along a straight line in L-U direction inside and outside the first BZ. The experimental data are in good agreement with the gap position. It is important to note that the gap exists for a large range of  $k$  vectors along this line.

The peaks associated with (200) diffraction are depicted in figure 6.20 together with the band structure calculations along the X-U line inside and outside the first BZ. Only the three data points associated to (200) reflections are plotted. These peaks exist only in the vicinity of the U point and there is a good agreement with the band structure calculation since the gap along this line is open only in the vicinity of the U point. This gives a clear explanation of the existence of double peaks only for external angles near  $\theta_{ext} = 51.84^\circ$ , which corresponds to internal angles near the U point.

Moreover, multiple band mixing that occurs at the U point presumably decreases the frequency of the bands. This phenomenon is well known in solid state physics. It explains the deformation of the bands near the U point. The discrepancy between the position of the experimental peaks and the Bragg curves of figure 6.17 near the crossing point occurs because the Bragg law does not take the band mixing into account. Therefore, by making reference to the band structure of these materials, the presence of double peaks is explained by a photonic band branching at the U point of the Brillouin zone.

An alternative explanation has been given to the double peak in reflectance spectra in (100) direction as the result of stacking faults in the *fcc* lattice [79]. In our case the experimental conditions are quite different from those in Ref. [79], namely, the RIC is much higher (1.49:1.00 against 1.45:1.47) and the spectrum was measured under inclined light propagation with regard to the sample surface, which both impose stronger scattering.

---

<sup>††</sup> band structure calculations were performed by Dr. D. Cassagne, Groupe d'Étude des Semiconducteurs, Université de Montpellier II, France using the PWM similar to Refs. [21, 51].

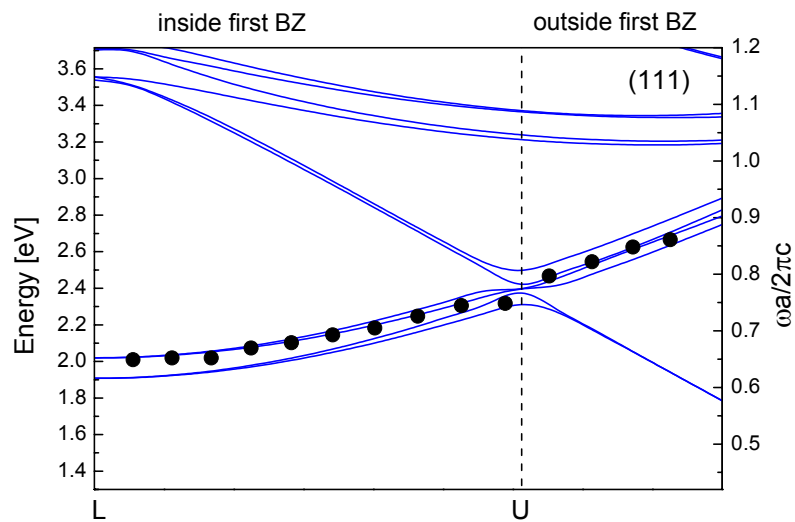


**Figure 6.19:** Photonic band structure calculations (solid lines) and experimental data (circles) of peaks associated to (111) reflections. The calculations were done for a straight line along the L-U direction inside and outside of the first BZ

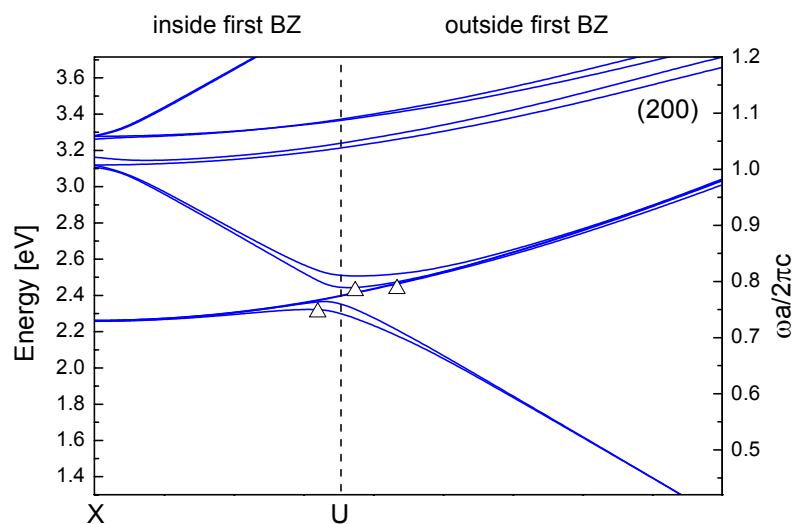


**Figure 6.20:** Photonic band structure (solid lines) calculated along the (XU) line inside and outside the first Brillouin zone. The triangles indicate the experimental peaks associated with (200) planes.

### 6.5. Band branching in inverted opals

Similar measurements to PMMA based samples were carried out on inverted SnS<sub>2</sub> replicas.

A series of reflectance measurements on a SnS<sub>2</sub> replica is shown in figure 6.21. The sample under study was prepared from a template consisting of beads with a diameter of 289 nm. The

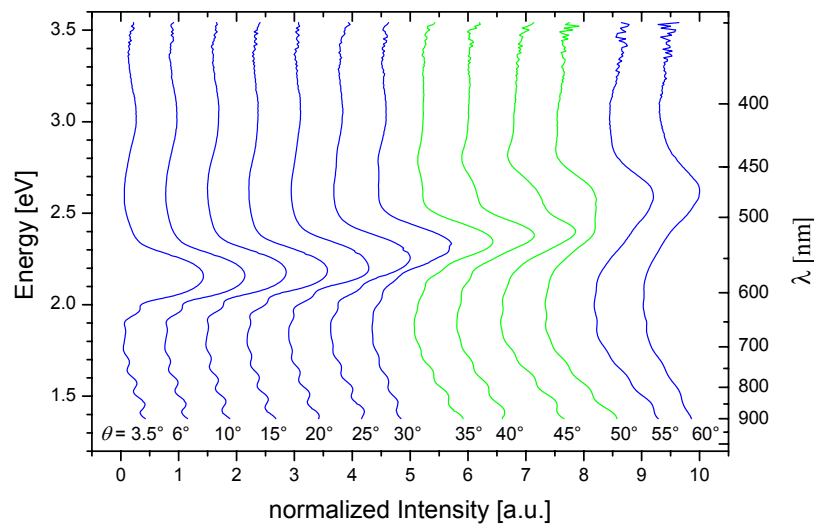


**Figure 6.21:** Reflectance spectra of a SnS<sub>2</sub> replica. Band branching can be observed for external angles  $\theta_{\text{ext}}$  between ca. 35° and 55°, similar to PMMA templates (cf. figure 6.16)

RI of the semiconductor framework was determined to be  $n = 1.86$ . (cf. table 6.3, sample 3).

From figure 6.21 it is seen that the band branching spans a larger range of angles for SnS<sub>2</sub> replicas compared to PMMA templates. For external angles between 35° and 50° a splitting of the Bragg peak into two resonances can be observed, compared to 40°-55° in PMMA opals. In complete analogy to figure 6.17 the peaks can be associated to reflections from (111) and (200) planes. The behaviour found for PMMA samples (cf. sect. 6.4) have been confirmed as well for the replicas. I.e. reflections from (111) planes are seen in a wide angular range, whereas reflections from (200) planes are observed only at the vicinity of the U-point.

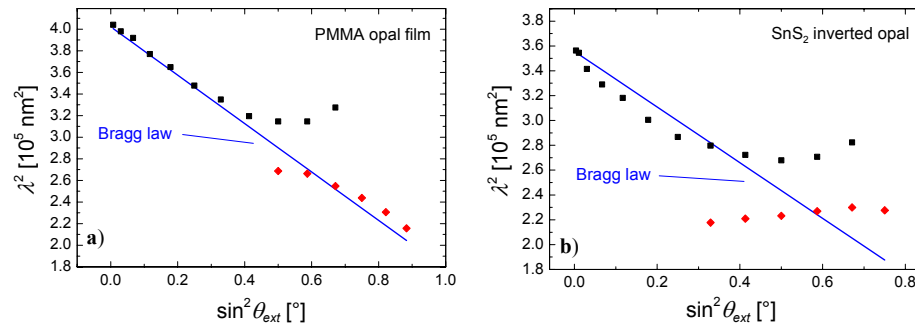


**Figure 6.22:** Band branching in PMMA- (a) and SnS<sub>2</sub>-opals (b). The SnS<sub>2</sub> sample exhibits a much stronger band repulsion and the dispersion loses the relation to the Bragg law after the branching point.

Additionally, a comparison of branching in PMMA and SnS<sub>2</sub> opaline films reveals much stronger band repulsion, moreover, the dispersion after the branching point loses its relation to the Bragg law as it can be seen from figure 6.22b. In this figure the deviation of the obtained peak positions from the reflectance measurements are shown by plotting  $\lambda^2$  vs.  $\sin^2 \theta_{ext}$ . In this representation the Bragg law transforms to a straight line making any deviations easily visible.

The reflection peaks from the PMMA PhC approximate to the Bragg line again after the branching region as depicted in figure 6.22a. In contrast the inverted PhCs show firstly a much more pronounced deviation from the Bragg line in a wider angular range and, secondly, after the band crossing region the relation to the Bragg law is lost in the experimentally accessible range.

This behaviour is attributed to the higher RIC in the opaline replicas leading to a much stronger effect.

## 6.6. Polarisation dependence of Bragg reflection

Studies of the Bragg-diffraction peaks in two orthogonal polarisations reveal important information concerning the light scattering in opal PhCs. The most impressive feature observed with unpolarised light – the band branching at high angles of diffraction – appears differently depending upon the polarisation. Measurements with *s*- (*p*-) polarised light (electrical vector perpendicular (parallel) to the plane of incidence) were undertaken. The effect was observed for both, PMMA opal and inverted SnS<sub>2</sub> opal and is analysed in this chapter.

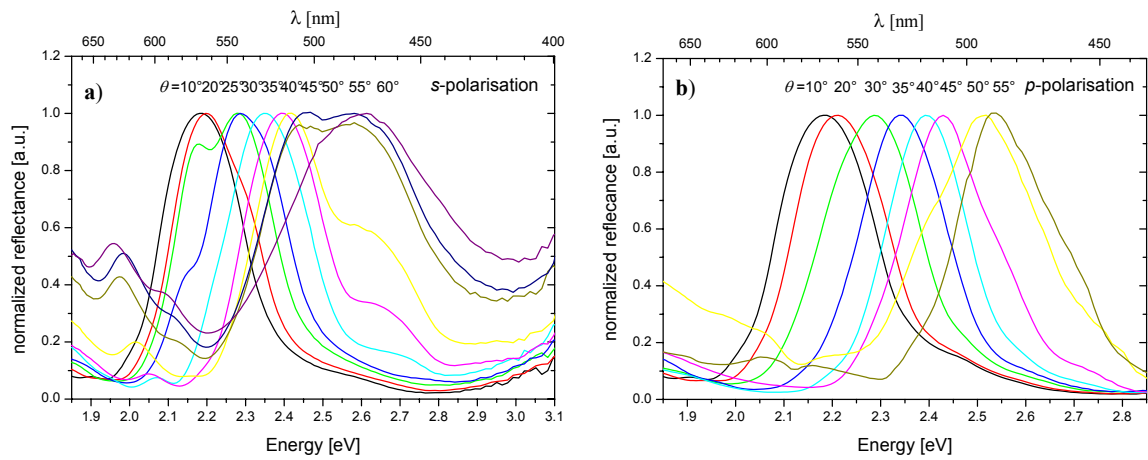


**Figure 6.23:** Changes of the Bragg resonance for varying incident angles for *s*-polarised light (a) and *p*-polarised light (b).

The obvious difference from reflections done with *s*- and *p*-polarised light is illustrated in figure 6.23. The left panel shows the reflectance of a  $\text{SnS}_2$  inverted PhC done with *s*-polarised light. As it was explained in chapter 6.4, the branching shown in figure 6.23a is the result of a simultaneous observation of resonances from (111) and (200) opal planes.

In contrast, the right panel, which shows the reflectance of the same sample examined with *p*-polarised light, does not provide any evidence for band branching.

This becomes more obvious when  $\lambda^2$  is plotted vs.  $\sin^2 \theta_{ext}$  as done in figure 6.24. Again the left panel shows the experiment done with *s*-polarised light, where the band branching and band repulsion is obvious. The data depicted in the right panel follow closely the Bragg line and no sign of band branching could be found. The dispersion line shows a discontinuity close to external angles corresponding to the U-point ( $\sin^2 \theta \approx 0.6$ ). This discontinuity is the visualisation of the band branching, which happens due to uncertainty of the dispersion when approaching the branching point.

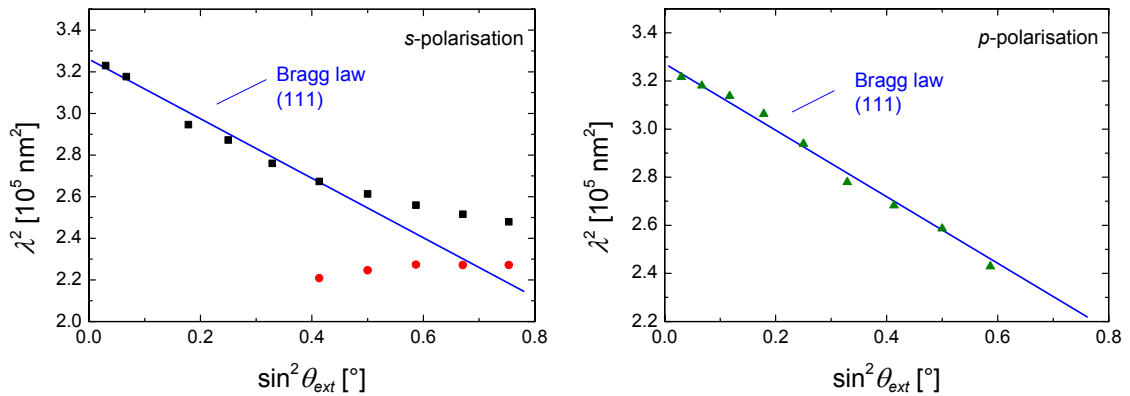


**Figure 6.24:** Angular dispersion of the Bragg resonance of  $\text{SnS}_2$  inverted opal for *s*-polarisation (left) and *p*-polarisation (right). No deviation from the Bragg law is evident for *p*-polarised light, in contrast to *s*-polarised light.

To investigate this behaviour reflectance experiments with fixed angles of incidence at the branching point ( $\theta \approx 50^\circ$ ) were performed for various polarisation directions of the incident beam with respect to the (111) planes.

A gradual and reversible transformation of the double peak of the resonance into a single peak and back was found (figure 6.25). The polarisation angle  $\varphi$  defines the polarisation of the incident beam with respect to the plane of incidence, where  $\varphi = 0^\circ$  corresponds to *p*-polarised light, consequently  $\varphi = 90^\circ$  is equivalent to *s*-polarisation.

The double peaks can be decomposed into two components. Their centre frequencies were determined from Gaussian fits as shown in figure 6.26 for *s*-polarisation from the PMMA opal.

In these measurements, the low-frequency resonance was found to remain nearly at the same frequency but the high-frequency resonance moves from its highest frequency position for *s*-polarisation to its lowest frequency position for *p*-polarisation, when scanning through different values of intermediate polarisations (i.e. different values of  $\varphi$ ).

This behaviour was confirmed both, for PMMA and  $\text{SnS}_2$  based opals as depicted in figure 6.25. The more pronounced splitting in two peaks for the PMMA sample is attributed to the higher crystalline quality of the direct sample compared to the inverted structure.

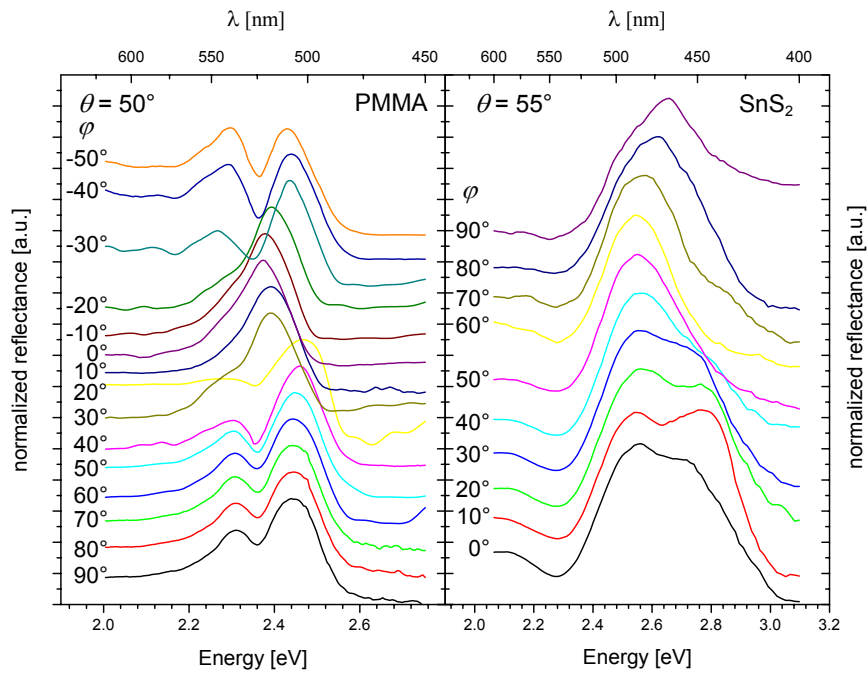


**Figure 6.25:** Modification of the Bragg peak for  $\text{SnS}_2$  (right) and PMMA opal (left) for different polarisations of the incident beam.  $\varphi = 90^\circ$  corresponds to  $s$ -polarised light with respect to the plane of incidence.  $\theta$  denotes the angle of incidence.

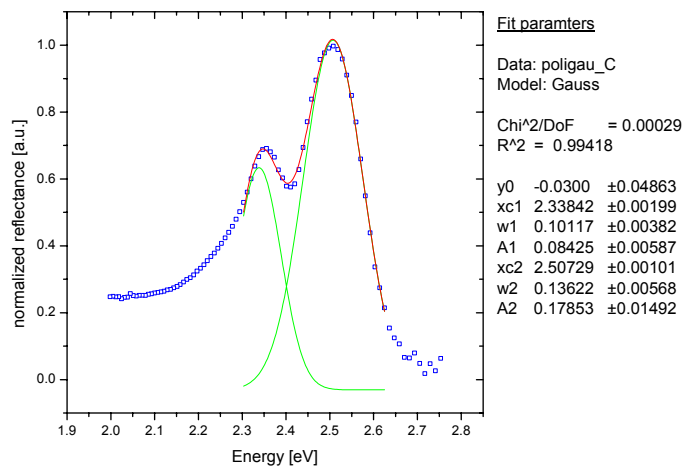


**Figure 6.26:** Gaussian fit of the double Bragg resonance from the PMMA sample at  $\theta = 50^\circ$  for  $s$ -polarisation. The data points (square) were fitted with the sum (red) of two Gaussian curves (green).

The rotation of the sample around the [111] direction (azimuthal rotation,  $\phi$ ) while maintaining a fixed angle of incidence and polarisation of the  $E$ -vector is another experimental configuration used in this work.

Incoming EM waves probe basically two different configurations of spheres in the (111) planes, depending of their azimuthal angle of incidence. They can be described as first-neighbour direction (FND) (i.e. nearest neighbour) and second-neighbour direction (SND) (i.e. 2<sup>nd</sup>-nearest neighbour), as depicted in figure 6.27.

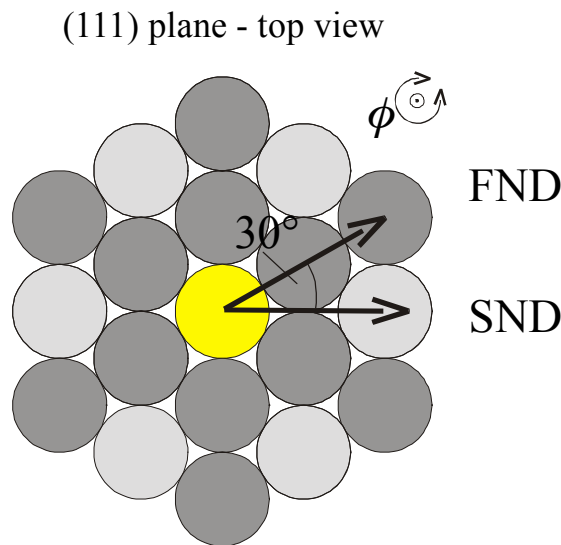


**Figure 6.27:** The (111) plane of fcc crystals can be characterised by two different sphere configurations described as ‘first neighbour direction’ (FND) in which the spheres are packed closest (dark grey circles) and ‘second neighbour direction’ (SND) in which the spheres are packed loosely (light grey circles). The two directions are separated by an azimuthal angle  $\phi = 30^\circ$

The FND is characterised by a dense package of neighbouring spheres, whereas in the SND the spheres are packed in the loosest possible way. The diffracted light thus interacts with the crystalline lattice differently in different azimuthal directions.

In the constant polarisation experiments with azimuthal rotation of the sample the following behaviour was found: The high-frequency peak shows no dependence upon the rotation of the sample, whereas the low-frequency peak changes rapidly with the azimuthal angle  $\phi$ . The position of the low-energy peak was obtained from Gaussian fits and plotted in figure 6.28 as a function of the angle  $\phi$ .

A 60° periodicity has been revealed in the variation of the low-energy resonance, which correlates with symmetry of the bead package in the (111) plane of opal. Larger distance from

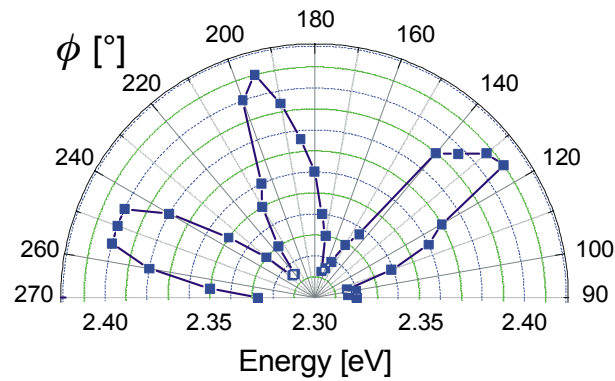


**Figure 6.28:** Contribution of reflections associated with (200) planes for different azimuthal angles  $\phi$  (unpolarised light)

the central bead to the next neighbour (SND) corresponds to lower resonance frequency and vice versa. The azimuthal variation of the Bragg resonance thus reflects the variation of this distance. The high-energy component of the double resonance arises mostly from the inter-plane diffraction, because the (111) inter-plane distance is shorter than one bead diameter and it does not vary with the angle  $\phi$ .

Two questions arise, first, why is band branching not observed for p-polarised waves and, second, why for unpolarised (or s-polarised waves) a clear dependence on the azimuthal angle is observed.

To analyse this effect a numerical simulations, which take into account the azimuthal orientation of the sample with respect to the incident beam have been undertaken<sup>\*\*</sup>.

Simulations using the Transfer Matrix Method (TMM) as introduced by Pendry and MacKinnon [110] have been used to calculate the propagation of the electromagnetic waves with different incident and azimuthal angles. A unitary cell oriented in the [111] direction with  $17 \times 10 \times 8$  grid points was used to obtain good convergence. The calculations were done for both, s- and p-polarised light.

As it can be seen from figure 6.29 and figure 6.30 it makes a big difference whether diffraction from FND or SND is concerned. In SND a strong branching can be observed for s-polarised waves (figure 6.29). This has been confirmed experimentally (black line) as multiple Bragg scattering from (111) and (200) planes. TMM calculation allow a modified description of the nature of the double peak. The branching observed experimentally is the

<sup>\*\*</sup> TMM calculations were done by Dr. D. Cassagne, Groupe d'Étude des Semiconducteurs, Université de Montpellier II, France

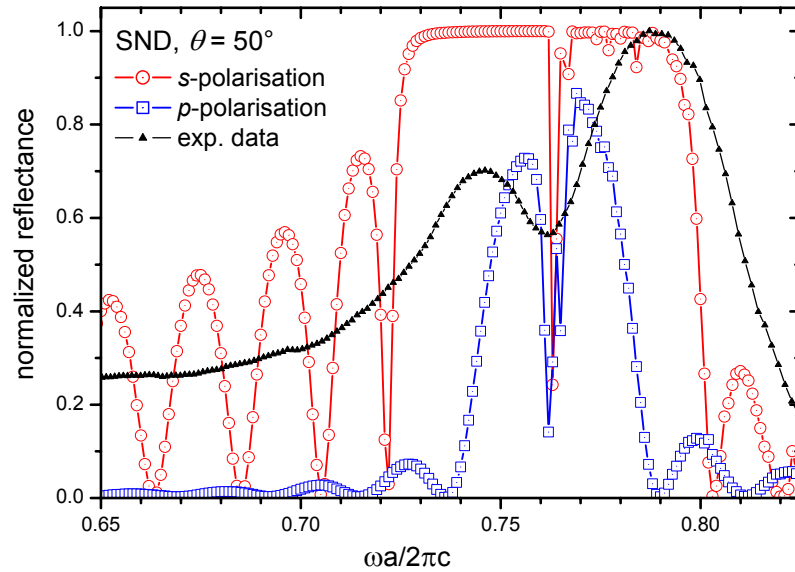


**Figure 6.29:** Simulated reflection spectra in the SND. The  $s$ -polarised reflection spectrum (circles) shows a strong manifestation of the double peak, which is seen for the  $s$ -polarisation resolved experiment (triangles). The  $p$ -polarisation reflection spectrum (squares) shows a weaker peak and the Fabry-Pérot oscillations die out faster.

average of  $s$ - and  $p$ -polarisation. But the two polarisations contribute differently to the resulting averaged peak.

For  $s$ -polarised light peak doubling is very strong. In contrast, for  $p$ -polarisation, the double peak has a smaller intensity. Its intensity is reduced by the proximity to the Brewster angle.

Interesting behaviour is also found from the Fabry-Pérot oscillations. FP oscillations, as described in chapter 6.2, is a phenomenon related to thickness of thin films. The FP oscillations are much more pronounced for  $s$ -polarisation than for  $p$ -polarisation. This is again, because the spectra were taken at incident angles  $\theta$  near the Brewster angle. Effectively, the Brewster angle for the thin film (PMMA) is determined to be  $\theta_B = \tan^{-1}(n_{eff}) = 54.05^\circ$ , where  $n_{eff} = 1.379$ . Theory and experiments show reasonable agreement here.

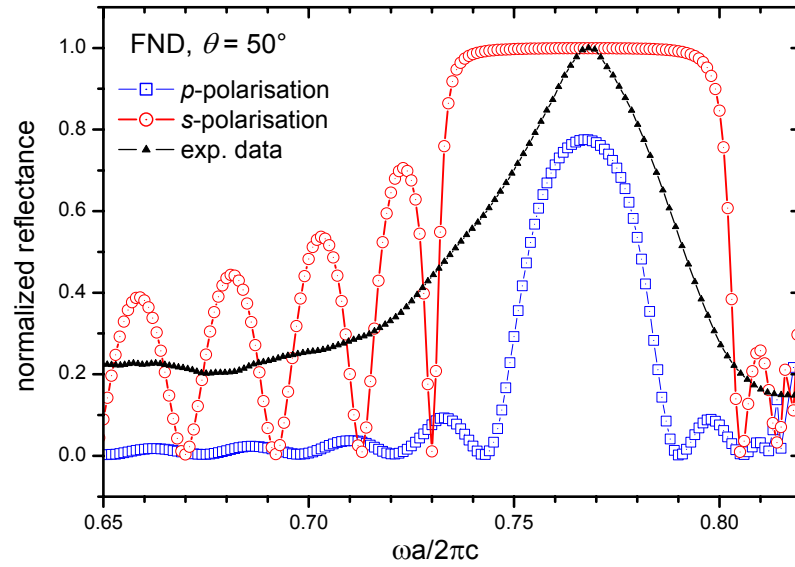


**Figure 6.30:** Reflection spectra in FND for  $\theta = 50^\circ$ . No peak doubling is observed in this direction. The TMM *s*-polarisation spectrum (circles) shows a well defined (111) diffraction plateau. The TMM *p*-polarisation spectrum (squares) has a less pronounced diffraction plateau, resulting in a substantially reduced reflectivity coefficient with the Fabry-Pérot oscillations disappearing faster.

Keeping the incident angle of  $50^\circ$  constant, the sample was turned by  $\phi = 90^\circ$  to the SND. No splitting can be observed either in *s*- or *p*- polarised waves for this configuration, there is only one peak visible, corresponding to (111) reflections (figure 6.30). This means that the contribution from (200) planes varies with the azimuthal angle. This can be qualitatively understood it is taken into account that reflections from (200) planes are most pronounced in L-U direction (SND), when the [200] direction is parallel, but inclined by  $45^\circ$  to the direction of observation (see figure 6.18, sketch of a look onto the Brillouin zone from  $[\bar{1} \bar{1} 1]$ ). Turning the sample into L-W direction (FND) the contribution from (200) reflections vanish. Thus a periodic pattern of the (200) intensity with a period of  $60^\circ$  is expected and experimentally confirmed (see figure 6.28).

A less pronounced double peak is found for  $\theta = 56^\circ$ , plotted in figure 6.31. Here the incident light is in the SND and a double peak is visible on the low energy side of the experimental spectrum. The (200) peak is present in the numerical simulation for *s*-polarisation ( $\omega a/2\pi c \approx 0.73$ ), but significantly weaker for the *p*-polarisation, in agreement with the experimental data.

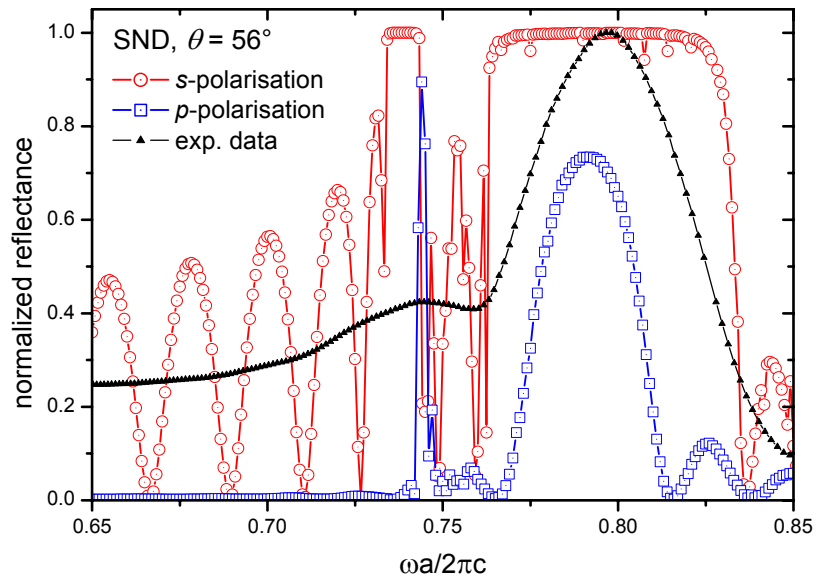


**Figure 6.31:** Reflection spectra in the SND for  $\theta = 56^\circ$ . The TMM *s*-polarisation spectrum (circles) clearly shows the double peak confirmed by the *s*-polarisation resolved experiment (triangles). The TMM *p*-polarisation spectrum (squares) has a weaker double peak and the Fabry-Pérot oscillations disappear rapidly.

## 6.7. Conclusions

Angle resolved reflectance and transmission measurements done on PMMA direct opal samples and their inverted semiconductor replicas revealed a good agreement with the Bragg law for low incident angles. At higher angles substantial deviations from this behaviour were found that can not be explained using only the Bragg law. Nevertheless detailed band structure calculations show excellent agreement with the experimental data.

Fabry-Pérot fringes were observed for highly ordered samples. It was shown that these fringes can be used as a non-destructive optical method to determine the thickness of thin film opal PhCs. Once more theoretical calculations showed excellent agreement with the experimental data and were used to explain small differences from a simple 1D Fabry-Pérot model found in the analysis of the experimentally observed FP-oscillations. The asymmetry of FP oscillation amplitude on the low- and high energy side and the variations in their period were reproduced by TMM calculations.

The occurrence of FP oscillations underline the high crystalline quality of the samples under investigation since they rapidly vanish as disorder increases.

The existence of double peaks at incident angles in the vicinity of  $\theta_{ext} = 51.84^\circ$  was explained by the effect of diffraction from (200) planes. This effect can be understood by a branching of the band at the U point in the photonic band structure.

Optical branching, seen by the presence of features associated with (111) and (200) reflections, was proved to be dependent of the azimuthal angle and polarisation of the incident  $E$ -vector. Depending on these two parameters the proportion of the two parts in the reflection spectrum peak varies.

Band branching was not observed in  $p$ -polarised light, but it is present in  $s$ -polarised light. This seems to reflect the neighbourhood of the scattering centres and was confirmed by TMM modelling.

The contributions from (200) diffraction are reduced in FND and for  $p$ -polarised light. Additionally, the Fabry-Pérot oscillations are attenuated for  $p$ -polarisation due to the vicinity to the Brewster angle. Numerical and experimental results have shown a good agreement.

## 7. Emission from opal Photonic Crystal structures

One of the most interesting phenomenon concerning photonic crystals is the study of the influence of the presence of a (partial or full) PBG on the emission properties of light emitting species inside a photonic crystal environment. Investigation on this topic have been undertaken for several years [8, 115-117].

To make significant progress certain conditions are necessary:

- The presence of a light source should not compromise the RIC. It should be incorporated either in the body of the PhC or it should appear as a coating spread over the internal surface of the PhC. Examples are:
  - a) the body of a PhC made out of bright emitting CdS or CdTe nanoparticles [102, 118].
  - b) Opals loaded with dye molecules [119] or rare earth ions [117] in the spheres or their replicas. While they would allow independent tuning of the PBG and the emission band they are limited by chemical compatibility of materials.
  - c) Opal and its replicas with dye molecules attached to the inner surface of their voids [75]. This approach offers good tunability but its efficiency is low and the lifetime of the dye molecule emission might be compromised by the presence of the opal surface.
- The width of an emission band should to be much narrower than the PBG width, i.e. significantly less than 5% of the midgap frequency in order to avoid re-distribution of the emission intensity towards the direction of the allowed propagation. Most organic dyes do not satisfy this demand, but rare earth ions and uniform semiconductor quantum dots do.
- The emitting component must have a long lifetime under strong laser pumping or electrical excitation.

One of the most interesting influences of a PBG structure upon the emission is the enhancement or suppression of the spontaneous emission (SE). The physical reason for the difference in the spontaneous emission (SE) rate is the modification of the density of photon states.

Another PBG induced effect on light emitting is the redistribution of the emission flux due to the structure of the dispersion surfaces in PhCs near the PBG. Both, spectral and spatial re-distribution of the emission intensity has been found in PMMA and inverted semiconductor replicas.

To probe the changes of the emission properties of embedded light sources, photoluminescence (PL) spectra were excited by an  $\text{Ar}^+$ -ion laser operating in continuous wave (cw) mode. The excitation power was kept low to avoid the degradation of the dye emission as sketched in figure 7.1 (“photo-bleaching”). If the optical pumping power is too high, the excited laser dyes start to degenerate due to strong thermal vibrations that eventually lead to breaking bonds and to the destruction of the dye molecules. Pulsed excitation is therefore preferable but this was not possible due to experimental restrictions at that time. The intensity plot in figure 7.1 was recorded under optical pumping power of 10mW at 351 nm. The luminescence of Pyrene dyes under study decreases rapidly with a half-life period of  $t_{1/2} = 242$  s. Since this time is shorter than the typical experimental time standard PL experiments were performed at optical power outputs  $< 1$  mW. Photoluminescence spectra were collected in transmission configuration from a small solid angle of  $\approx 5^\circ$  to allow angle resolved measurements using the set up described in 4.2.2.

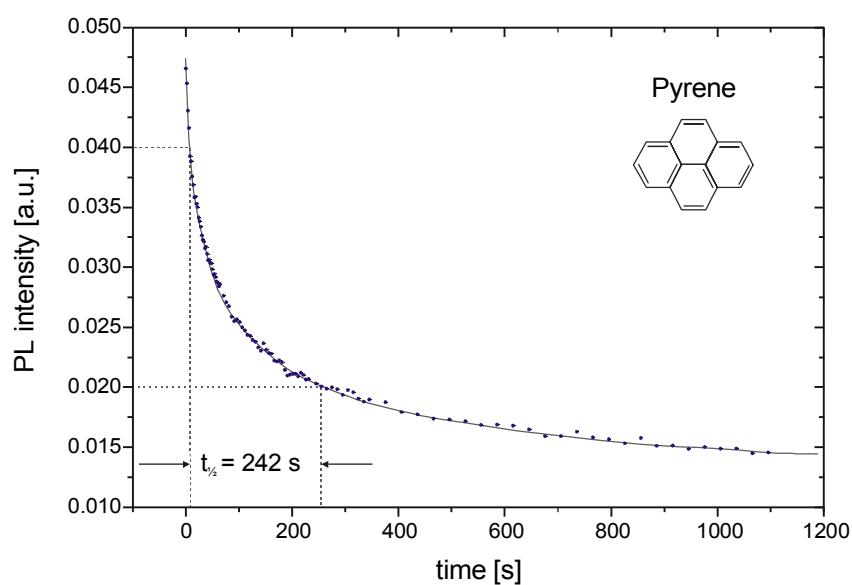


**Figure 7.1:** Degradation of the photoluminescence intensity from Pyrene with time at high optical pumping energies. The luminescence was excited using the 351 nm emission line of an  $\text{Ar}^+$  laser with 10 mW power.

PMMA opal and  $\text{SnS}_2$  inverted opal samples were studied to compare the PBG effect upon the emission.

PMMA based opal films were doped with Coumarin dye molecules and  $\text{SnS}_2$  inverted opal films were loaded in a similar way with Perylene, by infilling the dye solution in the voids of the opal and inverted opal samples, respectively. After evaporation of the solvent the dye molecules remain attached to the inner surfaces of the voids. Laser dyes were chosen as

emitting species because of their flexibility and relative ease of handling. To match the emission spectrum of the embedded dye with the PBG, different dyes were chosen for PMMA opal and the SnS<sub>2</sub> replica, so a direct comparison can not be given. The Perylene dye was chosen for the SnS<sub>2</sub> replica because of its stability against degradation in the laser beam, although the spectrum appears to need a more elaborated analysis.

PL spectra of dye-doped PMMA PhCs clearly show a partial suppression of the dye radiation intensity in these crystals for certain frequency ranges in the direction of observation [116, 120]. The Bragg stop-band is in fact a partial PBG and therefore the emission is spatially redistributed, leading to an anisotropic emission pattern.

Remarkably, the depth of the stop-band in the PL is less than 50%, whereas the dip in the transmission spectrum of the same sample often is about two orders of magnitude (figure 7.2).

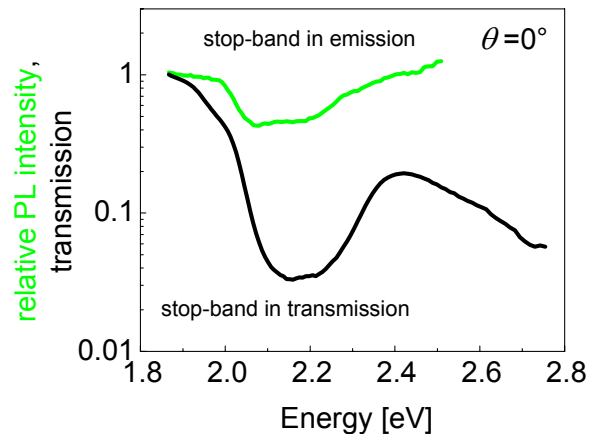


**Figure 7.2:** Relative PL and transmission spectra from an inverted SnS<sub>2</sub> thin film sample doped with Perylene. The magnitude of the transmission dip exceeds the minimum in the PL spectrum by one order of magnitude.

The relative spectra shown in figure 7.3 were obtained by collecting the PL spectra as well as reference spectra from unstructured samples of the same material and dividing the spectra by this reference spectrum to get the relative intensities. The unstructured reference samples were obtained by deliberate destruction of a dye doped PMMA PhC with an organic solvent. This way a an unstructured, dye doped PMMA film was obtained.

It appears that the emission from the near-surface region leaves the PBG structure unaffected and, additionally, that defects produce leakage modes within the PBG, thus allowing part of the emission to escape unaffected from the PhC.

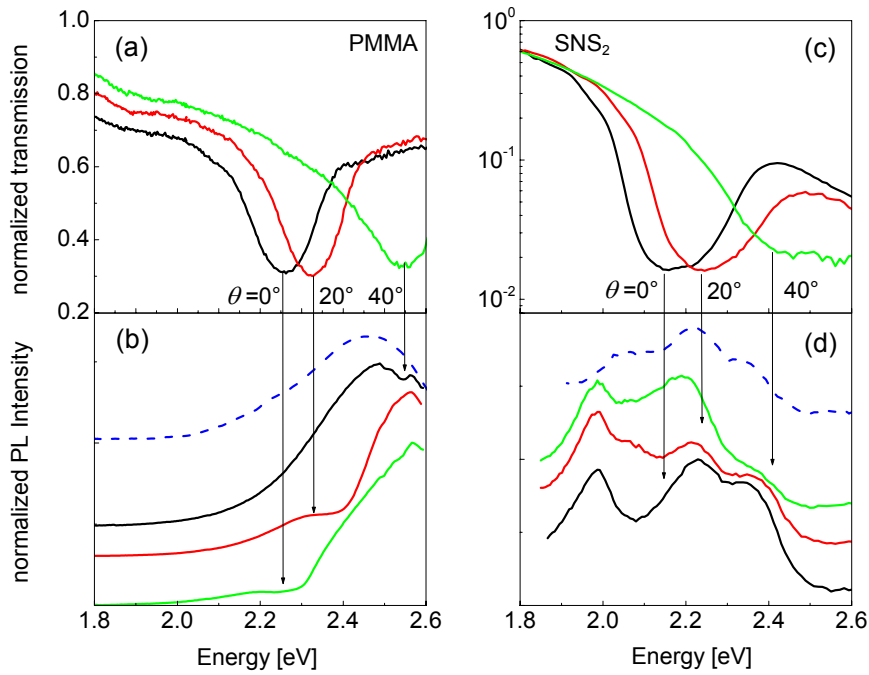


**Figure 7.3:** Photoluminescence of a PMMA PhC (a,b) and an inverted  $\text{SnS}_2$  film (c,d) collected at incident angles of  $0^\circ$ ,  $20^\circ$  and  $40^\circ$  compared to transmission spectra at the same angles. The PL spectra of the reference samples are shown by dashed blue lines. The central frequency of the stop band at the angle of the emission collection is indicated by arrows. Curves in panels (b) and (d) are shifted vertically for clarity.

Both, PMMA based opals and their  $\text{SnS}_2$  replicas exhibit a similar spectral change of the suppression of the emission intensity with angle variation of the stop-band (figure 7.3).

### 7.1. Spectral redistribution of the emission intensity

Figure 7.4a shows the transmission spectrum of a PMMA based thin film photonic crystal infilled with Coumarin (curve 1). The transmission intensity is practically proportional to the number of modes available along the direction of detection. To compare this to the emission spectrum of the dye in free space the PL of an unstructured, dye loaded, film is also plotted (curve 2).

A reduction of the emission intensity in the spectral range of the stop-band due to the decrease of the density of photonic states was observed. The crucial question here is whether this suppression is caused by the change of the emission probability or it is a mere filtering of the emission propagated in a direction of the observation ( $[111]$  for  $\theta=0^\circ$ ). To answer this

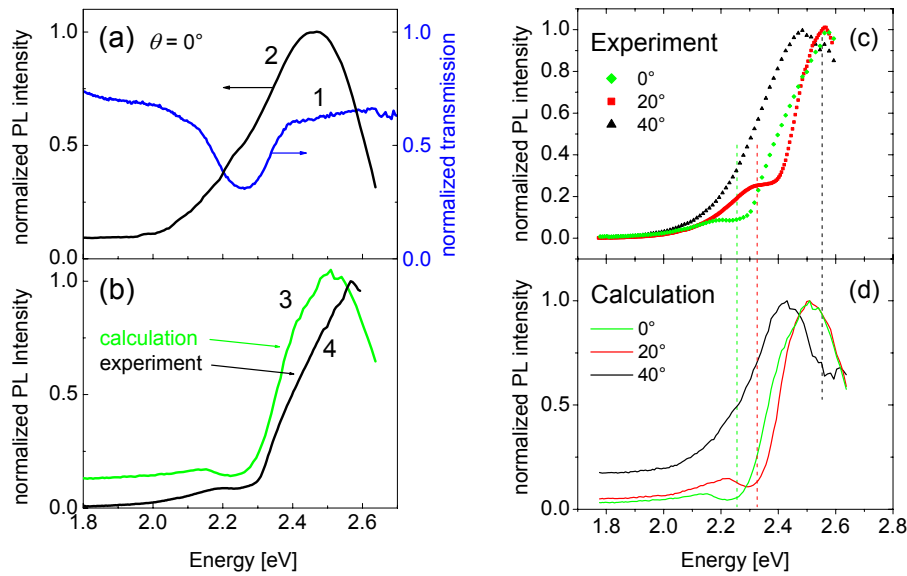


**Figure 7.4:** Reconstruction of the photoluminescence spectra of a Coumarin doped PMMA photonic crystal from the reference spectrum of an unstructured film (a, curve 2) and the transmission spectrum of the sample (a, curve 1). The experimental data (b, curve 4) are compared to the calculated spectrum for  $\theta = 0^\circ$  (b, curve 3). The same comparison is done in panels (c) – experimental data and (d) calculated spectra for different angles of detection. The vertical lines indicate the positions of the PBGs. The experimental and reconstructed spectra are in qualitative agreement.

question the transmission spectrum and the reference spectrum are multiplied point by point in order to simulate the effect of the PBG on the spectrum of the light source.

This calculated PL spectrum is plotted in figure 7.4b (curve 3) together with the experimental PL curve (curve 4). A clear similarity of experimental and simulated spectra at  $\theta = 0^\circ$  as well as at other angles (see figure 7.4c/d) leads to the conclusion that changes in the spontaneous emission rate are too small to have an impact on the appearance of the PL spectrum. In other words, there is no feedback between emission and emitter, thus only a simple band-pass filtering of the emitted radiation by the superimposed stop-band can be observed [94].

Compared to the free space conditions the emission rate is not modified in the Coumarin/PMMA direct photonic crystal apparently because the RIC is not high enough to localise photons in the vicinity of the emitter. Once radiated, photons propagate in the allowed directions and suffer from scattering at defects of the opal lattice. Moreover, the probability of self-interference as the result of completing the return path is not much higher than in the free space. The emission flow in such photonic crystals is redistributed over the angle but the spontaneous emission rate is not affected. This conclusions agree well with calculations of the profile of the density of photonic states (pDOS) in bare opals [29].

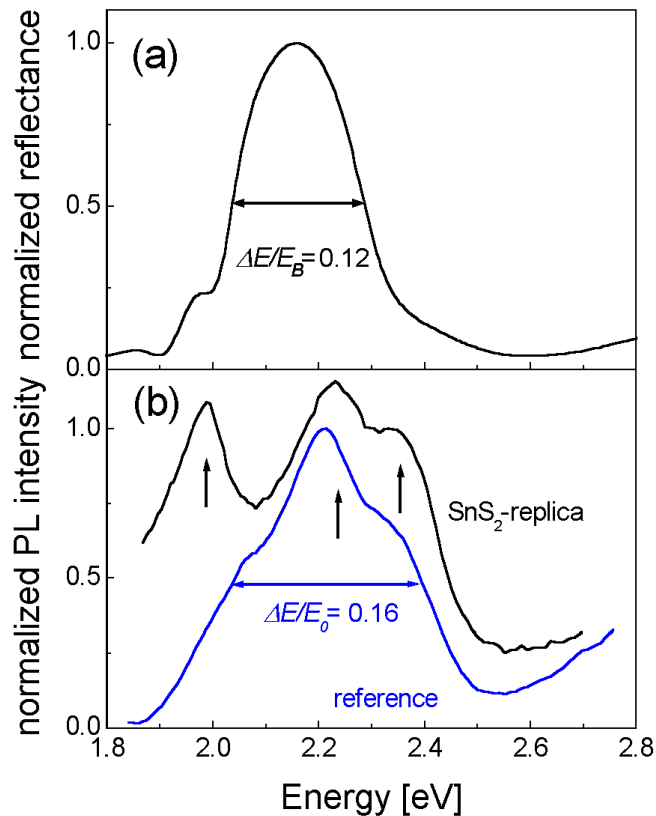


**Figure 7.5:** Reflectance spectrum of a Perylene doped  $\text{SnS}_2$  thin film PhC at  $\theta = 5^\circ$  (a). PL spectra of a  $\text{SnS}_2$  reference film (blue line) and of the PhC (black line) at  $\theta = 0^\circ$  (b). The intrinsic emission bands of the Perylene dye are indicated by arrows. The curves are vertically offset for better readability. Note that the Bragg resonance (a) covers almost the whole emission band of the Perylene dye (b).

To increase the rate of photon localization and approach the onset of the “dressed” state of an emitter photonic crystals of higher RIC are needed, where the gap in the pDOS is more pronounced. For this purpose a  $\text{SnS}_2$  inverted photonic crystal doped with Perylene was examined. If the PL spectrum for these samples is calculated from the transmission spectrum and the reference spectrum by a similar procedure as described in the previous paragraph, a different result is obtained: The product of the reference emission and opal transmission spectra would be entirely dominated by the minimum in the pDOS if the transmission spectrum was applied in its full depth (cf. figure 7.6). This indicates that a more sophisticated model is needed to explain the spectra.

First a more detailed analysis of the emission spectrum of Perylene from an unstructured reference film compared to the PhCs emission is necessary to get an idea of the emission

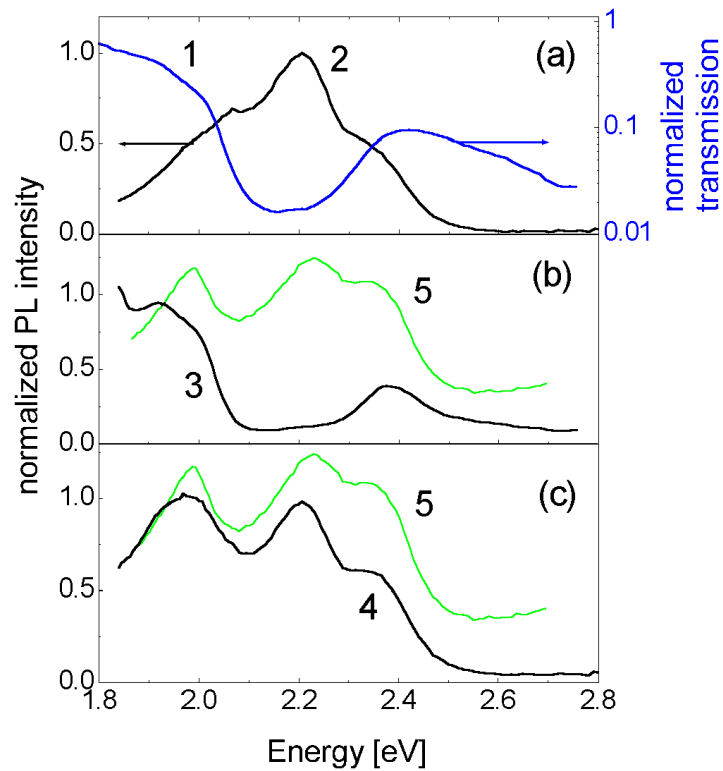


**Figure 7.6:** Reconstruction of the PL spectrum for a Perylene/SnS<sub>2</sub> replica. Reference PL spectrum (2) and raw transmission spectrum of the composite (1) (a). Reconstructed PL spectra for  $\theta = 0^\circ$  (3) in comparison with experimental PL spectra (5) (b). Reconstruction (4) with a 10 times reduced depth of the transmission minimum (c).

properties of the Perylene dye molecule in an SnS<sub>2</sub> environment. The reflectance spectrum of a Perylene/SnS<sub>2</sub> opal-replica shows, as expected, a Bragg resonance, which represents the stop-band in this photonic crystal (figure 7.5a). The stop-band in [111] direction overlaps completely with the emission band of the Perylene dye in an unstructured reference sample (figure 7.5b), but its 0.25 eV FWHM is less than the FWHM of 0.36 eV in the emission spectrum.

The PL spectrum is composed of two main bands centred at 2.21 and 2.36 eV and a weak shoulder at 2.05 eV, each band representing the transitions between different electronic bands of dye molecules on SnS<sub>2</sub> surface. Since the stop-band is shifted to higher energies for increasing observation angles  $\theta$ , it passes over the whole spectral range of the Perylene emission. The PL spectrum of Perylene embedded in the SnS<sub>2</sub> opaline film differs significantly from that of reference, though the dye concentrations used for the SnS<sub>2</sub> PC and the reference sample were the same (figure 7.5b). The observed difference in the shape of PL

spectra is accounted for by the presence of the PBG. Particularly, the interference of the emission with the band gap leads to the appearance of the 1.98 eV band and to the enhancement of the 2.37 eV band of Perylene/SnS<sub>2</sub> PhC at  $\theta = 0^\circ$ .

In order to convert the reference Perylene emission spectrum into that observed in the SnS<sub>2</sub> replica, the reference PL spectrum was multiplied by the transmission spectrum of the PhC – similar to the process described for PMMA opal.

As mentioned, if the transmission spectrum is used in its full depth, the minimum dominates the reconstructed PL spectrum (figure 7.6 curve 3). To fit the relative intensities of emission peaks in the experimental and reconstructed PL spectra, the depth of the transmission minimum was reduced by  $\approx 10$  times. Remarkably, this simple approach allows to reproduce the complicated PL spectrum satisfactorily (figure 7.6, curve 4). This reflects, apparently, the fact that the emission from the sample side facing the detector contributes significantly in the measured signal.

Note, that bleaching of the dye in the volume near the surface, as suggested in Ref. [114] is not applicable in for thin opal films. An adequate fitting was also achieved for  $\theta = 20^\circ$  (see figure 7.7). However, the reconstructed spectra at higher angles reproduce only the central band, underestimating the 1.98 eV emission band.

Two factors determine the emission from a PC environment namely the pDOS and the diffraction resonance. The pDOS is an integral characteristic of the PBG structure, whereas the frequency of the diffraction resonance changes with the observation angle. The lowest frequency pDOS minimum is centred at the Bragg frequency. For *fcc* opal structures this pDOS minimum corresponds to an incomplete gap due to symmetry considerations. However, it certainly becomes deeper and wider with increasing RIC since the stop band covers an increasingly larger fraction of the *k*-space. Thus, the angle insensitivity of the 1.98 eV PL band can be related to the pDOS spectrum of SnS<sub>2</sub> inverted opal.

Alternatively, the spectral redistribution of the emission intensity occurs with varying the angle of observation due to the angular dispersion of the stop-band. This is effectively the band-pass filtering of the emission intensity due to the suppression of the electromagnetic wave propagation within the stop band.

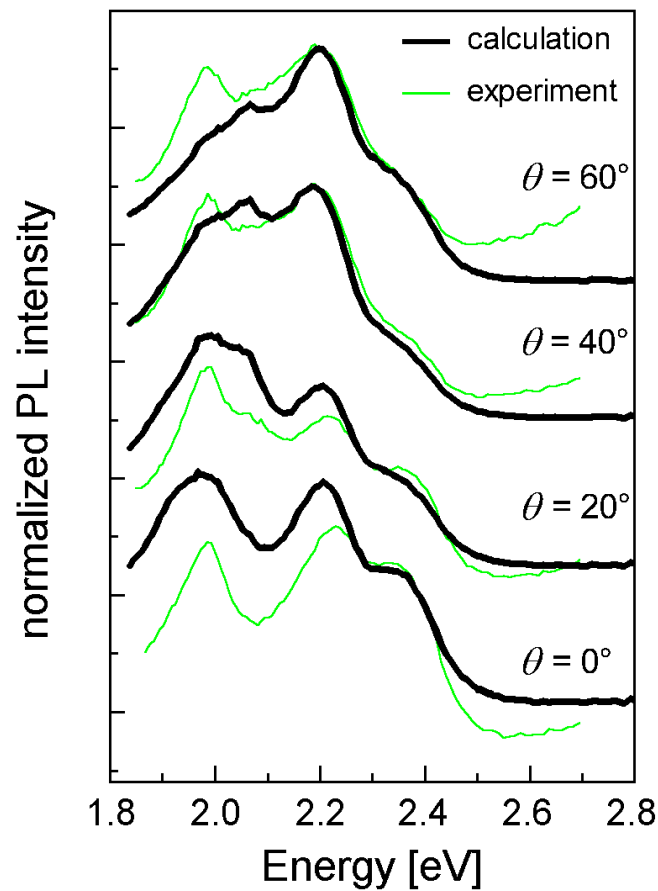


**Figure 7.7:** Reconstructed PL spectra at different observation angles (thick lines) in comparison with experimental PL spectra (thin green lines). The agreement of the two curves is surprisingly good for small angles, taking the simple model into consideration.

Since angle resolved measurements were performed, the PL intensity is averaged over a very limited solid angle around the detection direction defined by the angle  $\theta$ . To reveal the filtering effect due to the stop-band, the relative PL intensity was obtained by dividing the PL spectra of the Perylene/SnS<sub>2</sub>-replica by its reference spectrum (cf. figure 7.5b). The result is plotted in figure 7.8. The emission bands are sufficiently narrower than the FWHM of the stop-band, e.g. 0.13, 0.20 and 0.25 eV apply for the 2.38 and 2.22 eV emission bands and the stop-band, respectively. Thus the emission bands could not be resolved in the relative PL intensity spectrum and angular changes in this spectrum appear as a shift of the centre of mass of the broad minimum towards higher frequencies with increasing angle  $\theta$ . A similar behaviour to the transmission minimum (figure 7.8a).

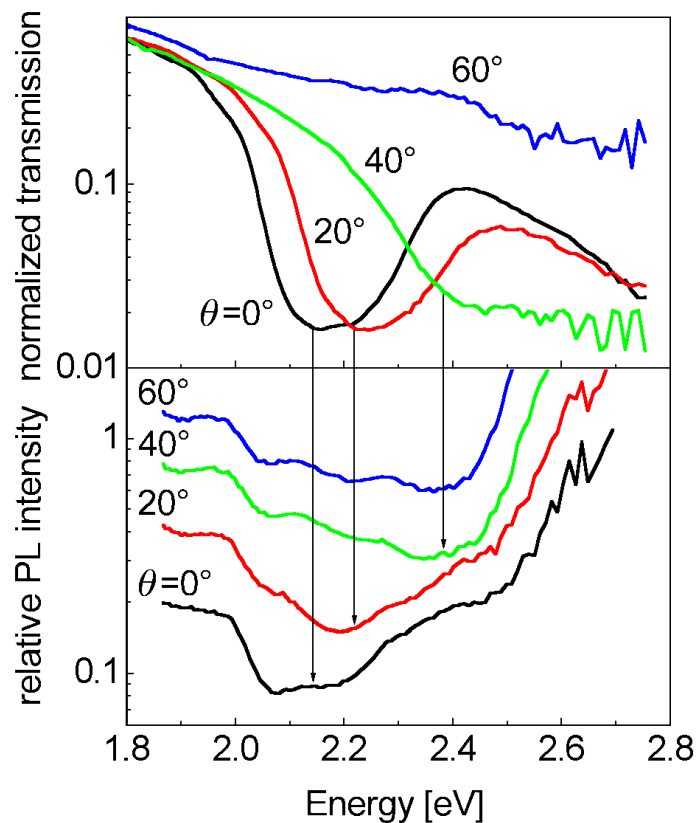


**Figure 7.8:** Transmission spectra at different angles of observation  $\theta$  (a). Relative PL spectra at the same angles (b). Arrows indicate the corresponding positions of the PBGs.

Consistently, the 1.98 eV band, which lies outside the PBG frequency range, shows no dependence upon the angle. Correspondingly, PL spectra contain both angular dependent and independent contributions. This feature is the phenomenon that distinguishes the emission from high RI contrast opal replica from that of low RI contrast PCs, where only the filtering was observed.

The obtained spectral redistribution is in agreement with theoretical calculations made for Bragg gap in high RI contrast PhCs [121]. Thus, whereas a Coumarin/PMMA based opal seems to act mainly as a band pass filter, integrated with the light source, the emission of the Perylene/SnS<sub>2</sub> sample acquires distinct features related both to the minimum in the pDOS and to an enhancement of the spontaneous emission rate.

## 7.2. Changes of the emission rate

It is expected that a photon radiated with a frequency in a PBG frequency range finds itself localised to some degree in the vicinity of the emitter. The anticipated effect is two-fold:

- i. the emission rate is reduced compared to the free space emission due to the minimum in pDOS if the frequency of a radiative electronic transition falls within the PBG,
- ii. the probability of emission is enhanced if the transition occurs at the stop-band edge [122] where the pDOS is higher.

If a broad emission band overlaps with the PBG, the spontaneous emission at different parts of the spectrum will be either amplified or suppressed. Correspondingly, the PL spectrum will experience a distortion which increases the number of photons emitted in accord with the spectral distribution of the emission probability.

Experimentally, the emission intensity follows the increase of the excitation power. The distortion of the emission spectrum was measured as the ratio between PL spectra obtained at different excitation power levels. The ratio spectra – recorded as a function of observation angle  $\theta$  – reveal the spectral profiles of this distortion. Obviously, this profile depends on the number of factors beyond the PBG. In free space it accounts for spectra of the matrix element and the density of electronic states available, for a saturation of transition and two photon absorption, among others but it also reflects the number of photon modes in a given direction. Thus, if the ratio profile correlates with the stop-band spectral position this is interpreted as an indication of a change in the spontaneous emission.

In order to minimise the disturbing effects, the pDOS was set constant by choosing a fixed point on the sample and observation angle and changing only the excitation power. To prevent unnecessary complications the excitation power was chosen low to avoid dye degradation effects. Assuming, that the emission rate is not a function of the emission power i.e. no saturation level reached, the ratio should remain frequency independent.

However, experimentally found was an uneven spectrum, amplitude of whose features correlates with the position of the PBG. Intensity ratios of the PL spectra were calculated for excitation powers of 0.5, 1, 5 and 15 mW, giving power ratios of 30, 15 and 3 for the photonic crystal and 0.02, 0.2 and 2.0 mW for the unstructured SnS<sub>2</sub> reference film, as indicated in figure 7.9.

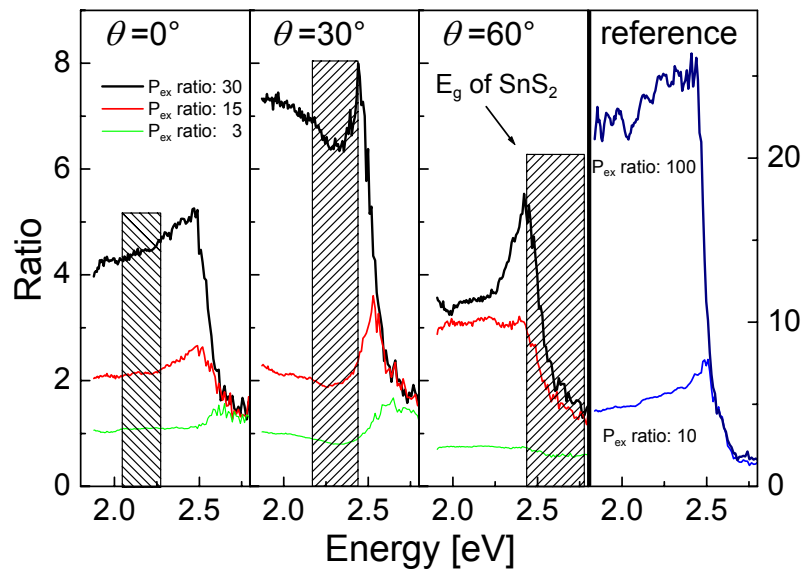


**Figure 7.9:** Enhancement of the spontaneous emission of a Perylene dye at the edges of the stop-band in Perylene doped  $\text{SnS}_2$  inverted opal for power increments of 3, 15 and 30 ( $P_{\text{ex}}$  ratio). Shaded regions show the position of the stop-band at the different angles of observation. The electronic gap of  $\text{SnS}_2$  ( $E_g$ ) at 2.4 eV is indicated by the arrow. The ratio spectra for an unstructured reference film (power ratio 10 and 100) is shown in the rightmost panel.

Ratio values obtained at different angles were corrected to the optical path, which increases like  $1/\cos\theta$  with the increase of the angle  $\theta$  in a back window experiment. All ratios demonstrate a peak at  $\approx 2.5$  eV, which is the onset of the Perylene emission band. As the comparison with the similar ratios obtained for a reference sample shows (figure 7.9, rightmost panel), the 2.5 eV peak originates from the electronic energy structure of the Perylene. For lower frequencies ratios descend slowly in the reference sample and in  $\text{SnS}_2$  opal, when the ratio peak is far from the stop-band ( $\theta=0^\circ$ ). In contrast, the 2.5 eV peak appears enhanced when it is near the stop-band edge of the  $\text{SnS}_2$  opal (panels for  $\theta=30^\circ$  and  $60^\circ$ ). Besides, ratios show a minimum at the frequency range of the stop-band, typical profile is shown in the panel of  $\theta=30^\circ$ . No absolute enhancement of the emission was observed. The ratio magnitudes (figure 7.9) are less than the excitation intensity increment, apparently, due to effective non-radiative relaxation processes.

However, the plotted ratios represent a pessimistic estimate of the emission rate profile because of the strong contribution from the surface emission. On the other hand, the general behaviour of the ratio correlates with the expectation of the emission rate difference between the centre and the edge of the PBG. This conclusion is supported by the idea, that the suppression of the emission intensity within the stop-band (cf. figure 7.6) will not lead to the

observed profiling the ratio spectra because the filtering function, being linearly superimposed on the emission function, does not depend upon the emission intensity.

An alternative hypothesis, which explains the angle-dependent enhancement/suppression of the radiation from a PC, is drawn from the frequency vs. angle dependence of the minimum in the ratio spectrum. Within this approach the suppression is explained as the result of the filtering of the emission intensity by the stop-band and the enhancement of the intensity at the stop-band edge is due to expelling the radiation from the stop-band frequency range. The necessary condition for the observation of this effect is a permanent pumping. Under this condition the balance between radiative and non-radiative channels of the energy relaxation appears shifted in favour of the non-radiative relaxation within the stop-band due to the presence of the PBG. However, this model cannot explain why the enhancement is observed only in the vicinity of the electronic transition in the Perylene molecule.

Concluding, the ratio spectra can be interpreted as an evidence for feedback between the radiation and the dye molecule provided by the SnS<sub>2</sub> photonic crystal.

### 7.3. Directionality of emission in SnS<sub>2</sub> replicas

Anisotropy is a very prominent feature of the emission from an incomplete PhC. The Frequency of the incomplete PBG changes with the direction of observation thus it shows a strongly anisotropic behaviour. The emission spectrum of emitters embedded inside of a PhC can also be expected to vary with changing observation angle.

The sample under study was a SnS<sub>2</sub> replica impregnated with Perylene, similar to the sample used for reflectance measurements. The laser-dye was infilled into the crystal by immersing it into a Perylene / Chloroform solution of 2.5 mg/ml. The emission band of the laser-dye overlaps with the PBG for this sample. It is assumed that the laser-dye uniformly covers the internal surfaces of the replica. Since the semiconductor itself is porous (cf. chapter 6.3) it can be assumed that it is distributed over the whole 26 vol-% of space that is occupied by the SnS<sub>2</sub>.

The PL was excited by the 351 nm line of the Ar<sup>+</sup> ion laser using the back window configuration (cf. figure 4.5). The solid angle from which the emission was collected was confined to a 5° cone. The detection angle  $\theta$  was measured with respect to the surface normal ([111] direction).

The emission from an opal-integrated light source is made up of two components – the ballistic component, the photons of which leave the opal without scattering, and the diffuse component composed of photons, which experience scattering. The latter component becomes essential, if the path-length of photons within the PhC exceeds the mean free path (MFP). The MFP in the opal decreases from infinity for an ideally perfect lattice, to  $l^* = 7-15 \mu\text{m}$  in the

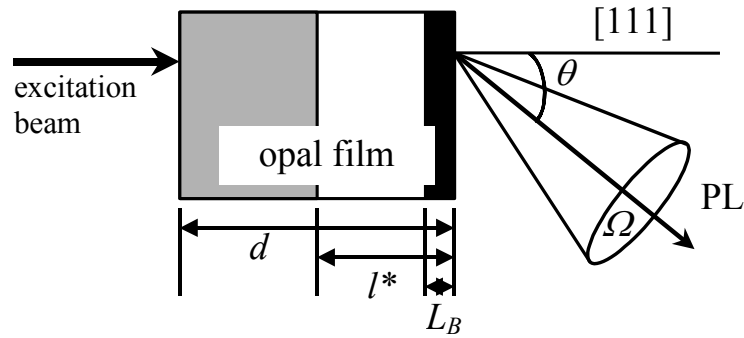


**Figure 7.10:** Layout of the PL set up with characteristic length scales and quantities of the experiment.  $\theta$  – angle of detection,  $\Omega$  – solid angle of the light collection,  $L_B$  - Bragg attenuation length,  $l^*$  - mean free path of photons in opal,  $d$ - film thickness

current research quality opals [123]. Correspondingly, the emission radiated inside an opal is doomed to be converted into the diffuse component. This is the reason why the minimum in the emission spectrum of the PhC-embedded light source is limited to approximately 50% or more of the emission intensity outside the PBG, depending on the sample quality.

The necessary condition to observe the minimum in the emission spectrum is  $L_B < l^*$ , where  $L_B$  is the Bragg attenuation length. It corresponds to the length over which the emission intensity drops by a factor of  $e^{-1}$  because of Bragg reflections. It is deduced from  $\Delta E / E_B = 2d / \pi L_B$ , where  $d = 0.816D$  is the (111) inter-plane distance of beads with diameter  $D$  and the term  $\Delta E / E_B$  gives the full width at half Bragg minimum in transmission ( $\approx 12\%$  for the  $\text{SnS}_2$  sample under study). The derived value of  $L_B = 1 \mu\text{m}$  for  $\text{SnS}_2$  opal replicas suggests a 150 times decrease of the emission intensity of the light source at the Bragg resonance frequency, if it is located  $5 \mu\text{m}$  away from the opal surface. The observed small decrease of the PL intensity indicates that most of the detected luminescence is coupled to defect modes or originates from the near-surface volume and thus remains unaffected by the PBG.

It is instructive to describe the spatial anisotropy of EM wave propagation in opals using the concept of the Bragg cone, which is defined as the angle interval covered by the first band gap at a given energy or the corresponding interval of wavevectors in the  $k$ -space. The circles in the momentum space or corresponding holes in the real space defined on the wave front in figure 7.11 are examples of these Bragg windows. If the aperture of the collecting optics is less than the angular width of the Bragg cone, then there will be no ballistic eigenmodes of the opal propagating linearly along the PBG direction. The Bragg cone changes its direction and width with frequency, which allows comparison of the radiative relaxation probability inside and outside the band gap at the same frequency.

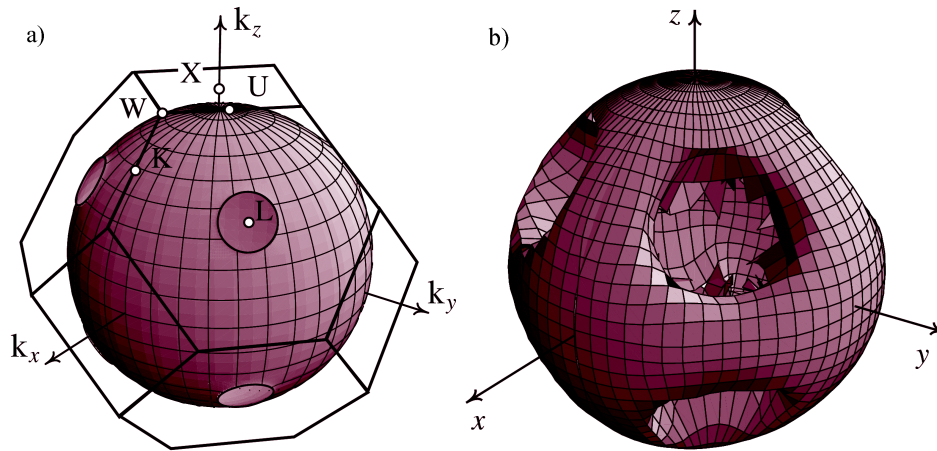


**Figure 7.11:** An iso-energy surface of a 3-dimensional, opal PhC for a frequency within the Bragg band gap calculated by the PWM (a). The wave front of an isotropic point source inside a PhC in the real space (b).

To get a qualitative impression of the expected angular distribution of the emitted energy it is instructive to analyse the directionality pattern in connection with the PBG diagram. To do this the intersection of the 3D band structure with a plane corresponding to the energy of interest can be plotted to obtain the iso-energy surfaces (IES) in specific directions. From their shape the principle angular distribution of emission energy can be read.

The photonic band structure of a close-packed *fcc* lattice of air balls in  $\text{SnS}_2$  for all  $k$ -directions in the  $\text{LUX}\Gamma$  plane were calculated using the method and software package of Ref. [26]. From these results the IES were obtained that are shown in figure 7.12, for energies below, in and above the PBG.

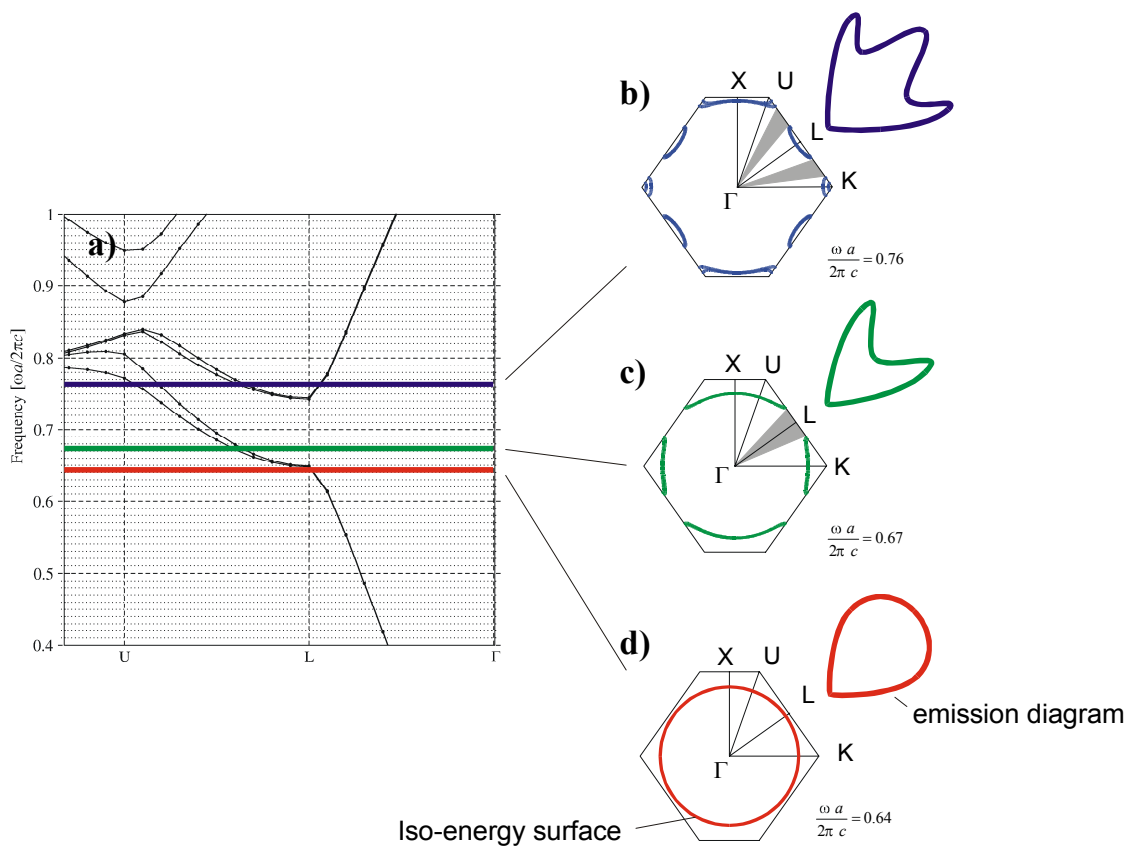


**Figure 7.12:** Iso-energy surfaces and resulting emission diagrams. From the band structure diagram (a) Iso-energy surfaces can be generated (b-d). Their shape corresponds to the angular distribution of emission from PhCs with embedded laser-dyes. The grey shaded regions (b-d) indicate the positions of the PBG at different energies.

If the energy is below the pseudo-gap the IES, has circular shape, as for isotropic media (figure 7.12b). However, for the energy range of the Bragg stop-band, the form of the IES is strongly different from spherical mostly near the direction of the partial gaps (cf. sect. 2.3.3). When the frequency is within the pseudo-gap, then optical modes with corresponding wavevectors are forbidden and the surface of constant energy becomes multiple-connected (figure 7.12c) For energies above the upper band edge the structure changes further since the projection of the 3<sup>rd</sup> band becomes visible in L-direction (figure 7.12c).

In the directions of the PBG the emission is suppressed. They are detected as minima in experimental directionality diagrams leading to the qualitative emission pattern indicated in figure 7.12c. The gaps in the IES-diagram correspond to the forbidden Bragg cones in real space

The experimentally obtained directionality diagrams are plotted in figure 7.13 together with the calculated band structure diagram. The measured energies cover the whole pseudo-gap as indicated. The radiation pattern of a Lambert emitter [37] is also shown for comparison.

The experimental data are in a good agreement with the topology of calculated dispersion surfaces. Below the PBG the measured emission intensity shows an angular distribution that is close to that of an emitter in free space (Lambert law:  $\cos\theta$ ), indicated by the red line in the plots. As soon as the [111] pseudo-gap is entered from the low energy side a pronounced dip in the emission spectrum in L direction ( $\theta = 0^\circ$ ) is observed. Additionally enhanced emission intensity is observed at both sides of the stop band ( $\theta \approx \pm 30^\circ$ ). As the energy increases the central peak ( $\theta = 0^\circ$ ) re-appears and the separation of the side-peaks increases to ( $\theta \approx \pm 40^\circ$ ) while their magnitude decreases. For energies above the upper band edge the emission pattern is elongated in [111] direction.

It can be shown that if an effective non-radiative recombination channel exists in the PhC the PL intensity is proportional to the spontaneous emission rate [124]. Thus the emission pattern of the dye in the PhC environment reflects a suppression of the spontaneous emission rate in the direction of the PBG and an enhancement in other directions.

Detailed theoretical simulations of the emission pattern of dye molecules in opal replicas can be found in Ref. [39].

An added complexity of the emission directionality comes from self-focusing of the light propagating in opals. This effect originates from the variable curvature of IES occurring close to gap regions. These curves contain points where the curvature changes sign. Bearing in mind that in a PhC the energy flows along the direction of the group velocity vectors, which are always oriented along the normal to the constant energy surface, the concentration of the emission intensity along directions defined by group velocity vectors is expected to be pinned to these points as sketched in sect. 2.3.3.

If this effect is taken into account as well as the above mentioned contribution from diffuse scattered photons that contribute to the measured intensity, the experimental data show reasonable agreement with a theoretical model developed by D.N. Chigrin. For a detailed analysis see Ref. [39].

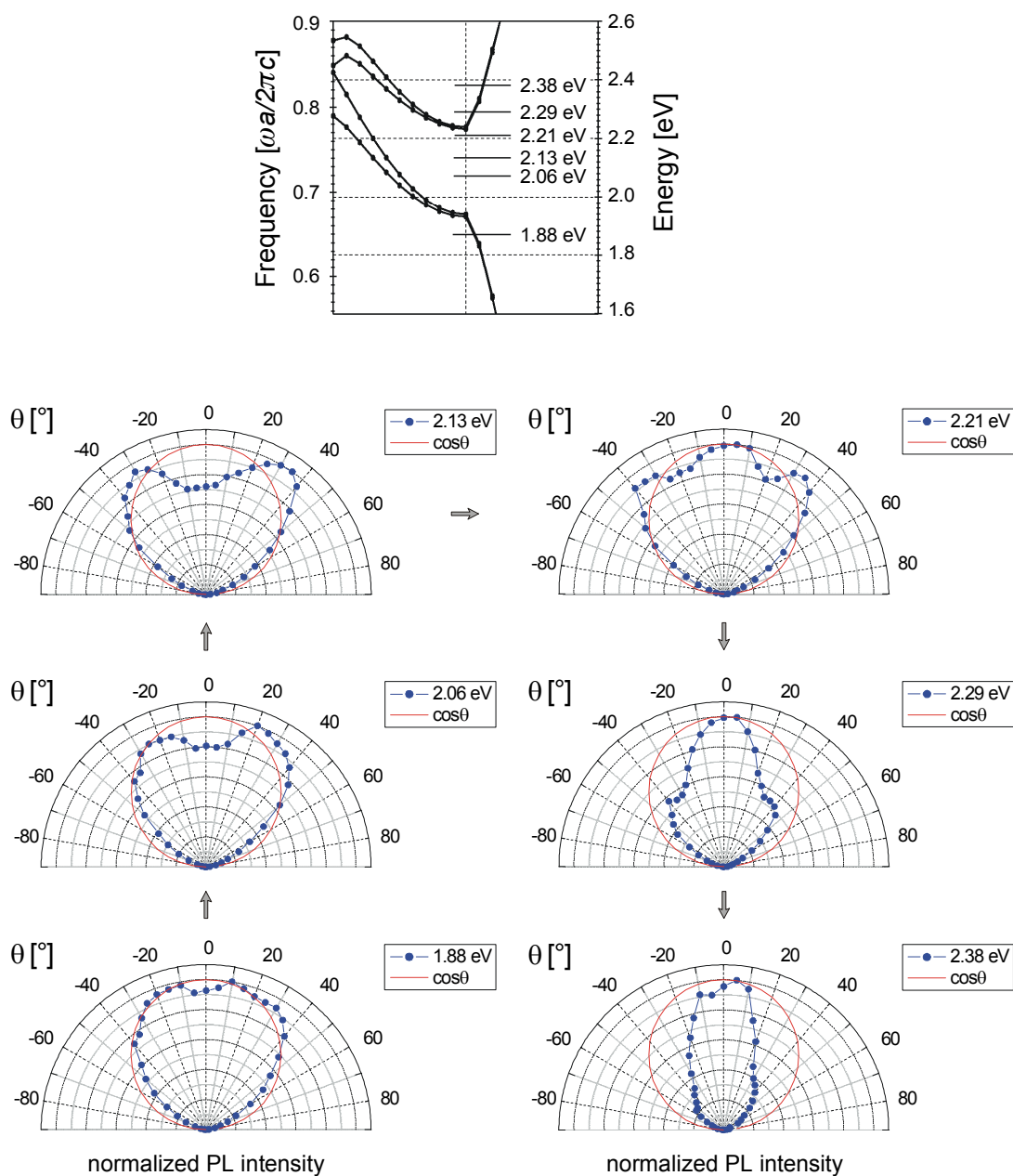


**Figure 7.13:** Directionality diagrams obtained by angle resolved PL measurements. The experimental data (blue dots) were taken at energies crossing the PBG region as indicated in the band structure diagram. The intensity distribution of a Lambert emitter is plotted for comparison (red line)

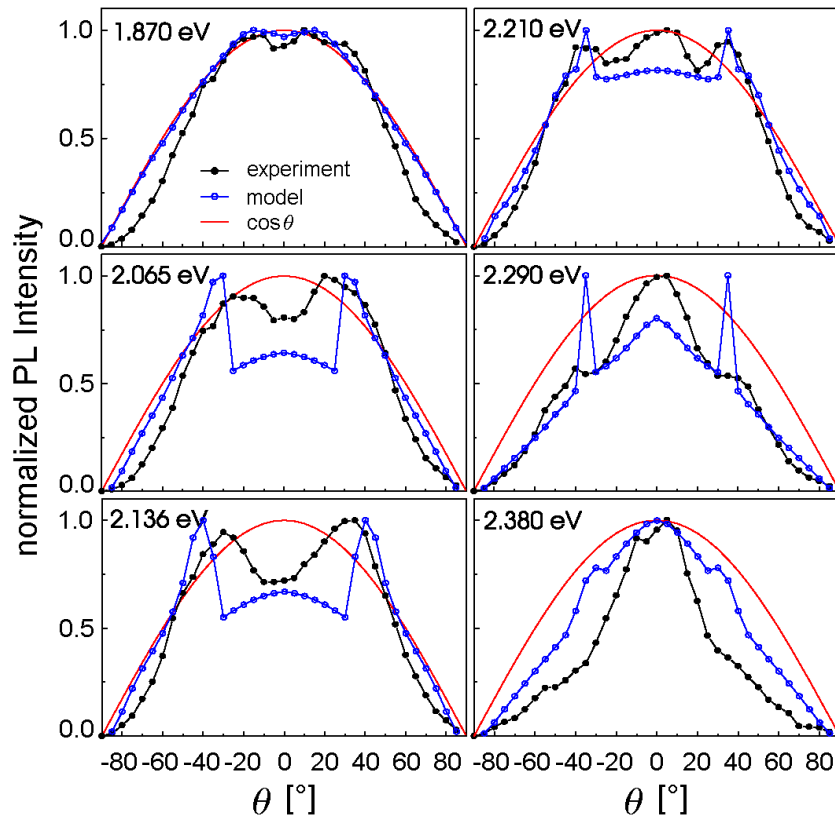


**Figure 7.14:** Experimental data (black dots) and theoretical model of the angular distribution of the PL from a dye-doped opal PhC replica (blue dots). The contribution of ballistic photons and a diffuse background was taken into account in the calculations.

Both, experimental data and modelled PL intensities are shown in figure 7.14. The enhancement of the emission pattern in certain directions at the edges of the PBG can be explained by photon focussing induced by the curvature of the IES. This is best seen in the 2.290 eV curve where the model shows two sharp peaks at  $\approx \pm 35^\circ$ . They coincide with regions of vanishing curvature of the IES for this energy. The fact that they are not resolved clearly in the experimental data is attributed to the sample quality and restrictions of the model that seems to overestimate the contribution of this effect to the observed intensity.

The only moderate suppression of emission intensity in the direction of the PGB compared to a perfect crystal is attributed to the contribution of diffuse scattered photons. Due to the small MFP compared to the sample's thickness, photons generated at the rear side of the sample are diffusely scattered before they reach the detector and therefore acquire an isotropic emission pattern. Also photons generated at the front side of the sample i.e. from a layer smaller than the Bragg attenuation length are not affected strongly by the PBG and thus also contribute to

the diffuse background. Even photons generated in the middle part of the crystal can experience multiple scattering from defects in the crystalline lattice and thus contribute also to the diffuse background. By including these effects the theoretical model a good agreement with the experiment can be obtained [39], taking the complexity of the structure into account.

#### 7.4. Emission from CdTe loaded opal films

Reflectance and transmission spectra of CdTe infiltrated opal films were collected by illuminating a  $0.03\text{cm}^2$  sample area with the white light from a tungsten halogen lamp and subsequently detecting the diffracted light with a spectral resolution of 2 nm and an angular resolution of, approximately,  $2^\circ$  in the  $\theta$ - $2\theta$  configuration. To track the angular dependence, the angle of incidence was varied from  $0^\circ$  to  $70^\circ$ .

PL spectra were excited in a continuous wave regime by the 457.9 nm line of an  $\text{Ar}^+$ -laser focused on a 0.1 mm diameter spot, the excitation power was varied between 0.5 and 10 mW. PL spectra were collected within a  $\Omega = 10^\circ$  fraction of the solid angle using a similar set up as shown in figure 7.10. Angle resolved emission spectra were measured with a spectral resolution of 1.5 nm.

##### *Spectrum shaping*

In figure 7.15a,b the PL emission spectrum of CdTe opal and the corresponding transmission spectrum are shown for the direction along [111] axis. In the case of an incomplete PhC, like opal, the photonic pseudo-gap is highly anisotropic, which means that the PBG-induced suppression of light propagation can be observed only within the Bragg cone. In order to reveal the PBG-related alteration of the PL spectra, it is convenient to track the variation of the PL spectrum with the angle of detection  $\theta$  and then to compare them to the angular variation of the transmission spectrum (figure 7.15c). The conditions for an emitting dipole inside the PhC change with the dipole orientation and position in the PhC unit cell, i.e., the emission spectrum and emission rate become a function of the coupling of the dipole with eigenmodes of the PhC. Space-dependent coupling conditions are described by the local density of photonic states (pDOS) [29]. Considering a large number of randomly oriented dipoles, one can replace them with a point source, then the directional PBG-induced suppression of the emission intensity will be completely determined by the availability of PhC eigenmodes along this direction at the position of the emitter. To prove this assumption, the PL spectrum of CdTe-opal at  $\theta = 0^\circ$  has been simulated by multiplying the reference CdTe PL spectrum, which is obtained from the CdTe-opal sample at  $\theta = 70^\circ$ , and the transmission spectrum, obtained at  $\theta = 0^\circ$  (figure 7.15c, blue line). The simulated and experimental data differ from each other in that the PBG suppression is much stronger in the simulated case. There are two main reasons for this dissimilarity: the emission from nanocrystals unaffected by PBG, i.e. nanocrystals at the PhC-air interface and the diffusively scattered emission. In an

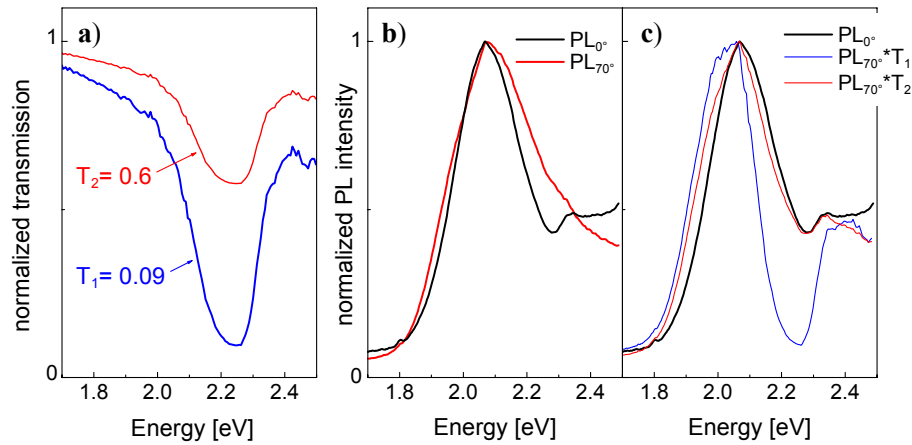


**Figure 7.15:** Transmission spectrum of CdTe-opal (blue line) at  $\theta=0^\circ$  (a). PL spectra at  $\theta=0^\circ$  (black line) and  $70^\circ$  (red line) (b). Reconstruction of PL spectrum at  $\theta=0^\circ$  obtained by multiplying the PL spectrum at  $70^\circ$  and the transmission spectrum at  $\theta=0^\circ$  as measured (panel (a), blue line) or after  $\approx 6$  times depth reduction (panel (a), red line) (c). The former reconstruction overestimates the emission suppression, whereas the latter reproduces the experimental PL spectrum at  $\theta=0^\circ$  correctly.

ideally packed opal, photons coupled to the Bloch waves traverse a PhC without scattering. Lattice defects destroy ballistic propagation leading to a diffuse scattering characterised by the photon mean free path. If the light path exceeds this value, the accidental scattering on defects leads to a mixture of ballistic and diffusively scattered photons in the detected signal. Because the  $\approx 10 \mu\text{m}$  MFP is less than the thickness of our opal films, the diffuse component is relatively strong. A better fitting can be achieved if the PBG dip in the transmission spectrum is artificially reduced by a factor of  $\approx 6$  as shown in figure 7.15a, red line. The multiplication with the reference PL spectrum leads to a much better reproduction of the experimental data (figure 7.15c, red line)

Figure 7.16 shows the angular dispersion of the Bragg band gap and the corresponding variation of the emission spectrum. Note, that due to the lattice disorder the emission dip disappears in the  $\theta=40^\circ$  spectrum. Correspondingly, no further change of the spectrum occurs along the angle increase. This is an indication of the fact, that the dip in the emission spectrum is more fragile with respect to the disorder than the dip in the transmission spectrum.

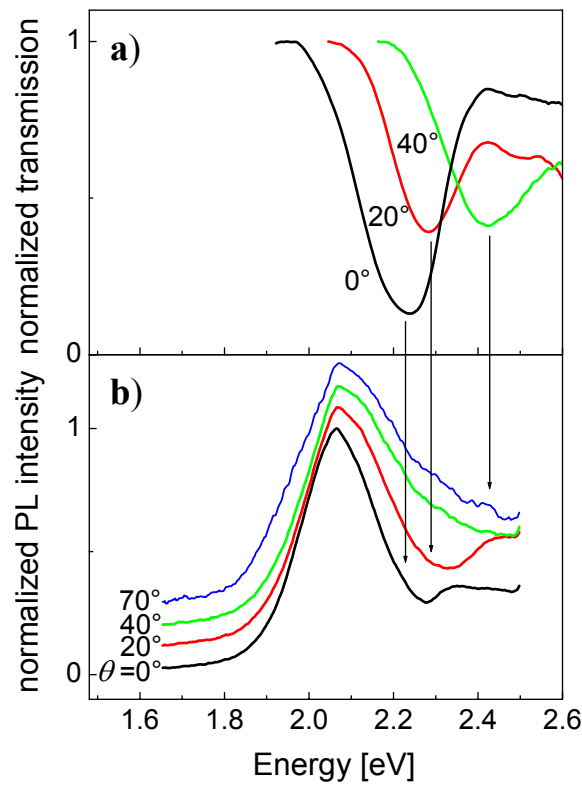


**Figure 7.16:** Transmission spectra at angles  $\theta = 0^\circ$ ,  $20^\circ$  and  $40^\circ$  (a). Emission spectra at angles  $\theta = 0^\circ$ ,  $20^\circ$ ,  $40^\circ$  and  $70^\circ$ . The curves are shifted vertically for clarity (b).

### *Emission directionality*

The conditions for spontaneous emission (SE) of a dipole change as soon as the pseudo-gap overlaps with the emission band. Due to the anisotropy of a pseudo-gap this variation occurs only in the Bragg cone. Moreover, the strong frequency dispersion of pseudo-gap leads to a frequency dependence of emission directionality diagram.

Figure 7.17 shows several directionality diagrams measured at different frequencies in the vicinity of the Bragg gap. In first approximation, the directionality at a given frequency can be explained as the superposition of the emission from a point source in a homogeneous medium and a spatial pattern of pseudo-gaps of the *fcc* lattice.

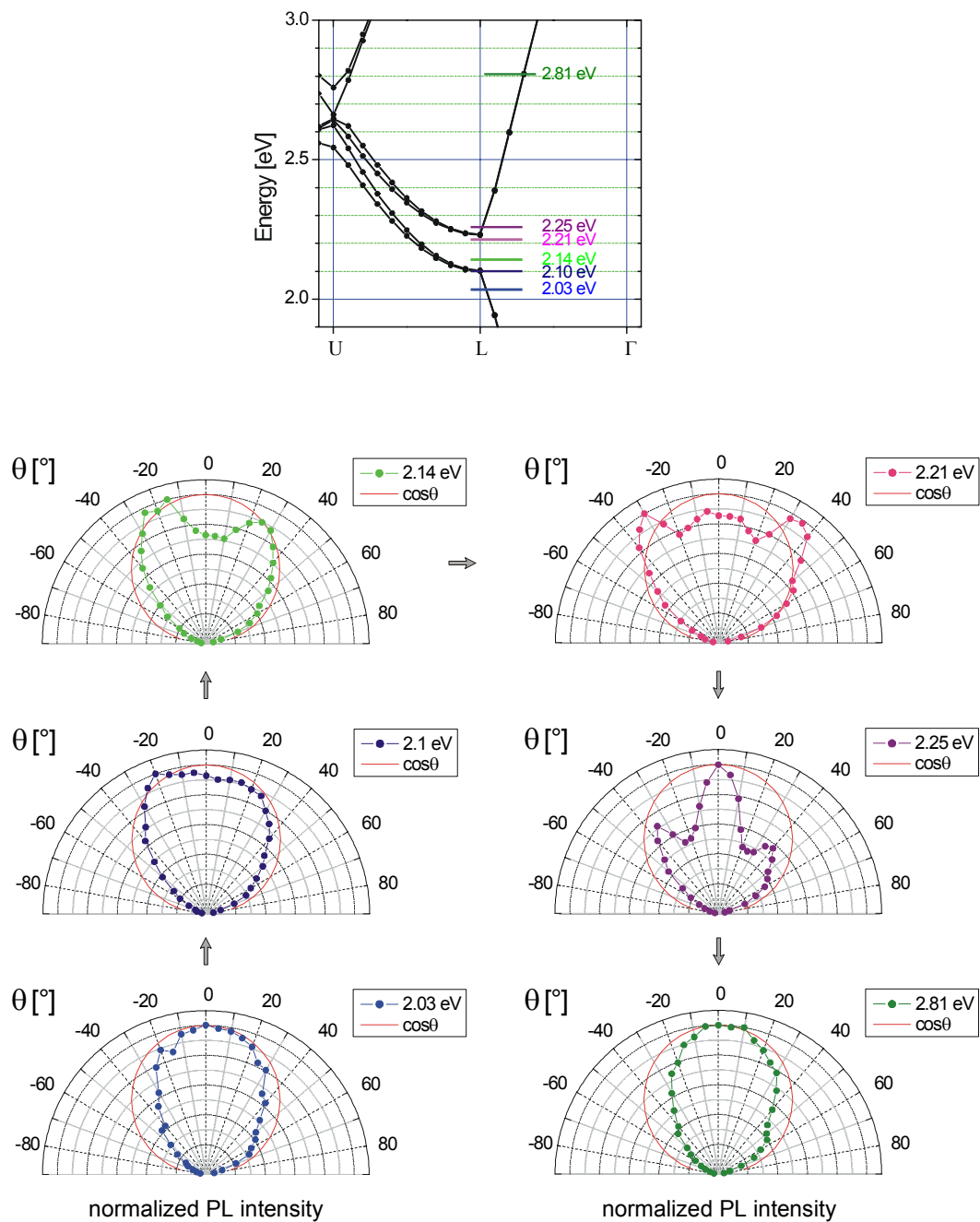


**Figure 7.17:** Directionality diagrams of the PL emission from a CdTe infiltrated opal at different energies across the PBG energy range as indicated in the band structure diagram.. The intensity distribution of a Lambert emitter is plotted as a red line in each diagram.

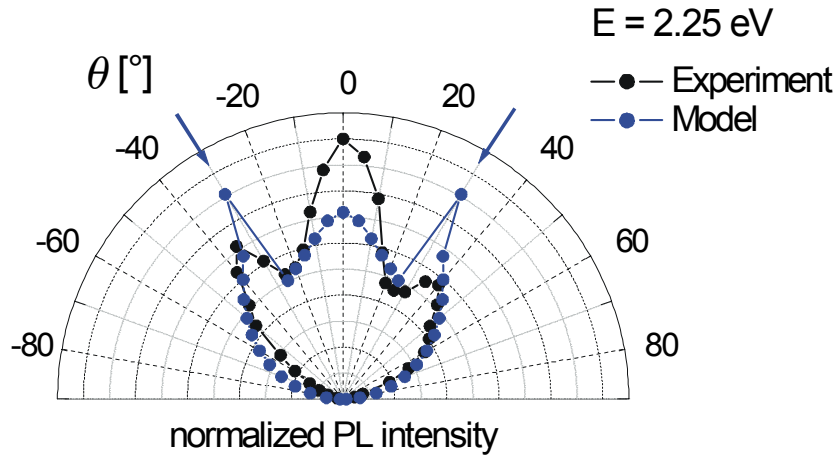


**Figure 7.18:** Comparison of simulated and experimental emission directionality diagrams at  $E = 2.25$  eV (just above the PBG). The simulation includes emission focusing along special directions in the vector diagram (indicated by arrows). To fit the experimental pattern, a diffuse scattered light has been added to the simulated pattern as a  $\cos\theta$  background, similar to the  $\text{SnS}_2$  case.

As for the  $\text{SnS}_2$  emission spectra diffuse and ballistic components have to be taken into account. The diffuse component provides the background, the intensity of which varies as  $\cos\theta$ , and the ballistic component carries the fingerprint of the pseudo-gap [39].

### Emission stimulation

A crucial question to be experimentally addressed is whether the incomplete PBG environment provides sufficiently strong feedback to an emitting dipole to change the emission rate. Time-resolved emission spectroscopy experiments have been inconclusive so far with respect to the SE rate. Apparently, the SE rate should qualitatively follow the minimum in the emission spectrum, if the reason for this minimum is the deficit of the optical modes along the diffraction resonance. This linear component of the emission rate is fully determined by the availability of optical modes at the location of the excited atom. On the other hand, if the emitted radiation influences back the emission probability of the atom as it happens in the case of the localization of the photons with PBG frequencies, this results in the variation of the emission rate. This non-linear rate depends on the actual strength of the EM field on the emitter site.

To demonstrate the non-linearity of the emission rate variation, the emission of CdTe-opal upon increasing excitation power was studied. The PL was measured at different angles  $\theta$  with respect to [111] axis of the opal under different intensities of the exciting laser beam.

The input-output characteristics  $I_{PL}(P_{ex})$ , where the emission intensity  $I_{PL}$  is plotted as a function of excitation power  $P_{ex}$ , shows a saturation-type behaviour. The double-logarithmic plot in figure 7.19a illustrates this dependency. The PL intensity is plotted over the excitation power and fitted to the rate equation:

$$I_{PL} = I_0(1 - \exp(-P/P_0)) \quad (7.1)$$

where  $I_0$  is the emission intensity in the case of saturating all available emitters at this frequency and  $P_0$  is the saturation threshold. Assuming identity of all emitters radiating with the same frequency, the saturated emission intensity is, effectively, the measure of the SE rate.

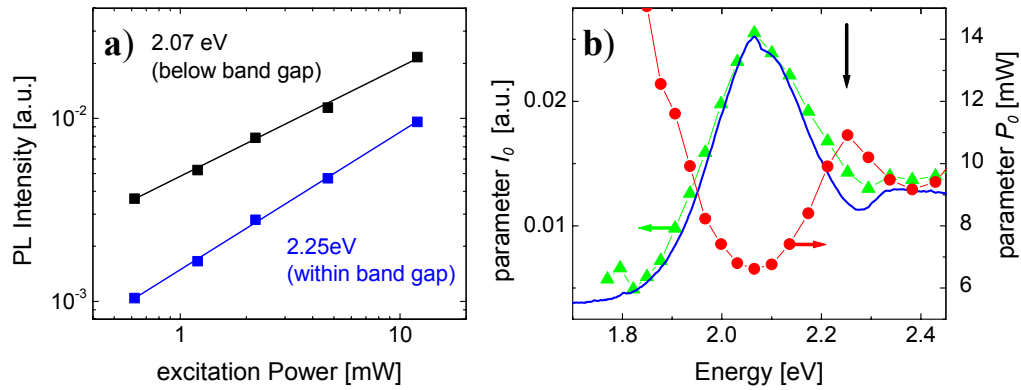


**Figure 7.19:** PL intensity as a function of excitation power in double-logarithmic coordinates (a).  $I_0$  (triangles) is the intensity pre-factor and  $P_0$  (circles) is the saturation threshold of intensity spectra taken at different energies at  $\theta = 0^\circ$ . The corresponding PL spectrum (line) is shown for reference. The vertical arrow indicates the central frequency of the directional PBG at (b).

A fit of the experimental data to the rate equation is shown in figure 7.19a for two different energies, 2.07 and 2.25 eV, which are below and inside the PBG for this sample, respectively. As it can be seen from the slope and position of the two curves the two parameters  $I_0$  and  $P_0$  change with the frequency. Therefore they were calculated by fits from similar intensity plots at energies between 1.8 and 2.5 eV and represented as a function of frequency in figure 7.19b. Remarkably, the  $I_0$ -spectrum reproduces very well the emission spectrum.

This coincidence supports our idea of representing the SE rate spectrum by the PL spectrum. In accord to a common point of view, the SE rate is higher at the PL band maximum and suppressed at the PBG. Opposite behaviour is demonstrated by the  $P_0$ -spectrum. It has a minimum at the PL band maximum and a maximum at the band gap (figure 7.19b).

This analysis was done for different angles of observation  $\theta$  to analyse the behaviour in different directions. The  $P_0$  minimum stays at the same frequency when the angle of emission detection is varied (not shown), whereas the  $P_0$  maximum shifts to higher frequencies with increasing angle (figure 7.20). Moreover, this maximum obeys the same angular dispersion as the Bragg resonance, i.e. it is directly related to the band gap. The threshold spectra at  $\theta = 40^\circ$  and  $70^\circ$  look similar in accord with the absence of the dip in the emission spectra of figure 7.16b for corresponding angles that were taken from the same sample.

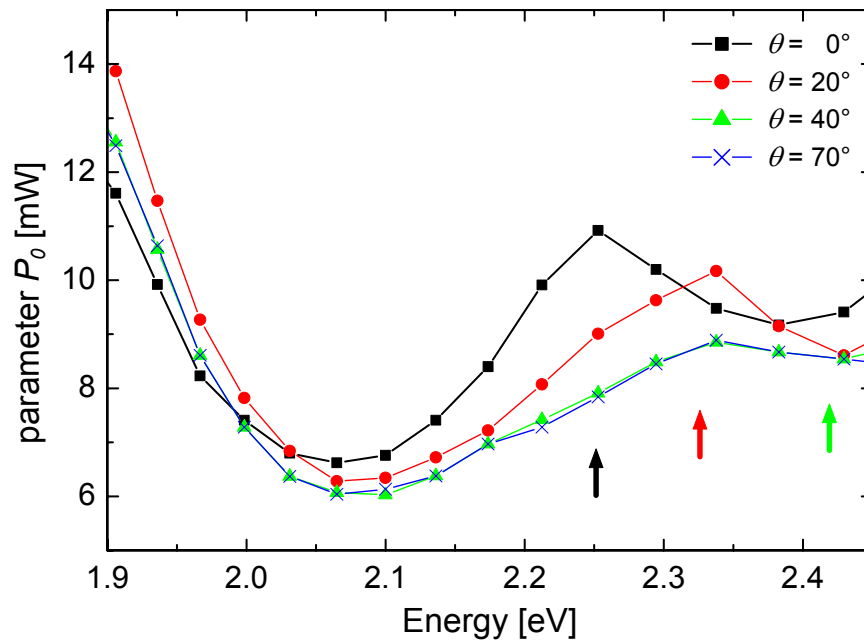


**Figure 7.20:**  $P_0$ -spectra for  $\theta = 0^\circ$ ,  $20^\circ$ ,  $40^\circ$  and  $70^\circ$ . Arrows indicate the mid-gap frequency at corresponding angles. The maxima of  $P_0$  follow the same angular dispersion as the Bragg resonance indicating a direct relationship to the PBG.

The rate of non-radiative relaxation in CdTe-opal is a super-linear function of the carrier concentration, which leads to the sub-linear growth of the emission intensity with increasing excitation power. If the SE rate decreases in a band gap, the radiation lifetime of the excited atom should be even longer compared to the lifetime of the same atom outside the PBG. This would lead to the decrease of the saturation threshold. However, the  $P_0$ -spectrum reaches its maximum in a band gap suggesting the decrease of the radiative lifetime. This contradiction can be resolved, if the stimulation of the radiative recombination occurs at PBG frequencies due to the influence of the far-field from the same or other atoms radiating at this frequency. The difference of this regime from the amplified spontaneous emission is the angle-dependent resonant conditions imposed by the PBG upon the photon propagation.

The global minimum in  $P_0$  spectra, which coincides with the PL band maximum, appears due to the faster non-radiative relaxation as compared to the radiative process. The saturated population of the emitters radiating with frequencies at the band maximum can be achieved at relatively low excitation power. Then further pumping increments become ineffective and result in a faster population of states around the emission band maximum. The spectral broadening of the emission band reflects this competition.

To understand the emission stimulation, the nature of optical modes in a PBG should be considered. On the one hand, there is a high concentration of defects in the opal lattice. Some of defects can have a resonance frequency in the band gap, which leads to the localization of photons coupled to the defect modes. On the other hand, the energy in the Bragg cone can be carried by modes, the wavevector of which is not parallel to the group velocity vector. The group velocity of these modes is about 1/10 of that of the Bloch modes in allowed bands. Correspondingly, photons of these slow modes have a longer interaction time with excited atoms favouring the stimulation of radiative recombination. The quality factor of in-gap defect states is relatively low and the density of slow propagating modes does not exceed 10% of the mode density in allowed bands, which limits the magnitude of emission rate stimulation. The absolute value of the emission rate stimulation from the figure 7.20 is about 30-40% above the SE rate.

## 8. Feasibility studies

During the work on Photonic crystals a number of feasibility studies have been undertaken to evaluate the suitability of alternative materials or approaches in the context of photonic crystals.

- To enhance the relative width of the PBG of opals and improve its robustness – especially regarding disorder – it has been suggested to infill opals with dispersive materials, i.e. build metallo-dielectric nanocomposites. A test has been done to infill silica opals with metallic silver and determine its optical properties.
- A pressure sensor based on a (reversible) shift of the Bragg resonance depending on the pressure applied to a deformable photonic crystal is one possible device application based on photonic crystals. In the framework of the EU project PHOBOS [50] the fabrication of an elastometer or pressure sensor was planned. Tests to evaluate the suitability of PMMA based thin film opals for this application have been done.
- One of the key processes that have to be developed having optical devices based on opaline photonic crystals in mind is nano-structuring of the samples. Various approaches have been suggested [50], including growth in confined cavities or on patterned substrates, polishing, and lithographic structuring by direct e-beam writing into PMMA thin film photonic crystals. A preliminary study was done to evaluate the prospects and limits (i.e. induction of structural damages by the e-beam, removal of exposed material, necessary irradiation doses, available feature sizes). Meanwhile these first investigations have led to further results including the preparation of nano-structured PMMA PhCs.

### 8.1. Metallo-dielectric opals.

The gap-width-to-midgap-frequency ratio of the complete gap, which is a measure of the PBG width, is expected to be within 5% in even in defect-free inverted opal photonic crystals, which places a high challenge to the fabrication of photonic crystals at optical wavelengths. Bearing this in mind, the use of dispersive materials has been suggested to build photonic crystals, in particular, metallodielectric (MD) nanocomposites. In contrast to the pure dielectric (DD) PhCs, MD structures are supposed to make the PBG a more robust effect. More important, MD PhCs have been predicted to tolerate a sufficient level of disorder and to lift off the refractive index contrast problem. The combination of both, dielectrics and metals in one MD PhC is anticipated to enhance the gapwidth-to-midgap frequency ratio dramatically to about 10% [125]. To date, no successful experiments have been reported with MD PhCs in the visible and the theoretical treatment suffers from some uncertainty.

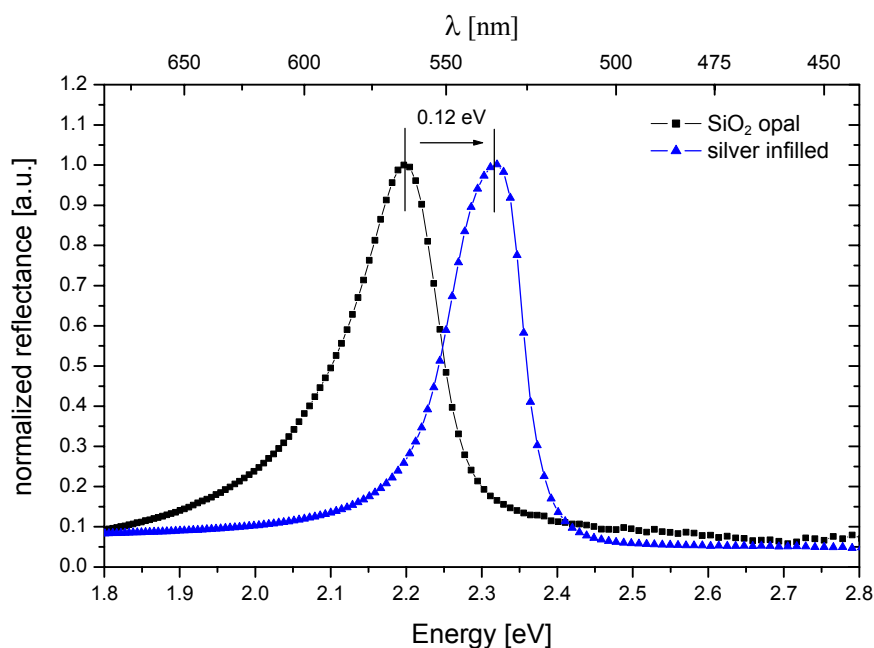


**Figure 8.1:** Reflectance spectra of a  $\text{SiO}_2$  bulk-opal prior (black squares) and after (blue triangles) infilling with metallic silver. The spectra were taken at near-normal incidence ( $\theta_{\text{ext}} = 6^\circ$ ). The blue-shift is attributed to the reduction of the effective RI induced by the silver

Metals showing a Drude-like behaviour are typically lossy at optical frequencies except in a certain frequency window, where they behave as a conventional dielectric, although a highly dispersive one. The RI contrast can become extremely large for frequencies around the plasma frequency. Silver is the first metal to come to mind for energies in the region of 2.4–4.0 eV, having the zero crossing of the real part of the RI around 3.78 eV.

Preliminary experiments to infill silica opals with metallic silver have been performed<sup>§§</sup> and their optical properties were determined by reflection measurements. Figure 8.1 shows reflectance measurements from a  $\text{SiO}_2$  bulk opal undertaken prior and after infilling with silver. A clear blue-shift of the reflectance peak is evident. This is attributed to a decrease of the effective refractive index of the whole structure due to the silver infilling. The magnitude of the shift of 0.12 eV corresponds to a decrease of the RI inside of the voids from 1.0 (air) to 0.70 due to the silver-infill. A widening of the stop-band has not been observed. The fraction of the voids that has been occupied by silver and whether the metal forms a cermet or a network topology has not yet been confirmed. However, the topology of metal component is

<sup>§§</sup> the sample was prepared by Dr. Manfred Müller, Institute for Organic Chemistry, Dept. of Chemistry and Pharmacy, Johannes Gutenberg University Mainz, Germany

an important issue since the PBG of a MD PhC of cermet topology resembles that of a DD PhCs. Similar transmission spectra of opals infilled with a small amount of Ag nanoparticles exhibit a blue shift and a widening of the stop-band have been observed by Zhou et. al. [126].

The principle success of the infilling process has been shown. The silver precursor obviously penetrated the opal voids and metallic silver was deposited within the opal voids without damaging the supporting silica structure.

Detailed statements on the extend of the infill and a comparison of the optical data to numerical simulations could not be done with these preliminary results. Nevertheless, the principle practicability of the approach could be demonstrated. More detailed investigations are subject to future work.

## 8.2. Photonic crystal pressure sensor

The principle feasibility of the idea to use photonic crystals made from soft materials as pressure or strain sensors has been proven by different groups.

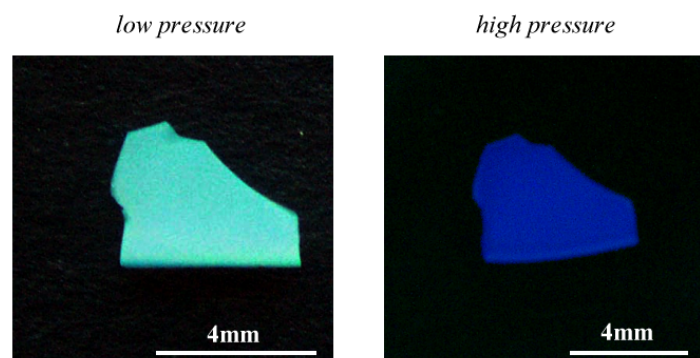


**Figure 8.2:** Elastomeric PhC replicas from crosslinked polysiloxanes in a solvent. A clear blue shift of the Bragg resonance is evident under lateral pressure of about 50 kPa (images from [50]).

Photonic crystals with a tuneable band gap can be realised, in particular, if the photonic band gap structure is made from elastically expandable/compressible materials. In this case changes of the lattice constant will result, empirically, in the shift of the diffraction resonance. In fact, this leads to the full reconstruction of the band gap energy diagram. Several successful attempts to make elastic PhCs from opals or inverted opals have been reported [127, 128]. Consequently, elastic opal can be used either to filter different wavelength depending on the applied pressure or to measure the pressure by the shift of the resonance.

Elastomeric replicas provide PhCs, the PBG of which can be tuned by applying external pressure. If the pressure is applied along one direction of the lattice, the lattice constant decreases and a blue shift is observed. As in all periodic dielectric structures with low refractive index contrast the shift of the band gap remains angle dependent.

Two attempts have been made to fabricate elastomeric replicas within the scope of the project PHOBOS [50]. In both cases the elastomer used, consisted of crosslinked polymer with a glass transition temperature far below room temperature.

Inverted opal photonic crystals from crosslinked polysiloxanes were prepared and analysed at the University of Mainz. The samples showed a pronounced pressure-dependent shift of the Bragg resonance as depicted in figure 8.2. The protection of the elastomeric replica in organic solvents seems to be the key in these experiments. When these structures are exposed to air, they irreversibly collapse. This problem may be, possibly, resolved by using a higher crosslinking density, however, this leads to a higher Young's module of the structure, which would make the structure less sensitive to pressure changes

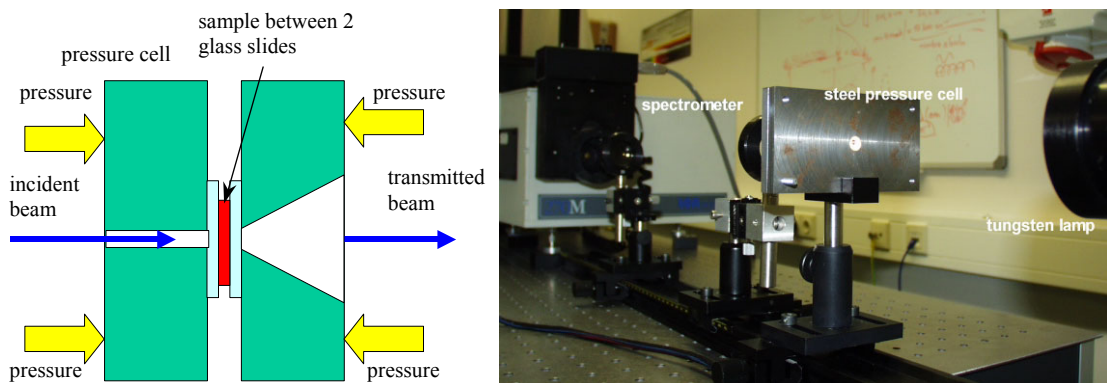


**Figure 8.3:** Sketch of a pressure cell for measurements of the transmission/reflectance from opals under the uniaxial pressure(left). Image of the experimental set up used with the cell (right)

Nevertheless, investigations of the elastometer require a measurement cell, which allows optical transmission and reflectance measurements under the uniaxial pressure to be performed. As a first approach, the pressure cell shown in figure 8.3 was build and tested with PMMA opals to test the set up and the feasibility to use direct PMMA opal PhCs in a pressure sensor, avoiding the need of closed, solvent-filled cells.

With the thin film opals, the only accessible direction is the [111] axis, along which the opal lattice has the highest density.

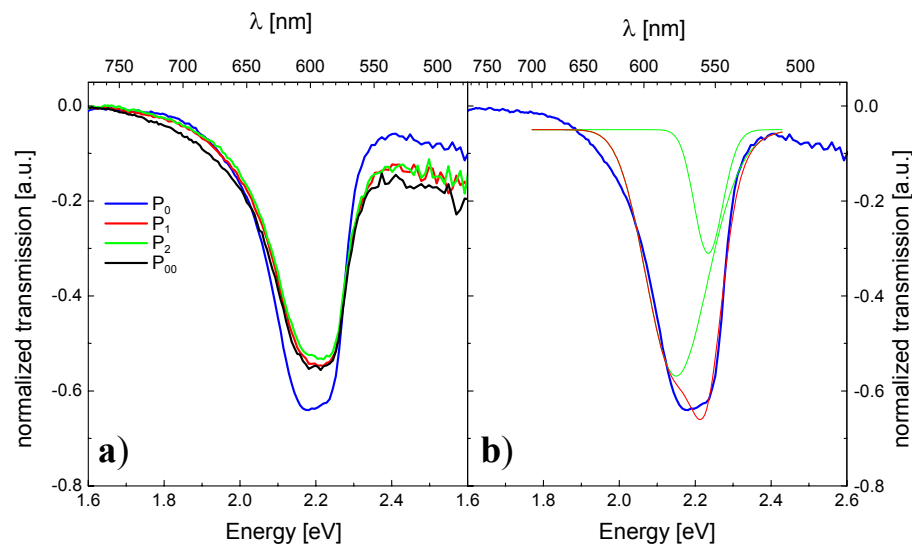


**Figure 8.4:** Transmission spectra of a 40  $\mu\text{m}$  thick PMMA opal film at different pressures:  $P_0 = P_{00} < P_1 < P_2$ ;  $P_0$  and  $P_{00}$  denote the transmission spectra obtained at zero pressure before and after compression, respectively (a). Deconvolution of the transmission minimum into two bands by a two-peak Gaussian fit (b).

Test experiments were done with PMMA films deposited on glass substrates. The Bragg minimum in the optical transmission spectrum of has been used to trace pressure-induced changes along [111] axis of the lattice. The spectra shown in figure 8.4 were taken from a ca. 40  $\mu\text{m}$  thick, well ordered PMMA sample at different pressures. The PhC was sedimented from spheres with a diameter of  $\approx 245$  nm, thus consisting of  $\approx 200$  monolayers of silica spheres in [111] direction.

The transmission dip degrades with the application of the pressure, but no detectable shift of the transmission minimum occurs as evident from figure 8.4. Moreover, the opal spectrum recovers only to a small extent after releasing the pressure (cf. curves  $P_0$  and  $P_{00}$ ). The Bragg minimum can be deconvoluted into two bands as shown in figure 8.4b, where a Gaussian fit with two peaks to the experimental data is shown. The degradation of the Bragg dip proceeds as follows: the short wavelength band does not move with the pressure, but reduces its magnitude, whereas the long wavelength band moves slightly to higher energies, but keeps its magnitude. The absolute magnitude of the shift is about 7 nm, which is about 8 times smaller than the full width at half minimum of the Bragg transmission dip. Thus, we conclude, that direct opals cannot be used as an indicator of applied pressure because of the relatively wide bandwidth of its diffraction resonance compared to the observed blue-shift.

The results of the transmission measurements show that direct opals made from polymer spheres are not suitable for pressure sensors because the compression along [111] axis is

accompanied with the increase of the density of the material along the same direction. The latter increase leads directly to the increase of the index of refraction.

Taking the Bragg law for normal incidence  $\lambda = 2d \cdot n_{eff}$ , where  $n_{eff}$  is the effective index of refraction and  $d$  the inter-plane distance, it is reasonable to assume that the pressure-induced variation of these variables balances the overall change of the resonance wavelength. Additionally, this resonance, being 5% of the relative bandwidth, becomes even broader because in a 3D package the squeezing the lattice along one direction leads to the lattice distortion along other directions.

Apart from that it is a priori not clear how uniaxial pressure is distributed and compensated inside the crystal. It might induce – especially in the inverted structures – strong lattice distortions in the first layers, leaving the deeper layers unperturbed.

Inverted opals are easier to squeeze with pressure due to their 3 times lower volume of the polymer in the structure. Correspondingly, they demonstrate a higher sensitivity of the Bragg resonance to the pressure. However, the relative width of the Bragg resonance in inverted opals is about 2 times larger as compared to the sphere-made opal of the same refractive index contrast and the lattice distortion should be larger as well. Both factors result in the great uncertainty in determining the resonance wavelength as a function of applied pressure.

A prospective design of an elastometer might be the following: small hard scatterers of about one tenth of the wavelength size need to be crystallised in a 3-dimensional lattice within a rectangular shaped piece of elastic polymer. This is advantageous compared to direct or inverted opals because:

- i. the low difference between the refractive indices of spheres and the environment provide a narrow diffraction resonance
- ii. the large separation of spheres ensure the larger shift of the resonance with changing the lattice parameter.
- iii. For the small uniaxial variation of the inter-sphere distance the overall lattice distortion will be negligibly small,
- iv. non-squeezable scatterers ensure the same form-factor for the resonance line at any pressure applied.

It should be emphasised that the proposed optimised design solution for an elastometer or pressure sensor is not, as a matter of fact, a photonic crystal.

Thus, it can be concluded that the wavelength of the diffraction resonance in opals is a pressure-sensitive parameter, but, they are, certainly, not suitable as pressure sensors.

### 8.3. Structuring of opal based thin film Photonic Crystals

To harness the optical properties of opal based PhCs – inverted or direct structures – in optical device applications it is inevitable to tailor the PBGs locally at will.

In the case of opaline materials, the complexity of this task is related to the necessity of combining macro-scale structuring either with the self-organised growth of the opal or selective in space modification of the opal

Possible routes towards PhC based devices are:

- post-growth (or during-growth) structuring of the PhC film on the sub- $\mu\text{m}$  scale e.g. to define waveguides, cavities or defects
- sedimentation on textured substrates to induce the growth of other crystal structures (hcp, diamond) or growth directions other than [111].
- synthesis of multi-layered opal structures to gain access to a set of additional parameters – i.e. the difference of sphere diameters, RICs, structure of the interface between the different PhCs (in fact a defect plane), among others – than can be used to modify the photonic properties of the composite.

Several approaches to reach this goal have been tested, including the sphere-by-sphere assembly of diamond lattices by a nano-manipulator [42] – which seems to be promising but slow and expensive –, cutting of opals with an ultramicrotome, growth in confined areas of  $\mu\text{m}$  size [96], on patterned substrates and synthesis of bi-layered opal films [50].

#### 8.3.1. Sedimentation on patterned substrates

Deposition of opaline films on patterned substrates is believed to be a way of improving the crystallinity of the sphere package. Several patterns can be suggested in order either to enhance the forces leading to the ordering of the sphere sediment or to change the symmetry of the package.

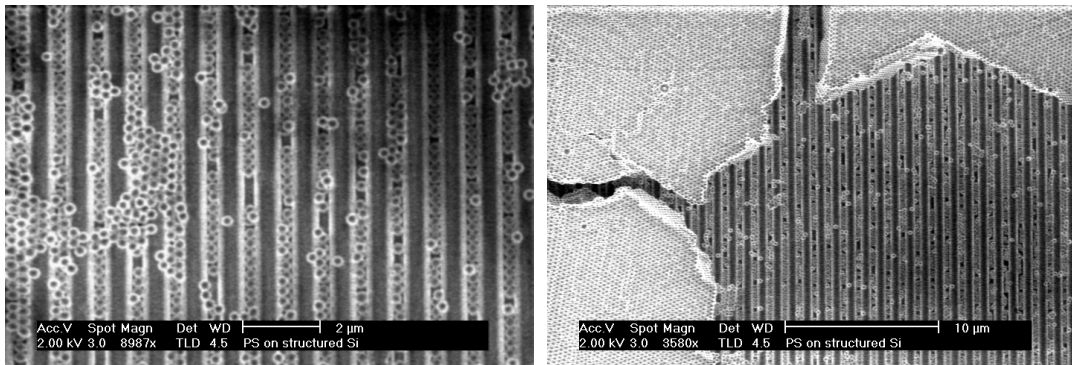


*Figure 8.5: Initial stage of the film growth on a patterned substrate (left). Complete film grown on patterned substrate. The information about the substrate anisotropy is lost during the film growth and a regular fcc film is formed (right).*

The aim of the experiments carried out was to find out how strong is the influence of the substrate upon the opaline package. The pilot experiment was made with an anisotropic substrate consisting of a regular groove pattern with a width comparable with the bead diameter ( $\approx 250$  nm). The periodicity was incommensurable with the sphere diameter, thus a film possessing a distorted lattice or showing preferably cracks in the direction of the substrate's grooves was expected.

Figure 8.5 shows the distribution of the spheres over the grooves of the substrate at the initial stage of the film deposition. Clear evidence for a correlation is demonstrated. The spheres seem to seed preferably along the grooves, forming chains.

However, when a thick film is formed, the effect of the substrate anisotropy is lost. The resulting film resembles those grown on homogeneous substrates. It is evident that the orientation of sphere rows does not follow exactly the groove direction (cf. figure 8.6). The cracks induced during drying and the domain sizes of  $\approx 50 \times 50 \mu\text{m}^2$  do not differ at all from those found on comparable films grown on unstructured substrates.

At which stage the effect of profiled substrate is lost and whether the used groove profile might have been a poor choice is a matter of further investigation. It can be concluded that no evidence for crystallisation into crystallographic directions other than [111] has been found, not was a distorted lattice observed

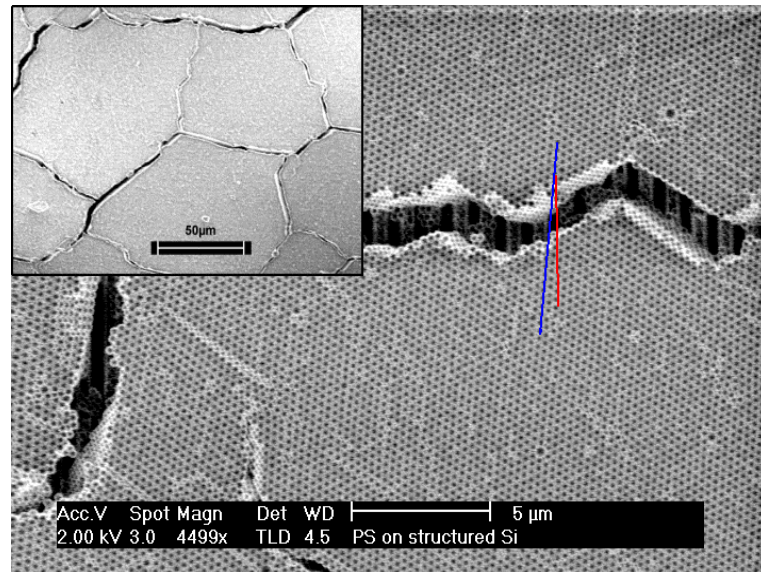


**Figure 8.6:** Thick film on patterned substrate. The orientation of the spheres does not exactly follow the anisotropy on the substrate (cf. blue and red lines). As in films grown on homogeneous substrates, the crystallographic orientation is preserved over the crack boundaries. The domain sizes (inset) are also comparable to these films.

Meanwhile further experiments to grow opals in structured silicon wafers with feature sizes in the 10  $\mu\text{m}$  range have been undertaken [96]. A much reduced crack density was found and it has even been proven possible to detach the films from their substrates. This novel approach, using the substrate as a mould and releasing the PhC after sedimentation, seems to be a promising way to overcome some measurement challenges of 3D PhC. For instance, detached structures can be investigated from the lateral sides, e.g., in and out-coupling for waveguide measurements, without requiring sawing and polishing. Moreover, by suspending the crystal, emission studies avoiding the critical influence of the substrate will be possible.

### 8.3.2. Multi-layer opals

The feasibility of this approach was first demonstrated with a PhC based on bulk opal [129] and then confirmed with thin film opals [130]. The overall optical transmission/reflectance of multi-layered opals can be represented, in the first approximation, as the linear superposition of stop bands of individual layers. The most desirable feature of the PBG material, namely, the suppression/enhancement of the emission is expected to undergo further modification in the case of increased complexity of the PBG.

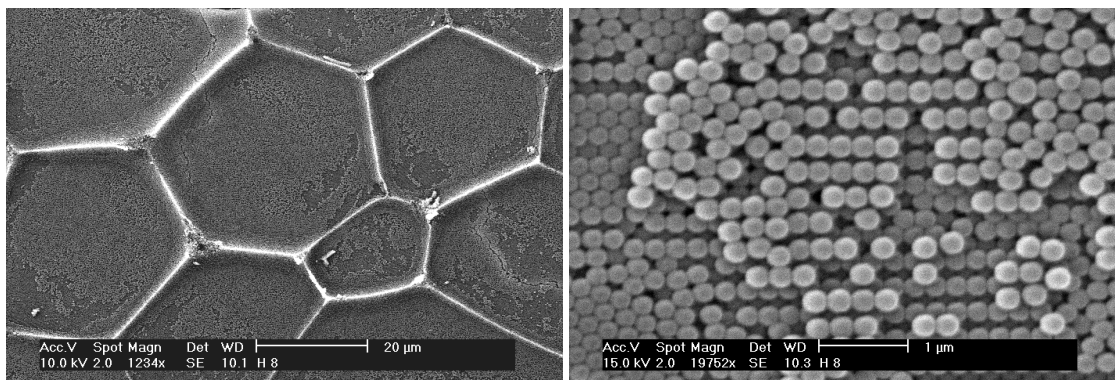


**Figure 8.7:** Two layered opal structure consisting of 240nm latex beads deposited on top of a film made from 270 nm beads. Initial growth stage at two different magnifications.

Preparation and characterisation of double-layer opaline film is the test routine towards the experimental realisation of a planar defect in opaline films. The first task is to develop the fabrication technique and the next is to examine the optical properties.

The crystalline quality of a heterogeneous sample has been investigated by SEM. The sample was prepared by deposition of, first, 270 nm latex beads on a glass substrate. Successively, the second film of 240 nm beads was grown on top of this bottom layer<sup>\*\*\*</sup>.

The very early stage of the deposition of the incommensurable opaline film on top of the other film is shown in figure 8.7. The hydrodynamics of this process is of high complexity because of the porous nature of the substrate, which is the opaline film itself.

Optical investigations on the heterostructures have not been performed during this preliminary studies but will be subject to further research.

It can be deduced from SEM observations that with the increase of the thickness of the “top” film its own order takes over the destructive influence of the “bottom” layer, leaving the disordered interface layer behind.

This makes further investigations and optimisation on these structures a promising approach.

Meanwhile a lot of work on heterostructures prepared from PMMA beads has been done: Light emitting bi-layer opals were prepared<sup>†††</sup>, their structural quality was greatly improved

<sup>\*\*\*</sup> the sample was prepared by Dr. A. L. Rogach, Institute of Physical Chemistry, University of Hamburg

<sup>†††</sup> heterostructures made from PMMA spheres were prepared by Dr. Marc Egen,, Institute for Organic Chemistry, Dept. of Chemistry and Pharmacy, Johannes Gutenberg University Mainz, Germany and optically analysed in collaboration with Dr. Sergei G. Romanov, Institute of Materials Science, University of Wuppertal, Germany

and optical measurements have discovered a range of unique optical features, such as a strong anisotropy of the photonic emission properties [131] and modifications of the PBG structure do to the presence of surface modes and other peculiar physical phenomena, which are, actually, the aim of the heterostructuring activities.

Intensive work on that field is currently in progress. More details can be found in Ref. [50].

### 8.3.3. Electron-beam structuring of PMMA opals

An advantage of poly(methylmethacrylate) (PMMA) opals compared to others is their sensitivity to electron beam (e-beam) irradiation. In fact, PMMA is a well known e-beam resist. This opens a way for post-crystallisation tuning of opals, in particular, to introducing artificial defects. Main issues to be addressed for successful application of e-beam lithography are the correct choice of the dose, the alignment of the pattern with the orientation of the opal lattice and the selection of the most appropriate e-beam sensitive polymer. Achieving the desired depth and the flatness of the patterned areas as well as minimising the corner rounding are objectives of further experiments.

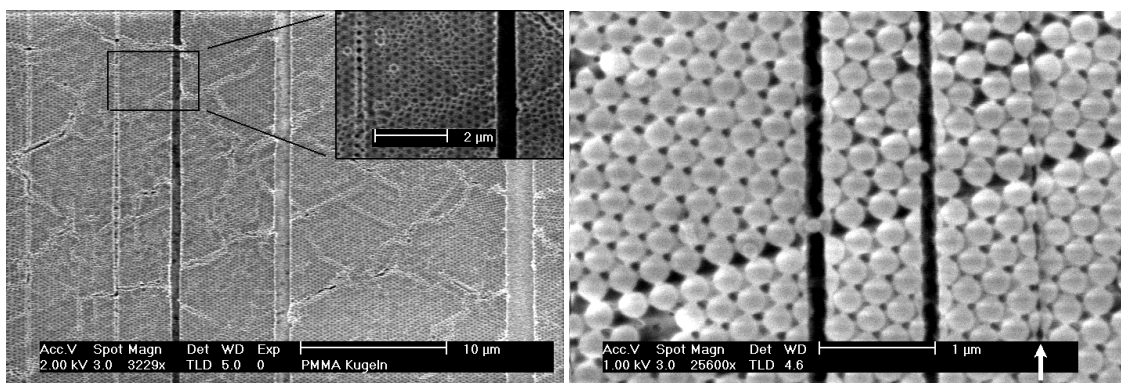


**Figure 8.8:** Demonstration of possibility to write down a line pattern of desirable configuration on PMMA opaline films. Left: lines were written with different beam diameters and irradiation doses. The inset is a close-up of the 500 nm and 250 nm lines (left). Feature sizes down to one sphere diameter can be realised with optimised parameters (right). Note the faint 3<sup>rd</sup> line indicated by the arrow that was written with a smaller dose.

To write a pattern matching the PC orientation is a challenge, because of the chance to overexpose the scanning field. The writing process is therefore a “shot in the dark” made under assumption of the long-range crystallinity of opal films

Testing of the write-on capabilities of an electron beam writer, available in Wuppertal (attached to a Philips or XL 30 SFEG microscope) have been done to prove the principle feasibility of this approach<sup>†††</sup>.

A range of different patterns (feature size ca. 200nm) and periodicities (down to 1  $\mu\text{m}$ ) have been written onto PMMA opal PhC films. The samples were subsequently developed using an organic solvent (Iso-propanol) or a commercially available e-beam resist developer. Although not much effort were spent into the optimisation of the development process the precision of writing down to a fraction of one sphere could be demonstrated (cf. figure 8.8). The pattern area is normally up to 500 $\times$ 500 micrometer square without the stitching problem arising when the microscope stage has to be translated. Lines with different beam diameters and irradiation doses were written. Feature sizes down to one sphere diameter can be realised with optimised parameters. In figure 8.8 (left) differently well reproduced lines are visible, depending on the irradiation dose. Note the faint 3<sup>rd</sup> line in figure 8.8 (right), indicated by the arrow, that was written with a too small dose. The diagonal line defect visible was introduced while looking at the image after the development process do to shrinkage of the beads under the e-beam irradiation. This is no problem under standard writing conditions since the doses are usually small enough to avoid shrinkage of the beads.

Subsequent inversion of patterned opals with semiconductors of wide electronic gap will result in waveguide structures capable to carry the visible light. The important problems to be studied with regard to the technological process are related to the penetration depth and the scattering of the electron beam in a porous medium. These processes define the pattern depth and its conformity with the lattice symmetry. Further progress in this direction is also related to the improvement of the etching process.

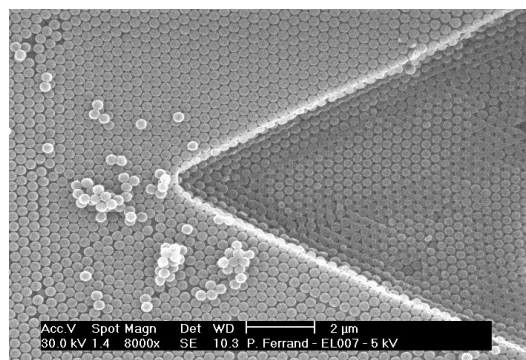


**Figure 8.9:** SEM micrograph of a structure (triangle) written on an opal film using e-beam lithography. Note that the structure was written to a defined depth of  $\approx 6$  monolayers (image from [50]).

<sup>†††</sup> The tests were done in collaboration with J.U. Bruch and further extended by Dr. P. Ferrand, both Institute of Materials Science, University of Wuppertal, Germany

Meanwhile, based on this study, further investigations on e-beam lithography including optimisation and the development of a process to write arbitrary structures with defined depths and further reduced feature sizes were done [50].

The patterning of a triangular structure on PMMA opaline film, where the pattern matches the lattice orientation could be archived (figure 8.9). By choosing the parameters for the electron beam, it was possible to restrict the exposure to an effective depth of 1.5  $\mu\text{m}$  (6 layers)

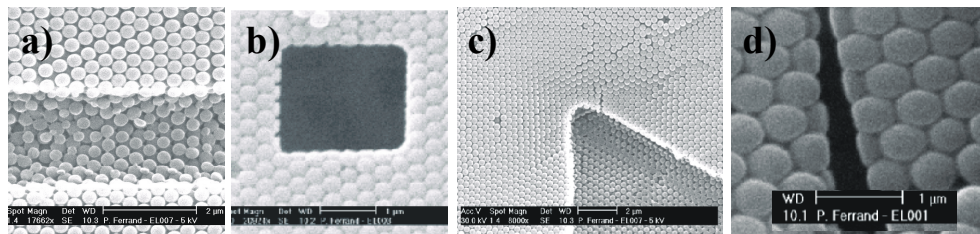


**Figure 8.10:** Examples of different structures made by e-beam lithography on PMMA opal films highlighting different aspects of the process (from [50]):

- (a) – line (wall-corner transition);
- (b) – cavity (arbitrary shape, corner rounding);
- (c) – triangle (alignment with crystal orientation, arbitrary depth);
- (d) – wedge (resolution)

However, further experiments with opals made from other e-beam resists are necessary to put the corner rounding and the flatness of the pattern near the vertical walls under control. Figure 8.10 illustrates the quality of the pattern after completing the developing of exposed PMMA opal. In particular, the typical scale of the wall-to-bottom transition, which is of a size of about 1-2 sphere diameters is evident. Corners are another pattern element, which are very sensitive to the dose (figure 8.10b, c). Currently, investigations on the optimisation of the pattern shaping are in progress. The resolution limit of this method is far less than the sphere diameter along straight lines (figure 8.10b, d) but remains restricted to one sphere diameter at corners (figure 8.10b).

Concluding, the feasibility of e-beam lithography as a prospective technology to insert arbitrarily shaped pattern into a polymer opal film was proved. But, so far, the resolution of this technique is not enough to produce single mode cavities for wavelengths in resonance with the opal PBG in the visible. Intense research on this topic is in progress.

## 9. Conclusions

Photonic crystals are an agile research topic and have rapidly grown into an important area of photonics. Most importantly, PhCs offer a potentially high impact on the next generation of optoelectronics devices. Nevertheless, the fabrication of these nanostructures still bears many technological challenges. A robust synthesis route to generate high quality PhCs is therefore an important issue for both application and fundamental research. Simultaneously, a deeper understanding of the light-matter interaction inside of PhCs is another vital problem that requires comparison between experimental data and existing theories.

The scope of this thesis was to evaluate a self-assembling approach towards the preparation of PhCs, namely, the crystallisation of thin film PhCs from polymer beads, and specifically to the strength of their photonic properties and suitability as a model system of 3D PhCs. The experimental data obtained over the course of this research were also used to understand the underlying physical processes in PhCs possessing incomplete photonic band gaps by cross-checking them with theoretical models.

This thesis addressed several aspects of thin-film PhCs:

### *Morphology of PMMA based thin film PhCs and their semiconductor replicas*

Addressed were the SEM observations of different PhC thin films – made by casting of PMMA spheres on substrates and by production of their inverted semiconductor replicas.

Thin film PhCs made from PMMA spheres have been found competitive to silica opal PhCs. They offer several advantages over their bulk counterparts, such as their cheap and easy growth on many different substrates, and the possibility to cover large areas up to several cm<sup>2</sup>.

- Casting PMMA suspensions on different substrates has been proven as an appropriate growth method.
- Thin film PhCs have been found to grow along the [111] axis of the *fcc* lattice.
- Opal films consist of single crystalline domains of  $\approx 100$   $\mu\text{m}$ , which is acceptable for possible device application. The crystallographic orientation is preserved over the crack boundaries allowing the formation of large area (several cm<sup>2</sup>) opal films of good crystalline quality.
- The research demonstrated the doping of PMMA opals and their semiconductor replicas with different laser-dyes.
- The inversion of thin film opals has been performed with high refractive index semiconductors, such as SnS<sub>2</sub> and TiO<sub>2</sub>.

- The experiments did not yield an omnidirectional PBG in the visible because the density of SnS<sub>2</sub> synthesised inside opal voids was well below the value of a bulk SnS<sub>2</sub> crystal.
- The crystalline quality and homogeneity and the planar geometry of opal films has been confirmed by the observation of Fabry-Pérot interference oscillations in their optical reflectance spectra.

#### *Optical properties of thin film PhCs*

The research undertook optical measurements on PMMA thin film opals, in some cases doped with fluorescent dyes, to probe their photonic band gap properties in the vicinity of the first L-pseudo-gap.

#### *Reflectance and Transmission*

- Angle resolved reflectance and transmission revealed substantial deviations from the Bragg law that were attributed to multiple diffraction at different sets of opal crystal planes. The band branching appears as a splitting of the Bragg resonance at certain angles of incidence in the vicinity of  $\theta_{ext} = 51.84$ , when resonances from (111) and (200) planes are of the same frequency. The effect was more pronounced in inverted structures due to the enhanced refractive index contrast.
- Fabry-Pérot oscillations were observed for highly ordered samples. These fringes can be used as a destruction-free optical method to determine the thickness of thin film opal PhCs and as a qualitative criterion of their crystalline quality. Theoretical calculations are in agreement with the experimental data. The asymmetry of FP oscillation amplitude on the low- and high-energy side were reproduced by TMM calculations. A variation of the FP oscillation period was interpreted as a sign for the theoretically expected increase of the effective refractive index at the band gap edges.
- The optical band branching was proven to be dependent of the azimuthal angle and polarisation of the incident electromagnetic wave. Depending on these two parameters the relative contribution of opal crystal planes to the total reflectance is different. In particular, the diffraction at (200) planes is reduced in certain directions and for *p*-polarised light. Additionally Fabry-Pérot oscillations are attenuated for *p*-polarisation due to the vicinity to the Brewster angle. Numerical and experimental results have shown an excellent agreement.

*Emission from incorporated laser-dyes*

This thesis also addressed photoluminescence studies of opal films with laser-dyes incorporated in beads or filled with CdTe nanoparticles, as well as semiconductor inverted opals filled with dyes, to reveal the influence of a directional PBG on the emission intensity, directionality and the emission rate.

- The PL spectra of dye-doped PMMA PhCs and inverted opals show a partial suppression of the dye radiation intensity at the PBG frequency range.
- The emission is spatially redistributed following the anisotropy of the directional PBG, leading to an anisotropic emission pattern.
- No evidence of a modification of the spontaneous emission rate has been found in opal films assembled from PMMA beads doped with a Coumarin dye. Once radiated, photons couple to different eigenmodes of the opal lattice. Due to wide distribution of these mode properties, emission rate appears both accelerated and suppressed in a total detected signal. As a result, only band-pass filtering of the emission intensity in accord to the PBG-induced mode number variation with direction has been observed.
- In order to accomplish emission studies in the visible spectrum, a nano-composite consisting of opal infiltrated with CdTe nanocrystals was utilised. This CdTe-opal structure allows a mutual tuning of the interband optical emission frequency of CdTe nanoparticles and the photonic band gap position of the opal film. Emission studies were performed with the prospect of observing an optimised shape of the emission spectrum, the directionality diagram of the emission and the emission rate.
- In the case of high refractive index contrast semiconductor inverted opals feedback between the radiation and embedded dye molecules provided by the PBG has been found that leads to spectral re-distribution of the emission rate.
- The directionality of the emission in opals at the Bragg gap frequency range has been convincingly associated with the topology of the iso-frequency surfaces.
- An evaluation of the emission rate in PBG materials has been suggested by exploiting the dependence of the emission saturation upon the frequency across the PBG frequency range.
- Emission stimulation due to coupling of CdTe nanoparticle radiation to the inhomogeneous optical modes of the PBG frequency propagating with low group velocity has been demonstrated. The observation of the emission rate acceleration was associated with obtaining a narrow spatial distribution of the emitter along the profile of the electromagnetic wave intensity in the opal's interior.

*Feasibility studies*

- First studies of the morphology and physical properties of opals with complex architectures, namely, opals grown on structured substrates and double film hetero-opals, have been performed by means of SEM studies and optical reflectance/transmission measurements. No influence of the substrate-induced anisotropy on the opal structure has been found. Further advanced studies and detailed optical measurements on multi-layer PhC film revealed many interesting features.
- It was shown that a pressure sensor based on PMMA PhCs is, in practice, not competitive with other approaches and conceptually questionable.
- A shift of the Bragg resonance in silver infilled metallo-dielectric PhCs was attributed to a decrease of the effective refractive index due to the silver infill.
- The possibility to modify the structure of PMMA thin opal films by direct e-beam lithography was proven. This approach gives a prospect of post-synthesis modification of the light dispersion in 3D opal-based PhCs.

Photonic crystals will remain an active research topic with numerous fascinating and yet uninvestigated effects. As they steadily evolve into device applications, the need to understand, match, and tailor their linear and non-linear optical properties will increase. Thin film opal-based PhCs can be used as a readily accessible system to investigate many optical effects connected to the photonic band structure. Moreover, PhC-integrated light sources open another dimension to design novel optical devices with engineered optical properties.

## Bibliography

- [1] V.P. Bykov, "Spontaneous emission in a periodic structure" *Sov. Phys. JETP* **35**, 269 - 273 (1972)
- [2] E. Yablonovitch, "Inhibited spontaneous emission in solid-state physics and electronics" *Phys. Rev. Lett.* **58**, 2059 - 2062 (1987)
- [3] S. John, "Strong Localisation of Photons in Certain Disordered Dielectric Superlattices" *Phys. Rev. Lett.* **58**, 2486 - 2489 (1987)
- [4] J. Miles, "Photonic Crystals head toward the marketplace" *Opto & Laser Europe* **Nov 2002**, 17 - 19 (2002)
- [5] G. Tayeb, B. Gralak and S. Enoch, "Morpho butterflies wings color modeled with lamellar grating theory" *Opt. Expr.* **9**, 567 - 578 (2001)
- [6] A.R. Parker, R.C. McPhedran, D.R. McKenzie, L.C. Botten and N.A. Nicorovici, "Photonic engineering: Aphrodite's iridescence" *Nature* **409**, 36 - 37 (2001)
- [7] H. Míguez, F. Meseguer, C. López, A. Mifsud, J.S. Moya and L. Vázquez, "Evidence of FCC Crystallization of SiO<sub>2</sub> Nanospheres" *Langmuir* **13**, 6009 - 6011 (1997)
- [8] S.G. Romanov, A.V. Fokin, V.V. Tredijakov, V.Y. Butko, V.I. Alperovich, N.P. Johnson and C.M. Sotomayor Torres, "Optical Properties of ordered three-dimensional arrays of structurally confined semiconductors" *J. Cryst. Growth* **159**, 857 - 860 (1996)
- [9] C.M. Soukoulis, *Photonic Crystals and Light Localization in the 21st Century* (NATO ASI Series C, Vol. 563), Kluwer Academic Publishers, Dordrecht (2001)
- [10] Y. Xia, B. Gates, Y. Yin and Y. Lu, "Monodispersed Colloidal Spheres: Old Materials with New Applications" *Adv. Mater.* **12**, 693 - 713 (2000)
- [11] J.D. Joannopoulos, R.D. Meade and J.N. Winn, *Photonic Crystals: Molding the Flow of Light*, Princeton University Press, Princeton NJ (1995)
- [12] R. Biswas, M.M. Sigalas, G. Subramania and K.-M. Ho, "Photonic Band Gaps in Colloidal Systems" *Phys. rev. B* **57**, 3701 - 3705 (1998)
- [13] H.S. Sözüer, J.W. Haus and R. Inguva, "Photonic bands: Convergence problems with the plane-wave method" *Phys. Rev. B* **45**, 13962 - 13971 (1992)
- [14] E. Yablonovitch, T.J. Gmitter, R.D. Meade, A.M. Rappe, K.D. Brommer and J.D. Joannopoulos, "Donor and Acceptor modes in photonic band structures" *Phys. Rev. Lett.* **67**, 3380 - 3383 (1991)
- [15] E. Yablonovitch, "Photonic Band-Gap Crystals" *J. Phys.: Cond. Matter* **5**, 2443 - 2460 (1993)
- [16] John David Jackson, *Classical Electrodynamics*, 2. ed., John Wiley & Sons, New York (1975)
- [17] Ch. Kittel, *Einführung in die Festkörperphysik*, 12. ed., Oldenbourg, München-Wien (1999)
- [18] B.E. Warren, *X-ray diffraction*, Addison-Wesley, Reading (1969)
- [19] E. Yablonovitch, "Photonic crystals" *J. Mod. Opt.* **41**, 173 (1994)

- [20] Z.Y. Li and Z.Q. Zhang, "Fragility of photonic band gaps in inverse-opal photonic crystals" *Phys. Rev. B* **62**, 1516 - 1519 (2000)
- [21] K.-M. Ho, C.T. Chan and C.M. Soukoulis, "Existence of a Photonic Gap in Periodic Dielectric Structures" *Phys. Rev. Lett.* **65**, 3152 - 3155 (1990)
- [22] Z.Y. Li, X.D. Zhang and Z.Q. Zhang, "Disordered photonic crystals understood by a perturbation formalism" *Phys. Rev. B* **61**, 15738 - 15748 (2000)
- [23] Z. Zhang and S. Satpathy, "Electromagnetic Wave Propagation in Periodic Structures: Bloch Wave Solution of Maxwell's Equations" *Phys. Rev. Lett.* **65**, 2650 - 2653 (1990)
- [24] K.M. Leung and Y.F. Liu, "Full Vector Wave Calculation of Photonic Band Structures in fcc dielectric media" *Phys. Rev. Lett.* **65**, 2646 - 2649 (1990)
- [25] R.D. Maede, A.M. Rappe, K.D. Brommer and J.D. Joannopoulos, "Accurate theoretical analysis of photonic band-gap materials" *Phys. Rev. B* **48**, 8434 - 8437 (1993)
- [26] S.G. Johnson and J. D. Joannopoulos, "Block-iterative frequency-domain methods for Maxwell's equations in a planewave basis" *Optics Express* **3**, 173 - 190 (2001)
- [27] S. John, "Localization of Light - theory of photonic band gap materials", in *Photonic Band Gap Materials*, edited by C.M. Soukoulis (Kluwer Academic Publishers, Dordrecht, 1996), NATO ASI Series E Vol. 315, pp. 563 - 665
- [28] K. Busch and S. John, "Tunable Photonic Crystals", in *Photonic Crystals and Light Localization in the 21st Century*, edited by C.M. Soukoulis (Kluwer Academic Publishers, Dordrecht, 2001), NATO Science Series C Vol. 563, pp. 41 - 57
- [29] K. Busch and S. John, "Photonic band gap formation in certain self-organizing systems" *Phys. Rev. E* **58**, 3896 - 3908 (1998)
- [30] J. Hama, M. Watanabe and T. Kato, "Correctly weighted tetrahedron method for k-space integration" *J. Phys.: Cond. Matter* **2**, 7445-7452 (1990)
- [31] C. Gerthsen, H.O. Kneser and H. Vogel, *Physik*, Springer Verlag, Heidelberg (1992)
- [32] F. García Santamaría, "Photonic Crystals based on Silica Microspheres", *PhD thesis*, Instituto de Ciencia de Materiales de Madrid (2003)
- [33] K. Sakoda, *Optical Properties of Photonic Crystals*, Springer Verlag, Heidelberg (2001)
- [34] S. Datta, C.T. Chan, K.M. Ho and C.M. Soukoulis, "Effective dielectric constant of periodic composite structures" *Phys. Rev. B* **48**, 14936-14943 (1993)
- [35] T.C. Choy, *Effective Medium Theory: Principles and Applications*, Oxford University Press, New York (2000)
- [36] J.C. Maxwell-Garnett, "Colours in metal glasses and in metallic films" *Philos. Trans. R. Soc. London* **203**, 385 - 420 (1904)
- [37] E. Hecht, *Optik*, 2. ed., Addison-Wesley, Bonn (1992)
- [38] H. Kosaka, T. Kawashima, A. Tomita, M. Notomi, T. Tamamura, T. Sato and S. Kawakami, "Superprism phenomena in photonic crystals" *Phys. Rev. B* **58**, R10096 - R10099 (1998)
- [39] D.N. Chigrin, "Electromagnetic waves propagation in photonic crystals with incomplete photonic band gap", *PhD Thesis*, Fachbereich Elektrotechnik, Informationstechnik und Medientechnik, Bergische Universität Wuppertal (2004)

- [40] S. Rowson, A. Chelnokov and J.M. Lourtioz, "Two-Dimensional Photonic Crystals in Macroporous Silicon: From Mid-Infrared (10 $\mu$ m) to Telecommunication Wavelengths (1.3 - 1.5 $\mu$ m)" *J. Lightwave Technol.* **17**, 1989 - 1995 (1999)
- [41] F. Müller, A. Birner, U. Gösele, V. Lehmann and H. Föll, "Structuring of Macroporous Silicon for Applications as Photonic Crystals" *J. Porous. Mater* **7**, 201 - 204 (2000)
- [42] F. García-Santamaría, H.T. Miyazaki, A. Urquía, M. Ibisate, M. Belmonte, N. Shinya, F. Meseguer and C. López, "Nanorobotic manipulation of microspheres for on-chip diamond architectures" *Adv. Mater.* **14**, 1144 (2002)
- [43] E. Yablonovitch, T.J. Gmitter and K.M. Leung, "Photonic band structure: the face-centered-cubic case employing nonspherical atoms" *Phys. Rev. Lett.* **67**, 2295 -2298 (1991)
- [44] S. Noda, K. Tomoda, N. Yamamoto and A. Chutinan, "Full Three-Dimensional Photonic Bandgap Crystals at Near-Infrared Wavelengths" *Science* **289**, 604 - 606 (2000)
- [45] S.Y. Lin, S.Y. Lin, J.G. Fleming, D.L. Hetherington, B.K. Smith, R. Biswas, K.M. Ho *et al.*, "A three-dimensional photonic crystal operating at infrared wavelengths" *Nature* **394**, 251 - 253 (1998)
- [46] C. López, L. Vázquez, F. Meseguer, R. Mayoral, M. Ocaña and H. Míguez, "Photonic crystal made by close packing SiO<sub>2</sub> submicron spheres" *Superlattice Microst.* **22**, 399 - 405 (1997)
- [47] P.A. Kralchevsky, N.D. Denkov, V.N. Paunov, O.D. Velez, I.B. Ivanov, H. Yoshimura and K. Nagayama, "Formation of two-dimensional colloid crystals in liquid films under the action of capillary forces" *J. Phys.: Cond. Mat.* **23A**, A395 - A402 (1994)
- [48] M. Müller, R. Zentel, T. Maka, S.G. Romanov and C.M. Sotomayor Torres, "Dye containing polymer beads as photonic crystals" *Polymer preprints* **41**, 810 - 811 (2000)
- [49] J.F. Bertone, P. Jiang, K.S. Hwang, D.M. Mittleman and V.L. Colvin, "Thickness dependence of the optical properties of ordered silica-air and air-polymer photonic crystals" *Phys. Rev. Lett.* **83**, 300 - 303 (1999)
- [50] C.M. Sotomayor Torres, *Photonic Crystals based on Opal Structures*, Periodic Progress Report EU Project IST-1999-19009 PHOBOS, Report No. 3 (2002)
- [51] A. Reynolds, F. López-Tejeira, D. Cassagne, F.J. García-Vidal, C. Jouanin and J. Sánchez-Dehesa, "Spectral Properties of Opal-Based Photonic Crystals having a SiO<sub>2</sub> Matrix" *Phys. Rev. B* **60**, 11422 - 11426 (1999)
- [52] G. Parker, "Photonic Integration takes things forward" *Fibre Sys. Eur.* **6**, 9 (2003)
- [53] O. Graydon, "Researchers report photonic crystal fibers with record low-loss operating at telecoms wavelengths", (Internet: <http://optics.org/articles/news/8/9/18/1>, 2002)
- [54] R. Colombelli, K. Srinivasan, M. Troccoli, O. Painter, C. F. Gmachl, D.M. Tennant, A.M. Sergent *et al.*, "Quantum Cascade Surface-Emitting Photonic Crystal Laser" *Science* **302**, 1374 - 1377 (2003)
- [55] A. Forchel and M. Kamp, "Mikrolaser mit Potenzial (in German)" *Physik Journal* **3**, 18 - 20 (2004)
- [56] P.V. Parimi, W.T. Lu, P. Vodo and S. Sridhar, "Imaging by flat lens using negative refraction" *Nature* **426**, 404 (2003)

- [57] C. Palmer, *Diffraction Grating Handbook*, 5. ed., Richardson Gratings, Rochester (2002)
- [58] J. J. Laserna, *Modern Techniques in Raman Spectroscopy*, John Wiley & Sons, New York (1996)
- [59] H. Bethge and J. Heydenreich, *Electron Microscopy in Solid State Physics*, Elsevier, Amsterdam (1987)
- [60] M. Haider, S. Uhlemann, E. Schwan, H. Rose, B. Kabius and K. Urban, "Electron microscopy image enhanced" *Nature* **392**, 768 (1998)
- [61] P.E. Batson, N. Dellby and O.L. Krivanek, "Sub-Ångstrom resolution using aberration corrected electron optics" *Nature* **418**, 617 - 620 (2002)
- [62] J.M. Brock, M.T. Otten and W.M.J. Coene, "High resolution imaging with a coherent electron source: The field emission gun" *Micron* **23**, 149 - 150 (1992)
- [63] U. Werner and H. Johansen, "Scanning Electron Microscopy: Physical foundations of contrast formation", in *Electron Microscopy in Solid state physics*, edited by H. Bethge and J. Heydenreich (Elsevier, Amsterdam, 1987)
- [64] W. Stöber, A. Fink and E. Bohn, "Controlled Growth of Monodisperse Silica Spheres in the Micron Size Range" *J. Colloid. Interface Sci.* **26**, 62 - 69 (1968)
- [65] H. Míguez, F. Meseguer, C. López, A. Blanco, J.S. Moya, J. Requena, A. Mifsud and V. Fornés, "Control of the Photonic Crystal Properties of fcc-Packed Submicrometer SiO<sub>2</sub> Spheres by Sintering" *Adv. Mater.* **10**, 480 - 483 (1998)
- [66] G. Subramania, K. Constant, R. Biswas, M.M. Sigalas and K.-M. Ho, "Optical Photonic Crystals Synthesized from Colloidal Systems of Polystyrene Spheres and Nanocrystalline Titania" *J. Lightwave Technol.* **17**, 1970 - 1981 (1999)
- [67] M. Müller, R. Zentel, T. Maka, S.G. Romanov and C.M. Sotomayor Torres, "Dye containing polymer beads as photonic crystals" *Chem. Mater.* **12**, 2508 - 2512 (2000)
- [68] M. Holgado, F. García-Santamaría, A. Blanco, M. Ibisate, A. Cintas, H. Míguez, C.J. Serna *et al.*, "Electrophoretic Deposition To Control Artificial Opal Growth" *Langmuir* **15**, 4701- 4704 (1999)
- [69] N. D. Deniskina, D. V. Kalinin and L. K. Kazantseva, *Precious Opal, Their Synthesis and Genesis In Nature (in Russian)*, Nauka, Novosibirsk (1980)
- [70] V.G. Balakirev, V.N. Bogomolov, V.V.Zhuravlev, Y.A. Kumzerov, V.P. Petranovsky, S.G. Romanov and L.A. Samoilovich, "Three-dimensional superlattices in opals" *Sov. Phys. Crystallogr* **38**, 348 - 353 (1993)
- [71] R. Mayoral, J. Requena, J. S. Moya, C. López, A. Cintas, H. Míguez, F. Meseguer *et al.*, "3D Long Range Ordering in an SiO<sub>2</sub> Submicrometer-Sphere Sintered Superstructure" *Adv. Mater.* **9**, 257 - 260 (1997)
- [72] A. van Blaaderen and A. Vrij, "Synthesis and Characterization of Monodisperse Colloidal Organo-silica Spheres" *J. Colloid. Interface Sci.* **156**, 1 - 18 (1993)
- [73] A. van Blaaderen, J. van Geest and A. Vrij, "Monodisperse Colloidal Silica Spheres from Tetraalkoxysilanes: Particle Formation and Growth Mechanism" *J. Colloid. Interface Sci.* **154** (1992)

- [74] V.N. Bogomolov, D.A. Kurdyokov, A.V. Prokofiev and S. M. Samoilovich, "Effect of a photonic band gap in the optical range on solid-state SiO<sub>2</sub> cluster lattices - opals" *JETP Lett.* **63**, 520 - 525 (1996)
- [75] V.N. Bogomolov, S.V. Gaponenko, I.N. Germanenko, A.M. Kapitonov, E.P. Petrov, N.V. Gaponenko, A.V. Prokofiev *et al.*, "Photonic band gap phenomenon and optical properties of artificial opals" *Phys. Rev. E* **55**, 7619 - 7626 (1997)
- [76] V.N. Astratov, V.N. Bogomolov, A.A. Kaplyanskii, A.V. Prokofiev, L.A. Samoilovich, S.M. Samoilovich and Yu. A. Vlasov, "Optical spectroscopy of opal matrices with CdS embedded in its pores: Quantum confinement and photonic bandgap effects" *Il Nuovo Cimento* **17D**, 1349 - 1354 (1995)
- [77] V. N. Bogomolov, A.V. Prokofiev, S.M. Samoilovich, E.P. Petrov, A.M. Kapitonov and S.V. Gaponenko, "Photonic band gap effect in a solid state cluster lattice" *J. Luminescence* **72**, 391 - 392 (1997)
- [78] personal communication: Dr. D. Cassagne, Groupe d'Etude des Semiconducteurs, Université de Montpellier II, France
- [79] Yu.A. Vlasov, V.N. Astratov, A.V. Baryshev, A.A. Kaplyanskii, O.Z. Karimov and M.F. Limonov, "Manifestation of intrinsic defects in optical properties of self-organized opal photonic crystals" *Phys. Rev. E* **61**, 5784 - 5793 (2000)
- [80] Yu. A. Vlasov, M. Deutsch and D.J. Norris, "Single-domain spectroscopy of self-assembled photonic crystals" *Appl. Phys. Lett.* **76**, 1627 - 1629 (2000)
- [81] T. Maka, S.G. Romanov, C.M. Sotomayor Torres, M. Müller and R. Zentel, "Dye-Polymer-Opal Composites as Photonic Crystals" *phys. stat. sol. (b)* **215**, 307 - 312 (1999)
- [82] A. Rogach, A. Susa, F. Caruso, G. Sukhorukov, A. Kornowski, S. Kershaw, H. Möhwald, A. Eychmüller and H. Weller, "Nano- and Microengineering: 3-D Colloidal Photonic Crystals Prepared from Sub- $\mu$ m-sized Polystyrene Latex Spheres Pre-Coated with Luminescent Polyelectrolyte/Nanocrystal Shells" *Adv. Mater.* **12**, 333 - 337 (2000)
- [83] M.D. Lechner, K. Gehrke and E.H. Nordmeier, *Makromolekulare Chemie*, 1. ed., Birkhäuser, Basel (1993)
- [84] J. W. Goodwin, J. Hearn and C.C Ho, "Studies on the Preparation and Characterisation of Monodisperse Polystyrene Latices" *Colloid Polym. Sci* **252**, 464 - 471 (1974)
- [85] B. Saunders and B. Vincent, "Microgel particles as model colloids: theory, properties and applications" *Adv. Colloid. Interface Sci.* **80**, 1 - 25 (1999)
- [86] M. Egen, "Herstellung und Modifizierung von monodispersen Polymerlatices", *Diploma Thesis*, Fachbereich Chemie, Bergische Universität Wuppertal (2000)
- [87] B. Griesebock, "Herstellung von Photonischen Kristallen aus Kolloidlösungen", *Diploma Thesis*, Fachbereich Physik der Bergischen Universität Wuppertal und Inst. für organische Chemie der Johannes Gutenberg Universität Mainz (2001)
- [88] B. Gates, D. Qin and Y. Xia, "Assembly of Nanoparticles into Opaline Structures over Large Areas" *Adv. Mater.* **11**, 466 - 469 (1999)
- [89] O.D. Velev, N.D. Denkov, V.N. Paunov, P.A. Kralchevsky and K. Nagayama, "Direct measurement of lateral capillary forces" *Langmuir* **9**, 3702 - 3709 (1993)
- [90] H. Ströcker, *Taschenbuch der Physik*, 2. ed., Harry Deutsch, Frankfurt/Main (1994)

- [91] N. Ekdawi and R.J. Hunter, "Sedimentation of disperse and coagulated suspensions at high particle concentrations" *Colloids and Surfaces* **15**, 147 - 159 (1985)
- [92] R.C. Salvarezza, L. Vázquez, H. Míguez, R. Mayoral, C. López and F. Meseguer, "Edward-Wilkinson Behavior of Crystal Surfaces Grown By Sedimentation of SiO<sub>2</sub> Nanospheres" *Phys. Rev. Lett.* **77**, 4572 - 4575 (1996)
- [93] Gerhard Müller, "Trocknungsrisse in Stärke (in German)" *Physikalische Blätter* **55**, 35 - 37 (1999)
- [94] S.G. Romanov, T. Maka, C.M. Sotomayor Torres, M. Müller and R. Zentel, "Thin Film Photonic Crystals" *Synth. Met.* **116**, 475 - 479 (2001)
- [95] R. Amos, J.G. Rarity, P.R. Tapster and T.J. Shepherd, "Fabrication of large-area face-centered-cubic hard-sphere colloidal crystals by shear alignment" *Phys. Rev. E* **61**, 2929 - 2935 (2000)
- [96] P. Ferrand, M. Egen, B. Griesebock, J. Ahopelto, M. Müller, R. Zentel, S. G. Romanov and C. M. Sotomayor Torres, "Self-assembly of three-dimensional photonic crystals on structured silicon wafers" *Appl. Phys. Lett.* **81**, 2689 - 2691 (2002)
- [97] W.L. Vos and H.M. van Driel, "Higher order Bragg diffraction by strongly photonic fcc crystals: onset of a photonic bandgap" *Phys. Lett. A* **272**, 101 - 106 (2000)
- [98] J.E.G.J. Wijnhoven and W.L. Vos, "Preparation of Photonic Crystals Made of Air Spheres in Titania" *Science* **281**, 802 - 804 (1998)
- [99] A. Blanco, E. Chomski, S. Grachtchak, M. Ibsate, S. John, S. W. Leonard, F. Meseguer C. López *et al.*, "Large-scale synthesis of a silicon photonic crystal with a complete three-dimensional bandgap near 1.5 micrometres" *Nature* **405**, 437 - 440 (2000)
- [100] S.G. Romanov, H.M. Yates, M.E. Pemble and R.M. de la Rue, "Impact of GaP layer deposition upon photonic bandgap behaviour of opal" *J. Phys.: Cond. Matter* **12**, 339 - 348 (2000)
- [101] S.G. Romanov, D.V. Shamshur and C.M. Sotomayor Torres, "Conductivity of the three-dimensional self-organised lattices of quantum dots", in *Quantum Confinement: Quantum wires and dots*, edited by M. Cahay, S. Bandyopadhyay, J.P. Leburton and M. Razegu (Electrochemical Society Proceedings, Pennington, USA, 1996) Vol. PV 95-17, pp. 3 - 13
- [102] Yu.A. Vlasov, N. Yao and D.J. Norris, "Synthesis of Photonic Crystals for Optical Wavelengths from Semiconductor Quantum Dots" *Adv. Mater.* **11**, 165 - 169 (1999)
- [103] G. Domingo, R.S. Itoga and C.R. Cannewurf, "Fundamental Optical Absorption in SnS<sub>2</sub> and SeS<sub>2</sub>" *Phys. Rev.* **143**, 536 - 541 (1966)
- [104] H. Cohen, M. Folman, T. Maniv, R. Brenner, E. Lifshitz and Z. Esterlit, "Electronic Excitations in SnS<sub>2</sub>: An electron-energy-loss-spectroscopy study" *Phys. Rev. B* **46**, 4446 - 4455 (1992)
- [105] L.S. Price, I.P. Parkin, A.M.E. Hardy, R.J.H. Clark, T.G. Hibbert and K.C. Molloy, "Atmospheric Pressure Chemical Vapor Deposition of Tin Sulfides (SnS, Sn<sub>2</sub>S<sub>3</sub>, and SnS<sub>2</sub>) on Glass" *Chem. Mater.* **11**, 1792 - 1799 (1999)
- [106] L.S. Price, I.P. Parkin, T.G. Hibbert and K.C. Molloy, "Atmospheric Pressure CVD of SnS and SnS<sub>2</sub> on Glass" *Chem. Vapor Depos.* **4**, 222 - 225 (1998)
- [107] A. Theoharidis, "Project on Photonic Crystals", *MSc Thesis*, Institute of Materials Science, BUGH Wuppertal / University of Essex (2000)

- [108] J. Brandrup and E.H. Immergut, *Polymer Handbook*, 3. ed., Wiley, New York (1989)
- [109] S. G. Romanov, T. Maka, C. M. Sotomayor Torres, M. Müller, R. Zentel, D. Cassagne, J. Manzanares-Martinez and C. Jouanin, "Diffraction of light from thin-film polymethylmethacrylate opaline photonic crystals" *Phys. Rev. E* **63**, 056603 (2001)
- [110] J.B. Pendry and A. MacKinnon, "Calculation of photon dispersion relations" *Phys. Rev. Lett.* **69**, 2772 - 2775 (1992)
- [111] P.M. Bell, J.B. Pendry, L.M. Moreno and A.J. Ward, "A program for calculating photonic band structures and transmission coefficients of complex structures" *Comp. Phys. Comm.* **85**, 306 - 322 (1995)
- [112] H. Míguez, V. Kitaev and G.A. Ozin, "Band spectroscopy of colloidal photonic crystal films" *Appl. Phys. Lett.* **84**, 1239 - 1241 (2004)
- [113] H.M. van Driel and W.L. Vos, "Multiple Bragg wave coupling in photonic band-gap crystals" *Phys. Rev. B* **62**, 9872 - 9875 (2000)
- [114] H.P. Schriemer, H.M. van Driel, A.F. Koenderink and W.L.Vos, "Modified spontaneous emission spectra of laser dye in inverse opal photonic crystals" *Phys. Rev. A* **63**, 011801(R) (2001)
- [115] J. Rarity and C. Weisbuch, *Microcavities and Photonic Bandgaps: Physics and Applications* (NATO ASI Series E, Vol. 315), Kluwer, Dordrecht (1996)
- [116] T. Yamasaki and T. Tsutsui, "Spontaneous emission from fluorescent molecules embedded in photonic crystals consisting of polystyrene microspheres" *Appl. Phys. Lett.* **72**, 1957 - 1959 (1998)
- [117] S.G. Romanov, A.V. Fokin and R.M. de la Rue, "Eu<sup>3+</sup> Emission in an Anisotropic Photonic Bandgap Environment" *Appl. Phys. Lett.* **76**, 1656 - 1658 (2000)
- [118] S.G. Romanov, D.N. Chigrin, V.G. Solovyev, T. Maka, N. Gaponik, A. Eychmüller, A.L. Rogach and C. M. Sotomayor Torres, "Light emission in a directional photonic bandgap" *phys. stat. sol. (a)* **197**, 662 - 672 (2003)
- [119] M. Megens, JEGJ Wijnhoven, A. Lagendijk and W.L. Vos, "Light sources inside photonic crystals" *J. Opt. Soc. Am. B* **16**, 1403 - 1408 (1999)
- [120] S. G. Romanov, T. Maka, C. M. Sotomayor Torres, M. Müller and R. Zentel, "Emission properties of dye-polymer-opal photonic crystals" *J. Lightwave Technol.* **17**, 2121 - 2127 (1999)
- [121] T. Suzuki and P.K.L. Yu, "Emission power of an electric dipole in the photonic band structure of the fcc lattice" *J. Opt. Soc. Am. B* **12**, 570 - 582 (1995)
- [122] S. John and T. Quang, "Spontaneous Emission near the edge of a photonic band gap" *Phys. Rev. A* **50**, 1764 - 1769 (1994)
- [123] J. Huang, N. Eradat, M. E. Raikh, Z. V. Vardeny, A. A. Zakhidov and R.H. Baughman, "Anomalous coherent backscattering of light from opal photonic crystals" *Phys. Rev. Lett.* **86**, 4815 - 4818 (2001)
- [124] A.F. Koenderink, L. Bechger, A. Lagendijk and W. L. Vos, "An experimental study of strongly modified emission in inverse opal photonic crystals" *phys. stat. sol. (a)* **197**, 648 - 661 (2003)
- [125] A. Moroz, "Three-dimensional complete photonic-band-gap structures in the visible" *Phys. Rev. Lett.* **83**, 5274 - 5277 (1999)

- [126] J. Zhou, Y. Zhou, S.L. Ng, H.X. Zhang, W.X. Que, Y.L. Lam, Y.C. Chan and C.H. Kam, "Three-dimensional photonic band gap structure of a polymer-metal composite" *Appl. Phys. Lett.* **76**, 3337 - 3339 (2000)
- [127] K. Yoshino, Y. Kawagishi, M. Ozaki and A. Kose, "Mechanical tuning of the optical properties of plastic opal as a photonic crystal" *Jpn. J. Appl. Phys.* **38**, L786 - L788 (1999)
- [128] K. Sumioka, H. Kayashima and T. Tsutsui, "Tuning of the optical properties of inverse opal photonic crystals by deformation" *Adv. Mater.* **14**, 1284 - 1286 (2002)
- [129] S.G. Romanov, H.M. Yates, R.M. de la Rue and M.E. Pemble, "Opal-based photonic crystal with double photonic bandgap structure" *J. Phys.: Cond. Matter* **12**, 8221 - 8229 (2000)
- [130] P. Jiang, G.N. Ostojic, R. Narat, D.M. Mittelman and V.L. Colvin, "The Fabrication and Bandgap Engineering of Photonic Multilayers" *Adv. Mater.* **13**, 389 - 393 (2001)
- [131] S.G. Romanov, T. Maka, V.G. Solovyev, P. Ferrand, C.M. Sotomayor Torres, B. Griesebock, M. Egen *et al.*, "Photonic Crystals Based on Two-Layer Opaline Heterostructures", in *Materials and Devices for Optoelectronics and Microphotronics*, edited by R.B. Wehrspohn, S. Noda, C. Soukoulis and R. März (MRS Proceedings, 2002), pp. L7.7.1 - 6

## List of Publications and Presentations arisen from this work

### I. Selected talks at international conferences:

*Photonic Crystals – basic concepts,*

Instituto de Microelectrónica de Madrid, Seminar talk 18. Nov. 1998

*Photonische Kristalle aus Opal- Halbleiter- und Opal-Polymer Verbundstrukturen,*

MPI für Mikrostrukturphysik Halle, Vorbereitungstreffen zum DFG Schwerpunkt Photonische Kristalle, Halle, 8. Jun. 1999

*Three-dimensional anisotropic Photonic Crystals working in the visible,*

SPIE-Photonic West Conference, San Jose, USA, 26. Jan. 2000

*Photonic Crystals – basic concepts of opal based structures,*

Boston University, USA, Photonics Center, Group Seminar Prof. B. Goldberg, 3. Feb. 2000

*Dye/Polymer Opal Composites as Photonic Crystals,*

DPG Frühjahrstagung Regensburg, 28. Mar. 2000

*Dielectric-polymer nanocomposites and thin films as Photonic Crystals,*

2<sup>nd</sup> SFB 513 Workshop „Nanostructures at Surfaces and Interfaces“, Konstanz, 6. Jul. 2000

*Self-Focusing of Emission From Thin Film Photonic Crystals,*

CLEO/Europe-IQEC, Nice, France 14. Sept. 2000

*Angle resolved photoluminescence studies of thin film Photonic Crystals and their replicas,*

DPG Frühjahrstagung Hamburg, 27. Mar. 2001

### II. Publications:

T. Maka, S.G. Romanov, C.M. Sotomayor Torres, M. Müller, R. Zentel, “Dye-Polymer-Opal Composites as Photonic Crystals”, *phys. stat. sol. (b)* **215**, 307 - 312 (1999)

S.G. Romanov, T. Maka, C.M. Sotomayor Torres, M. Müller, R. Zentel. “Photonic band gap effects upon the light emission from a dye-polymer-opal composite”, *Appl. Phys. Lett.* **75**, 1057 - 1059 (1999)

S.G. Romanov, T. Maka, C.M. Sotomayor Torres, M. Müller, R. Zentel, “Emission Properties of Dye-Polymer-Opal Photonic Crystals”, *Journal Lightw. Technol.* **17**, 2121 - 2127 (1999)

M. Müller, R. Zentel, T. Maka, S.G. Romanov, C.M. Sotomayor Torres, “Dye containing polymer beads as photonic crystals”, *Polymer preprints* **41**, 810 - 811 (2000)

M.V. Maximov, I.L. Krestnikov, Yu.M. Shernyakov, A.E. Zhukov, N.A. Maleev, Yu.G. Musikhin, V.M. Ustinov, Zh.I. Alferov, A.Yu. Chernyshov, N.N. Ledentsov, D. Bimberg, T. Maka, C.M. Sotomayor Torres, “InGaAs-GaAs Quantum Dots for Application in Long Wavelength (1.3  $\mu\text{m}$ ) Resonant Vertical Cavity Enhanced Devices”, *JEM* **29**, 486 - 493 (2000).

M. Müller, R. Zentel, T. Maka, S.G. Romanov, C.M. Sotomayor Torres. “Dye Containing Polymer Beads as Photonic Crystals”, *Chem. Mater* **12**, 2508 - 2512 (2000)

N.N. Ledentsov, M.V. Maximov, D. Bimberg, T. Maka, C.M. Sotomayor Torres, I.V. Kochnev, I.L. Krestnikov, V.M. Lantratov, N.A. Cherkashin, Yu.M. Musikhin, Zh.I. Alferov, "1.3  $\mu\text{m}$  luminescence and gain from defect-free InGaAs-GaAs quantum dots grown by metal-organic chemical vapour deposition", *Semicond. Sci. Technol.* **15**, 604 - 607 (2000)

M. Müller, R. Zentel, T. Maka, S.G. Romanov, C.M. Sotomayor Torres. "Photonic crystals with high refractive index contrast", *Adv. Mater.* **12**, 1499 - 1503 (2000)

T. Maka, S.G. Romanov, C.M. Sotomayor Torres, M. Müller, R. Zentel, "Three-Dimensional Photonic Crystals Working in the Visible", in *Micro and Nano-Photonic Materials and Devices*, Eds: J.W. Perry, A. Scherrer, Proceedings of SPIE, Vol 3937, 18 - 31 (2000)

S.G. Romanov, T. Maka, C.M. Sotomayor Torres, M. Müller, R. Zentel, "Thin Film Photonic Crystals", Proc. Int. Symposium *Nanostructures: Physics and Technology*, St. Petersburg 2000

S.G. Romanov, T. Maka, C.M. Sotomayor Torres, M. Müller R. Zentel, "Thin film photonic crystals", *Synthetic Metals* **116**, 475 - 479 (2001)

S.G. Romanov, T. Maka, C. M. Sotomayor Torres, M. Müller, R. Zentel, D. Cassagne, J. Manzanares-Martinez and C. Jouanin, "Diffraction of light from thin-film polymethylmethacrylate opaline Photonic Crystals", *Phys. Rev. E* **63**, 056603 (2001)

C.M. Sotomayor Torres, S.G. Romanov, T. Maka, M. Müller, R. Zentel, "Dielectric-Polymer Nanocomposites and Thin Film Photonic Crystals: Towards Three-Dimensional Photonic Crystals with a Bandgap in the Visible Spectrum", in *Frontiers of Nano-Optoelectronic Systems*, Eds: L. Pavesi and E. Buzaneva, NATO ASI series 23 - 39 (2001)

S.G. Romanov, T. Maka, C.M. Sotomayor Torres, M. Müller, R. Zentel, "Thin opaline Photonic crystals" in *Photonic Crystals and Light Localization in the 21<sup>st</sup> Century*, Ed: C.M. Soukoulis, NATO ASI Series Vol. 563, 253 - 262 (2001)

S.G. Romanov, T. Maka, C.M. Sotomayor Torres, M. Müller, R. Zentel, "Emission in a  $\text{SnS}_2$  inverted opaline photonic crystal" *Appl. Phys. Lett.* **79**, 731 - 733 (2001)

S.G. Romanov, T. Maka, C.M. Sotomayor Torres, M. Müller, R. Zentel, "Suppression of spontaneous emission in incomplete opaline photonic crystals", *J. Appl. Phys.* **91**, 9426 - 9428 (2002)

S.G. Romanov, T. Maka, V.G. Solovyev, P. Ferrand, C.M. Sotomayor Torres, B. Griesebock, M. Egen, M. Müller, R. Zentel, N. Gaponik, A. Eychmüller, A.L. Rogach, J. Manzanares-Martinez, and D. Cassagne. "Photonic Crystals Based on Two-Layer Opaline Heterostructures", in *Materials and Devices for Optoelectronics and Microphotonics*, MRS Proc., Vol.722 Eds: R.B. Wehrspohn, S. Noda, C. Soukoulis, R. März, L7.7.1 - 6 (2002)

S.G. Romanov, D.N. Chigrin, V.G. Solovyev, T. Maka, N. Gaponik, A. Eychmüller, A.L. Rogach, C. M. Sotomayor Torres, "Light emission in a directional photonic bandgap", *phys. stat. sol. (a)* **197**, 662 - 672 (2003)

T. Maka, D.N. Chigrin, S.G. Romanov, C.M. Sotomayor Torres, "3-D Photonic Crystals in the Visible Regime", in *Progress in Electromagnetics Research*, PIER 41, Eds: A. Priou and T. Itoh, 307 - 335 (2003)

## Acknowledgements

I would like to take the opportunity to thank those people who contributed by their support to this thesis.

First of all I would like to express my gratitude to my supervisor, Prof. Clivia M. Sotomayor Torres, for the opportunity to work in her group and for introducing me into the world of photonic crystals. I also would like to thank for her continuous support and all the backstage work she did to keep the lab running.

A special thank to Dr. Sergei G. Romanov for his help, suggestions and explanations. His experience and expertise have been invaluable.

I am grateful to Prof. Rudolf Zentel and his colleagues – especially Drs. Manfred Müller, M. Egen and B. Griesebock – for the uncomplicated collaboration and continuous supply with samples.

I would like to thank Dr. Dmitry Chigrin for his help and contribution to the theoretical analysis of the experimental data and many interesting discussions.

TMM and PWM calculations done by Dr. David Cassagne are gratefully acknowledged as well as the good collaboration within the PHOBOS project.

I would also like to thank the former and present secretaries, C. Runte and R. Gärtig for their help with the paperwork and guidance through the jungle of administration ...

I enjoyed the time at the Institute of Materials Science very much. Many thanks to all former and present colleagues for many fruitful discussions, and the good atmosphere in the lab, in particular to J.U. Bruch, N. Roos, Drs. J. Seekamp, T. Sidiki, V. Soloviev, P. Ferrand, and S. Zankovych.

Last but not least all my gratitude to my family, especially to my wife Susanne for her patience and continuous mental support.